Interfacial Nanostructure and Wetting Behavior of Thin Ionic Liquid Films on Solid Surfaces

Rita Moreira Carvalho
Master's in Chemistry
Department of Chemistry and Biochemistry
2023

Supervisor
José Carlos da Silva Costa, Investigador Auxiliar, Faculty of Sciences of the University of Porto

Co-supervisor
Margarida Maria Henriques Mesquita Bastos, Professora Associada, Faculty of Sciences of the University of Porto

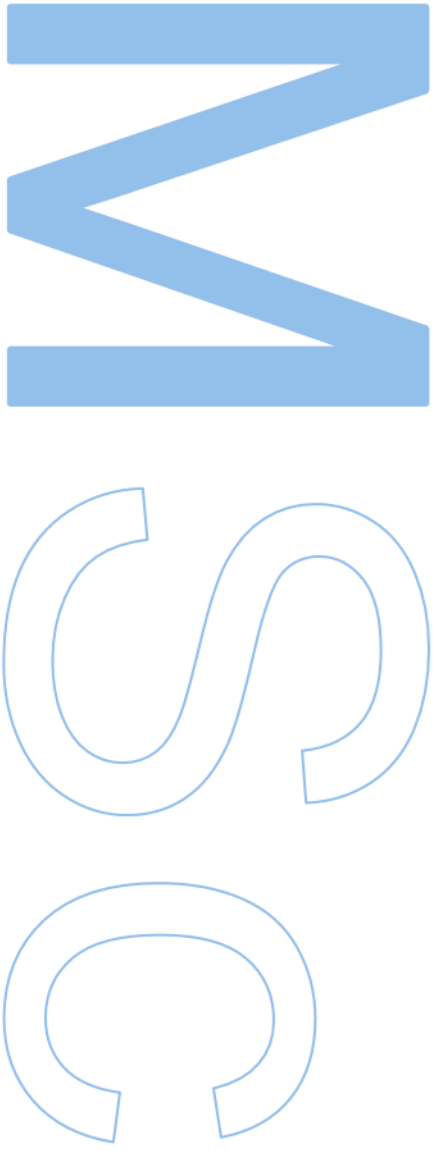


U.PORTO
FACULDADE DE CIÊNCIAS
UNIVERSIDADE DO PORTO

Acknowledgments

During the research work for my dissertation, I inevitability found myself in reliance upon the assistance of several individuals. In this vein, I wish to extend my sincerest gratitude to all those who, in various capacities, contributed to my academic and personal life over the past academic year:

I wish to express my profound appreciation to Dr. José Carlos da Silva Costa for his unwavering guidance throughout these recent months, his expert tutelage in laboratory techniques, and his valuable counsel and critiques, both during the experimental phase and in the composition of this dissertation.

I also express my appreciation to Professor Dr. Margarida Maria Henriques Mesquita Bastos for her scholarly guidance, which encompassed recommendations regarding potential research directions and her meticulous scrutiny of the dissertation, replete with constructive suggestions and insightful discussions aimed at enhancing the quality of the written work.

I extend my gratitude to Professor Dr. Luís Manuel das Neves Belchior Faia dos Santos for his attention since my involvement in his research group during my undergraduate project, ensuring my seamless integration into the realm of Physical Chemistry.

My heartfelt thanks go to Cândida Neto for the countless hours we spent together conducting SEM analyses, thereby yielding the comprehensive results presented herein. Her boundless patience and genuine care greatly facilitated our collaborative efforts.

I wish to extend my appreciation to all my colleagues and friends from the Master's in Chemistry class of 2022/2023 and the Physical Chemistry group for their warm reception, companionship, and unwavering support throughout this academic odyssey.

To my family, I offer my gratitude for their attention, understanding, and steadfast encouragement, not only throughout my academic journey but throughout the entirety of my life.

I would like to thank you all.

Resumo

Esta dissertação descreve o estudo da influência das condições de deposição na morfologia de filmes de líquidos iónicos obtidos através da deposição a vapor, usando uma metodologia de evaporação térmica a vácuo que permite um controlo preciso dos parâmetros de deposição para a produção de filmes finos com maior reprodutibilidade. Foram examinados quatro líquidos iónicos (ILs) baseados no catião alquilimidazólio: $[C_2C_1im][NTf_2]$; $[C_2C_1im][OTf]$; $[C_8C_1im][NTf_2]$; $[C_8C_1im][OTf]$. O comprimento da cadeia alquílica (C_2C_1 ou C_8C_1) e o tipo de anião (NTf_2 ou OTf) foram variados para investigar o impacto destes nucleação e crescimento dos filmes. O processo de deposição foi realizado em vários substratos como oxido de índio dopado com estanho (ITO), prata (Ag), ouro (Au), e carbono. As diferentes morfologias nestes substratos permitiram avaliar as interações físicas e químicas dos pares iónicos com a superfície e consequentemente, os mecanismos de nucleação e crescimentos dos filmes de ILs.

Os mecanismos de nucleação e crescimento foram significativamente influenciados pelos parâmetros de deposição, particularmente a taxa de fluxo de massa e a temperatura de substrato. Aumentos em ambos os parâmetros levaram a uma intensificação dos mecanismos de coalescência devido ao aumento da difusão superficial dos ILs. Em termos de interações com a superfície, a deposição de pequenas quantidades de ILs levou à formação de gotículas mais pequenas na superfície de Ag em comparação com a superfície de ITO, resultado de uma maior afinidade substrato-IL ou um incremento da rugosidade da superfície. A morfologia dos filmes de IL foi significativamente alterada quando a deposição foi realizada perto da interface metal-ITO. A mobilidade dos pares iónicos foi notavelmente aumentada nestas regiões, com uma maior tendência para a difusão dos pares iónicos ao longo da superfície de ITO em direção ao metal. O aumento do comprimento da cadeia alquílica do catião melhorou o comportamento de espalhamento dos ILs, especialmente em superfícies metálicas, onde foi observada a formação de filmes coalescidos. Por último, investigou-se o efeito do revestimento dos substratos com carbono na morfologia e molhabilidade dos filmes de IL. Especialmente, para ILs com cadeia alquílica curta, a superfície do filme de carbono induziu um crescimento bidimensional do filme de IL, seguido pelo subsequente crescimento em ilhas. Em contraste, para ILs com cadeia alquílica longa, ocorreu um crescimento em camadas sem a formação de gotículas, resultando em filmes de IL altamente uniformes e coalescidos. A extensão das mudanças morfológicas observadas nos filmes de IL foi influenciada por dois fatores cruciais: a espessura do filme de carbono na superfície do substrato e a quantidade de deposição de IL.

Palavras-chave: líquidos iónicos, filmes finos, evaporação térmica, *sputtering*, nucleação e crescimento, micro- e nanogotículas, filme continuo, condições de deposição, interface, revestimento de carbono.

Abstract

This dissertation describes the study of the influence of the deposition conditions on the morphology of ionic liquid films obtained through vapor deposition, using a customized vacuum thermal evaporation methodology that provides precise control over the deposition parameters for producing thin films with higher reproducibility. Four alkylimidazolium ionic liquids (ILs) were examined: $[C_2C_1im][NTf_2]$, $[C_2C_1im][OTf]$; $[C_8C_1im][NTf_2]$, $[C_8C_1im][OTf]$. The cation alkyl side chain length (C_2C_1 or C_8C_1) and the anion type (NTf_2 or OTf) were varied to investigate their impact on the nucleation and growth of the films. The deposition process was carried out on various substrates such as indium-tin oxide (ITO), silver (Ag), gold (Au), and carbon. The different morphologies observed on these substrates allowed insight into the physical and chemical interactions of the ion pairs with the surfaces and the consequent nucleation and growth mechanisms of IL films.

The nucleation and growth mechanisms were significantly influenced by deposition parameters, particularly the mass flow rate and substrate temperature. Increases in both of these parameters were found to enhance droplet coalescence mechanisms, characteristic of higher surface diffusion. In terms of surface interactions, the deposition of small amounts of ILs led to the formation of smaller droplets on Ag surfaces when compared to ITO surfaces, resulting from either better substrate-IL affinity or an increase in surface roughness. The morphology of the IL films was significantly altered when the deposition was conducted near a metal-ITO interface. The mobility of the ion pairs was notably enhanced in these regions, with a greater tendency for the ion pairs to diffuse along the ITO surface towards the metal. An increase in the length of the cation alkyl side chain enhanced the spreading behavior of the ILs, especially on metal surfaces, where the formation of coalesced films was observed. Lastly, the effect of carbon coating on the morphology and wetting behavior of IL films was investigated. Specifically, for short-chain ILs, the carbon film surface induced two-dimensional growth of the IL film, followed by subsequent island growth. In contrast, for long-chain ILs deposited, layer-by-layer growth occurred without island formation, resulting in highly uniform and coalesced IL films. The extent of morphological changes observed in the IL films was found to be influenced by two crucial factors: the thickness of the carbon film on the substrate surface and the amount of IL deposition.

Keywords: ionic liquids, thin films, thermal evaporation, sputtering, nucleation and growth, micro- and nanodroplets, continuous film, deposition conditions, interface, carbon coating.

Table of Contents

List of Tables

List of Figures

List of Abbreviations, Acronyms and Symbols

$[C_nC_1im]$	1-alkyl-3-methylimidazolium
$[C_2C_1im]$	1-ethyl-3-methylimidazolium
$[C_8C_1im]$	1-octyl-3-methylimidazolium
$[C_nC_1im][PF_6]$	1-alkyl-3-methylimidazolium hexafluorophosphate
$[C_2C_1im][NTf_2]$	1-ethyl-3-methylimidazolium bis[(trifluoromethyl)sulfonyl]imide
$[C_2C_1im][OTf]$	1-ethyl-3-methylimidazolium triflate
$[C_4C_1im][Ac]$	1-butyl-3-methylimidazolium acetate
$[C_4C_1im][NTf_2]$	1-butyl-3-methylimidazolium bis[(trifluoromethyl)sulfonyl]imide
$[C_4C_1Pyrr][NTf_2]$	1-butyl-3-methylpyrrolidinium bis[(trifluoromethyl)sulfonyl]imide
$[C_4C_1im][PF_6]$	1-butyl-3-methylimidazolium hexafluorophosphate
$[C_4C_1im][BF_4]$	1-butyl-3-methylimidazolium tetrafluoroborate
$[C_6C_1im][NTf_2]$	1-hexyl-3-methylimidazolium bis[(trifluoromethyl)sulfonyl]imide
$[C_8C_1im][NTf_2]$	1-octyl-3-methylimidazolium bis[(trifluoromethyl)sulfonyl]imide
$[C_8C_1im][OTf]$	1-octyl-3-methylimidazolium triflate
[OTf]	Triflate Anion
$[NTf_2]$	Bis(trifluoromethylsulfonyl)imide Anion
$[PF_6]$	Hexafluorophosphate Anion
$[BF_4]$	Tetrafluoroborate Anion
3D	Three Dimensions
2D	Two Dimensions
ΔG	Gibbs energy in a surface
ΔG_v	Gibbs energy associated with vapor condensation
Δf	Crystal Resonance Frequency Variation with the Deposited Mass

Γ	Interfacial Tension
$\gamma_{l\text{-}v}$ or γ_{lg}	Vapor-Liquid Superficial Tension
$\gamma_{s\text{-}v}$ or γ_{sg}	Solid- Vapor Superficial Tension
$\gamma_{s\text{-}l}$ or γ_{sl}	Solid- Liquid Interfacial Tension
θ_c	Droplet Contact Angle
$\Phi_{\text{Knudsen cell}}$	Mass Flux that exits the Knudsen Cell
$\Phi_{\text{substrate}}$	Mass Flux that reach the Substrate
Φ	Mass Flow Rate / Deposition rate
Ω /square	Sheet Resistance
Å/s	Angstrom per second
A_0	Effusion Cell Orifice Area
AT	Crystal Cut with temperature compensation
BETI	Bis((perfluoroethyl)sulfonyl)imide Anion
Br	Bromide Anion
BSE	Backscattered Electron
CAS	Critical Alkyl Size
CD	Chemical Deposition
CF_3SO_3	Trifluoromethanesulfonate Anion
CNTs	Carbon Nanotubes
CVD	Chemical Vapor Deposition
CW-IR	Continuous Infrared Waves
FAP	Tris(pentafluorethyl)trifluorophosphate
g	Geometric Factor
h	Monolayer Thickness
IL	Ionic Liquid

ILs	Ionic Liquids
ITO	Indium Tin Oxide
L	Mobile Wire Length
l	Orifice Thickness
M	Molar Mass
MBE	Molecular Beam Epitaxy
ML	Monolayer
MOFs	Metal-Organic Frameworks
p	Pressure
ρ	Density
PD	Physical Deposition
PTFE	Polytetrafluoroethylene
PVD	Physical Vapor Deposition
QCM	Quartz Crystal Microbalance
R	Gas Constant
r	Orifice Radius
r_{cr}	Critical Radius or Minimum Radius for Cluster Formation
RTILs	Room Temperature Ionic Liquids
SE	Secondary Electron
SEM	Scanning Electron Microscopy
T	Temperature
T_{evp}	Evaporation Temperature
T_{subst}	Substrate Temperature
T_m	Fusion Temperature
T_g	Glass Transition Temperature

UHV	Ultra-High Vacuum
w_0	Transmission Probability Factor

1. Motivations and Goals

Ionic liquids have gained increased attention due to their exceptional physical and chemical properties. Notably, their negligible vapor pressure at room temperature and high thermal and chemical stability make these materials exceedingly versatile and applicable, particularly in the development of new materials and in industrial contexts. Many applications require the combination of ionic liquids with solid surfaces, emphasizing the importance of understanding these interactions. Furthermore, as the use of ionic liquids increases, new questions about their deposition on solid surfaces have emerged. Previously these studies of ionic liquids were primarily focused on the understanding of their interactions with ITO and metallic surfaces. It has also been demonstrated that differentiation of the alkyl chain may influence the morphology of ILs on ITO and metallic surfaces.

To further improve the knowledge of ionic liquid films, three main objectives were envisaged for this dissertation: i) to gain insight into the influence of deposition conditions on the nucleation and growth of IL films; ii) to understand the impact of an ITO/Ag interface on the morphology of ionic liquids films; and iii) to examine the effect of carbon contamination on the morphology of ionic liquids films (by applying an amorphous carbon coating on the ITO surface).

As part of the experimental strategy, ionic liquids featuring different combinations of cations and anions were deposited. This led to the formation of micro- and nanodroplets or continuous films, depending on the interactions between the IL and the substrate.

2. Introduction

2.1. Ionic Liquids

Over the past decade, society has become more aware of how we use available resources and the environmental consequences of their usage. With the increase in demand for the development of new materials and alternative solutions to more toxic processes, the scientific community has been focusing on research into more environmentally sustainable materials and methodologies. One class of materials that is generating interest are the ionic liquids (ILs), due to their outstanding physical and chemical properties [1-3]. ILs can be broadly defined as materials formed by a large organic cation and an organic or inorganic anion, which are stable liquids at broad and relatively low-temperature ranges. In fact, many of these salts are liquids at room temperature, being denominated as room temperature ionic liquids (RTILs) [3-8]. These salts have much lower melting points than the molten salts. Examples of these ILs are those composed of complex organic cations, such as imidazolium, pyrrolidinium, or phosphonium, and different anions, such as chloride, hexafluorophosphate, triflate (OTf), or bis(trifluoromethylsulfonyl)imide (NTf_2).

The structure of ILs can be described as formed by a network of polar domains, where charges are located, and embedded non-polar domains (the alkyl chain of ILs), showing thus a nanostructuration at a molecular level, that influences their properties in bulk and/or at the surface. Canongia Lopes *et al*. did extensive computational simulation studies on ILs with imidazolium cation ($[C_nC_1im][PF_6]$), to analyze the effect of the increase in the alkyl chain [4]. The authors found that with the increase of the alkyl chain, the ILs tended to assemble, interacting with each other through van der Waals interactions, creating a non-polar domain in the IL and that the size of the non-polar domains increases with the increase in the length of the alkyl chain. This leads to a microphase separation, that has been called IL's nanostructuration. The alkyl chains, being nonpolar, at a certain alkyl chain size, that was called the critical alkyl size (CAS) [9,10], the alkyl chain is long enough to show a non-polar behavior. In the case of $[C_nC_1im]$-based ILs, the CAS occurs at $n = 6$, meaning that ILs with shorter alkyl chains ($n < 6$) exhibit a polar behavior with properties similar to molten salts, while ILs with longer alkyl chains ($n > 6$) exhibit non-polar domains and corresponding nonpolar properties. This structural differentiation into polar and nonpolar parts is illustrated in Figure 1.

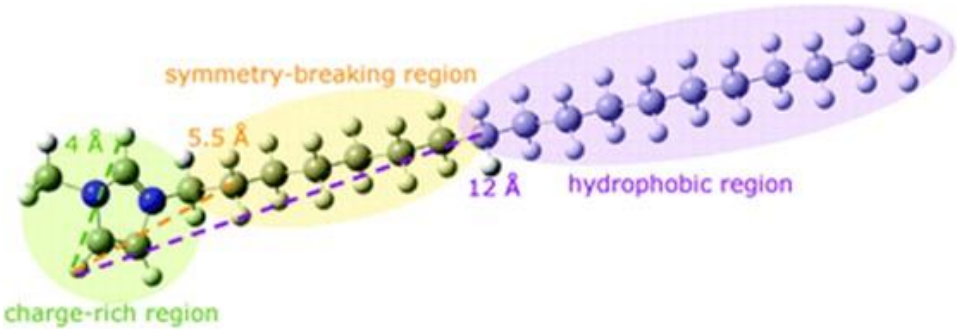

Figure 1. Schematic representation of polar and non-polar areas in 1-methyl-3-octadecylimidazolium cation [$C_{18}C_1$im]. (adapted from [17]).

Independently of the flexibility of roles played by the ions, the asymmetry of cations, and the delocalization of electrostatic charges, strong electrostatic interactions (attraction or repulsion) are felt for all ILs. However, with the increase of the alkyl chain, there's an increase in the number of intermolecular interactions, such as van der Waals, dipole-dipole, and hydrogen-bonding, that compete for the predominance until reaching CAS, where the ILs start to have domains. This junction of polar and non-polar behavior allows to ILs have amphiphilic properties [3-8,11-17].

The different combinations of cations and anions in ILs give them distinct properties. However, most ILs have some common properties such as high viscosity, high ionic conductivity, high thermal and chemical stability, negligible vapor pressure at room temperature, and a particular wetting behavior [3-6,12,16-25]. The lower vapor pressure can be explained by the strong Coulombic interactions between the ions, which hampers the IL from changing to the gas phase. This is shown in their enthalpies of vaporization, where the [$C_nC_1$im]-ILs have typically vapor enthalpies order of 120 to 150 kJ/mol, much superior when compared to water (40.7kJ/mol) [26]. The low vapor pressure allows the use of these materials at high-vacuum techniques not only to evaporate ILs, such as thermal evaporation under reduced pressure or sputtering, as well as in material analysis that requires a high vacuum, such as scanning electron microscopy (SEM) or X-ray photoelectron spectroscopy (XPS).

Another important property of ILs is their viscosity, as some applications require ILs to be used in engineering processes such as stirring, mixing, and/or pupping operations. In general, ILs can be considered viscous liquids, with viscosity values typically ranging from 10 to 500 mPa·s at room temperature [27-29]. The viscosity of ILs is influenced by their molecular structure, particularly by the presence of strong intermolecular interactions. The viscosity of ILs is also affected by their molecular geometry. ILs with

spherical anions or high symmetry are typically more viscous than those with less symmetrical structures [28,30]. The delocalization of charges of the anion, such as in the presence of fluorine, weakens the hydrogen bonding of the ILs and consequently decreases their viscosity. They can exhibit higher viscosity compared to other materials such as oils, with differences of up to 2 or 3 magnitudes. This can be a disadvantage in some applications of ILs [29]. When considering different anions, it is possible to observe an increase in viscosity as follows: NTf_2^- < FAP^- < $BETI^-$ < $CF_3SO_3^-$ < BF_4^- < PF_6^- < Cl^- < Br^-. The ILs with the anion NTf_2^- have lower viscosities due to the high flexibility of their conformation compared to other ILs, such PF_6^- or BF_4^-, with have a more rigid conformation [31]. When examining the variation in cation while keeping the anion and alkyl chain constant, the viscosity of ILs increases in the following sequence: imidazolium < alkylimidazolium < *n*-alkyl pyridinium < pyrrolidinium. In all cases, as the length of the alkyl chain increases, the segregation into polar and non-polar domains also increases, leading to the higher viscosity of the ILs [4-6,31-36]. Conductivity (*k*) is another important property in ILs, especially for electrochemical applications. This property reflects the charge that is carried and the IL's mobility within the system. While ILs have good conductivity, it is generally lower than that observed for a solution of electrolytes with higher concentration. This difference can be attributed to two properties: the interactions between the cation and anion, which hampers the dispersion of charge carriers in the system, and the size of the cation, which reduces the mobility of the carriers within the system [4,37].

ILs have received significant attention due to their versatility and applicability in various fields, such as electrochemistry (e.g., electrodeposition of metals, gas sensors, and biosensors), additives (e.g., lubricants agents and detergents), extraction and separation processes (e.g., micro-extraction or water treatment technologies), carbon capture, fuel purification and as a “design solvent” [3,12,17-19,38,39].

ILs are commonly used as coatings or films in various industrial applications, particularly when prepared under vacuum conditions, due to their unique properties. For many applications, the ILs must interact with solid surfaces. Hence, it is important to study the behavior of the IL at interfaces to design better ILs for the desired applications based on solid grounds [18,40-43].

2.2. Thin Films

The main objective of this point is to emphasize the understanding of ionic liquid properties at the micro- and nanoscale, the techniques used to fabricate thin films, and the potential applications of thin films obtained from ILs. The term “thin films” can be ambiguous, as it is often used to describe any kind of coating layer on a material. However, in general, thin films are defined as layers of material with thicknesses ranging from atomic layers to several micrometers. Thin films made from a particular material often demonstrate distinct properties from their bulk counterparts. The crystallinity, morphology, and functionalities are some parameters that can be used to differentiate between different nanostructured thin films (Figure 2).

Thin films are in a metastable phase because of the lower density of intermolecular interactions in this state, as compared to bulk materials. This means that there’s a tendency for the material to rearrange into more favorable energetic states. The deposition techniques used, and the experimental variables controlled during the process can impact the nucleation and growth of the ionic liquid film, which in turn, affects the inherent structure and thus applicability of the film. Ionic liquid films have a wide range of important applications in various fields, and their distinctive characteristics make them attractive for use in different technologies such as lubricants, electrolytes in batteries and supercapacitors, effective catalysts in a range of chemical reactions, as well as sensors and biosensors [18,41-43].

The selection of a deposition technique can be based on a variety of criteria, but one of the most common factors taken into consideration is the material characteristics, especially at the interface [44]. The next subchapter will present an overview of several deposition techniques utilized for the fabrication of thin films.

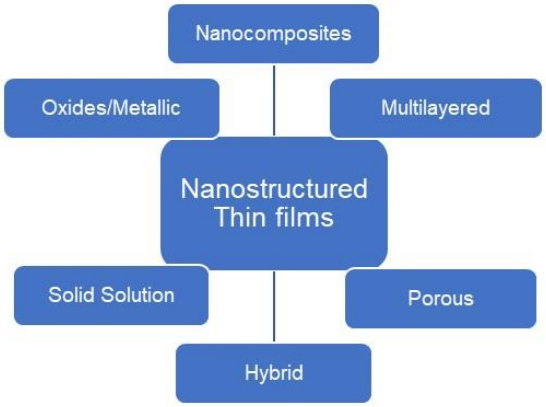

Figure 2. Classification of nanostructured thin films (adapted from [44]).

2.2.1. Deposition Techniques

To create new materials at a nano- and mesoscale with specifications for various applications, new methods of deposition of different materials for the formation of thin films have been developed. Generally, thin films can be obtained using top-down or bottom-up methodologies. Top-down methods involve reducing bulk materials into the nanoscale using physical or chemical exfoliant processes. This allows the production of laminar nanostructures such as nanosheets or nanoflakes. Bottom-up methods are used to fabricate complex nanostructured thin films from atoms or molecules and can be categorized as physical deposition (PD) and chemical deposition (CD) [44]. In chemical deposition, it is necessary to chemically alter the substrate surface to enable the material to interact with the surface and create a film. In physical deposition techniques, the formation of films occurs through only physical processes and does not involve any chemical alteration of the substrate, or the material used for the deposition [45,46].

The scheme below (Figure 3) summarizes the different methodologies and techniques used to form thin films, which include vapor methodologies (physical vapor deposition, PVD, and chemical vapor deposition, CVD) and Wet chemistry methodologies (sol-gel, Langmuir-Blodgett, and electrodeposition).

The timescale for the formation of a thin film using vapor or solution methodologies is very distinct. In solution processes, slower methods can be used to obtain thermodynamically controlled products. On the other hand, vapor-deposition methods are usually preferred to obtain kinetic control, since the vapor-deposition methodologies allow for control of the quantity of material that evaporates and arrives at the surface. This control on the flow that arrives at the surface allows for control of the film formation in a determinate surface. PVD and CVD are commonly used to produce high-quality films, due to the elimination of possible contaminates by using a vacuum chamber system. These methods allow the transfer of material, atom by atom, from the source into a substrate where the film is formed. Film formation by vapor deposition can be described as a process in which the generated vapor condenses on a surface, resulting in the formation of a film or a coating. This type of deposition is carried out in a vacuum chamber to control the deposited material and reduce possible contamination. The vapor can be generated by changing the physical state of the material, classified as PVD, or by chemical reaction, classified as CVD [44].

This work employed two PVD techniques: thermal evaporation under reduced pressure and sputtering.

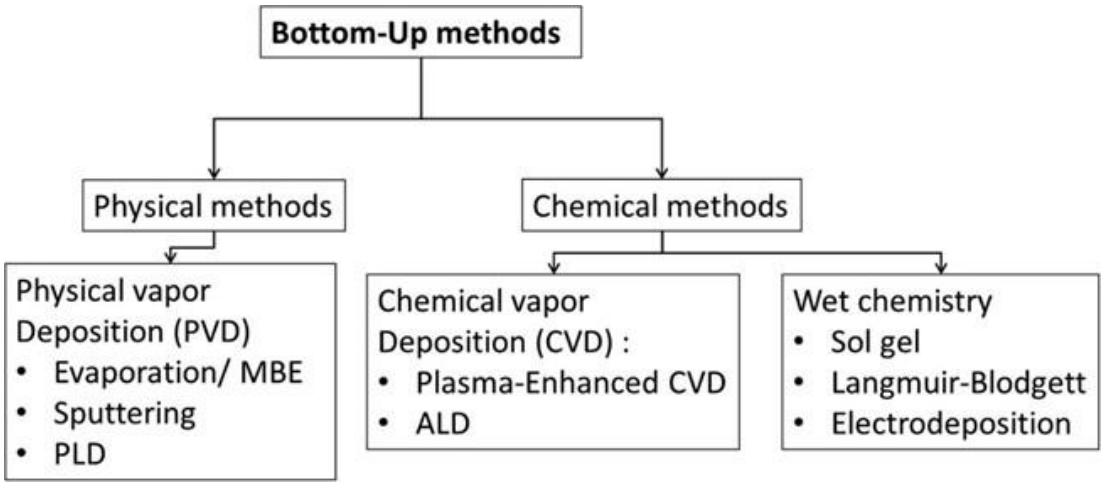

Figure 3. A general categorization of bottom-up approaches for thin film synthesis, accompanied by particular instances for each technique (adapted from [44]).

2.2.1.1. Physical Vapor Deposition

The PVD process enables the formation and growth of thin films through the evaporation or sublimation of the source material. The film is formed at an atomic level without involving any chemical reactions. The thickness of thin films can range from angstroms (Å) to micrometers (µm). The PVD process can be summarized in three steps: first, vaporizing the source material; second, transporting the vapor to the substrate; and third, condensing the vapor onto the substrate to form a thin film or a coating. To ensure a uniform film, the PVD methodology requires precise control over the conditions of deposition, such as vacuum conditions, vapor quantity, and substrate movement. Various techniques are used to generate the vapor, including resistance-heated filaments, electron beams, lasers, conduction, radiation, or radio frequency (RF) induction to heat the source material [44].

Thermal evaporation under reduced pressure

One of the most studied PVD techniques is thermal evaporation under reduced pressure. By using an ultra-high vacuum environment, it is possible to form thin films that are uniform and have the desired thickness. In this technique, the source material is heated to its sublimation or vaporization temperature, causing it to change into the gas phase and condense onto the substrate, forming a thin film. Generally, thermal evaporation with reduced pressure is used to fabricate films of organic compounds, ionic liquids (ILs), and some metals, although higher temperatures are required for the latter. The deposition

occurs in an ultra-high vacuum environment inside a chamber to minimize the presence of residual gases, enabling more particles to evaporate and arrive at the substrate, resulting in a larger film formation. In this technique, the substrate temperature is lower than the source material temperature, promoting particle condensation onto the surface. The final result is a high-purity film that enables cost-effective and efficient deposition [46,47].

In the case of ILs, their evaporation is particularly useful for gaining insight into their volatilities, structure, and cohesive energy [9,47,48].

The main advantages of this methodology are its reproducibility, reduced material usage, and elimination of solvents, as well as the ability to create films with multiple layers of different materials, which number can be controlled. However, there are some disadvantages, such as the use of higher temperatures for metal deposition, the thermal decomposition of certain materials, the inability to deposit some organic materials with low vapor pressure, and the relatively long deposition times. Figure 4 above provides a schematic representation of a thermal evaporation system that utilizes the Joule effect, which can be described as the process where the electric energy is converted into heat through a resistance of the material when the current goes through them [46,49].

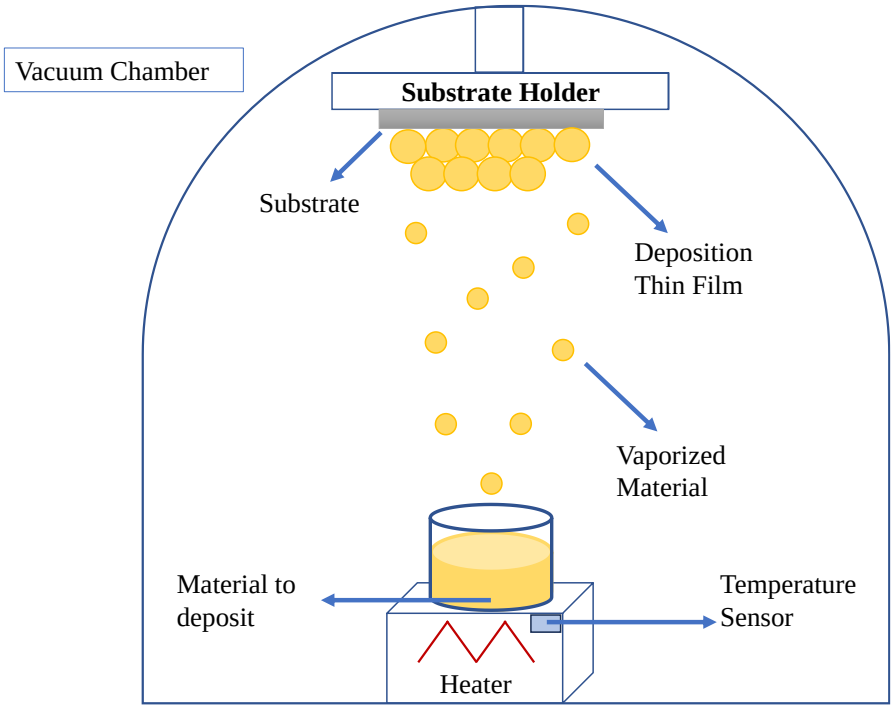

Figure 4. Schematic of the conventional thermal evaporation.

Molecular Beam Epitaxy

Molecular beam epitaxy (MBE) is an advanced form of thermal evaporation. MBE is a technique that allows for the fabrication of a thin film in precise control over the crystal structure in an ultra-high vacuum (UHV) environment. In this technique, the source material is heated to form a vapor, and the resulting atoms or clusters are deposited onto a heated surface, where they diffuse and incorporate into the growing film. The UHV environment prevents interactions between the evaporated atoms/ molecules in the vapor phase, and the evaporation of the material is controlled by a Knudsen effusion cell, which regulates the quantity of material that is released into the chamber by adjusting the orifice area and the temperature of the cell. The substrate temperature is a key point in the formation of thin films using MBE. The substrate must be kept at a lower temperature than that of the vapor so that the atoms/ molecules that arrive at the surface condense and form a film. The number of effusion cells used in the process depends on the complexity of the crystal film being formed and can range from 8 to 14 cells. Each cell emits a different beam of molecules, which condense onto the substrate to allow for the slow growth of thin films, typically one atomic layer at a time [44,50-54].

III-V semiconductors, such as gallium nitride (GaN) or gallium arsenide (GaAs), are among the most studied materials in MBE [49,50]. However, other materials such as silicones, metals, insulators, and ceramics can also be deposited using this technique [41,45]. MBE offers several advantages, including precise control over crystal structure and film thickness, as well as the ability to deposit multiple layers of different materials. However, MBE also has some limitations, such as a slow growth rate, the requirement for UHV conditions, and the need for complex equipment and procedures. Figure 5 provides a schematic representation of an MBE technique [50,52,53].

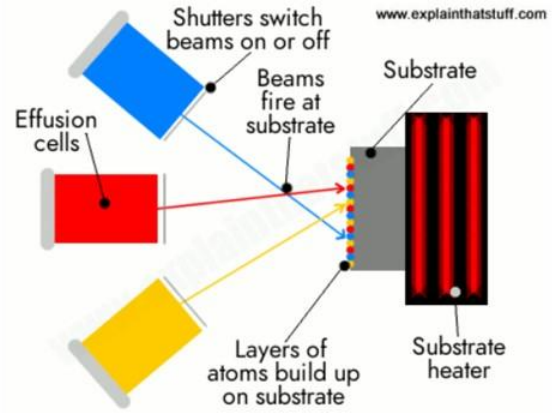

Figure 5. Schematic of the formation of a film using the Molecular Beam Epitaxy technique (adapted from [50]).

For ILs, it has been previously reported that continuous infrared waves are used in a UHV environment (CW-IR) for film deposition. In this technique, the material must absorb radiation in the IR spectrum. In cases where the material does not absorb in the IR spectrum (like the ILs), a precursor like silicic power may be used. This technique allows for real-time, *in situ* monitoring and precise control of the composition, growth, and purity of the formed film [46,54,55].

Sputtering

Sputtering is a deposition technique used to coat surfaces with metals and metal alloys and create metallic nanoparticles. In this technique, plasma is generated inside a chamber to erode the target, liberating atoms that will arrive at the substrate and form a film (Figure 6) [56]. Initially, the vacuum chamber is evacuated to a high vacuum to eliminate most of the air and contaminants present in the chamber. After that, a gas is introduced into the chamber, and the pressure is regulated to the desired level. The gas is typically an inert gas such as argon, which is used to create the plasma that will cause the erosion of the target. The gas pressure and the electrical potential applied to the target can be controlled to optimize the sputtering process and achieve the desired film properties.

In sputtering, a high voltage is applied to the chamber, generating a plasma in which accelerated atoms and electrons collide, causing ionization of the atoms. The positively charged ions are attracted to the negatively charged cathode (located behind the sputtering target), allowing these ions to collide with the target surface and eject atoms from the surface into the vacuum environment and onto the substrate surface. An inert and high molecular weight gas such as argon or xenon is usually used to form the plasma. This reduces the possibility of reactions with other ions and increases the momentum of the ion impact on the substrate, leading to higher deposition rates. Compared to other PVD technologies, sputtering has several advantages. It allows for the deposition of materials regardless of their melting point and can maintain a composition similar to the bulk material when forming films, which is important, especially for alloys [44,57,58].

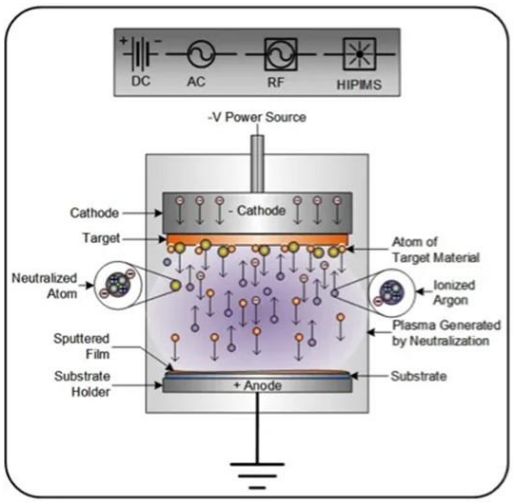

Figure 6. Schematic of a sputtering technique (adapted from [58]).

For fabricating thin films in different applications, the most used sputtering methods are DC sputtering (also known as cathodic or diode sputtering) and RF sputtering. RF sputtering uses frequencies in the range of 5-30 MHz and is generally preferred for dielectric materials [44]. A schematic representation of the sputtering process is shown in Figure 6.

2.2.1.2. Chemical Vapor Deposition

Chemical vapor deposition (CVD) is a versatile technique used for growing thin films with different stoichiometries of elemental and compound semiconductors, metal alloys, and amorphous or crystalline compounds. Basically, CVD processes involve a reaction between a volatile compound of the material to be deposited and other gases, resulting in the formation of a non-volatile solid that is deposited on a specific substrate at the atomic level. A wide variety of reactants and precursors can be used to form thin films, and the type of precursor, deposition conditions, and energy used to initiate the reaction can influence the CVD process. CVD reactors can be classified into two types: hot-wall CVD and cold-wall CVD. In hot-hall CVD, the reactor walls are heated using resistance heating. In cold-wall CVD, the heating occurs in the substrate holder, while the walls are air- or water-cooled. One common variation of CVD is plasma-enhanced CVD (PECVD), where plasma is used to promote chemical reactions at lower temperatures than traditional CVD, providing an advantage in some applications [44].

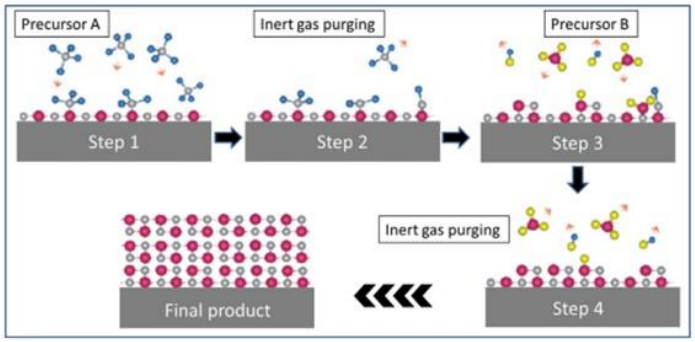

Figure 7. Scheme that represents the fabrication of a film using the atomic layer deposition process. In the first step, a precursor is deposited on a surface and reacts with this surface. Secondly, an inert gas is pumped into the system to eliminate the excess of the first precursor in the chamber and allow an inert environment for the deposition of the second precursor (step 3). Finally, a new purge in the system occurs to eliminate the excess precursor and possible co-products in the chamber. Steps 1 to 4 are repeated until the film achieves the desired thickness (final product) (adapted from [44]).

Atomic Layer Deposition (ALD) belongs to the CVD techniques. ALD is a type of thin film deposition that limits reactions to the surface, resulting in a coating. ALD uses gaseous precursor molecules that react with the substrate alternately, resulting in layer-by-layer deposition and the formation of a film. This alternate reaction allows for the precise deposition of atomic layer thicknesses of films ranging from atomic monolayers to several micrometers. Typical ALD processes occur in UHV chambers, where the precursors are exposed to the substrate surface until saturation is reached. Then, an inert gas is introduced into the chamber to remove excess molecules from the environment. Next, a new precursor is evaporated/sublimated and interacts with the surface. This cycle is repeated until a uniform film is obtained. Advantages of this technique include precise thickness control, uniformity of the film, control of the nanostructure, the high reproducibility [44,59]. A schematic representation of the ALD process is shown in Figure 7.

2.2.2. Nucleation and Growth of Thin Films

The formation of thin films is highly influenced by the methodology used for their production, as well as surface characteristics and material properties. This chapter focuses on understanding the process of thin film formation using vapor methodologies, as used in this work.

When depositing materials (in our study, ILs) using vapor techniques, small quantities of material arrive at the substrate as atoms or molecules with some energy. When these atoms collide with the surface, energy transfer occurs through a process called thermal accommodation, which is dependent on the substrate temperature. Higher substrate temperatures can complicate energy transfer and consequently, thermal accommodation. In this case, atoms may undergo re-evaporation and saturate the environment. Thermal accommodation allows for the condensation of the atoms and initiates the film formation [60,61]. The condensation and adsorption of atoms during thin film formation involve the formation of interactions between arriving atoms and surface atoms. Depending on the type of interactions formed, adsorption can be physical or chemical. Physical adsorption involves intermolecular interactions and does not result in a chemical reaction or change to the adsorbed species, while chemical adsorption involves a reaction between the adsorbed atoms and the substrate surface, creating molecular bonds. In this type of adsorption, a new species with different characteristics from the initial material may be created, highlighting the importance of understanding the film characteristics that we want to fabricate. During physical adsorption, due to weaker interactions, it is possible for the material to diffuse into the surface, a process known as surface diffusion. The atoms move along the surface until they arrive at energetically favorable sites, where they become adsorbed and remain in place. These sites can be surface defects (such as kinks, ledges, or local defects) or agglomerates of atoms, that allow arriving atoms to be stabilized. The diffusion factors depend on the energy with which the molecules arrive at the surface and the interactions they form with the substrate, that is, the material-substrate affinity [46,61,62].

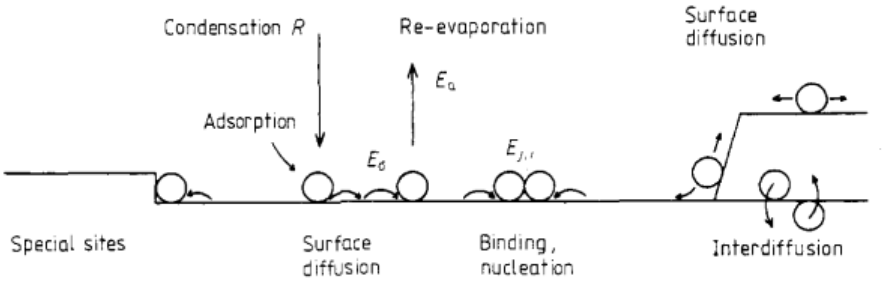

Figure 8. Diagram of the processes of nucleation and growth on surfaces and respective energies (adapted from [61]).

Theses atoms will interact with each other, creating new interactions between themselves, and forming agglomerates called *clusters*. This process is called nucleation, and the size of the clusters is determined by the minimum free area required to promote nucleation (MFAN), which depends on the material-substrate affinity. The clusters formed undergo some surface diffusion, which is typically smaller than the flux of atoms that arrive at the surface. Figure 8 provides a schematic diagram of the processes of nucleation and growth of thin films on solid surfaces.

With an increase in the amount of material that evaporates or sublimates, the number of clusters formed also increases, leading to the minimization of surface energy and the agglomeration of clusters. This process is known as first-order coalescence, which facilitates the formation of agglomerates with larger dimensions. As the material continues to vaporize or the flow rate of the arriving material increases, the first-order coalescence process intensifies, resulting in new coalescence between previously coalesced agglomerates or between native clusters and coalesced agglomerates. This process is called second-order coalescence. Both coalescence processes create spaces between the coalesced agglomerates formed, which can be filled by new atoms, leading to the formation of new clusters. In the case of ILs, the coalescence process allows for a higher surface coverage area. This phenomenon has a kinetic component because, thermodynamically, ILs tend to form larger droplets that cover the entire surface area [61,62].

In general, is possible to describe the nucleation and growth of a film on the surface in three distinct modes (Figure 9): in the island or Volmer-Weber mode (3D model), in layers or Frank-van der Merwe mode (2D model) and layer plus island or Stranski- Krastanov mode (2D+3D mode).

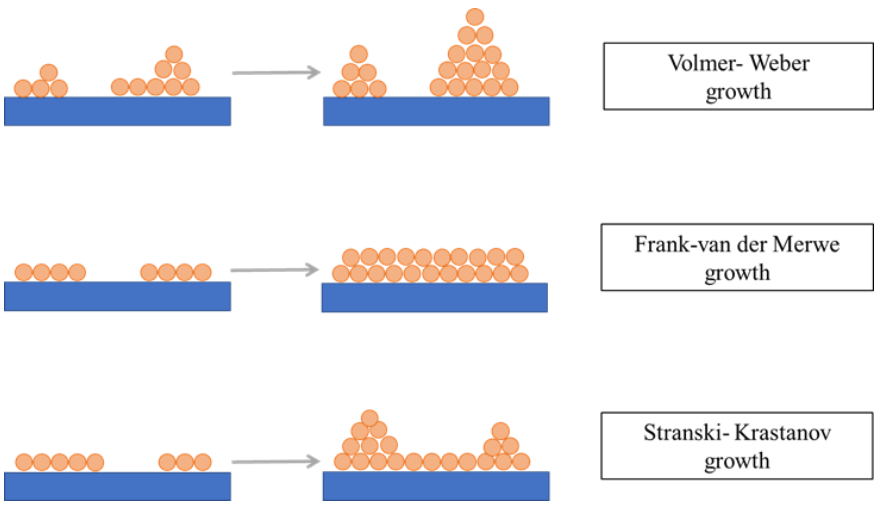

Figure 9. Schematic representation of the different models of thin film growth (adapted from [61]).

In the Volmer-Weber mode, the clusters formed tend to occupy less surface due to the lower affinity between the surface and the clusters. This results in agglomerates with vertical growth and regular morphology. In the Frank-van der Merwe mode, there is a better affinity between the atoms and the substrate as compared to the affinity of the atoms themselves, allowing the atoms to condense and form a monolayer on the surface. The successive deposition of material leads to the formation of a compact and uniform film across the entire area of study. In the Stranski-Krastanov mode, the growth occurs in two steps: initially, the clusters that arrive at the surface have a better affinity with the substrate, allowing them to spread and form a layer. After the layer forms, the atoms/molecules that arrive at the surface do not have a strong affinity for the material and tend to dislocate to preferential areas, reducing contact with the remaining material [61,62].

The formation stage of a film can be considered a metastable phase due to the higher area-to-volume ratio of the cluster that forms it. To form a film by coalescence of these clusters, the nucleation process requires the clusters to have a radius larger than the critical radius, which allows the Gibbs energy of the surface to be overcome. This process can be described by the equation bellow, equation 1:

$$\Delta G = a_3 r^3 \Delta G_V + a_1 r^2 \gamma_{l\text{-}v} + a_2 r^2 \gamma_{s\text{-}l} + a_2 r^2 \gamma_{s\text{-}v} \quad \text{(eq. 1)}$$

In the equation, ΔG represents the Gibbs energy in a surface, which is dependent on several factors: These factors include the free energy associated with vapor condensation (ΔG_v), as well as the interfacial tension (γ) of the system that creates the surface, that is the vapor-liquid superficial tension ($\gamma_{l\text{-}v}$), the solid-vapor superficial tension ($\gamma_{s\text{-}v}$) and solid-liquid interfacial tension ($\gamma_{s\text{-}l}$). Additionally, the geometric components obtained by the nucleus formed are also a factor, with $a_1 r^2$ representing the area of the curved surface, $a_2 r^2$ representing the circular area where the cluster occupied on the substrate, and $a_3 r^2$ representing the nucleus volume. To understand the energy barrier that needs to be overcome, it is necessary to determine the critical nucleus radius, as the clusters need to be larger than this critical radius for the coalescence process to occur. Assuming that the system is at thermodynamic equilibrium, the critical nucleus radius can be determined by setting the derivative of ΔG with respect to r equal to zero [$d(\Delta G)/dr = 0$]. The equation for the critical radius can be expressed as follows:

$$r_{cr} = \frac{-2\,(a_1 r^2 \gamma_{l\text{-}v} + a_2 r^2 \gamma_{s\text{-}l} + a_2 r^2 \gamma_{s\text{-}v})}{3 a_3 r^3 \Delta G_V} \quad \text{(eq. 2)}$$

Once the critical nucleus radius is known, it is possible to determine the Gibbs energy required to overcome the energy barrier and allow the growth of the film to occur. This

change in the energy of the system, for the formation of stable clusters, is described in Figure 10 and Equation 3:

$$\Delta G_{cr} = \frac{4\,(a_1\gamma_{l\text{-}v} + a_2\gamma_{l\text{-}s} - a_2\gamma_{s\text{-}v})^3}{27 a_3^2 r^3 \Delta G_V{}^3} \quad \text{(eq. 3)}$$

where ΔG_{cr} is the Gibbs energy when the radius of the nucleus is equal to the minimum radius for the clusters (r_{cr}) and ΔG_V is the Gibbs energy related to the vapor condensation [62,63].

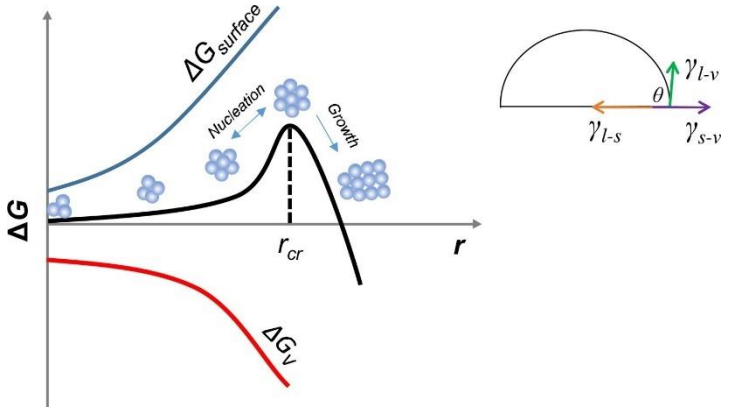

Figure 10. Schematic representation of the nucleation and growth processes and the changes of the Gibbs energy with the formation of clusters (adapted from the [61]).

2.2.3. Thin Films of Ionic Liquids

In this chapter, the focus is on the formation of thin films of ionic liquids (ILs) using physical vapor deposition (PVD) techniques, specifically thermal evaporation with reduced pressure. Contrary to what is observed for solids, where a continuous film is easily formed or at least three-dimensional crystals grow homogeneously, ILs are deposited as micro- and nanodroplets on various surfaces [48,62,64]. Previous studies have shown that the size distribution and shape of these micro- and nanodroplets depend on factors such as mass flow rate, deposition time, and film-substrate affinity. In a study by Costa *et al*., the morphology of $[C_4mim][NTf_2]$ and $[C_4C_1Pyrr][NTf_2]$ films deposited on various substrates, including glass, indium tin oxide (ITO), graphene/nickel, and gold-coated quartz crystal, was investigated using thermal evaporation with reduced pressure [62]. The results showed the formation of micro- and nanodroplets on all studied surfaces, interpreted as following a 3D growth model. The interfacial tensions and contact angles of the droplets can be analyzed to determine the film-substrate affinity [64-66]. The nucleation and growth processes occur during deposition, increasing the thickness of the films. However, even with increasing deposition time, a thin film with high surface coverage is not formed.

Based on these results, it was possible to develop a model that describes the formation of droplets in three main steps, as shown in Figure 11: (1) the minimum free area to promote nucleation (MFAN); (2) the first order of coalescence; (3) second order of coalescence [62]. Initially, the ion pairs arrive on the substrate surface with some kinetic energy, and through thermal accommodation and surface diffusion processes they agglomerate and form clusters of ILs in energetically stable locations. The clusters formed have a minimum size defined by the critical nucleus radius on the substrate surface. For ILs, it was found that the MFAN is above 5 μm^2 on the ITO surface.

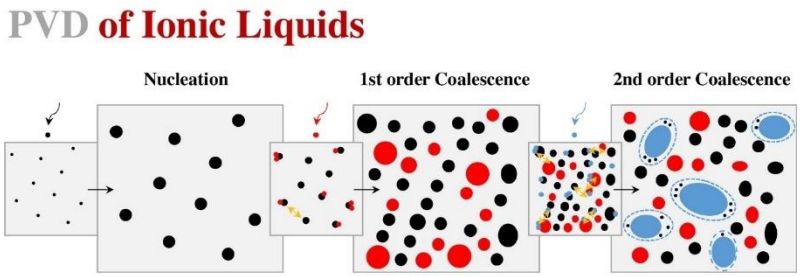

Figure 11. Representation of the different steps of nucleation and growth of ionic liquid droplets deposited by physical vapor deposition methodologies (adapted from [61]).

As ILs continue to vaporize and arrive on the surface, the volume and number of clusters increase, and the surface energy is minimized. This enables the native clusters to coalesce and form more stable clusters (first-order coalescence). With an increase in the quantity of ILs arriving on the surface, more stable clusters are formed, which can coalesce with native or previously coalesced clusters (second-order coalescence). After the coalescence process, empty spaces are available between the droplets, which are available for new nucleation processes. The results showed that smaller droplets surround larger droplets when the area between the larger droplets is greater than 5 μm^2. When the area is less than 5 μm^2, the coalescence process occurs for native clusters due to the high superficial diffusion of the ILs. With an increase in the time of deposition, there's an increase in the coalescence processes, which contributes to a larger surface coverage with lower sphericity. However, is not possible to fabricate a uniform film, as boundaries between the droplets are observed [62].

In general, it can be said that the nucleation and growth processes are dependent on the thermal accommodation, surface diffusion, and adsorption processes for the formation of a thin film, whether it is amorphous or crystalline [60-64]. In the case of the thin films of ILs, additional factors that influence substrate affinity and MFAN must be considered [61]. Usually, the thickness of thin films is measured by nanometers or micrometers. However, for ILs, the measurement unit generally used is the monolayer (ML) [61,66].

A monolayer can be described as a layer of material that covers the surface of the substrate. In the case of the ILs, a ML refers to a single layer of ion pairs that are arranged in a specific orientation, usually through electrostatic or other types of interactions with the surface. To determine the thickness of a ML in a particular interfacial layer, one can use equation 4.

$$h = \sqrt[3]{\frac{M}{\rho \cdot N_A}} \qquad \text{(eq. 4)}$$

where h is the monolayer thickness, ρ the density of the material, M is the molar mass, and N_A is the Avogadro constant [66,67].

2.2.4. Nanoconfinement

One of the most interesting applications of ILs is in the use of confinement matrices. Confinement matrices can expand the potential applications of ILs by addressing some of the issues related to their use, such as high viscosity, leakage, difficulty in packaging and transport, and poor gas diffusion [11]. Generally, ILs are confined when the interaction between the ILs and the surface becomes favorable for the ions that constitute the ILs. Incorporating ILs into pore structures allows for improvement in ionic conductivity and mechanical integrity, creating new hybrid materials with intrinsic characteristics of the constituted materials. Matrices in which ILs are nanoconfined have at least one dimension with a reduced length compared to the ion size [11,40,69]. The spatial geometry and low dimensionality promote strong interactions between the IL and the walls of the porous matrix, altering the physicochemical behavior of ILs in terms of phase transition behavior, wetting, and layering near the surface walls compared to their bulk properties [11,40,70,71].

Inorganic matrices, such as nonporous silicas and carbons, metal-organic frameworks (MOFs), carbon nanotubes (CNTs), and zeolites, are some of the most used porous matrices to form nanoconfined ILs [11,40,68-71]. The incorporation of ILs can modify the properties of both the ILs and porous matrices. By adjusting the porous properties (such as size and geometric structure), surface functionalities, or external conditions (such as electric field or temperature), the properties of the hybrid material can be tailored to meet specific application requirements [11,40]. The confinement of ILs within a porous matrix can be achieved through chemical coupling with the porous surface or physical confinement within nanopores (Figure 12).

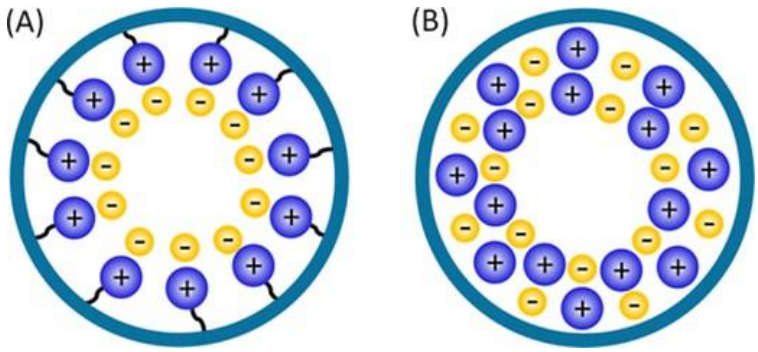

Figure 12. Incorporation of ILs into the porous structure by 2 different strategies: (A) covalent grafting of a monolayer IL on the pore wall an (B) physical confinement of multilayers of ILs into nanopores (adapted from [11]).

Covalent anchoring is a method for immobilizing ILs that reduces the amount required but has several drawbacks. This method may cause some bulk-phase properties of the ILs to be lost (such as solvation strength or conductivity) due to the connection to the material, which limits the free movement of the cation-anion pair. To improve catalytic activity, it is necessary to use more than one IL with the same anion since the chemical coupling results in self-assembly monolayers on the support, leading to low ion density. Some porous matrices with inert activity require pre-treatment to create "active" sites for the linkage with ILs to occur [11,72].

In the case of physical confinement, ILs can be confined without evaporation in vacuum conditions, unlike molecular liquids. The resulting ML allows for free mobility of the ionic pairs, as the ML is confined in the pore without any covalent linkage between the ion and the surface. This allows the IL to retain properties similar to the bulk phase. The weaker interactions between the IL and the surface make it possible to remove the IL from the porous material. Additionally, the structure and composition of the matrix and/or ILs can be modified to better suit a particular application [11].

The nanoconfinement of ILs can occur in various surface geometries, as illustrated below (Figure 13). In general, confinement occurs when the interaction between the IL and the surface is significant for the IL ions, which is determined by the ratio between the wall surface and the volume of the IL [11,40]. In this figure, different ways in which ILs can be confined are shown. In situation a), spatial confinement occurs due to the presence of an opposed mobile surface to the substrate where ILs are deposited. This situation is commonly observed when using probes to study surface topography. In situation b), ILs are confined between layers, where deposition occurs on a nonporous solid surface, forming a partial thin film that covers part of the substrate. This situation is like previous studies where ILs were deposited on a glass coated with semiconductors and/or metals using thermal evaporation under reduced pressure. In situation c), confinement of ILs occurs due to the surface roughness of the substrate. In situation d), ILs are confined in nanoporous material, allowing for interfacial confinement at the surface as well as confinement in the interior of the material in small spaces [11,40].

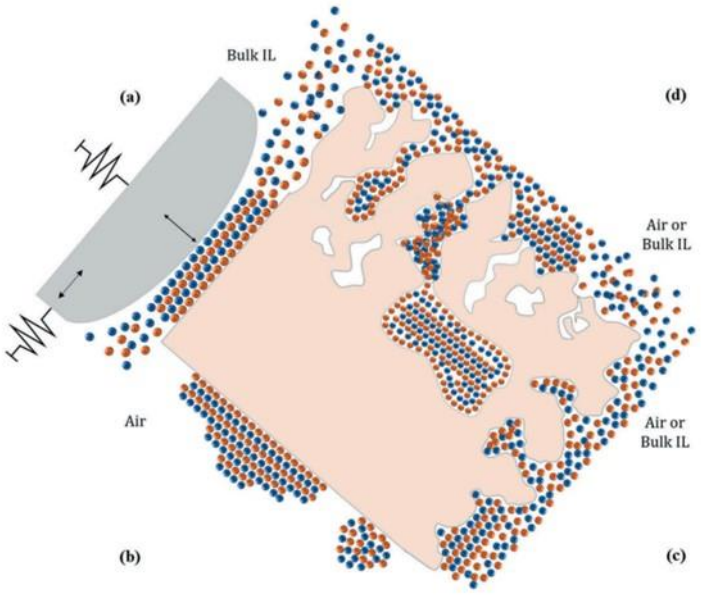

Figure 13. Ionic liquids in different nanoscale-confined geometries (adapted from [40]).

Previous studies have reported different behaviors related to phase transition, wettability, layering near-surface walls, changes in the glass transition, and changes in the melting and freezing temperatures. The environment surrounding the ILs confined in small pores is different from that of ILs in bulk, and the charges of the IL can affect the interactions between the pore wall and the IL, causing the IL to lose some bulk properties. One significant change observed when ILs are confined in smaller pores is the alteration of melting/freezing temperatures. It was shown that the reduction of the freezing-melting point is inversely proportional to the pore dimensions of the material and proportional to the difference in surface energy between the IL and the pore wall. Therefore, it can be concluded that there is a dependence between the freezing-melting point and the pore size and IL-pore interactions when studying an IL confinement system [11,40,74].

2.3. Interfacial Tension and Wettability

To better understand the behavior of IL droplets, it is necessary to understand the phenomenon of wettability. In general, the wettability behavior of ILs is influenced by their thermophysical properties, such as surface tension and contact angle. Surface tension can be described at a thermodynamic level as the reversible work required to transport molecules from the interior of the liquid to the surface, increasing the surface area. The molecules in the interior of the material are more stable than the ones at the surface due to the higher number of intermolecular interactions. At the interface, there is an unbalance between intermolecular interactions, with molecules on the surface being attracted by the sides and interior of the material, but not in the vapor or gas phase. This cohesion between the molecules creates a tangential force on the surface that behaves like an elastic membrane and comprises the liquid. For the estimation of the surface tension, it is possible to use different perspectives.

From a molecular perspective, the estimation of the surface tension is made through the vaporization enthalpy, together with the density and molar mass of the compound. This model assumes that each molecule can be represented as a cube and the intermolecular interactions occur along all the faces. So, to move a molecule from the bulk to the surface is necessary to break an interaction, as shown in Figure 14. The determination of the cubic face area and the energy needed to evaporate one molecule, and consequently break al the intermolecular interactions, can be a good estimation of the surface tension [74-76].

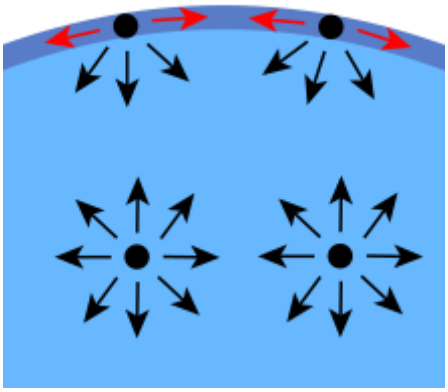

Figure 14. Schematic representation of the molecular interactions that a molecule feels when is in the interior/ bulk of a liquid and the surface of a liquid.

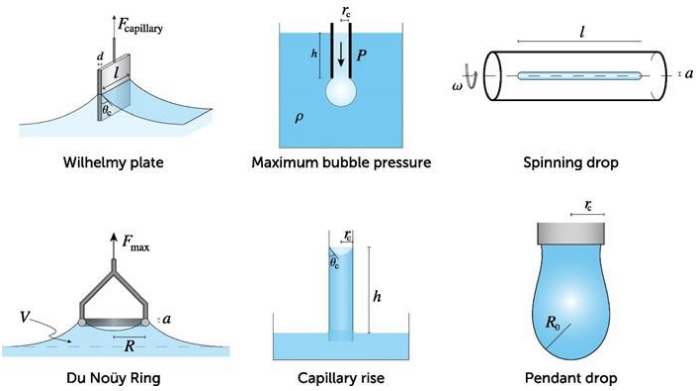

Figure 15. Schematic representation of some techniques used to measure the surface tension of a liquid (adapted from [75]).

The measurement of the surface tension of different liquids uses a mechanical perspective. The mechanical perspective describes surface tension as the work necessary to expand the surface area at a constant velocity. Imaging a rectangle with a film of a liquid that is necessary to study, were one side is a mobile wire. The necessary force to move the wire in a constant velocity (*F*) is described in equation 5:

$$F = 2L\gamma \qquad \text{(eq. 5)}$$

where *L* is the length of the mobile wire and γ is the surface tension of the liquid. Figure 15 illustrates some different methodologies used to measure surface tension [75,76]. The affinity of a liquid for a surface and the consequent wettability of the surface can be explained by the balance between the adhesive and cohesive forces of the liquid. The cohesive forces arise from the intermolecular interactions within the liquid, while the adhesive solid-liquid forces result from the interaction between the liquid and the material support. Figure 16 the different interfacial tensions and contact angles of a droplet adsorbed on a solid substrate is shown schematically.

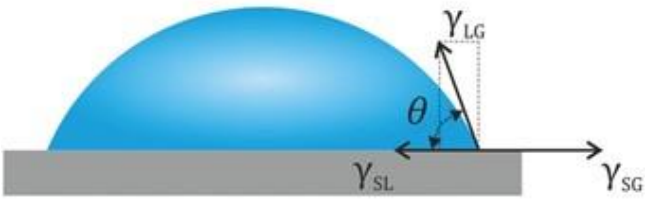

Figure 16. Schematic representation of a droplet with a specific contact angle (θ) and the different interfacial interactions in the system (solid- liquid interaction (γ_{SL}), liquid-vapor interaction (γ_{LG}) and solid-gas interaction (γ_{SG}) (adapted from [77])).

The contact angle is an indicator of the good or bad wettability of the liquid on the surface in the study. For instance, a droplet with a lower contact angle indicates a higher effect of the adhesive forces, allowing for a better spreading onto the surface and consequently a good wettability. On the other hand, when the liquid doesn't have a good affinity with the surfaces, the effect of the cohesive forces will promote the sphericity of the droplet onto the surface to decrease the contact area with the surface (increasing the contact angle). Young's equation relates the contact angle of a droplet on a solid surface to the interfacial tensions between the liquid, solid, and vapor phases (Figure 16). Mathematically, Young's equation can be expressed as:

$$\gamma_{sg} = \gamma_{sl} + \gamma_{lg} \cdot cos\ \theta_c \qquad \text{(eq. 6)}$$

where γ_{sg} is the solid-gas interfacial tension (surface tension of the substrate), γ_{sl} is the solid-liquid interfacial tension, γ_{lg} is liquid-gas interfacial tension (surface tension of the liquid) and θ_c is the droplet contact angle. Figure 17 illustrates the relationship between wettability (that depends on the interactions between the liquid and the surface) and contact angle. The balance of these forces results in a droplet with a certain degree of sphericity and a certain contact angle [76,77].

The study of the wettability and surface tension of ILs is crucial for a better understanding of their properties. However, the study of contact angles and wettability of ILs on different surfaces has been relatively unexplored. Pereira *et al.* conducted a study to investigate the contact angles of various ILs on polar glass surfaces and non-polar PTFE surfaces and compared their findings with literature data [78]. The table below displays some of the contact angle measurements obtained for the ILs on these surfaces.

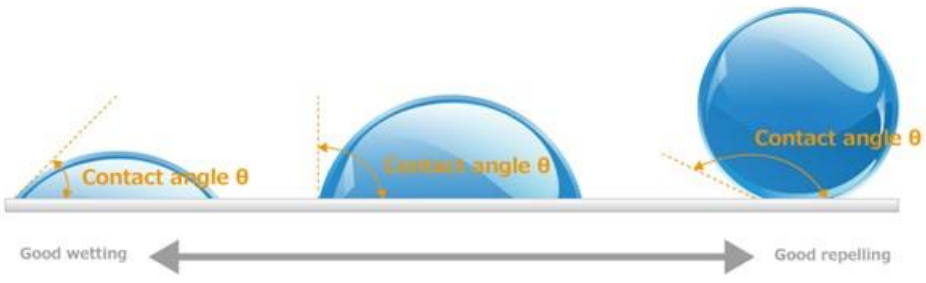

Figure 17. Schematic that illustrates how the droplet contact angle varies based on the surface wettability.

The data in the table indicates that for the same ILs, contact angles are lower on more polar surfaces compared to non-polar surfaces. Additionally, for the same glass surface, the contact angles are lower for more hydrophilic ILs, such as $[C_4C_1im][Ac]$, whereas on non-polar surfaces, the contact angles are higher, even for ILs with fluorinated anions like $[NTf_2]$ or $[PF_6]^-$. PTFE is a polymer where carbon atoms are surrounded by electronegative atoms, minimizing interactions between ILs and the surface, resulting in decreased wettability on the PTFE surface. Conversely, glass surfaces have hydroxyl groups that interact with the IL, decreasing surface tension and improving wettability. These results also highlight the impact of the structural variation of ILs on their wettability.

The change in anion can modify the contact angle. In the case of the glass surface, hydrophilic ILs like $[C_4C_1im][Ac]$ have a lower contact angle compared to more hydrophobic ILs. The researchers concluded that the ability of the anion to accept protons is an important factor in the wettability of ILs on polar surfaces, resulting in droplets with a lower contact angle. The opposite effect is observed on non-polar surfaces.

Another point of the study was the determination of the contact angles when the alkyl chain was increased. It was observed that for polar surfaces, there was an increase in the contact angle with the increase of the alkyl chain. A reverse trend is observed for the non-polar surfaces. However, this increase was less significant when compared to the change in the anion. For ILs with longer chains, the contact angles and wettability on the surfaces became very similar because the interactions between the ILs and the surface are more complicated [78].

Table 1. Contact angles of different ILs on glass and PTFE surfaces (adapted from [78]).

Ionic Liquids	Contact angles $(\theta \pm \sigma)$	
	Glass	PTFE
$[C_4C_1im][Ac]$	20.63 ± 0.03	98.03 ± 0.02
$[C_4C_1im][NTf_2]$	43.87 ± 0.12	66.76 ± 0.06
$[C_4C_1im][BF_4]$	45.63 ± 0.50	65.07 ± 0.07
$[C_4C_1im][PF_6]$	52.46 ± 0.93	60.11 ± 0.07
$[C_2C_1im][NTf_2]$	37.66 ± 0.35	66.93 ± 0.01
$[C_6C_1im][NTf_2]$	44.12 ± 0.10	66.10 ± 0.38
$[C_8C_1im][NTf_2]$	48.58 ± 0.23	65.60 ± 0.17

In general, the surface tension of ILs has a higher range (between 20 $mN \cdot m^{-1}$ and 80 $mN \cdot m^{-1}$) at room temperature compared to other liquids used as molecular solvents (an average of 25 $mN \cdot m^{-1}$). It is also generally observed that there is a decrease in surface tension with an increase in the alkyl chain length. For the majority of ILs, there is a small decrease in surface tension with an increase in temperature [78,79].

The contact angle of IL droplets is highly dependent on the droplet size and the method used to produce the film. For imidazolium-base ILs, the formation of nanodroplets with contact angles between 15 and 20 degrees has been reported when deposited on ITO and/or on silver surfaces [10,62,64,80,81]. However, lower values (< 10 degrees) were experimentally observed for the same ILs deposited on gold and or on organic surfaces [10,80,81]. Moreover, ILs comprising long alkyl chains have shown increased wetting ability. The surface roughness, the cleanliness of the surface, and the presence of impurities can also affect the contact angle measurements. Therefore, it is essential to carefully control the experimental conditions and to perform multiple measurements to ensure the accuracy and reproducibility of the results.

3. Methodologies

In this chapter, the research strategies adopted are presented, together with the methodologies utilized for fabricating thin films of ILs, and the substrates employed.

As such, the characterization of the physical vapor methodology used is presented, namely thermal evaporation with reduced pressure based on the effusion Knudsen method. The research group where this work was made developed and optimized this equipment, enabling the deposition of different ILs onto various surfaces.

This chapter also describes the diversity of surfaces used and the methodologies applied to modify them. Some of the substrates were commercially obtained, such as gold-coated quartz crystals and glass substrates coated with indium tin oxide (ITO). Surface modification of the substrates was achieved using PVD methodologies to coat them with metals and/or carbon. A sputtering system was employed to coat the ITO with metals, wherein the substrates underwent argon plasma treatment to facilitate the deposition of metals on the surface. For the carbon surfaces, e-beam evaporation, available at the Centro de Materiais da Universidade do Porto (CEMUP), was utilized.

The morphological analysis involved the use of optical microscopy and scanning electron microscopy (SEM) to examine the fabricated films. Optical microscopy allowed for immediate analysis of results after the deposition, but can only visualize larger structures, at an amplification of 640x. To obtain more detailed imaging and visualize structures of varying sizes, SEM was employed, as it offers significantly higher magnification, thus enabling the examination of structures with greater precision and across different scales.

Regarding the ILs used in this study, they can be divided into two distinct groups. The first group consists of ILs with the same imidazolium cation but varying alkyl chain lengths, along with different anions. These ILs include 1-ethyl-3-methylimidazolium bis[(trifluoromethyl)sulfonyl]imide, $[C_2C_1im][NTf_2]$, and 1-ethyl-3-methylimidazolium triflate, $[C_2C_1im][OTf]$. The second group comprises ILs with the same imidazolium cation but with a longer alkyl chain length, again with different anions. This group includes 1-octyl-3-methylimidazolium bis[(trifluoromethyl)sulfonyl]imide, $[C_8C_1im][NTf_2]$, and 1-octyl-3-methylimidazolium triflate, $[C_8C_1im][OTf]$.

3.1. Ionic Liquids

One of the strategies employed in this work was the categorization of ILs into different groups by varying the anionic group (NTf_2 or OTf) and altering the size of the alkyl chain (C_nC_1im) while maintaining the imidazolium cationic group constant, as referred just above. This methodology has been previously utilized by the research group to investigate various properties of ILs, as there is a significant differentiation in ILs based on alkylimidazolium cations depending on the chain length of the alkyl chains.

Four ILs were study: 1-ethyl-3-methylimidazolium bis[(trifluoromethyl)sulfonyl]imide ($[C_2C_1im][NTf_2]$); 1-octyl-3-methylimidazolium bis[(trifluoromethyl)sulfonyl]imide ($[C_8C_1im][NTf_2]$); 1-ethyl-3-methylimidazolium triflate ($[C_2C_1im][OTf]$); and 1-octyl-3-methylimidazolium triflate ($[C_8C_1im][OTf]$). The variation in alkyl chain sizes allows for the evaluation of the alkyl chain's effect on the deposition process and its potential interactions with the substrate used. Previous research demonstrated the influence of the alkyl chain on the behavior of ILs and, consequently, on the properties of the fabricated thin film. It has been observed that ILs with shorter alkyl chains ($n < 6$) tend to form droplets with small sizes and high sphericity, while ILs with longer alkyl chains exhibited a wider range of droplet sizes and morphologies [64]. The variation in the anions of ILs allows for the investigation of the influence of the anion on the interactions between ILs and the surface, as well as the prediction of the morphology obtained on a specific surface.

All the ILs used in the study were purchased from IoLiTec with a state purity of 99%. Prior to each deposition, the ILs underwent an *in-situ* purification process within the chamber of the thermal evaporation system, under reduced pressure ($p < 0.1$ Pa) at a temperature of $T = 423$K.

The molecular structures of all the ILs utilized in this study can be seen in Figure 18. Some relevant properties of the ILs are presented in Table 2.

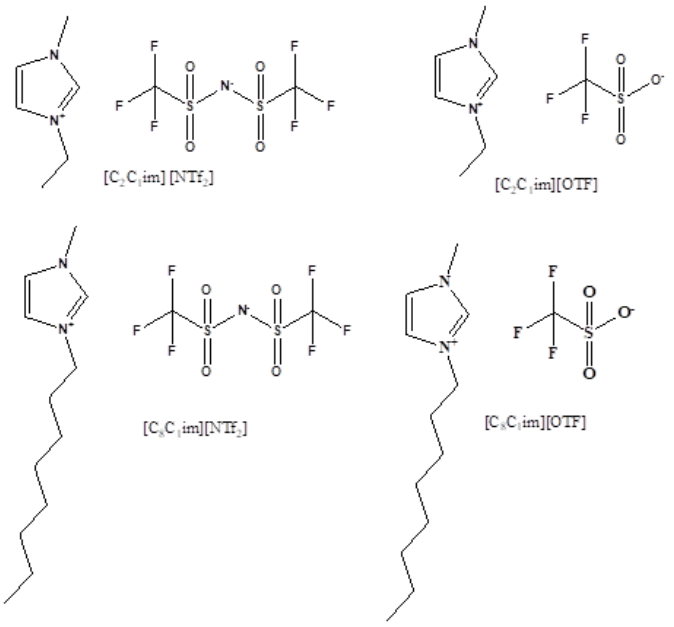

Figure 18. Schematic representation of the structures of the different ionic liquids used in this work.

Table 2. Density, viscosity, fusion temperature (T_m), glass transition temperature (T_g), and superficial tension values for the ionic liquids $[C_2C_1im][NTf_2]$, $[C_8C_1im][NTf_2]$, $[C_2C_1im][OTf]$ and $[C_8C_1im][OTf]$.

Ionic Liquid	Density (298K) / g·cm^{-3}	Viscosity / mPa·s	Fusion Temperature (T_m) / K	Glass Transition Temperature (T_g) / K	Superficial Tension / mN·m^{-1}
$[C_2C_1im][NTf_2]$	1.52 [23] 1.519 [34, 82]	33.0 [83] (298K)	260.0 [84] 255 [89] 254 [85]	178 [84] 180 [89]	36.9 [82] (293K) 35.2 [79] (298K)
$[C_8C1im][NTf_2]$	1.31 [80]	93.1 [83] (298K)	250-264 [86]	185 [86]	31.93 [87] (293K)
$[C_2C_1im][OTf]$	1.38593 [88] (297.94K)	45.67 [92] (298K)	258 [89]	175 [89]	39.2 [79] (298K)
$[C_8C1im][OTf]$	1.1932 [90]	127.4 [91] (296.74K)	-------	-------	28.5 [79] (298K)

3.2. Thin Film Production using Physical Vapor Deposition (PVD)

In this subchapter, two techniques of physical vapor deposition (PVD) are discussed: thermal evaporation with reduced pressure using a Knudsen effusion methodology; and sputter deposition (sputtering). Understanding the operation of these techniques and the conditions involved in fabricating new surfaces and thin films enhances the understanding of the subsequent chapters' result discussions.

3.2.1. Thermal Evaporation with Reduced Pressure using the Knudsen Effusion Methodology

To investigate the morphology of different ILs on various surfaces and understand the interaction between the ILs and the surfaces, thermal evaporation with reduced pressure was employed as a PVD technique. The deposition was carried out using equipment developed by the research group, as shown in Figures 19-23. The system enables the production of homogeneous films and provides reproducible results, being, however, a time-consuming process.

The methodology employed in this work follows the discoveries of Martin Knudsen, a Danish researcher who utilized cylindrical tubes at low pressures to study gas flow. Through his investigations, Knudsen established that Lambert's "cosine law" is applicable to the reflection of molecules in the gas phase when they collide with tube walls [93]. This knowledge allows for the application of methodologies based on Knudsen's findings to investigate the vapor pressure of materials with low volatilities (< 1 Pa) [94,95]. Additionally, by measuring the vapor pressure, it becomes possible to accurately determine the enthalpies of sublimation/vaporization.

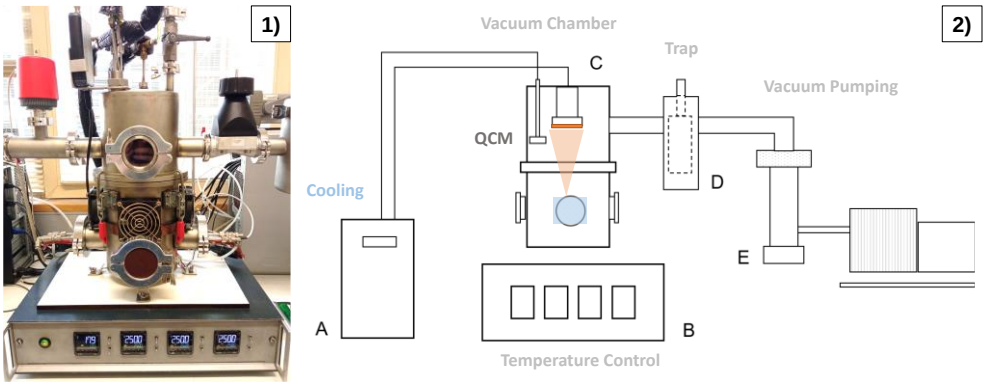

Figure 19. Image of the vacuum chamber of the vacuum thermal evaporation equipment, the ThinFilmVD system (1); Schematic representation of the vacuum thermal evaporation methodology (2): A- cooling system, B- instrumentation box for the T control, C- vacuum chamber, D- a metallic trap for N_2 (l), E- vacuum pumping system (adapted from [68]).

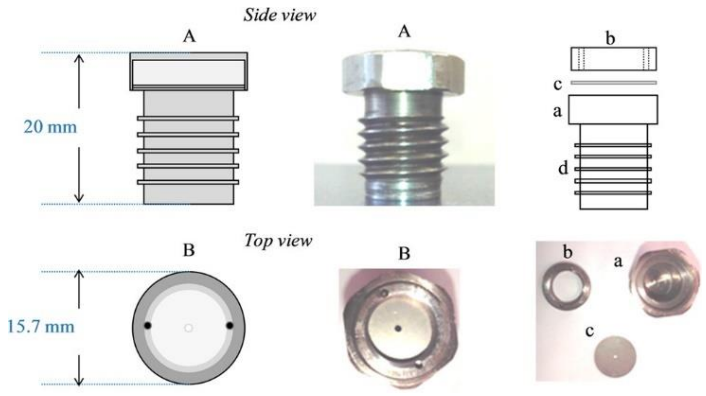

Figure 20. Schematic representation and images of a Knudsen effusion cell utilized in ThinFilmVD. The upper part of the image shows the side view of the cell (A), and the bottom part of the image shows the top view (B). On the right size of the image, the schematic and image of the different components of the cell are visible: a) cell body; b) cell lid; c) disk with an orifice; d) screwing system (adapted from [68]).

The equipment allows for the use of up to four Knudsen cells simultaneously, each containing different materials to be deposited. These cells are built in stainless steel with a cylindrical shape and connected to the oven by a screw system (Figure 20). The cells used are stainless steel instead of aluminum (which is commonly used in Knudsen cells due to its higher thermal conductivity). However, stainless steel is preferred in this case due to its higher thermal resistance and durability. As shown in Figure 20, the cell can be separated into 3 individual parts: the cell lid, the cell body, and the disk with the orifice. The disk can be used with different orifice diameters (1.0 mm, 2.1 mm, and 3.1 mm). In this work, disks with diameters of 2.1 and 3.1 mm were used. The smaller diameter provides better precision in controlling the vapor flow of the material; however, it also increases the risk of material accumulation and possible clogging of the orifice. On the other hand, using a larger orifice reduces the frequency of clogging incidents, but it results in a loss of precision in vapor pressure control. Therefore, it is necessary to find a balance between orifice clogging and precision loss when using these cells [46,68].

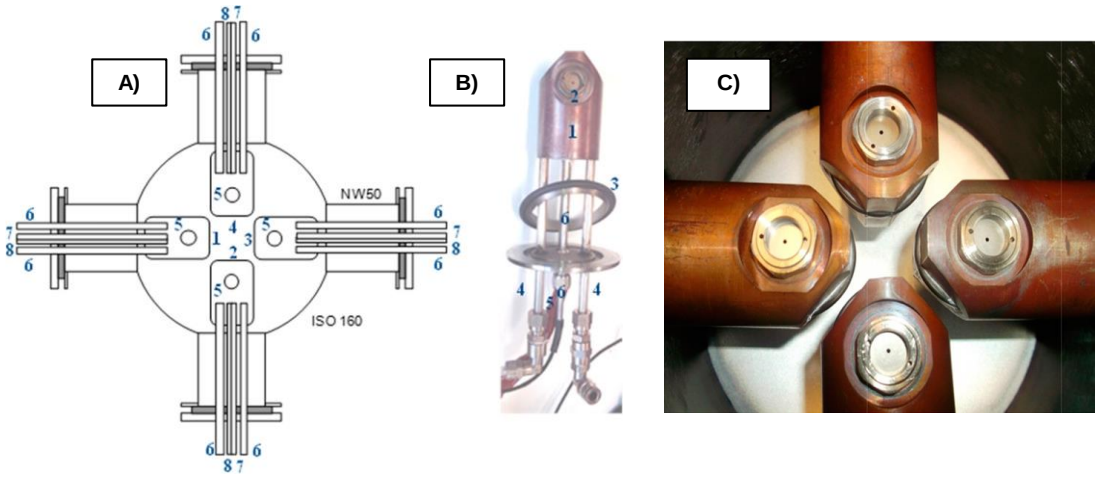

Figure 21. (A): Schematic representation of ovens and their location in ThinFilmVD equipment. 1,2,3,4-copper ovens; 5-cavity of the Knudsen cell screwing; 6- air cooling tube; 7- heater; 8- Pt100 sensor. (B): Top view image of an individual oven. 1- cooper block; 2- Knudsen cell; 3- O-ring; 4- air cooling tube; 5- heater; 6- Pt100 temperature sensor. (C): the image of the four ovens with the Knudsen (adapted from [68]).

The oven, where the effusion cell is placed, consists of a copper cylinder combined with an air-cooling stainless-steel tube, a 100 W cartridge-type heating element, and a temperature sensor (Pt100) for temperature measurement and control (Figure 21). To maximize the thermal contact, a thermal paste is applied to the heating resistance and temperature sensor. In this system, four individual ovens operate independently and are located at the lower part of the equipment (Figure 21). This instrument allows the deposition of up to four different materials simultaneously or sequentially, eliminating the need to open the system, thus minimizing the risk of contamination or changes in the sample [46,68].

The substrate support system is situated in the upper part of the equipment. It is connected to a cooper-cooled cylinder (20 mm in diameter) with an external cooling system, ensuring that the substrate remains at a constant temperature, lower than the temperature of the effusion cell temperature. This temperature difference facilitates the condensation of molecules onto the substrate. The substrate's support system consists of a stainless-steel disk with a diameter similar to that of the copper tube. The colocation of the support within the copper tube allows for the thermal regulation of the samples on

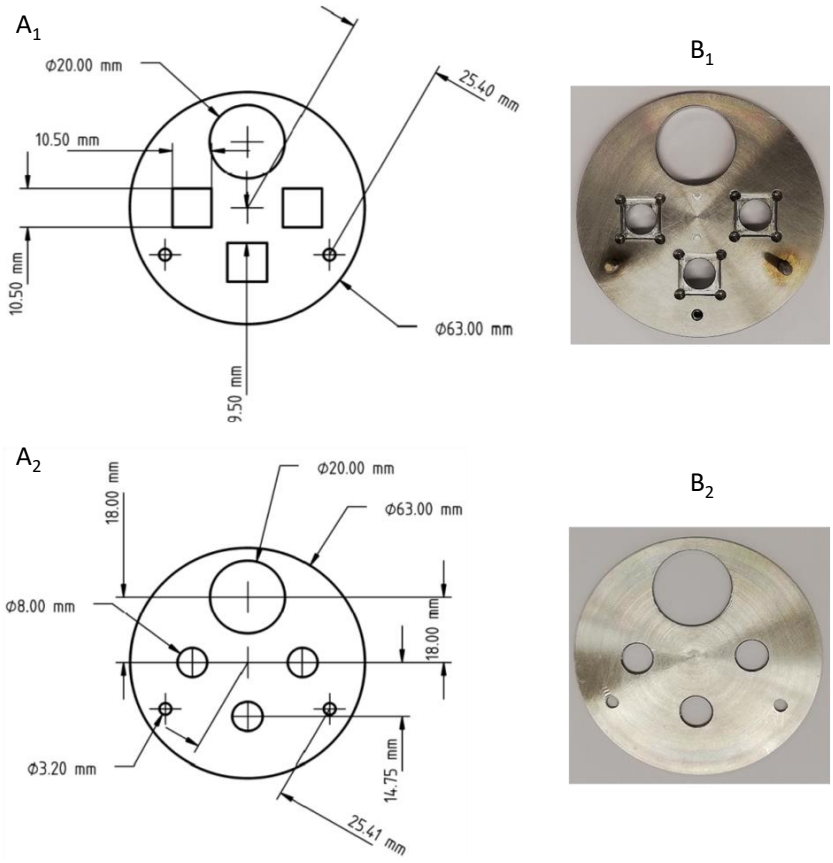

Figure 22. Schematic representation of the base (A_1) and the mask (A_2) of the substrates support system. Image of the base (B_1) of the substrate support and their mask (B_2). This system was utilized in all the depositions of each ionic liquid on different substrates employed in this work (adapted from [68]).

the support. The support is composed of two pieces, as shown in Figure 22. The base section contains three square cavities, each 10.5 mm in length, where the substrates are placed. This design includes some space in the corners to facilitate the removal of the substrates. The top section functions as a mask, featuring three circles that enable the deposition of material in a circular form with an 8 mm diameter. Additionally, the mask protects the borders of the materials, enabling the study of morphological differences between the substrate surface (borders) and the material (interior part) [46,68].

In addition, the deposition system also includes a quartz crystal microbalance (QCM), positioned near the cooper support tube (Figure 23). The microbalance is connected to software that enables real-time control of the deposition. The deposition rate is derived from the relationship between the change in vibration frequencies emitted by the crystal and the amount of vaporized material (the thickness of the film), per unity of time (Å/s) that is deposited onto the surface. Given the proximity between the substrate support

and the microbalance, it can be inferred that the deposition rate is approximately similar on both surfaces [46,68].

The quartz crystals used in this system are flat-convex quartz crystals of AT cut, with a frequency of 6 MHz, and diameter of 14 mm, acquired from the company Inficon. These crystals are coated with a layer of gold and possess piezoelectrical properties. When examining the morphology of these materials, it is noticeable that they exhibit an irregular morphology with various confined spaces (Figure 23).

When ILs are deposited, the ion pairs tend to accumulate in the confined spaces of the quartz crystals. Once these spaces are filled, an ionic liquid film may form droplets on the surface, that move freely on the surface. Due to this behavior, the mass limit for the detection of ILs is lower compared to materials that form a solid film. Santos *et al.* demonstrated that for evaporation of $[C_2C_1im][NTf_2]$ and $[C_6C_1im][NTf_2]$, the saturation point for the QCM was around Δf = 6 kHz. When the ionic liquid reaches the surface, the microbalance is unable to detect the formation of microdroplets on the surface [93].

The deposition of material occurs inside a vacuum chamber. Low-pressure conditions are provided by using rotative and diffusion bombs. The conjugation of these bombs allows for the reduction of the pressure in the chamber down to 10^{-6} Pa. Maintaining low pressure within the chamber is crucial for an efficient film deposition process as it prevents collisions between the evaporated material and other particles. The temperature of the ovens is carefully monitored, and each is chosen based on the evaporation temperature of each compound. Once the compound begins to evaporate, the resulting vapor freely travels to the substrates and QCM surfaces, where it condenses, initiating the film formation process. The monitoring of the vacuum level during the evacuation process and fabrication of film is achieved using two sensors located on opposite sides. This configuration enables the detection of possible leaks [46,68].

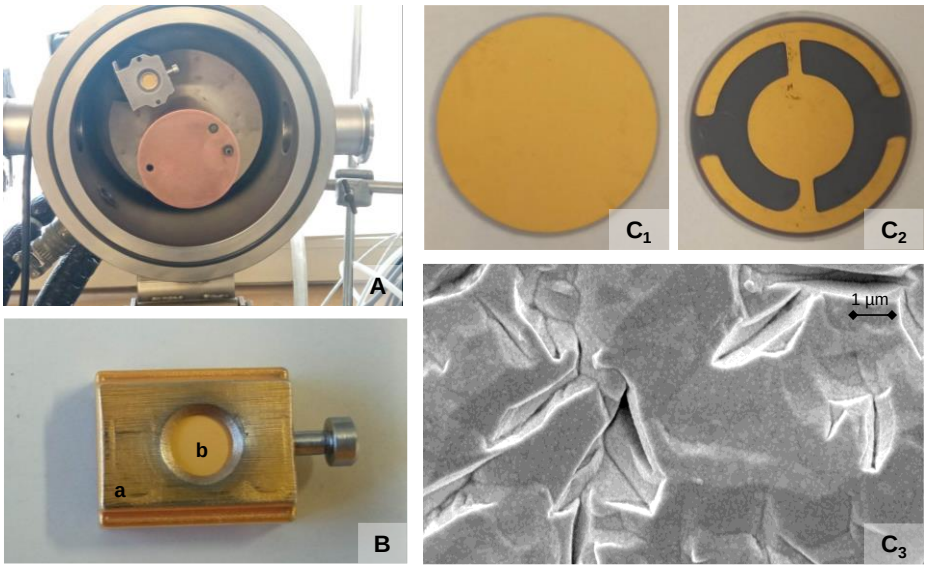

Figure 23. Image of the upper part of the equipment, where the QCM is located, and the substrates support are positioned (A). Image of the QCM support (a) and the crystal inside (b) (B). Front view (C_1) and back view (C_2) of the QCM. Morphology of the QCM by SEM micrography (C_3).

One of the main advantages of using Knudsen effusion cells is the capability to measure the vapor pressure of organic/inorganic materials with low volatilities (less than 1 Pa). The Knudsen cell is kept in thermal equilibrium, allowing the vapor to remain in equilibrium with the solid or liquid material. The orifice serves as the sole means for the vapor to escape from the interior of the cell. The loss of mass from the cell can be correlated to the vapor pressure by the following equation:

$$p(T) = \left(\frac{m}{\Delta t \cdot A_0}\right) \cdot \sqrt{\frac{2\pi RT}{M}} \qquad \text{(eq. 7)}$$

where p represents the vapor pressure, m is the sublimed/ vaporized mass, A_0 is the effusion cell orifice area, T is the cell temperature, Δt is the evaporation time, R is the gas constant, and M is the molar mass of the effused material. Is necessary to keep in mind that the application of equation 7 is subject to various conditions. These conditions include the absence of chemical reactions between the sample and the cell, identical temperatures for the sample and the cell, an equilibrium between the solid/liquid phase and gas phase within the cell, and the effusion orifice with negligible thickness [94,95].

However, it is impossible to achieve ideal conditions, such as the zero thickness of the effusion cell. In real conditions, the orifice diameter possesses a certain thickness, and some molecules may collide with the orifice and return to the cell, resulting in a reduced mass flow rate as compared to the ideal scenario. Therefore, a corrective factor is

required to account for the transmission probability of gas molecules passing through the effusion orifice (the transmission probability factor, w_0) [94,98]. The transmission probability factor can be determined using the Dushman equation:

$$w_0 = \frac{1}{1+\frac{3l}{8r}} \quad \text{(eq. 8)}$$

where *l* is the orifice thickness and *r* is the orifice radius. It is possible to incorporate the transmission factor and rewrite equation 7 as follows:

$$p(T) = \left(\frac{m}{\Delta t \cdot w_0 \cdot A_0}\right) \cdot \sqrt{\frac{2\pi RT}{M}} \quad \text{(eq. 9)}$$

From equation 9 it is possible to calculate the mass flow rate that came out of the Knudsen cell. However, to derive the mass flow rate that arrives at the substrate surface is necessary to consider a geometric factor (*g*), which depends on the distance, angle, and geometry of the deposition setup. The mass flux that exits the orifice ($\Phi_{\text{Knudsen cell}}$,) can be calculated by dividing the mass that exits the cell at a certain time by the orifice area ($\frac{m}{A_0 \cdot t}$). By rearranging the equation and incorporating the geometric factor, *g*, it becomes possible to calculate the mass flux that reaches the substrate ($\Phi_{\text{substrate}}$) as follows [93,94]:

$$\Phi_{\text{substrate}} = g \cdot \Phi_{\text{Knudsen cell}} = g \cdot p \cdot w_0 \cdot \sqrt{\frac{M}{2\pi RT}} = g \cdot \frac{m}{A_0 \cdot t} \quad \text{(eq. 10)}$$

This system presents several challenges, as the deposition conditions undergo changes over time. At the beginning of the deposition, a higher number of molecules (ion pairs in the case of ILs) are reflected by the chamber walls. As more molecules get adsorbed onto the wall surface, the tendency of reflection decreases. Additionally, obstruction of the orifice can influence the quantity of material reaching the substrate surface. Therefore, equation 10 does not allow for the direct calculation of the film thickness. However, it is possible to estimate the temperature required to achieve a desired mass flux by monitoring the real-time deposition rate using the QCM.

By understanding the equipment and principles of the deposition technique, it is possible to have better control over the deposition process, depending on the desired outcome. Before starting the study of vapor pressure and ideal evaporation temperatures for the sample, it is important to thoroughly clean the entire system, including the cells, QCM, and substrates support, using proper solvents such as ethanol and ketone. This cleaning process is essential to eliminate any potential contamination from previously deposited materials.

In the case of studying and fabricating thin films of an ionic liquid, it is indeed common to utilize a small quantity of the material. This approach maximizes thermal contact between the liquid and the cell, facilitating efficient heat transfer and providing better control over the deposition process for thin film fabrication. The utilization of a large amount of IL enables an obstruction of the orifice and the leakage of IL from the cell.

In all of the studies, the control of the mass flow rate was achieved by regulating the temperature of the Knudsen cell (evaporation temperature) and the cell orifice diameter. The values of the mass flow rate are described in each subchapter of the "Results and Discussion" chapter, due to the variation in flux for each study.

3.2.2. Sputtering

The modification of the ITO substrate through the application of a metallic film (Ag or Au) on its surface was accomplished using the sputtering technique, which has been previously employed by our research group [10,62,63,81,82,97]. Sputtering is indeed a technique commonly used for depositing inorganic semiconductors, particularly, metals. As an alternative to sputtering, thermal evaporation with reduced pressure can be used for the deposition of metals; however, it requires subjecting the material to high temperatures. The sputtering technique involves the formation of a plasma, usually using an inert gas such as helium or argon, which generates high-energy ions. Theses ions collide with the target material, transferring energy to it and causing the removal of atoms from the target surface. These atoms subsequentially migrate and deposit onto the substrate surface, creating a film or a coating. The coating of a surface enables the modification of the dynamic and morphological properties of the deposited ILs. In this specific study, the Cressington (model 108 auto) magnetron sputtering equipment, depicted in Figure 24, was utilized for the modification of the ITO substrate surface.

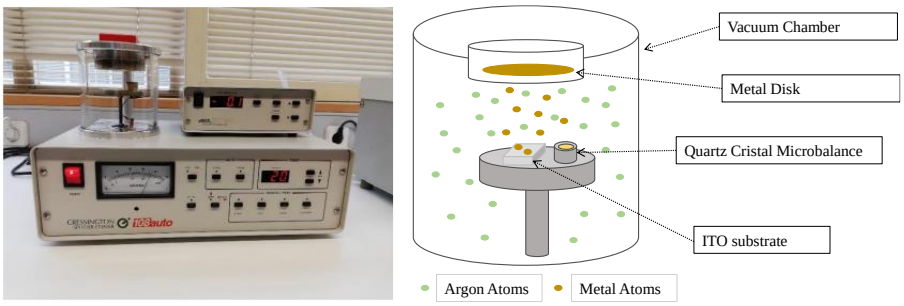

Figure 24. Image of the sputtering equipment used in the surface modification, Cressington (model 108 auto), (left image). Schematic representation of the way of a magnetron sputtering works, forming a metallic surface (right image).

This equipment is a direct current (DC) magnetron sputtering system that operates at low voltage. Magnets strategically are placed near the cathode to attract more particles toward it, intensifying the target removal process and increasing the quantity of material that reaches the surface. The target, depicted in Figure 25, is a metal disk, where the most commonly used magnetron sputter coaters are gold (Au), silver (Ag), platinum (Pt), and palladium (Pd). To prevent potential contamination by the air, it is necessary to evacuate the chamber. To accomplish this, a rotative pump system is employed to depressurize to 0.1 mbar. Following that, an inert gas is introduced into the chamber, and a direct current is applied to ionize the gas, which will collide with the target and remove metal atoms from its surface. For this particular study, a plasma was formed using argon gas, and the targets used were silver (Ag) and gold (Au) disks [98].

Several factors can influence the uniformity and thickness of the metallic film. It's crucial to consider that even minor variations on the film surface can lead to notable effects on the morphology and size distribution of the deposited ionic liquid droplets. Therefore, precise control of the deposition parameters is essential to achieve the desired film characteristics. Factors that can influence the film quality of metal coatings fabricated by sputter deposition include the voltage applied to generate the plasma, gas pressure, target-to-substrate distance, deposition time, and substrate temperature. Optimizing these parameters can help ensure a uniform and controlled deposition of the metallic film. The targets used in this study were commercially acquired from Micro To Nano with a high purity (which contains 99.99% of the metal). Over time, repeated depositions cause some abrasion on the surface due to the magnetic field. This phenomenon gradually diminishes the target's usability and prevents its complete utilization, as it shown in Figure 25.

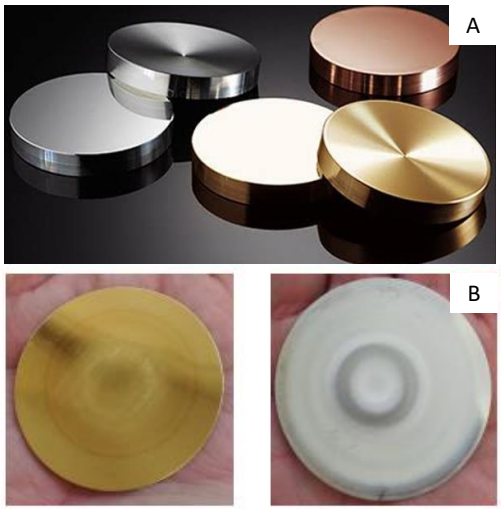

Figure 25. Image of different targets widely used in sputtering equipment (A). Image of erosion of gold (left) and silver (right) targets used in the sputtering equipment employed in this work.

3.3 Morphological Analysis

This subchapter aims to introduce the two methodologies employed for the morphological characterization of thin films of ILs on various surfaces.

Optical microscopy was employed as the initial method to quickly observe the IL film's behavior on the surface immediately after its removal from the thermal evaporator. This technique offers valuable preliminary insights into the film's overall appearance and macroscopic features.

For a more detailed and comprehensive analysis of the IL film's morphology, SEM was utilized. SEM allowed for higher magnification imaging, enabling the visualization of smaller structures and finer details that cannot be resolved with optical microscopy. By using SEM, it was possible to obtain a more in-depth understanding of the IL film's surface topography, including features such as surface roughness, droplet size and shape, and surface coverage. Combining optical microscopy for initial observations and SEM for detailed characterization provided a comprehensive morphological analysis of IL films on various surfaces, offering valuable insights into their behavior and structural properties.

3.3.1. Optical Microscopy

Optical microscopy, also known as light optical microscopy, is a technique utilized across various disciplines to observe small structures and/or objects. This technique originated in the 17th century, using visible light and a lens system to magnify images of small samples, enabling direct observation. As time progressed, microscope design was developed with the aim of improving image resolution and contrast [99,100].

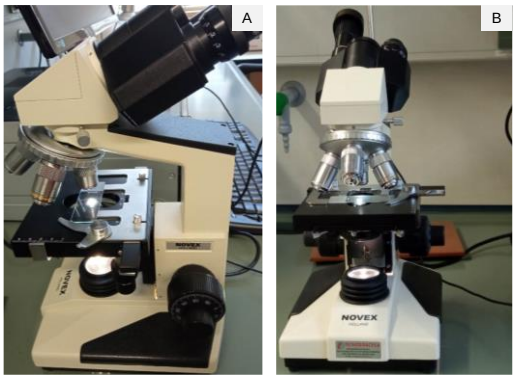

Figure 26. Optical microscope: side (A) and front (B) views.

Most of the microscopes incorporate an artificial light source to have better control over the intensity of the light. In these systems, the condenser lens shapes and filters the light, directing it onto the sample, achieving a high-resolution and contrast-inverted image. By conjugation of the different lenses, higher magnification, and quality can be achieved compared to a microscope with a single lens [99,100].

In this work, an optical microscope, NOVEX K-Range PB 4161 was used (Figure 26), with an observer lens ampliation of 16x and objective lens ampliations of 4x, 10x, 40x, and 100x. Optical images of ILs deposited on different surfaces were obtained with the ampliation of 640x, which involved an objective lens with a magnification of 40x and an ocular lens with a magnification of 16x. The microscope was also connected to a computer using a USB microscope camera, specifically the BRESSER MikrOkular Full HD eyepiece camera. Optical images were viewed using the ImageJ software.

3.3.2. Scanning Electron Microscopy

The ILs film's topography and morphology were studied in high detail using scanning electron microscopy (SEM), using two distinct equipments, as shown in Figure 27: a compact scanning electron microscope (SEM, Hitachi, FlexSEM 1000) located in the Department of Geosciences, Environment and Spatial Plannings of the faculty, and the high-resolution SEM located in the Laboratory of Scanning Electron Microscopy and X-Ray Microanalysis in the Centro de Materiais da Universidade do Porto (CEMUP).

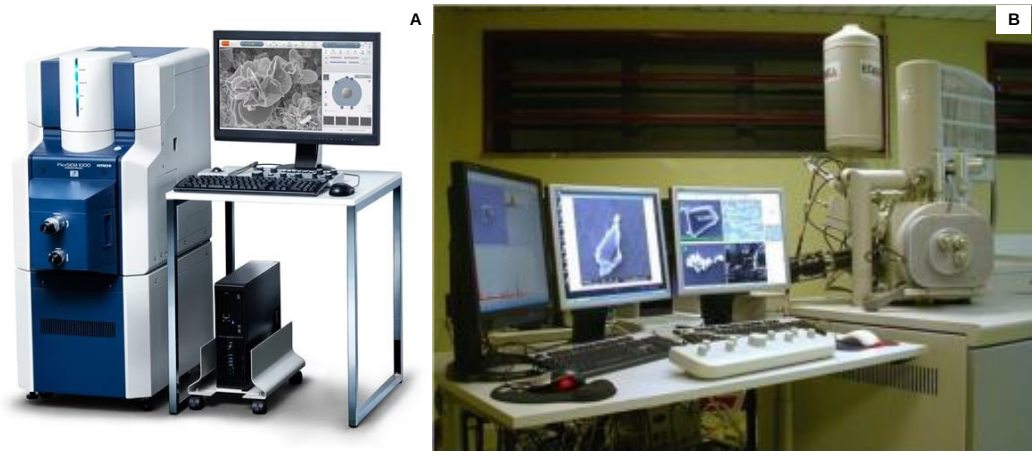

Figure 27. Image of the compact scanning electron microscope, FlexSEM 1000 of Hitachi (A), and the high-resolution scanning electron microscopy, FEI Quanta 400FEG ESEM/ EDAX Genesis X4M (B).

The operation of both equipments follows the same principles: an electron gun emits a high-voltage beam that focuses on the sample, leading to interactions between the beam and the sample. These interactions result in the production of electrons that are detected and converted into an image. The intensity of the beam allows to obtain different information about the surface [101].

When the beam has a low accelerating voltage, it interacts with the atoms near the surface, providing information about the surface of the sample (secondary electrons mode, SE mode). By increasing the voltage of the beam, it penetrates underneath the sample surface and reflects a signal related to the sample's internal morphology (backscattered electron mode, BSE mode) [101]. This is illustrated in the schematic below (Figure 28).

In this work, the morphology of ILs was analyzed using the two SEM modes, SE and BSE. The SE mode was employed to examine the surface morphology and investigate the influence of carbon in the morphology of ILs. On the other hand, the BSE mode was used to enhance the detection and quantify the IL droplets.

With the SEM technique, it was possible to quantify the number of droplets on the surface, analyze the morphology and distribution of sizes, and determine the coverage area of the droplets on different surfaces. The details of the imaging techniques employed are described below (Table 3).

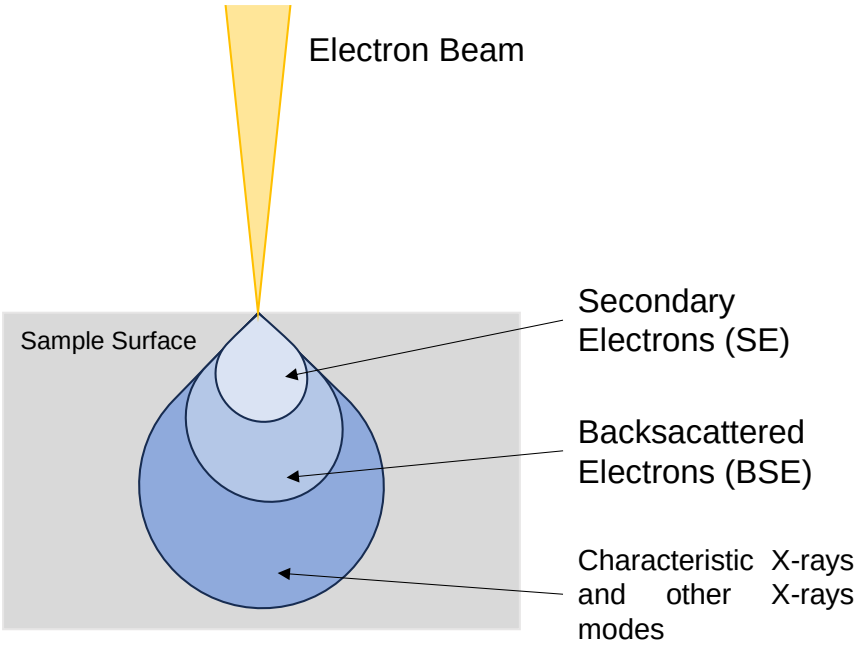

Figure 28. Schematic representation of the different depths of the SEM modes (adapted from [101]).

Table 3. Experimental parameters for image detection in the different SEM equipments.

	Compact SEM	High-Resolution SEM
Magnifications	800x 1600x 4000x	200x 2000x 5000x 20 000x
Detector	BSE (top views)	SE (lateral views at 45º)
Voltages	3.00 and 5.00 kV	10.00 kV
Detector distance	6.00 - 9.00 mm, approximately	12.00 mm, approximately

After capturing the SEM images of the IL droplets, the next step was to analyze the images in detail. The analysis was carried out using the ImageJ software [102], a widely used image processing and analysis tool. It performed a comprehensive examination of the SEM images that allowed the extraction of valuable information about the thin films. Various image processing and analysis techniques were applied to study the shape, surface coverage, and size distribution of the IL droplets.

3.4. Substrates

To study the deposition dynamics and morphology of the fabricated films, it is necessary to understand the interaction between the substrate and the material that originates the film. The substrate refers to the surface on which the deposition occurs, and its inherent characteristics can significantly influence the nucleation and growth processes of the film. Furthermore, the interaction between the material and the substrate can change the physical and chemical properties of the material compared to its bulk form. In this study, indium tin oxide-coated glass (ITO) and quartz crystals coated with gold were utilized as substrates. These substrates were specifically chosen for their distinct properties and suitability for the experimental aims.

3.4.1. Indium Tin Oxide (ITO)-Coated Glass and Modified ITO Surfaces

In previous work conducted by the research group, an ITO substrate was used as the primary surface for deposition, mainly for IL deposition [59,62,78,79,80,95]. The ITO substrate comprises a glass surface coated with a layer of indium tin oxide (ITO) on one side. ITO is a highly conductive material. To differentiate the conductive side of the ITO substrate from the glass side, it is necessary to measure the surface electrical conductivity using a multimeter, due to their similar appearance.

Due to the clear and transparent nature of ITO, this substrate finds application in various optoelectronic devices, including solar cells and OLEDs. Its transparency enables the transmission of light, facilitating optical measurements and characterization. The ITO-coated substrates can be coated using PVD techniques, such as sputtering or thermal evaporation [103].

In the context of this work, ITO substrates with a square shape and dimensions of 10 mm × 10 mm × 1.1 mm, with a theoretical thickness (provided by the supplier) of the ITO film is approximately 180 nm, were used, as illustrated in Figure 29. ITO-glass substrates were purchased commercially from Praezisions Glas & Optik GmbH. The ITO film allows for the surface to have a resistance between 10 and 17 Ω /square, approximately [104]. Before each deposition, the substrates were cleaned using high-purity ethanol and subjected to an ultrasonic bath.

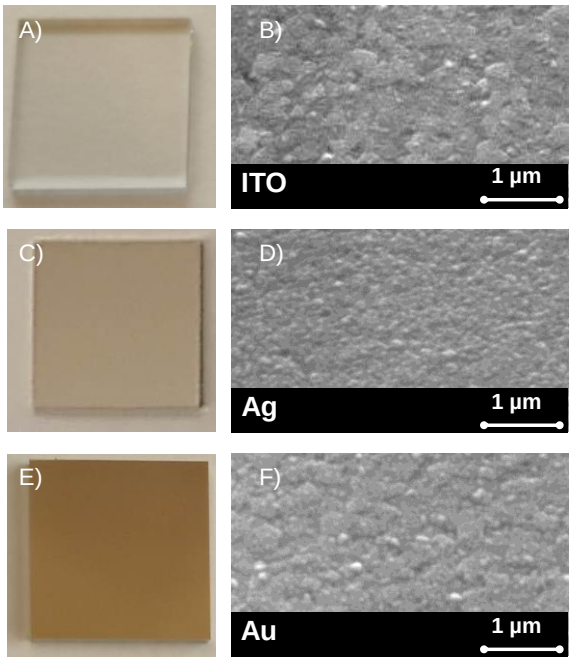

Figure 29. Picture of a glass coated with ITO (A), Ag/ ITO (C), and Au/ITO (E) and the respective detailed SEM image of their surfaces (B, D, and F).

Coated ITO Surfaces

The work here described aimed mainly at investigating the interactions between the ILs and the underlying substrate. For that, a range of substrate surfaces were used, including Au, Ag, and carbon surfaces. To expand the available surface options, an approach was devised to enable coating the ITO substrate with the material of interest in different ways and degrees of coverage. Figure 30 illustrates the different treatments applied to the ITO surface and shows a schematic representation of the resulting surfaces.

The sputtering technique was used to deposit metal coatings, Au (scheme 3 of Figure 30) and Ag (schemes 5 and 6 of Figure 30), onto the ITO surfaces. To achieve a partial Ag coating (scheme 5), a very precise procedure was designed and followed. The ITO surface was meticulously divided with Kapton tape, creating distinct sections (Figure 31). The divided ITO substrate was then subjected to sputtering, creating two different surfaces in the same substrate, allowing to study the behavior of the IL film in proximity to an interface. Variating the time and current to ionize the argon, it was possible to fabricate partial Ag surfaces with different Ag film thicknesses (in the case of this work, the films fabricated have thicknesses of 40 and 100 nm, approximately). The differentiation of the surface thickness provides flexibility in studying the impact of film thickness on the IL-substrate interactions and overall properties.

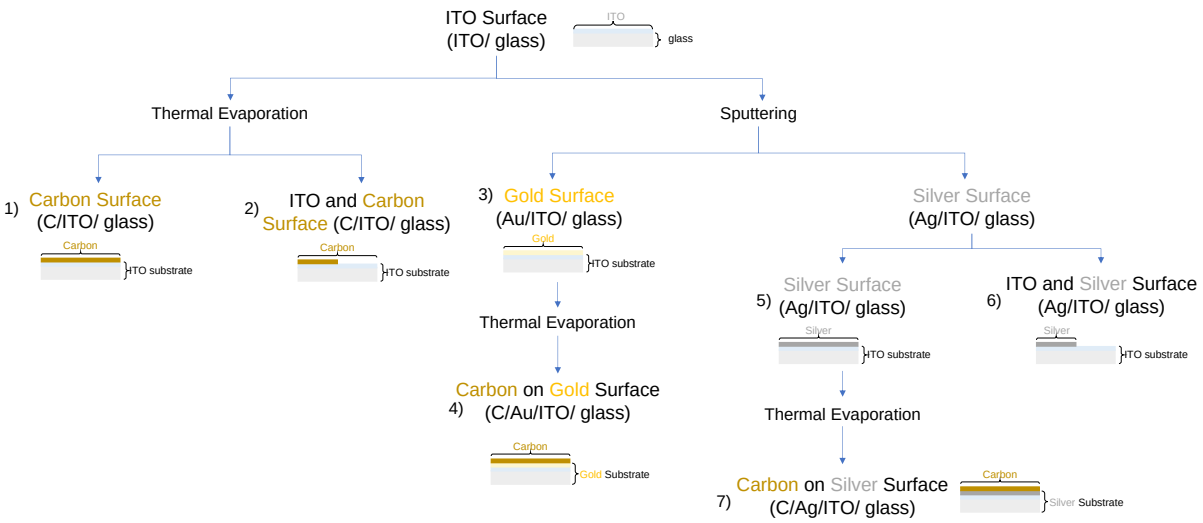

Figure 30. Schematic representation of the different treatments applied to ITO surfaces in order to obtain the different surfaces utilized in this work: 1) ITO substrate coated with carbon; 2) ITO substrate coated with carbon on one half on the available surface; 3) ITO substrate coated with gold; 4) ITO substrate coated first with gold and after with carbon; 5) ITO substrate coated with silver; 6) ITO substrate coated with silver on one half the available surface area; 7) ITO substrate coated first with silver and after with carbon.

To fabricate amorphous carbon films (schemes 1, 2, 4, and 7 of Figure 30), thermal evaporation equipment at CEMUP facilities was used. The equipment allowed the production of carbon films with different thicknesses. In this study, carbon films of approximately 10 nm, 20 nm, and 30 nm thickness were successfully fabricated using the PVD technique. These varying thicknesses of carbon films provided a range of samples to investigate the effects of film thickness on the IL-substrate interactions and properties. Furthermore, employing a similar approach to achieve a partially Ag-covered surface, a surface with partial carbon coverage was fabricated, enabling the study of IL affinity on these surfaces as well as the effect on an interface in the IL morphology.

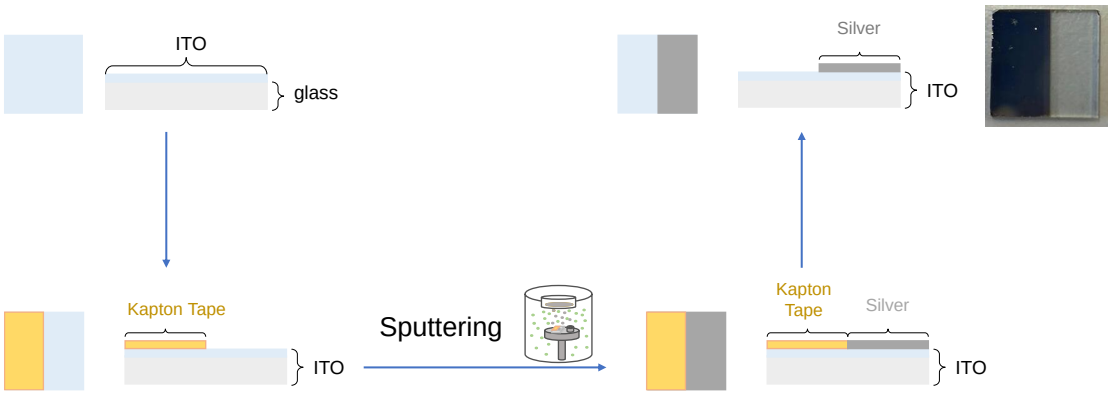

Figure 31. Schematic representation of the process to coat partially the ITO substrate with Ag.

3.4.2. Quartz Crystals

The quartz crystal microbalance is an instrument used commonly to monitor and control the thickness of films in PVD techniques. It operates by measuring the decrease in resonance frequency of a quartz crystal due to the amount of deposited material. By analyzing the frequency change, the quantity of material deposited on the crystal can be determined, enabling precise and continuous control over the deposition process [108].

The quartz crystals used in this study were commercialized by Inficon and have a convex plan with a 6 MHz AT cutting and a 14 mm diameter. These crystals have piezoelectric properties and were coated, by the fabricator, with a layer of gold. The SEM images of these materials revealed a highly irregular surface with confined spaces. The unique morphological characteristics of these crystals made them particularly suitable for studying the behavior of ILs within confined environments. Some of the quartz crystals were subjected to changes in their surface by adding some layers of carbon. This coating process involved depositing carbon on the QCM surface using an e-beam evaporator.

4. Results and Discussion

This chapter presents the experimental results divided into three subchapters. Each subchapter presents the experimental results regarding the influence of three main factors on the nucleation and growth of IL thin films – the deposition conditions, the interface, and the presence of amorphous carbon. Then results are discussed throughout to facilitate the final overall conclusions.

4.1. Influence of the Deposition Conditions in the Nucleation and Growth of Ionic Liquid Thin Films

One of the factors that significantly influence the morphology of IL films is the deposition conditions, as they influence both the quantity and kinetics of IL arrival at the surface. Therefore, it is crucial to understand the impact of these conditions on the structuring of distinct IL film types. The modification of the IL mass flow rate (Φ) reaching the surface or changing the substrate temperature provided insight into the impact of these conditions on the film morphology. To further discriminate these factors, IL films with a thickness of 40 ML were examined on two distinct surfaces (ITO and Ag, Figure 30). The film morphology analysis was conducted using the SEM technique in BSE mode. The resulting SEM micrographs were subsequently analyzed using ImageJ software, enabling the determination of droplet count, droplet size, and surface coverage. This information was organized into histograms and graphics to facilitate the understanding of the changes in the system's behavior.

4.1.1. Influence of the Mass Flow Rate

Based on the characteristics of the thermal evaporation equipment, which operates at reduced pressure as outlined in subchapter 3.2.1, the mass flow rate of ILs reaching the surface could be modified in two ways. First, by adjusting the IL evaporation temperature within the range of 473 K to 533 K. Secondly, by modifying the exit area of IL – either by changing the diameter of the Knudsen cell (2.1 or 3.1 mm) or without using the disk with the orifice. Increasing the evaporation temperature and the Knudsen orifice diameter for the ILs under study may lead to a change in the mass flow rate detected by the QCM.

The overall results related to the change in the evaporation temperature as well the exit area of the cell for each IL are presented in Figures A1-A18 from the Attachments. Figure

32 and Figure 33 demonstrate results when modifying one of the conditions in the study (evaporation temperature) for a shorter and larger alkyl side chain IL, respectively. Table 4 shows the different mass flow rates resulting from changes in the evaporation temperature and orifice diameter for each IL. Figures 32 and 33 illustrate the morphology of IL films on ITO and Ag surfaces, accompanied by the respective droplet size distribution analysis when changing the evaporation temperature (473, 503, 513, and 533 K) while maintaining a constant orifice diameter (3.1 mm). In these conditions - Knudsen cell orifice of 3.1 mm and different evaporation temperatures (473, 503, and 533 K), it was possible to obtain IL film surfaces at different mass flow rates: 0.12, 0.54, and 1.5 Å/s for $[C_2C_1im][NTf_2]$; 0.11, 0.47, and 1.5 Å/s for $[C_8C_1im][NTf_2]$; 0.06, 0.18, and 0.51 Å/s for $[C_2C_1im][OTf]$; 0.09, 0.24, and 0.73 Å/s for $[C_8C_1im][OTf]$. The temperature of the substrates was kept at T = 283 K. These changes allowed to infer the impact of using different mass flow rates (Φ) on the morphology of the obtained IL films: $[C_2C_1im][NTf_2]$ with Φ ranging from 0.12 to 1.5 Å/s; $[C_8C_1im][NTf_2]$ with Φ varying between 0.11 to 1.5 Å/s; $[C_2C_1im][OTf]$ with Φ increasing from 0.06 to 0.51 Å/s; and $[C_8C_1im][OTf]$ with variation between 0.09 and 0.73 Å/s. The differentiation in the mass flow rate between the $[NTf_2]$-based ILs and [OTf] congeners is attributed to the difference in their vapor pressure. Although precise vapor pressure values for $[C_2C_1im][OTf]$ and $[C_8C_1im][OTf]$ are unavailable, based on the detected mass flow rates, it appears that [OTf]-based ILs have lower vapor pressure when compared to their $[NTf_2]$ congeners (Table A1 of the Attachments) [107].

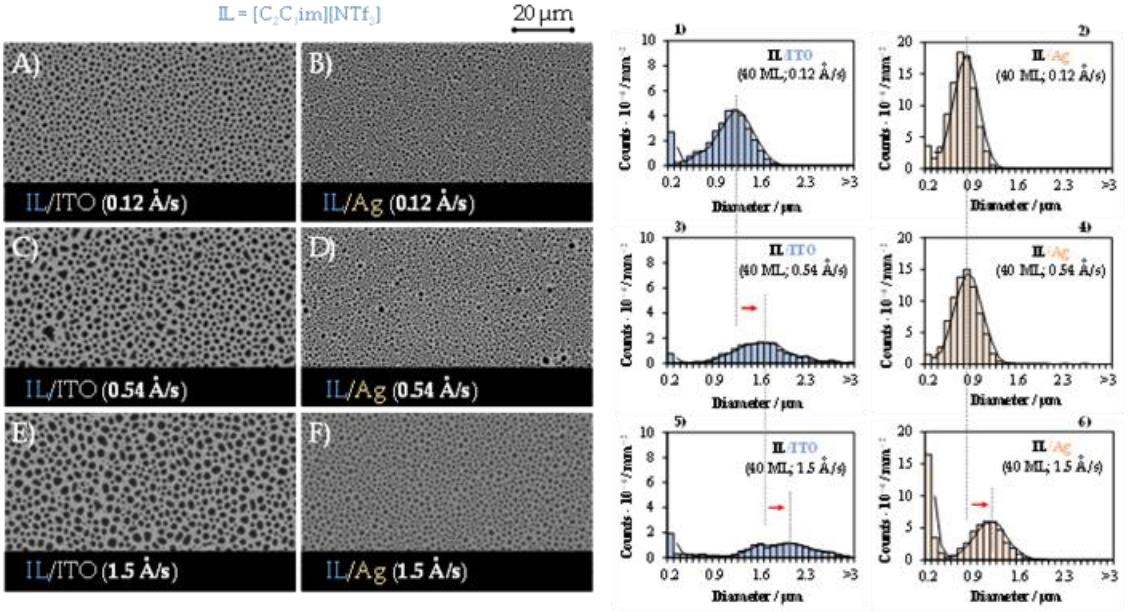

Figure 32. Morphology of $[C_2C_1im][NTf_2]$ thin films (micro- and nanodroplets) (A-F) and the respective droplet size distribution (histograms 1-6). The IL films were deposited (by PVD) simultaneously onto surfaces of ITO (images A, C, E) and Ag (images B, D, F) with a thickness of 40 ML. Using a Knudsen cell orifice with a diameter 3.1 mm and different evaporation temperatures (473, 503, and 533 K), it was possible to obtain IL film surfaces at different mass flow rates: 0.12, 0.54, and 1.5 Å/s. The temperature of the substrates was kept at T = 283 K. Surface coverages of 35.9, 33.8, 36.1, 34.6, 39.8, and 36.1 % were derived by image processing of Figures A, B, C, D, E, and F, respectively. Top views (A-F) were acquired through scanning electron microscopy by using a backscattered electron detector (BSE).

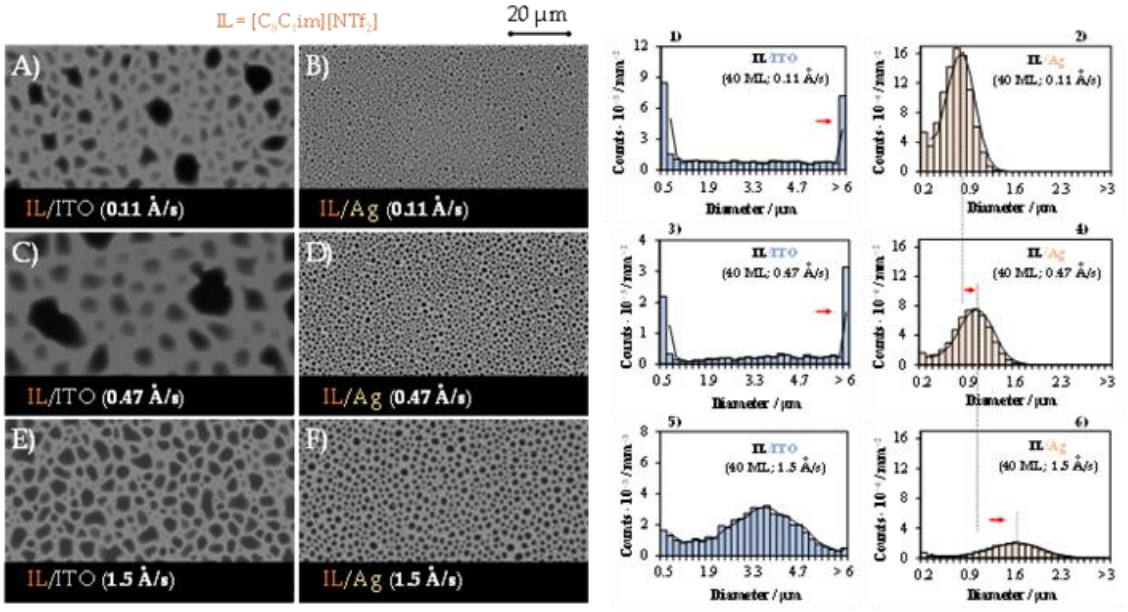

Figure 33. Morphology of $[C_8C_1im][NTf_2]$ thin films (micro- and nanodroplets) (A-F) and the respective droplet size distribution (histograms 1-6). The IL films were deposited (by PVD) simultaneously onto surfaces of ITO (images A, C, E) and Ag (images B, D, F) with a thickness of 40 ML. Using a Knudsen cell orifice with a diameter of 3.1 mm and different evaporation temperatures (473, 503, and 533K), it was possible to obtain IL film surfaces at different mass flow rates: 0.11, 0.47, and 1.5 Å/s. The temperature of the substrates was kept at T = 283 K. The image processing was not able to derive with accuracy the surface coverage of the films (it is estimated to be > 40 %). Top views (A-F) were acquired through scanning electron microscopy by using a backscattered electron detector (BSE).

Table 4. Experimental conditions of the thermal evaporation process for each ionic liquid: evaporation temperature ($T_{evp.}$); orifice diameter of the Knudsen effusion cell; and the deposition rate (Φ). These were used to study of the influence of mass flow rate on the morphology of different IL films (with a deposition amount of 40 ML) on both ITO/glass and Ag/ITO/glass substrates, maintaining the substrate temperature ($T_{subst.}$ = 283 K).

Precursor	$T_{evp.}$ / K	Orifice Diameter / mm	Φ / Å·s^{-1}
$[C_2C_1im][NTf_2]$	473	2.1	0.08 ± 0.01
	503	2.1	0.39 ± 0.08
	533	2.1	0.74 ± 0.10
	473	3.1	0.12 ± 0.05
	503	3.1	0.54 ± 0.05
	533	3.1	1.50 ± 0.18
	503	a)	4.50 ± 0.52
$[C_8C_1im][NTf_2]$	473	2.1	0.08 ± 0.01
	503	2.1	0.39 ± 0.04
	533	2.1	1.10 ± 0.11
	473	3.1	0.11 ± 0.05
	503	3.1	0.47 ± 0.06
	533	3.1	1.50 ± 0.26
	503	a)	2.96 ± 0.25
$[C_2C_1im][OTf]$	473	2.1	0.02 ± 0.02
	503	2.1	0.05 ± 0.04
	533	2.1	0.15 ± 0.06
	473	3.1	0.06 ± 0.01
	503	3.1	0.18 ± 0.07
	533	3.1	0.51 ± 0.04
	503	a)	0.77 ± 0.16
$[C_8C_1im][OTf]$	473	2.1	0.04 ± 0.02
	503	2.1	0.14 ± 0.02
	533	2.1	0.30 ± 0.05
	473	3.1	0.09 ± 0.02
	503	3.1	0.24 ± 0.09
	533	3.1	0.73 ± 0.05
	503	a)	0.75 ± 0.10

a) These experiments were conducted by removing the disk containing the orifice, maximizing the mass flow rate.

A detailed observation of the results allows for the comparison of the different morphologies of the IL films (with a deposition amount of 40 ML). It was observed that, for all the ILs studied and on both ITO and Ag surfaces, micro- and nanodroplets are formed, with well-defined boundaries, instead of a continuous film. This observation suggests a weak IL-substrate affinity. From a thermodynamic perspective, if a very large amount of IL were deposited on these substrates, a single large droplet would be expected to be formed, reducing the interfacial and surface tensions in the system. However, when using the thermal evaporation technique by the Knudsen effusion method, there is a slow deposition, and the ion pairs tend to migrate to places where the effect of the different interfacial tension is less significant. This behavior arises from the high surface mobility of the IL clusters on these surfaces. The interplay between interfacial and surface tensions can be considered a defining factor for the film growth

mechanism. In this case, for all the ILs studied, we consider that these films follow a 3D film growth mode, commonly referred to as island growth. This growth mechanism has previously been described in IL films fabricated using vacuum deposition methodologies with thicknesses in the mesoscopic scale, as observed in the IL films under examination in this study [62,108]. It has been shown that the interactions between the first ionic pairs and the surface determine the growth mode of the IL film. Consequently, the growth characteristics of the initial IL layers constitute a highly discussed topic within this research domain. Some researchers postulate that, on multiple surfaces, ILs form an initial layer that spreads across the entire surface (2D growth), followed by 3D growth, resulting in droplets of varying sizes [80]. Nevertheless, due to the mesoscopic scale employed in this work, it was not possible to ascertain the initial stage of nucleation and growth, prompting the formulation of theoretical possibilities based on the observed results.

When comparing the droplets on the Ag surface with those on the ITO surface, it can be observed that, for the same IL and mass flow rate, the droplets on the Ag surface exhibit a smaller size. This observation is supported by the analysis of the SEM images A, C, and F (left images for the ITO surface) when compared to images B, D, and E (images on the right for Ag surfaces) for Figures 32 and 33, as well as Figures A13, A14, A16 and A17 from the Attachments (this effect was also observed in the SEM micrographs A1, A4, A7 and A10 from the Attachments, where ITO images are presented in the top half and Ag images are in the bottom part). Furthermore, based on the histograms (Figures 32 and 33, as well as Figures A2, A3, A5, A6, A8, A9, A11, A12, A15, and A18 from the Attachments) obtained from the SEM micrographs, it is possible to observe a higher number of droplets on the Ag surfaces, for the same IL and mass flow rate. This behavior can be explained by the lower minimum free area of nucleation (MFAN) on metallic surfaces compared to ITO surfaces, which facilitates the formation of stable clusters in a reduced surface area. Additionally, the lower MFAN reduces the surface mobility of the clusters, leading to a delay in the coalescence processes [10,65,109]. In other words, imidazolium-based ILs have a good affinity with metal surfaces, which reduces their tendency to coalesce and form larger and spherical droplets even with higher deposition rates on these surfaces.

When analyzing the change of anion for ILs with shorter alkyl chains, it is possible to observe that an increase in the mass flow rate results in similar morphologies for $[C_2C_1im][NTf_2]$ and $[C_2C_1im][OTf]$ on both studied surfaces. This increase is more significant on the ITO surface compared to the Ag surface. Specifically, the modal

diameter for the $[C_2C_1im][NTf_2]$ on ITO surfaces ranges from 1.1 to 1.3 µm for Φ = 0.12 Å·s^{-1} (graph 1 in Figure 32 and Figure A15); 1.4 to 1.8 µm for Φ = 0.54 Å·s^{-1} (graph 3 in Figure 32 and Figure A15); and 1.5 to 2.1 µm for Φ = 1.5 Å·s^{-1} (graph 4 in Figure 32 and Figure A15), whereas on Ag surfaces, the modal diameter varies between 0.7-0.8 for the lowest Φ and the higher Φ, the variation was between 1.1 and 1.2 µm (graphs 2, 4, and 6 in Figures 32 and A15). Similar behavior is observed for the $[C_2C_1im][OTf]$ for both of the surfaces studied, where is possible to observe an enlargement of the droplet size distribution on the ITO surface when the deposition rate increased. Conversely, on the Ag surface, there is no significant change in the modal diameter with an increase in the mass flow rate, remaining in the range of 0.6-0.8 µm. For the ILs under study, the ITO surface can be considered a solvophobic surface. As a consequence, there is higher ion pair mobility, resulting in an intensification of the coalescence mechanisms. On the other hand, the lower effect of the mass flow rate on the Ag surface can be related to the higher affinity of the imidazolium cation into the Ag surface.

Upon examining SEM micrographs on ITO surfaces (Figures 32 and 33, and Figures A1-A18 from the Attachments), it becomes evident that $[C_8C_1im]$-ILs tend to form larger and more heterogeneous droplets then $[C_2C_1im]$-ILs. The $[C_8C_1im]$-based ILs exhibit droplets with better spreading, in agreement with previous work [10]. However, these droplets do not coalesce to form a continuous film. This is due to higher substrate-film interfacial tension, despite the lower film-vapor interfacial tension [23]. ILs with larger alkyl chains exhibit a predominant non-polar effect due to their larger alkyl chain size. In theory, the rearrangement of these ILs involves the ionic pairs dislocating to areas near the surface, while the alkyl chain transitions into the gas phase. The challenges faced by the ionic pairs in their interaction with the surface and their ability to organize themselves in a structured manner enhance surface mobility and promote interactions between ionic pairs. Furthermore, when these ILs are deposited on a solvophobic surface (like the ITO surface), it enhances the ionic pair surface mobility. As a consequence of these factors, theirs a facilitation of the second-order coalescence mechanism for the $[C_8C_1im]$-ILs on the ITO surface, leading to the formation of a *bulk* phase (formation of a single droplet with the total amount of IL deposited). This phenomenon leads to an increase in surface wettability [10,62,108]. The SEM micrographs (Figures 33, A7, A10, A16, and A17) and associated histograms illustrate this trend for the ITO surface. The film morphology remains similar across all deposition rates, characterized by the formation of larger droplets (the histograms show that the modal diameter is above 6 µm, even when applying lower Φ). On Ag surfaces, two distinct behaviors were found: $[C_8C_1im][NTf_2]$ exhibits similar behavior to $[C_2C_1im]$-based ILs, where there is an increase in the modal

diameter with an increase in Φ from 0.11 to 1.5 Å/s (Figure 33, graphs 2, 4, 6); for $[C_8C_1im][OTf]$, larger droplets are formed, similar to $[C_8C_1im]$-ILs on ITO surface. However, the coalescence mechanism is less intense compared to the ITO surface (Figure A18, graphs 2, 4, 6).

To better visualize the results of different ILs, the data was organized into graphical representations of the total count of IL droplets as a function of the deposition rate for $[C_2C_1im][NTf_2]$ (graph A), $[C_2C_1im][OTf]$ (graph B), $[C_8C_1im][NTf_2]$ (graph C), and $[C_8C_1im][OTf]$, for both ITO and Ag surfaces, as shown in Figure 34.

When analyzing the graphs, it is possible to observe that ILs with shorter alkyl chains (graphs A and B) exhibit a higher number of droplets count compared to $[C_8C_1im]$-based ILs (graphs C and D), which tend to spread more effectively on the surface forming larger droplets and, consequently, a reduced number of droplets (please see the yy scales in each case). The higher number of droplets in $[C_2C_1im]$-ILs indicates less intense coalescence mechanisms. It was observed that the number of droplet counts on Ag surfaces is higher compared to the ITO surface for all the studied ILs, in agreement with some previous works [10,62,108].

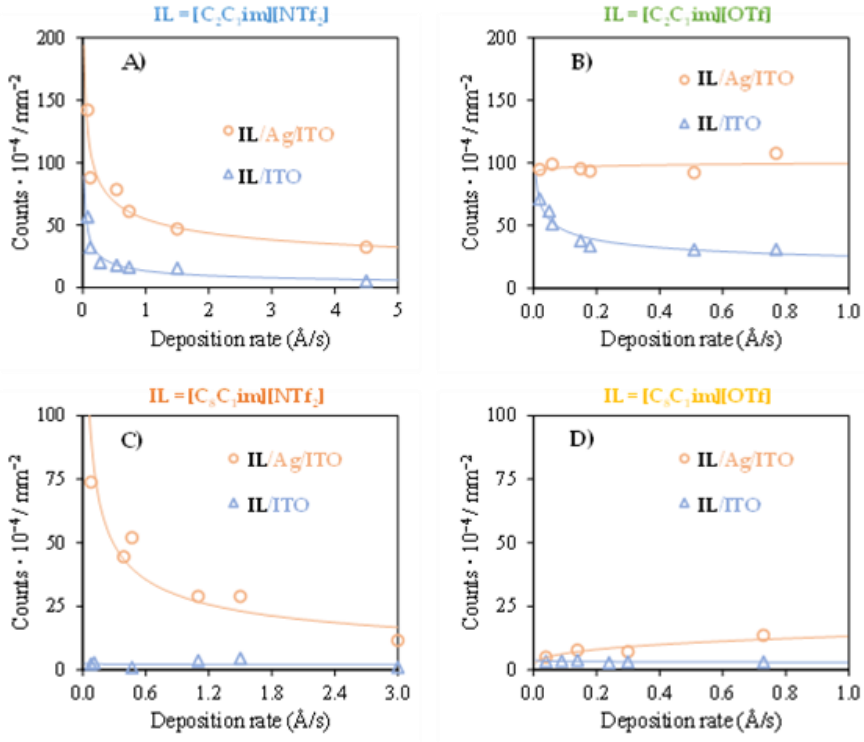

Figure 34. Graphical representations of the number of IL droplets obtained (all microdroplets with a minimum area of 0.02 μm^2) as a function of the deposition rate for $[C_2C_1im][NTf_2]$ (A), $[C_2C_1im][OTf]$ (B), $[C_8C_1im][NTf_2]$ (C), and $[C_8C_1im][OTf]$ (D). These results were derived from image processing of the SEM micrographs relative to the simultaneous deposition of each IL film (40 ML) onto the surface of ITO and Ag/ITO.

Focusing on graph A, related to $[C_2C_1im][NTf_2]$, the results exhibit a similar profile for both studied surfaces. However, overall the counts for Ag surfaces are higher compared to the ITO surface. The profile demonstrates that, at lower deposition rates, there is a higher number of droplets, whereas as the deposition rate increases, there is an exponential decrease in the number of droplets, eventually reaching a plateau. This observation suggests a high kinetic contribution to the nucleation and growth processes. At lower deposition rates, a lower number of ion pairs arrive at the surface, allowing nucleation and growth processes to occur with a reduced number of encounters. As the deposition rate increases, a higher quantity of ionic pairs arrives at the surface in a shorter period of time. Consequently, competition for the formation of clusters intensifies, resulting in a decrease in the availability of energetically stable locations. This behavior promotes the surface mobility of the new ionic pairs and clusters, enhancing the first-order coalescence mechanisms. Therefore, increasing the mass flow rate leads to an increase in the coalescence mechanisms, characteristic of higher surface diffusion. This behavior is also observed for the system $[C_2C_1im][OTf]$/ITO. However, the profile of $[C_2C_1im][OTf]$ on the Ag surface is different, as the increase in deposition rate does not significantly affect the droplet count. The result indicates the formation of highly stable clusters when the $[C_2C_1im][OTf]$ is adsorbed on the Ag surface. The formation of stable clusters is related to the affinity between the IL-Ag surface and the lower MFAN compared to the ITO surface. Consequently, the lower surface mobility of the ionic pairs, results in this case in a reduced first-order coalescence mechanism, even with an increase in the mass flow rate.

The graphs representing $[C_8C_1im]$-based ILs (graphs C and D) show a lower droplet count on the ITO surface regardless of the mass flow rate, which can be attributed to the intrinsic coalescence mechanisms (2^{nd} coalescence mechanisms) [10,62,108]. On the Ag surface, the droplet count profile displays two different behaviors: for $[C_8C_1im][OTf]$/Ag, it is similar to the observed on the ITO surface; however, for $[C_8C_1im][NTf_2]$/Ag, the behavior is similar to the $[C_2C_1im]$-based ILs on this surface. Comparing the SEM micrographs and histograms of $[C_8C_1im]$ ILs on the Ag surfaces it becomes evident that $[C_8C_1im][NTf_2]$ produces smaller droplets compared to $[OTf]^-$ (Fig 33). This behavior indicates a higher influence of the 2^{nd} coalescence mechanism in the $[C_8C_1im][OTf]$ compared to its congener $[NTf_2]$ IL, which, at lower deposition rates, forms stable clusters with lower surface mobility.

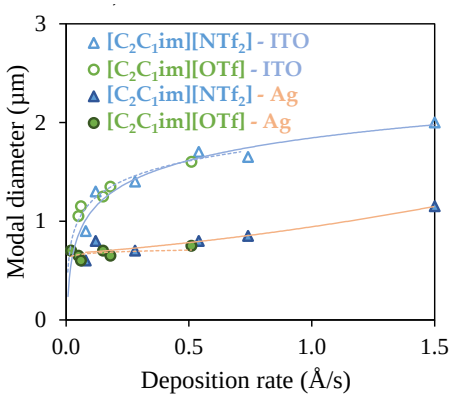

Figure 35. Graphical representations of the relation between the deposition rate and modal diameter of the IL droplets for $[C_2C_1im][NTf_2]$, and $[C_2C_1im][OTf]$. These results were derived from the analysis of the SEM micrographs relative to the simultaneous deposition of each IL film (40 ML) onto surfaces of ITO and Ag/ITO.

Due to a higher influence of the nucleation and first-order coalescence mechanisms for the smaller $[C_2C_1im]$-based ILs, the influence of the anion on the modal diameter on each studied surface was carried out considering the dependence on deposition rate (Figure 35). The results do not indicate a significant differentiation in the behavior on the surface when changing the anion. The curves for the ILs coincide on both surfaces. Importantly, two distinct behaviors can be observed: on the ITO surface, a small increase in the deposition rate leads to a larger increase in the modal diameter until reaching a plateau for higher deposition rates (above ≈ 0.5 Å/s), whereas on Ag the increment in modal diameter with the deposition rate is minimal and almost linear. When comparing the modal diameter for the same deposition on different surfaces, a higher modal diameter is observed on the ITO surface. Furthermore, the modal diameter for both ILs on ITO surfaces is, in general, (0.8 ± 0.1) µm higher compared to the droplet's modal diameter on the Ag surface. This result indicates that changing the anion doesn't significantly influence the nucleation and growth of the film for small ILs onto these two surfaces, in the range of thickness studied here. The intriguing aspect of this behavior arises from the fact that $[OTf]^-$ ILs exhibit reduced deposition rates under identical vaporization conditions. This difference implies the presence of stronger cohesive forces in $[C_2C_1im][OTf]$. This behavior in conjugation with the low affinity of the imidazolium ILs for the ITO surface may result in similar morphology for the C_2C_1im based ILs, even with lower deposition rates for the $[C_2C_1im][OTf]$.

A word of caution - it is crucial to acknowledge that the morphologies obtained in the study are influenced by various factors. Therefore, the experimental conditions, such as substrate thickness, substrate temperature, and the amount of IL deposited, were kept

consistent in all experiments, as even minor differences in these experimental conditions could lead to different observations. For instance, variations in the thickness of the Ag layer coated on ITO/glass can result in changes in surface roughness. Additionally, the amount of IL deposited can also play a significant role in the conclusions drawn from the experiments. Hence, careful consideration of these factors is essential when interpreting the results and drawing meaningful conclusions from the study, and thus the conclusions described above apply to the specific conditions here used.

4.1.2. Influence of the Substrate Temperature

In this study, another deposition parameter was analyzed, the influence of the substrate temperature ($T_{subst.}$) on the morphology of the ILs' film on the two surfaces, ITO and Ag. The deposition conditions were maintained constant, with an evaporation temperature of either 503 or 513 K and an orifice diameter of 3.1 mm as before, ensuring a similar deposition rate for each IL studied (Table 5). The substrate temperature was adjusted for the range of temperatures used in this study by modifying the temperature of the external cooling system, as well as turning it off to obtain the results of a deposition without thermal regulation of the substrate. The substrate temperatures used in this work were $T_{subst.}$ = 273 K, $T_{subst.}$ = 283 K, $T_{subst.}$ = 298 K, and without $T_{subst.}$ control (by turning off the external cooling system). When the external cooling system was turned off, the substrate reached much higher temperatures (above T = 298 K), as the substrate temperature began to depend on the temperature of the chamber walls, which is directly correlated to the oven's temperature used in the study. Figure 36 illustrates a representative result of the SEM micrographs and the corresponding histograms referent to $[C_2C_1im][NTf_2]$ film morphology. Detailed results for all ILs studied can be found in Figures A19-A26 and Table A2 of the Attachments section.

Table 5. Experimental conditions of the thermal evaporation process for each ionic liquid: evaporation substrate temperature ($T_{subst.}$); orifice diameter of the Knudsen effusion cell; and the deposition rate (Φ). These parameters enabled the study of the influence of substrate temperature on the morphology of different IL films (with a deposition amount of 40 ML) on both ITO/glass and Ag/ITO/glass substrates, maintaining the evaporation temperature ($T_{evp.}$= 503 K).

Precursor	$T_{subst.}$ / K	Orifice Diameter / mm	Φ / Å·s^{-1}
$[C_2C_1im][NTf_2]$	273	3.1	0.44 ± 0.09
	283		0.39 ± 0.09
	298		0.43 ± 0.08
	Without T control [a)]		0.43 ± 0.05
$[C_8C_1im][NTf_2]$	273	3.1	0.45 ± 0.05
	283		0.39 ± 0.04
	298		0.44 ± 0.08
	Without T control [a)]		0.41 ± 0.09
$[C_2C_1im][OTf]$	273	3.1	0.07 ± 0.03
	283		0.05 ± 0.04
	298		0.05 ± 0.02
	Without T control [a)]		0.04 ± 0.03
$[C_8C_1im][OTf]$	273	3.1	0.18 ± 0.03
	283		0.14 ± 0.02
	298		0.25 ± 0.01
	Without T control [a)]		0.20 ± 0.03

[a)] These experiments were conducted by turning off the refrigerated circulating bath responsible for keeping $T_{subst.}$ constant.

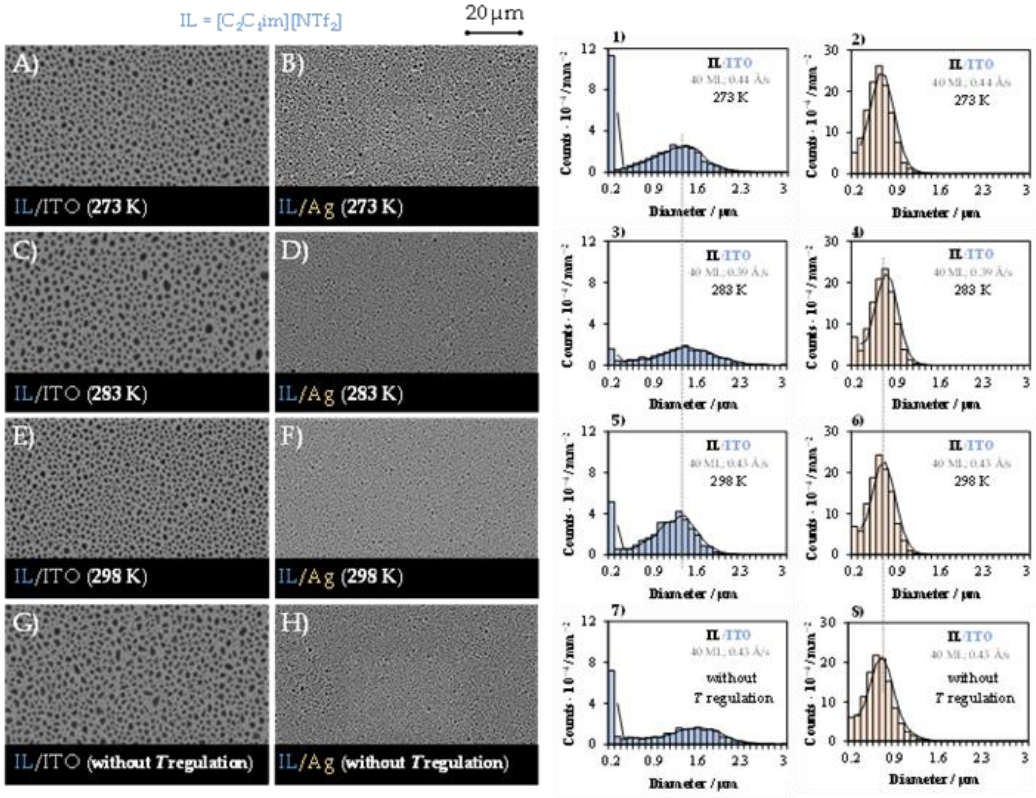

Figure 36. Morphology of $[C_2C_1im][NTf_2]$ thin films (micro- and nanodroplets) (A-H) and the respective droplet size distribution (histograms 1-8). The IL films were deposited (by PVD) simultaneously onto surfaces of ITO (images A, C, E) and Ag (images B, D, F) with a thickness of 40 ML. The IL film surfaces were subject to different substrate temperatures: T = 273 K (A, B); T = 283 K (C, D); T = 298 K (E, F); without thermal regulation of the substrate temperature (G, H). For all experiments, the deposition process was conducted using a consistent mass flow rate of approximately 0.4 Å/s. Top views (A-H) were acquired through scanning electron microscopy by using a backscattered electron detector (BSE).

A detailed analysis of SEM micrographs for $[C_2C_1im][NTf_2]$ indicates a consistent droplet morphology and size distribution when the substrate temperature is increased (273, 283, and 298 K). Once again, based on the SEM micrographs and histograms, it is possible to observe the formation of larger droplets on the ITO surface, with modal diameters ranging between 1.3 and 1.4 μm (graphs 1, 3, and 5 of Figure 36), in comparison to the Ag surface, where the modal diameter varies between 0.6 and 0.7 μm (graphs 2, 4 and 6 of Figure 36). This behavior is also observed in the SEM micrographs and histograms for the film sample produced on a substrate without thermal regulation. The similar droplet morphology and size distribution with the increase of substrate temperature may indicate a higher stabilization of $[C_2C_1im][NTf_2]$ on these surfaces. Furthermore, the increase of surface energy (by some increase in the substrate temperature) did not significantly contribute to the increase in the clusters' surface mobility, *i.e.*, the coalescence mechanisms were not significantly affected.

The analysis of the results related to $[C_2C_1im][OTf]$ film samples (Figure A21 and Figure A22 from the Attachments) reveals a differentiation in behavior across the studied surfaces. On the Ag surface, the morphology and size distribution remain consistent as the substrate temperature increases (modal diameter between 0.6 and 0.7 μm). However, on the ITO surface, the SEM micrographs illustrate a slight increase in droplet size with the increase in the substrate temperature. This observation is further supported by the histograms (Figure A22 from Attachments), which demonstrate a shift towards higher values of droplet size as the substrate temperature increases (modal diameter between 0.8-1.0 μm for T = 273 K, 1.0-1.1 μm for T = 283 K, and 1.2-1.4 μm for T = 298 K). Better stabilization of $[C_2C_1im][OTf]$ was observed in the metallic surfaces. However, on the ITO surface, the increase of the surface energy, caused by the rise of substrate temperature, is enough to slightly enhance the surface mobility of the clusters and, consequently, accelerate the coalescence mechanisms.

The results for $[C_8C_1im][NTf_2]$ exhibit similar behavior for the surfaces studied. The morphology of the droplets and size distribution (Figures A23 and A24 from Attachments) at T = 273 K differs from samples obtained for substrate temperatures of 283 K and 298 K. Furthermore, the results at T = 273 K seem to resemble the results related to the sample deposited without thermal regulation of the substrate. For the $[C_8C_1im][OTf]$, different outcomes were observed depending on the surface. On Ag surfaces, increasing the substrate temperature appears to favor an increase in the droplet size (Figures A25 and A26 from Attachments). On the ITO surface, larger droplets are formed regardless of the substrate temperature used. These larger droplets, particularly on the ITO surface, are the consequence of the weaker cohesive interactions and the lower superficial

tensions, that facilitate the occurrence of coalescence mechanisms. The different behavior on Ag surfaces indicates a better affinity of $[C_8C_1im][NTf_2]$ to Ag surfaces, as evidenced by the lower droplet growth with increasing substrate temperature. A deeper understanding of this behavior can be obtained by considering volatility and viscosity data. $[C_8C_1im][OTf]$ exhibits lower volatility and higher viscosity compared to its congener ($[C_8C_1im][NTf_2]$), indicating a higher influence of cohesive forces and consequently, a lower IL-substrate affinity. This reduced surface affinity promotes more intense coalescence mechanisms, leading to the formation of larger droplets. Therefore, increasing the substrate temperature enhances surface energy, favoring surface mobility and the second-order coalescence mechanisms.

It is not possible to study the influence of the anion on nucleation and growth of $[C_8C_1im]$-based ILs on solvophobic surfaces like ITO/glass, as the formation of larger droplets can be explained by the increase of the second-order coalescence mechanisms. On the other hand, the characteristics of the $[C_2C_1im]$-based IL film provide insights into how the substrate temperature affects the film morphology when the anion is changed (Figure 37). Again, it is possible to observe the formation of small droplets when ILs are deposited on the Ag surface. Furthermore, on Ag surfaces, there is no significant variation in the modal diameter [(0.6 ± 0.1) μm] with the increase of the substrate temperature. This suggests a strong interaction between IL clusters and the metallic surface, reducing surface diffusion and resulting in the formation of small clusters and, consequently, small droplets. On the other hand, on the ITO surface, a dependence of the modal diameter with an increase in substrate temperature is observed, particularly for $[C_2C_1im][OTf]$. These experimental results suggest that the $[NTf_2]$-based ILs might establish stronger adhesive forces with the ITO surface and, consequently, a better IL-substrate affinity. Therefore, as the substrate temperature increases, the rise in surface energy will have a more significant impact on $[OTf]^-$-based ILs, intensifying the second-order coalescence mechanisms.

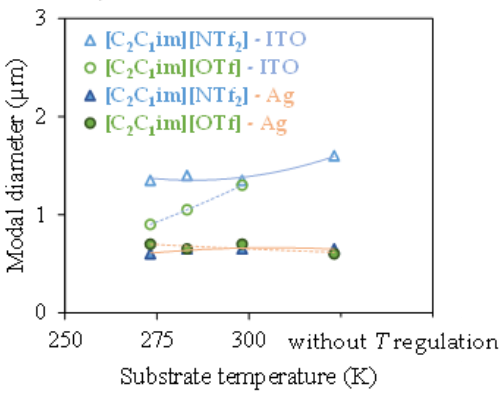

Figure 37. Graphical representations of the modal diameter of the IL droplets as a function of the substrate temperature for $[C_2C_1im][NTf_2]$, and $[C_2C_1im][OTf]$. These results were derived from the analysis of the SEM micrographs relative to the simultaneous deposition of each IL film (40 ML) onto surfaces of ITO and Ag/ITO.

4.2. Influence of the Interface in the Nucleation and Growth of Ionic Liquid Thin Films

Here we aim to understand the influence of the interface on the morphology of IL films, by studying the influence of an inserted interface on the nucleation and growth mechanisms of two ILs, namely $[C_2C_1im][OTf]$ and $[C_8C_1im][OTf]$. These ILs were selected due to the variations in morphology associated with changes in the alkyl side chain. For this, we used the thermal evaporation technique as before, but now varying the film thicknesses (20 ML, 40 ML, 80 ML, 100 ML, and 150 ML), and using ITO substrates that were partially coated with an Ag film, as shown in Figure 31 and Figure 38.

Throughout these studies, the deposition conditions were kept constant, with deposition rate at Φ = 0.30 Å/s and substrate temperature T = 283 K. The experimental conditions used for these studies are summarized in Table A3 (Attachments). SEM was employed for the analysis of the IL film morphology, utilizing different detectors (BSE and SE detectors) to enhance the visibility of the different aspects under investigation. The data collected by SEM was then structured into histograms and graphs to provide improved visualization of the trends and behavior exhibited by the various ILs under study.

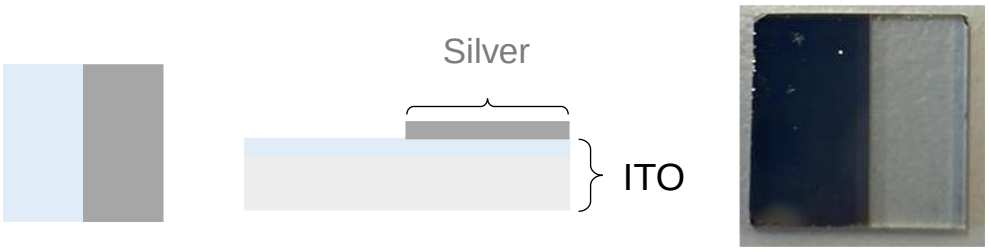

Figure 38. Schematic representation and image of an ITO substrate partially covered with an Ag film.

4.2.1. Influence of Amount of Ionic Liquid Deposited

We started by varying the IL thickness and see how it affects the behavior of the $[C_2C_1im][OTf]$ and $[C_8C_1im][OTf]$ films on ITO and Ag surfaces, different regions of the ITO substrate partially covered with an Ag film. The setup allowed for simultaneous deposition on these two regions while maintaining consistent deposition conditions. The results of the deposition of $[C_2C_1im][OTf]$ and $[C_8C_1im][OTf]$ on both ITO and Ag surfaces, with varying IL film thickness, are illustrated in Figures 39 and 40, respectively.

When examining the results concerning the $[C_2C_1im][OTf]$ sample, it becomes evident that an increase in the droplet size is observed as the amount of the IL deposited on the substrate increases. When analyzing the ITO region, for the thinner IL film (20 ML), small droplets with highly similar dimensions were formed. With the increase in IL film thickness, a corresponding enlargement in the droplet size was observed. For IL film thicknesses up until 80 ML, it appears that the droplets' size distribution across the C_2C_1im film remained consistent.

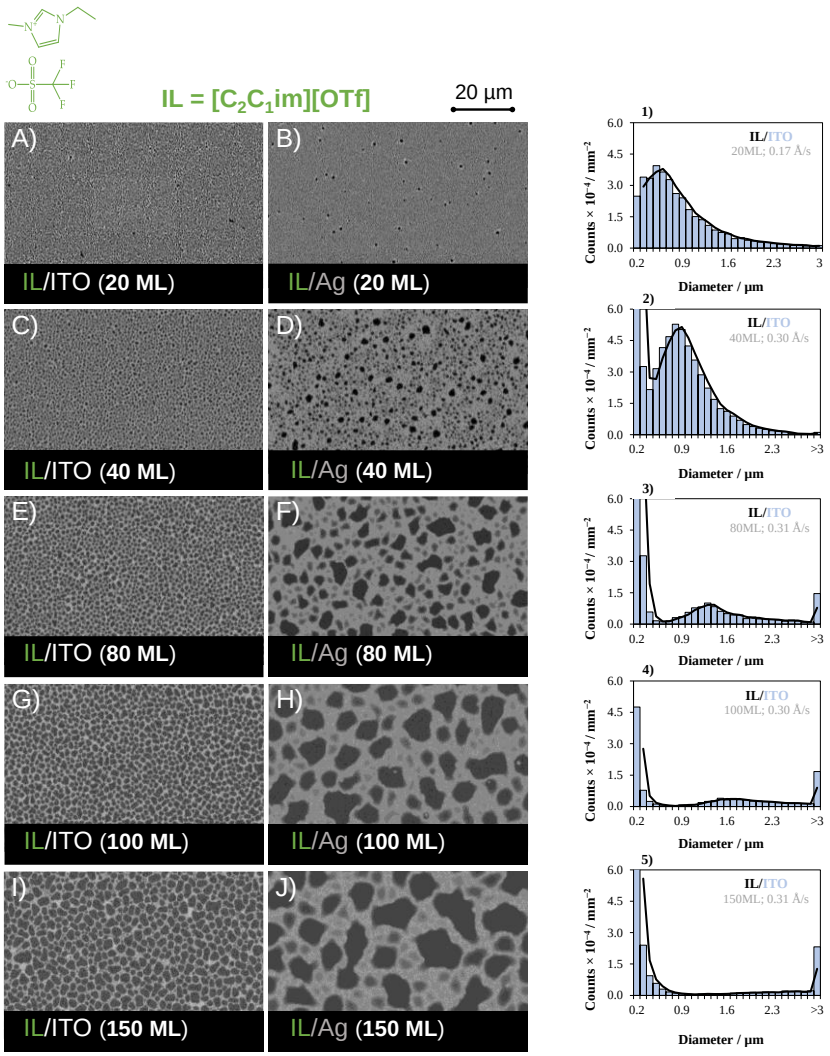

Figure 39. Morphology of [C_2C1im][OTf] thin films (micro- and nanodroplets (A-J) and corresponding histograms depicting the size distribution on the ITO surface (histograms 1-5). The IL films were simultaneously deposited (via PVD) onto both ITO (images A, C, E, G, H) and Ag (B, D, F, H, J) surfaces with varying thicknesses: 20 ML (A, B); 40 ML (C, D); 80 ML (E, F); 100 ML (G, H); 150 ML (I, J). All experiments were conducted at a consistent mass flow rate (≈ 0.30 Å/s). Top view images (A-J) were acquired through scanning electron microscopy by using a backscattered electron detector (BSE).

However, at 80 ML and beyond, a distinct pattern emerged: larger droplets became surrounded by smaller ones, revealing a bimodal distribution of droplet sizes. This description is clear on the histograms presented in Figure 39. The change in the droplet size distribution as a function of the IL film thickness can be elucidated by the nucleation and growth mechanisms. At lower IL thicknesses, a small number of clusters are formed on the surface, leaving available spaces for the formation of additional clusters. Owing to the presence of available surface area, the clusters move across the surface with a low probability of colliding with other structures (clusters or droplets). This diminished collision likelihood reduces the chances of larger droplet formation. Therefore, it can be inferred that, for thicknesses < 80 ML, the predominant processes at play are nucleation

and first-order coalescence. With an increase in the amount of [C_2C_1im][OTf] deposited on the surface, a larger number of clusters are generated. Because the clusters exhibit some degree of surface mobility, collisions between them occur more frequently, leading to the coalescence of droplets. Therefore, during the initial stages of deposition there is a predominance of first-order coalescence mechanisms, and, by increasing the amount deposited, there is an increase in the coalescence mechanisms, occurring in the coalescence of droplets that have already undergone coalescence (second-order coalescence).

Shifting the focus to the SEM micrographs that elucidate the behavior of [C_2C_1im][OTf] on the Ag surface with increasing IL film thickness, a similar trend was observed: below 80 ML we observe smaller droplets characterized by a uniform size distribution followed by the formation of larger droplets as the IL films grew thicker ($\geq$ 80 ML). Nevertheless, a remarkable difference is observed - droplets resulting from the deposition of small IL quantities exhibit reduced sizes on the Ag surface. Conversely, as the IL thickness increases, the Ag surface shows the formation of larger droplets characterized by more heterogeneous shapes as compared to those observed on the ITO surface. Based on the observations and prior knowledge, it is possible to theorize that for smaller amounts of IL deposited, the higher number of clusters formed can related to the stronger affinity of IL with metal surfaces (reducing surface mobility) as well as the lower MFAN, that allow the formation of a higher number of clusters in the same area, when compared to the ITO surface. As IL film thicknesses increase, the formation of larger and heterogeneous droplets becomes evident. These phenomena can be attributed to the intensification of the coalescence process and the proximity between the clusters in the Ag, which facilitates the coalescence mechanisms. The result is the formation of larger droplets in the Ag surfaces compared to the ITO, for higher amounts of [C_2C_1im][OTf] deposited.

As for the results concerning the increase of [C_8C_1im][OTf] film thickness on the ITO surface (Figure 40), a clear patter emerges: the droplets corresponding to C_8C_1im are significantly larger when compared with the IL with a shorter alkyl chain, [C_2C_1im][OTf]. This behavior is indicative of a higher wettability of the solid surfaces by C_8C_1im.

Again here, it is apparent that for lower IL film thicknesses, the distribution of droplet sizes remains consistent, exhibiting a Gaussian distribution pattern. However, as IL deposition increases, there is a gradual rise in the modal diameter of the droplets deposited on the ITO surface. As the amount of deposited IL increases, two predominant modal diameters become distinguishable, and one of these modal diameters shows an

increase as the IL film thickness grows. These observations are readily apparent in the histograms. As IL film thickness values exceed 80 ML, the presence of two distinct modal diameters becomes evident: one for smaller droplets and another for larger droplets. This behavior implies that in thinner IL films, the observed results align with nucleation and first-order coalescence, whereas for larger thicknesses, the second-order coalescence contributes to the formation of very large droplets.

In the case of the Ag surface, two different behaviors are also observed, but different from previous films in ITO. For IL films with lower thicknesses (20 ML and 40 ML), there is a formation of small droplets.

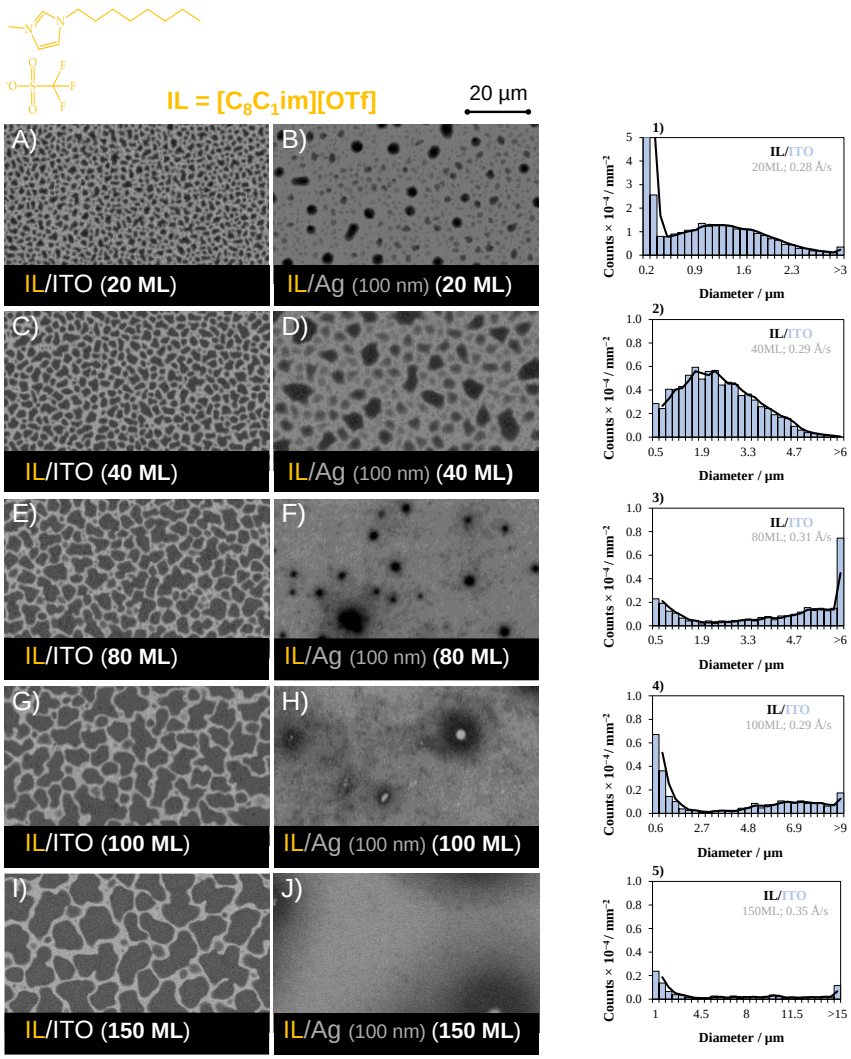

Figure 40. Morphology of $[C_8C_1im][OTf]$ thin films (micro- and nanodroplets (A-J) and corresponding histograms depicting the size distribution on the ITO surface (histograms 1-5). The IL films were simultaneously deposited (via PVD) onto both ITO (images A, C, E, G, H) and Ag (B, D, F, H, J) surfaces with varying thicknesses: 20 ML (A, B); 40 ML (C, D); 80 ML (E, F); 100 ML (G, H); 150 ML (I, J). All experiments were conducted at a consistent mass flow rate (≈ 0.30 Å/s). Top view images (A-J) were acquired through scanning electron microscopy by using a backscattered electron detector (BSE).

However, as the IL thickness increases (80 ML and 100 ML), it becomes evident that the IL film spreads across the Ag surface, accumulating in regions with defects, possibly where there is greater surface roughness. In the process of formation of Ag films thought sputtering methodology, certain regions of the ITO surface exhibit a better adsorption capability for the Ag particles. This phenomenon leads to the formation of localized areas characterized by the accumulation of Ag (as evident by the lighter areas of the Ag film with 100 ML IL film) while other areas exhibit lower amounts of Ag film (was in the case of the SEM micrograph of referent to the 80 ML on the Ag surface, where is possible to observe darker regions, indicators of a higher amount of IL in these areas). The accumulation of IL in these areas can be attributed to the higher affinity of IL for the metal surfaces, which leads to a reduction in interfacial tension, promoting and enhancing the spreading of the IL.

To facilitate a clearer comprehension of the droplet growth tendencies and the spreading behavior of the IL on the ITO surface, graphical representations of the modal diameter of IL droplets and the percentage of surface coverage as a function of the film thickness were constructed (Figure 41). It's worth emphasizing that the depositions were carried out on ITO substrate partially coated with an Ag film.

Focusing on the modal diameter (Figure 41A), a distinction in the growth behavior between the two IL studies (C_2C_1im and C_8C_1im) becomes evident, mirroring the observations made when analyzing the SEM micrographs. Firstly, it is apparent that for the same IL thickness, the C_2C_1im droplets are consistently smaller in comparison to those of C_8C_1im. For the smaller C_2C_1im, increasing the IL film thickness results in a small increase in the droplet size, with a linear trend of droplet growth. As regarding [C_8C_1im][OTf], the droplet size also shows minor variations for smaller IL thicknesses. However, as the IL thickness increases beyond a certain point, there is a change in behavior, with more pronounced changes in droplet size. For small IL thicknesses, the increase of IL film results in the increase of nucleation and first-order coalescence. As the IL film thickness increases, more clusters are formed on the surface, enhancing the coalescence process. However, when the IL film thickness becomes very large, the main process observed is second-order coalescence, involving the merging of larger clusters.

Shifting our attention to the percentage of surface coverage on the ITO surface (Figure 41B), a comparable trend to the modal diameter graph emerges for the IL with a longer alkyl chain (C_8C_1im) - for the lower quantities of IL deposited there is a lower percentage of surface coverage, that increases significantly as the IL film thickness grows, as expected. However, for [C_2C_1im][OTf], there is a significant difference in the behavior of

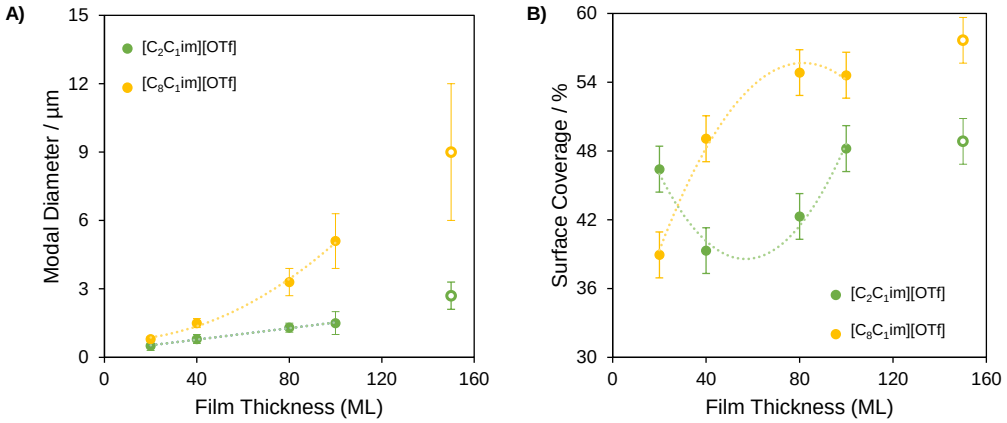

Figure 41. Graphical representations of the modal diameter (A) and percentage of surface coverage (B) of IL droplets as a function of the film thickness for [C_2C_1im][OTf] (green) and [C_8C_1im][OTf] (yellow). These results were obtained through SEM analysis of IL depositions on ITO substrates partially coated with a 100 nm Ag film. The presented outcomes are specific to the droplets formed on the portion of the substrate devoid of Ag coverage (ITO surface).

the percentage of surface coverage as the film thickness increases, as plot B in Fig 41 shows. For the lowest amount of IL deposited (20 ML), C_2C_1im exhibits a significant surface coverage (almost 45%), but as the IL film thickness increases, an initial decrease in the percentage of surface coverage is observed (at 40 ML). Curiously after this minimum, the surface coverage increases again for higher film thicknesses (80 ML, 100 ML, and 150 ML). This difference highlights the dependence of nucleation and growth mechanisms not only on the thickness of the IL film but also on the IL's length.

It should be further noticed that the percentage of surface coverage for 20 ML films is lower for [C_8C_1im][OTf] when compared to its C_2C_1im congener. This behavior in conjugation with the similar modal diameter for the two IL studied, may be an indicator of a higher MFAN, resulting in the formation of a lower number of droplets in contrast to [C_2C_1im][OTf].

The results obtained for both ILs indicate a clear influence of IL thickness on the nucleation and growth mechanisms occurring on the surfaces studied. In the case of [C_2C_1im][OTf] film, it was possible to observe the impact of film thickness on the modal diameter and surface coverage. In the thinner films, nucleation and first-order coalescence mechanisms are the main factors to influence droplet morphology. In thicker films, the growth of the films is regulated by the second-order coalescence. As for the [C_8C_1im][OTf] film, observing the distinct phases that regulate film formation proved challenging. The kinetics of nucleation and first-order coalescence exhibit rapid rates, resulting in the formation of nanostructures that are less spherical and more evenly dispersed across the surfaces, unlike [C_2C_1im]. This observation can be rationalized by

the known lower surface tension of $[C_8C_1im][OTf]$, which contributes to enhanced spreading behavior.

4.2.2. Influence of Ag Film Thickness

Another aspect under investigation was the influence of the thickness of the Ag film on the morphology of $[C_8C_1im][OTf]$. The choice of this IL was prompted by the distinct variations in IL film morphology when deposited on either an ITO or Ag surface. This study was performed using ITO substrates partially covered with Ag films, as shown in Figure 31 and Figure 38. The thickness of the Ag film was modified by adjusting the sputtering conditions. This manipulation led to the creation of ITO substrates with one-half covered by Ag films of varying thicknesses, specifically 40 nm and 100 nm. The sputtering conditions employed for producing the distinct Ag films are detailed in Table 6. The modification of the ITO substrate enabled simultaneous deposition on both ITO and Ag surfaces. Figure 42 suggests incomplete coverage of the ITO substrate. As can be seen, the IL (darker areas in the SEM micrograph) encircles the Ag particles (spherical structures appearing lighter in the SEM micrograph). This surface rugosity results in a heterogeneous distribution of the IL, where there are larger accumulations of IL for areas with larger amounts of Ag particles. Additionally, in the Attachments chapter (Figure A27 – Figure A29), are shown micrographs depicting the morphology of ILs on both ITO and Ag surfaces and histograms that provide a detailed analysis of droplet diameters (on ITO) are included.

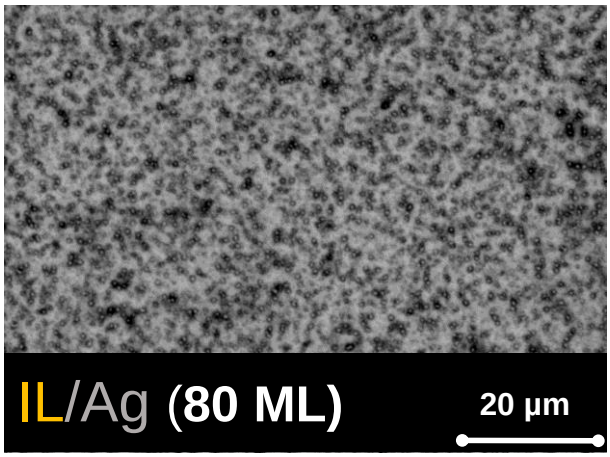

Figure 42. Morphology of $[C_8C_1im][OTf]$ thin film (80 ML) deposited on a 40 nm Ag film.

Upon initial examination of the substrate surfaces using both optical microscopy and SEM, it became apparent that the area covered by a 40 nm Ag film exhibited circular structures on its surface. This introduced a certain level of surface roughness when compared to the surface covered by the 100 nm Ag film. The latter surface displayed a homogeneous and flat texture with fewer surface defects. The irregular nature of the 40 nm Ag film´s surface suggests a non-homogeneous coverage of the ITO substrate, where there are regions with larger accumulations of Ag compared to others. This disparity led to the hypothesis that the IL's morphology on the surface could vary due to the distinct surface characteristics of the Ag film. This, in turn, could influence the nucleation and growth mechanisms. On the more irregular surface, the larger discrepancies in surface energy might guide the IL film toward more energetically stable regions. In contrast, when a uniform Ag surface is present, the IL film is more prone to being influenced by the IL's affinity for the surface due to reduced variations in energy across the surface.

Table 6. Experimental conditions for the sputtering process to partially coat ITO substrates with Ag film: applied current; deposition time; and film thickness.

	Ag (40 nm)	Ag (100 nm)
Current / mA	20.0	40.0
Time / s	90	100
Thickness / nm	37.5 ± 5	97.9 ± 5

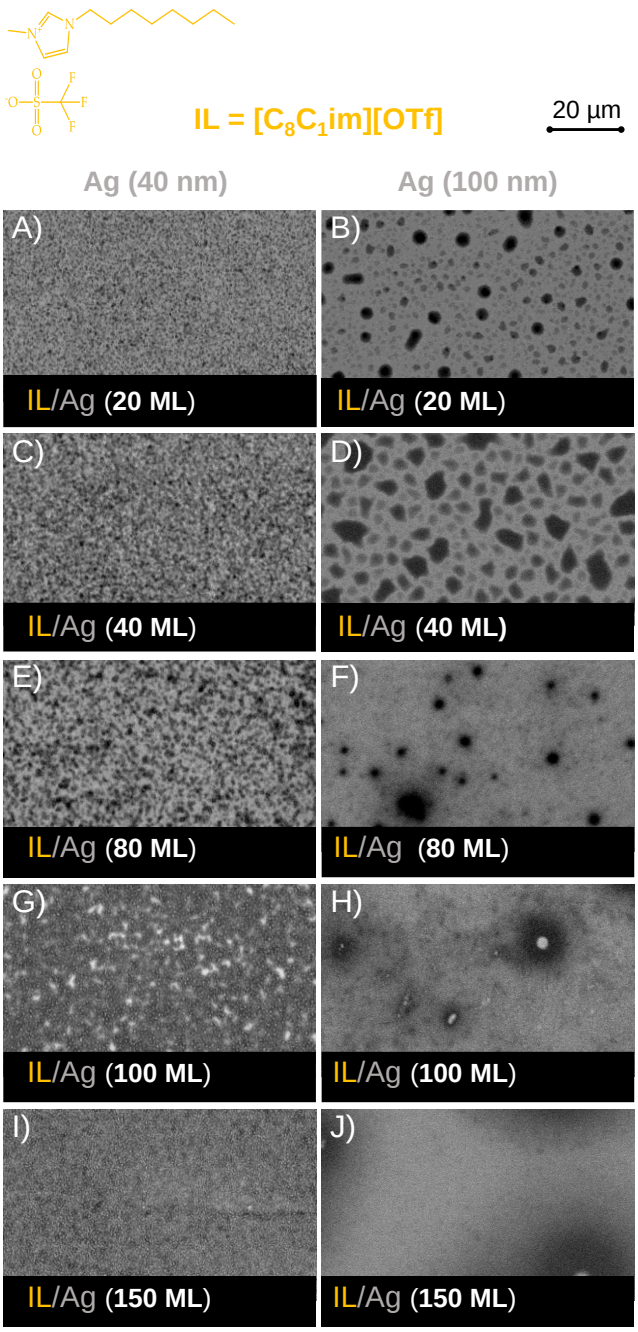

Figure 43. Morphology of $[C_8C_1im][OTf]$ thin films (A-J) deposited on Ag surfaces with different thicknesses: 40 nm (images A, C, E, G, H) and 100 nm (images B, D, F, H, J). The IL films were deposited (via PVD) at varying quantities: 20 ML (A, B); 40 ML (C, D); 80 ML (E, F); 100 ML (G, H); 150 ML (I, J). All experiments were conducted at a consistent mass flow rate (≈ 0.30 Å/s). Top view images (A-J) were acquired through scanning electron microscopy by using a backscattered electron detector (BSE).

The micrographs reveal variations in droplet morphology as the IL film thickness increases, both on ITO surfaces (Figure A27 – Figure A29) and on Ag surfaces (Figure 43) with different thicknesses. Examining the results for the $[C_8C_1im][OTf]$ deposited on

the Ag surfaces (Figure 43), it is apparent that, for the 40 nm Ag film, droplet formation on the surface is absent. Instead, is possible to observe that IL tended to distribute into the interstitial spaces of the larger Ag grounds, by the increase of the darker areas of the SEM micrographs as an increase in the amount of the IL deposited into this surface, signifying an adaption of the IL to the rugosity of the Ag film. As the IL quantity deposited increases, more interstitial spaces become occupied, enabling the IL to distribute onto more superficial spaces. This behavior is especially clear for 100 ML and 150 ML quantities. Shifting the focus to the results concerning droplet morphology on the 100 nm Ag film, distinct behavior is observed, according to the IL film thicknesses studied. Thinner IL films (20 ML and 40 ML) show the formation of droplets with similar size distribution for the quantity deposited. As IL thickness increases (80 ML, 100 ML, and 150 ML), it is possible to observe the spreading of droplets across the surface, tending to form a homogeneous IL film for higher amounts deposited (100 ML and 150 ML). This difference in the behavior with the change of the Ag film thickness reflects the impact of rugosity and surface energy on IL film growth.

It was mentioned before the tendency of IL to move to more energetic stable places. Herein, this phenomenon was observed for the films deposited on the 40 nm Ag film surface, where the $[C_8C_1im][OTf]$ tended to relocate to more energetic stable places. The more heterogenous growth pattern of the Ag film, the more interstitial places and defects of the film are exposed to the IL upon arrival, allowing for these places to be filled and, consequently, preventing the formation of IL droplets. In contrast, on a 100 nm Ag surface with a more homogeneous topography, the number of interstitial places and defects exposed is reduced, leading to reduced differences in surface energy, facilitating thus the formation of droplets and at higher IL contents, a more homogeneous growth of the films.

Examining the results for the ITO surface (Figure A27 – Figure A29), it becomes evident that the characteristics of an interface with Ag film with different thicknesses/morphologies influence the morphology of the droplets on ITO. The characteristics of this interface were found to condition the nucleation and growth of ILs on the ITO surface. Specifically, the droplets deposited on the ITO surface, which interfaces with a 40 nm Ag film, consistently exhibit a more spherical shape within a certain size range. This is in contrast with the droplets deposited on the ITO surface interfacing with a 100 nm Ag film, where it is possible to observe the formation of droplets with varying sizes and some heterogeneity in morphology. The observed divergence in droplet morphology and sizes highlights the role of Ag film thickness in shaping the surface energy of the substrate. This factor, in turn, impacts the affinity of the IL for the

surface, thus influencing the nucleation and growth processes of the IL film. The interaction with the metal interface, the film morphology across the entire ITO substrate exhibits a significantly larger level of heterogeneity compared to an ITO substrate without any neighboring Ag coating. Using the data extracted from SEM micrographs and histograms (Figure A27 - Figure A29 in the Attachments), it was possible to generate graphs related to the modal diameter and the percentage of surface coverage with the increase in [C_8C_1im][OTf] thickness. The resulting trends are presented in Figure 44.

Figure 44A illustrates the correlation between the modal diameter of the droplets (on the ITO surface) and the IL film thickness. Curiously, for lower IL quantities (20 and 40 ML), the modal diameter is similar, irrespective of the thickness of the Ag film interfacing with the ITO substrate. However, with the increase in IL quantity (80 ML, 100 ML, and 150 ML), the modal diameter exhibits a somewhat higher rise on the ITO substrate that is partially covered by a 40 nm Ag film. This leads to the creation of larger droplets within the ITO surface interfacing a 40 nm Ag film This trend is similarly observed for the 150 ML film, although the higher deviation in modal diameter values introduces limitations to the certainty of this measurement and conclusion.

Regarding the graph of the percentage of surface coverage (Figure 44B), we observe that thinner IL films (20 ML and 40 ML) exhibit larger surface coverages on the ITO surface that interface with the 100 nm Ag film. As the thickness of the IL film increases, the difference in surface coverage between the two systems must decrease, as for 80 ML and larger the surface coverage is the same (within uncertainty) of the ITO surface neighboring both Ag interfaces, 40 and 100 nm.

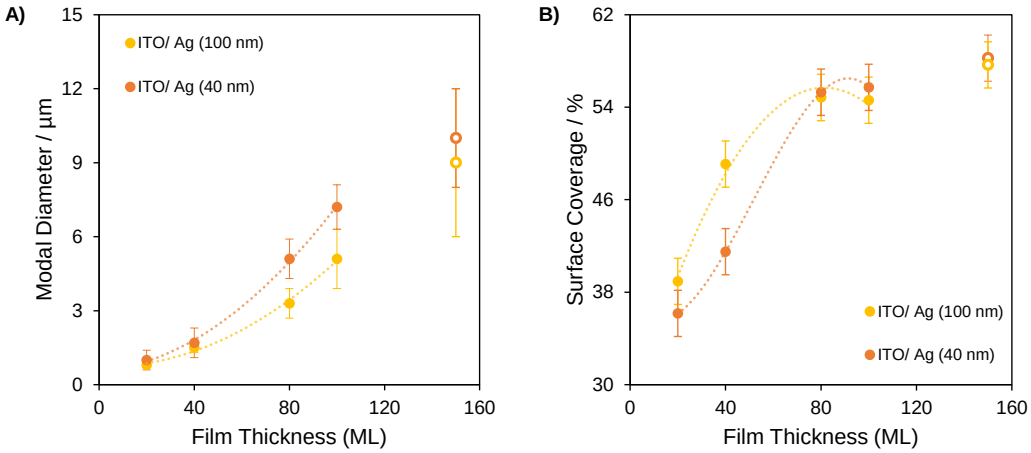

Figure 44. Graphical representations of the modal diameter (A) and percentage of surface coverage (B) of IL droplets as a function of the film thickness for [C_8C_1im][OTf] deposited on ITO substrates partially coated with a 40 nm Ag film and a 100 nm Ag film. The presented results are specific to the droplets formed on the portion of the substrate devoid of Ag coverage (ITO surface).

This behavior again indicates that the modification of the Ag film thickness on certain parts of the surface exposed to the IL changes the surface energy, which in turn influences the surface mobility of the ion pairs, affecting the growth process of IL film. The higher percentage of surface coverage observed on the ITO surfaces that have an interface with 100 nm Ag films at low IL coverage indicates a stabilization of surface energy. This stabilization facilitates improved adsorption of clusters on the surface, resulting in a larger surface occupation.

When the Ag film thickness is smaller (40 nm), the change in surface energy is small, allowing the clusters at the interface to move to the Ag surface, resulting in a decrease in the surface coverage on ITO. As the thickness of the IL film increases, although the percentage of surface coverage is then same, the modal diameter is higher when ITO is interfacing with a thinner Ag film. This difference can be attributed to the different surface energies that influence the nucleation and growth of IL films.

In cases where the IL is presented to a surface with a partially coated homogeneous Ag film, as observed in the results for the 100 nm Ag surface, the presence of a uniform metal film had a relatively minor impact on the morphology of IL droplets deposited on ITO regions located away from the interface. Conversely, in situations where the ITO surface is interfacing with a thinner and more heterogeneous Ag film (40 nm Ag film), there is an increase in the availability of energetic spaces, due to the existence of local defects within the Ag surface, more reactive in nature. Consequently, ion pairs were found to readily migrate towards these places. Overall, higher surface energy tends to enhance the mobility of the clusters, consequently promoting an increase in coalescence mechanisms.

4.2.3. Morphology of IL Films Near the ITO-Metal Interface

The use of an ITO surface partially coated with Ag film allowed for the simultaneous deposition of the IL onto two different surfaces. As discussed above, the interface between ITO and Ag surface can influence the nucleation and growth mechanisms of IL films. An interface is inherently reactive because of the energy differences at the junction caused by varying surface energies on the metal and ITO surfaces. When the IL encounters an interface, it tends to accumulate in these regions. The interactions between the IL and the interface can be distinct when compared to a homogenous solid surface, leading to a modification in the nucleation and growth mechanisms at the interface. This behavior can affect the IL film growth in the ITO and Ag areas.

Another aspect investigated here was the stability of IL films in the interface region. The morphology of IL films at the interface was examined for varying IL deposition amounts. ITO substrates partially covered with a 100 nm Ag film were used, and varying amounts of $[C_2C_1im][OTf]$ and $[C_8C_1im][OTf]$ were deposited. Figure 45 and Figure A30-A32 (Attachments) show the results of optical microscopy and SEM micrographs for $[C_2C_1im][OTf]$ and $[C_8C_1im][OTf]$ films at the ITO and Ag interface, together with the variation in IL film thickness. The similarity in results obtained through both techniques suggests that subjecting the samples to a vacuum system for SEM analysis does not alter the film morphology.

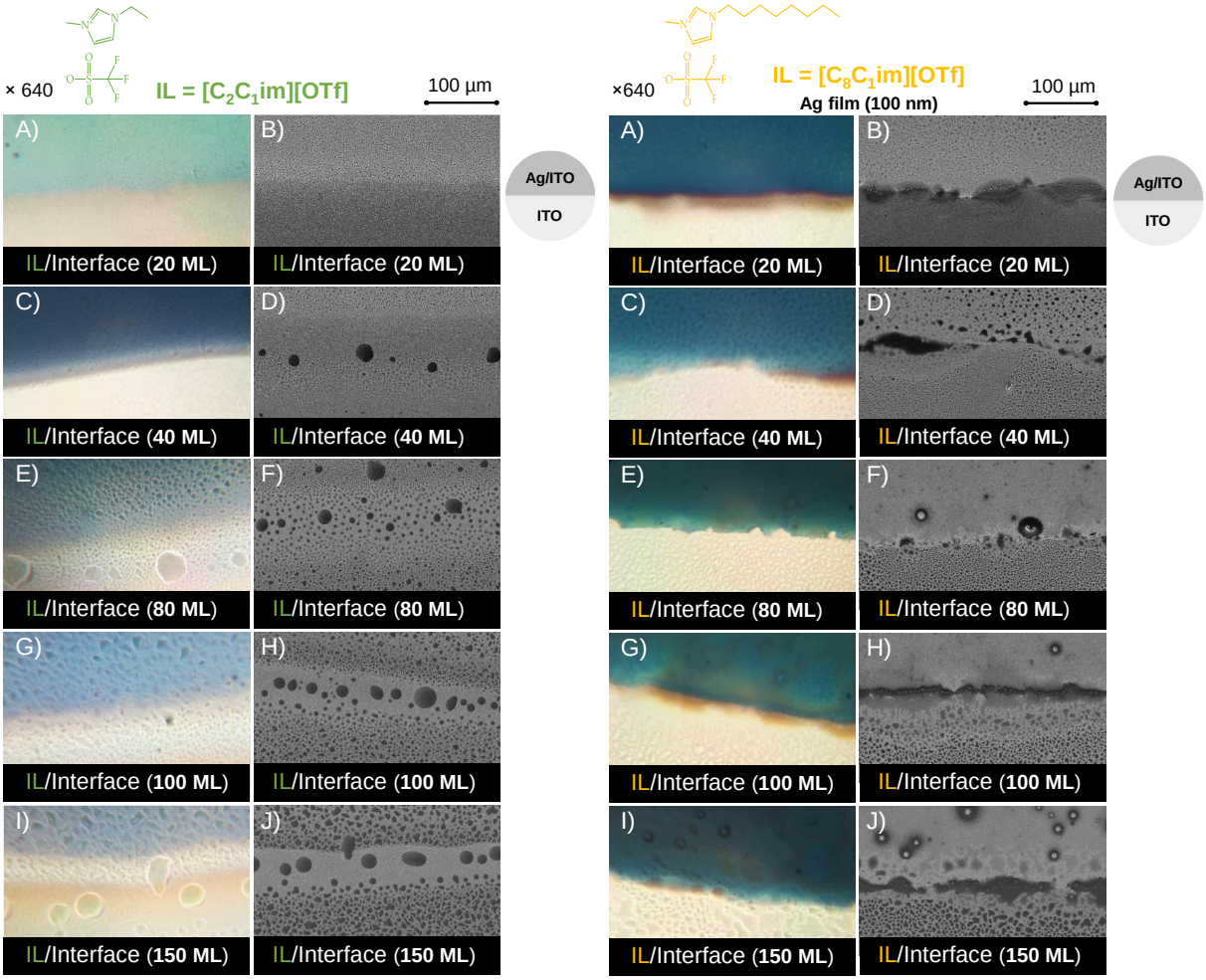

Figure 45. Morphology of $[C_2C_1im][OTf]$ (left) and $[C_8C_1im][OTf]$ (right) thin films (A-J) in the interface of Ag and ITO surfaces. The IL films were deposited simultaneously (by PVD) onto ITO and Ag surfaces at varying quantities: 20 ML (A, B); 40 ML (C, D); 80 ML (E, F); 100 ML (G, H); 150 ML (I, J). All experiments were conducted with a similar mass flow rate (≈ 0.30 Å/s). Optical microscopy images (A, C, E, G, I) were obtained with a magnification of 640x. Top views (B, D, F, H, J) were acquired through scanning electron microscopy by using a secondary electron detector (SE).

When examining the increase in $[C_2C_1im][OTf]$ film thickness increase at the interface (as shown in Figure 45 and Figure A30), it becomes evident that for the 20 ML film, the droplets on the Ag surface near the interface are larger compared to those on the ITO surface. Furthermore, above the interface between the Ag and ITO surfaces, there is no IL accumulation or formation of droplets with varying sizes or morphologies. With the growth of IL film thickness, there is a significant increase in the droplet size near the interface on the ITO side, whereas, on the Ag surface, the droplet size remains relatively constant. A closer view at the junction between the two surfaces reveals that in the ITO area, the droplet size increases in the proximity to the junction compared to the droplets formed further away. Furthermore, for the 40 ML film, above the interface, there is also the formation of some droplets with diameters much higher than the other droplets formed onto Ag and ITO surfaces. When the $[C_2C_1im][OTf]$ film reaches the 80 ML thickness, the droplet size at the interface appears to be quite similar in both Ag and ITO surfaces. Above the interface area, there is an evident formation of larger droplets, with some spacing between them. This behavior may indicate an intensification of the coalescence mechanism, particularly the second-order coalescence, in this region. At higher IL thicknesses (100 ML and 150 ML), a different behavior is observed. On the Ag surface, small droplets form at the interface, while larger droplets are observed in regions father from the interface. On the other hand, on the ITO surface, there is a reduction in droplet size as the distance from the ITO/Ag interface increases. Additionally, a rise in the droplet size is clear at the interface, accompanied by higher spaces between the droplets. This suggests an increase in coalescence mechanisms on the ITO side of the interface. In contrast, in the Ag area, droplets are smaller and more closely packed, indicating a higher degree of surface mobility stabilization near the interface in the Ag region. This behavior suggests that the interface may dislocate ion pairs arriving on the ITO surface towards the interface areas, potentially enhancing the coalescence mechanism. On the Ag surface, the surface energy of the metal has a stronger influence than the potential effects of the interface, resulting in a reduction of the observed effects compared to those on the ITO surface.

In the case of $[C_8C_1im][OTf]$ (Figure 45 and Figure A31), a behavior similar to the one described for $[C_2C_1im][OTf]$ on the ITO surface, that is an increase in the droplet size as an increase in the amount of IL deposited. However, in the case of the $[C_8C_1im][OTf]$, it is possible to observe an accumulation of IL on the ITO side of the interface area, indicating a stronger affinity of IL for the Ag surface. When analyzed on the Ag side, the droplets formed with $[C_8C_1im][OTf]$ are larger compared to those obtained with the shorter alkyl chain IL. As the IL thickness increases, a differentiation in droplet sizes for

the ITO surface as we approach the interface area is observed, that is as we move away from the interface area, a decrease in droplet size becomes apparent. For the Ag surface, an IL film thickness increase (≥ 80 ML) results in a change in the growth pattern, leading to the formation of a continuous film on this surface.

An important aspect relates to the study of the stability of the IL film under SEM conditions. This assessment aims to determine whether the vacuum and the electron beam can modify the surface and thereby influence the interpretation of the obtained results. To investigate this, the morphology of the 150 ML [C_2C_1im][OTf] film on the interface was studied over two consecutive days (Figure 46). The results showed that the morphology of the film remained unchanged after the sample was submitted to SEM conditions in the first day. Moreover, it should be noted that the droplets in the more reactive areas (*i.e.*, the interface area between the two surfaces) maintained their size and morphology, and there was no evidence indicating the movement of IL on the surface. These results illustrate the stability of the samples when exposed to SEM conditions and indicate that nucleation and growth processes occur only during the deposition of IL onto the surface.

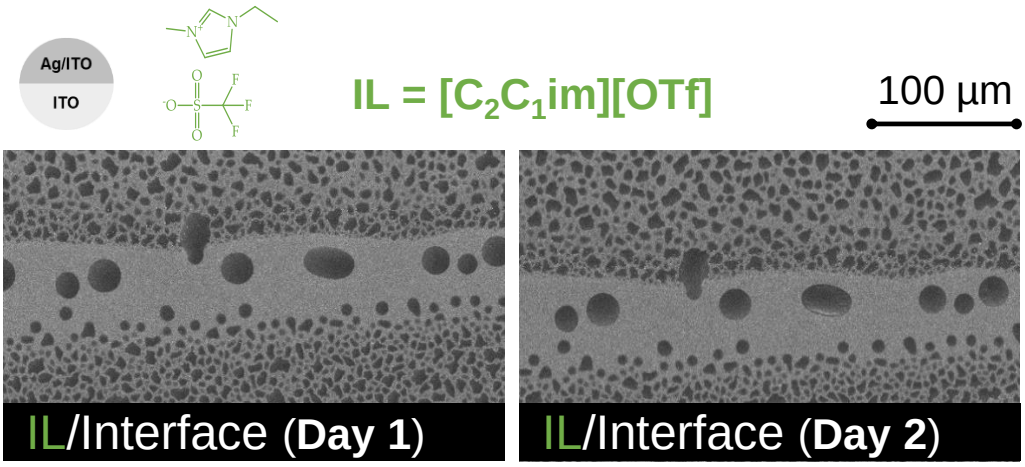

Figure 46. Morphology of [C_2C_1im][OTf] (micro- and nanodroplets) in the interface of Ag and ITO. The IL film (150 ML) was deposited simultaneously (by PVD) onto ITO and Ag surfaces with a mass flow rate of ≈ 0.30 Å/s. Top views were acquired through scanning electron microscopy by using a secondary electron detector (SE) for two consecutive days.

Finally, a comparison was made between the morphology of an ITO substrate and an ITO substrate partially covered with an Ag film. This comparison allows to know the variations in nucleation and growth mechanisms across different ILs when in the presence of an interface. For this investigation, the ImageJ software was employed to quantify the number and size of droplets on the ITO surface with an increase in the IL thickness. The collected data was organized into histograms. Figure 39, Figure 40, and Figure A29 present histograms for the droplet size distribution on the ITO surfaces that have an interface with Ag, whereas Figure A32 and Figure A33 depict the results for ITO surfaces without any interface with Ag (control samples). To better understand the influence of the interface on the nucleation and growth mechanism, the impact of increasing the Ag film thickness on the ITO substrate was studied. The SEM micrographs and the corresponding histograms were used to determine the modal diameter and its relationship with the film thickness. These findings are presented in the graphical representations of Figure 47 and Figure 48. These figures reveal the correlation between surface coverage and film thickness.

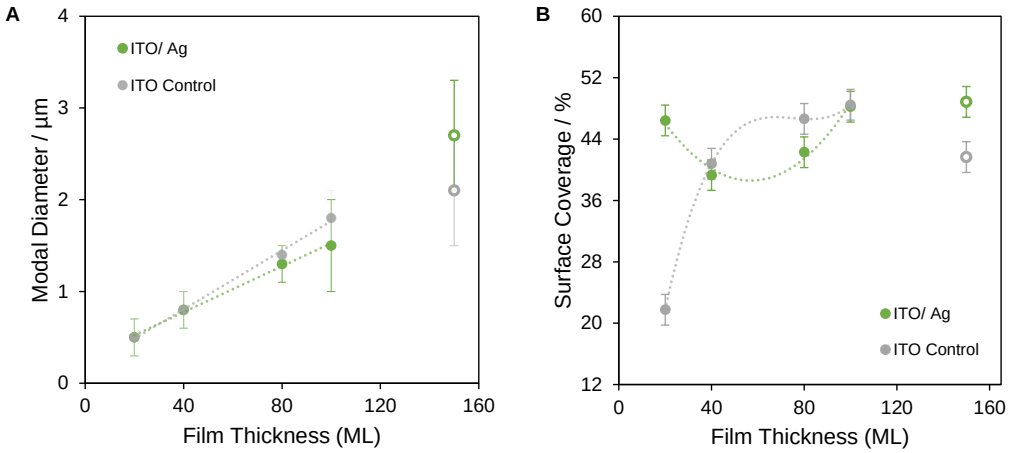

Figure 47. Graphical representations of the modal diameter (A) and percentage of surface coverage (B) of IL droplets as a function of the quantity of $[C_2C_1im][OTf]$ deposited on ITO surfaces that interface with 100 nm Ag films (green) and $[C_2C_1im][OTf]$ deposited on ITO substrates without any interface with Ag (ITO control, grey).

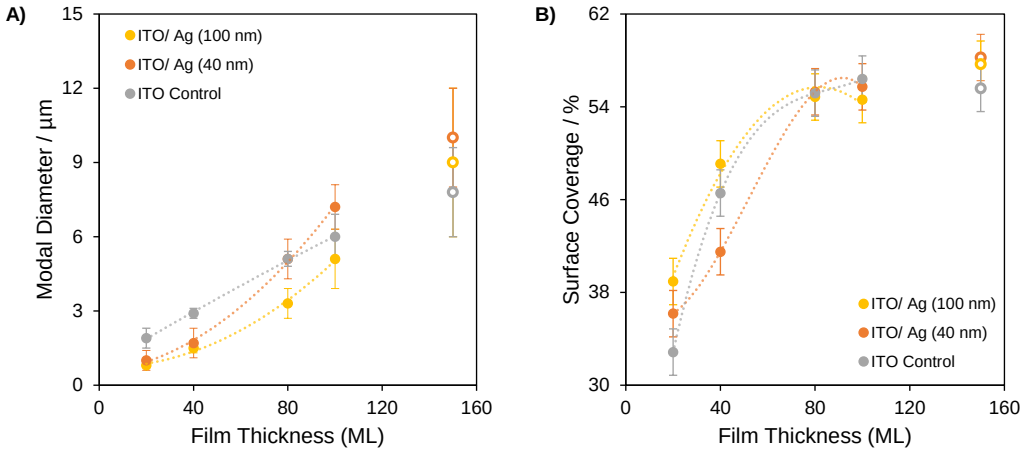

Figure 48. Graphical representations of the modal diameter (A) and percentage of surface coverage (B) of IL droplets as a function of the quantity of $[C_8C_1im][OTf]$ deposited on ITO surfaces that interface with 40 nm (orange) or 100 nm (yellow) Ag films and $[C_8C_1im][OTf]$ deposited on ITO substrates without any interface with Ag (ITO control, grey).

Figure 47 illustrates the dependence of the modal diameter (Figure 47A) and the surface coverage (Figure 47B) as the $[C_2C_1im][OTf]$ film thickness increases on the ITO surface, both with and without an interface with Ag. Examining the modal diameter results, it becomes evident that, for smaller film thicknesses (20 ML and 40 ML), the presence of an interface on the ITO surface does not exert a significant influence on droplet size and morphology. Similar modal diameters were found for the two studied systems. As the IL film thickness increases (80 ML and 100 ML), the ITO surface without the interface with the metal (ITO Control) shows slightly larger droplets compared to the ones observed in ITO with an interface. The IL film sample with a thickness of 150 ML was excluded from the trend analysis due to significant variations in droplet sizes resulting from intense coalescence mechanisms. Caution is thus advised when drawing conclusions from these results. In the case of the surface with the interface, the percentage of surface coverage decreases when increasing the IL film thickness from 20 ML to 40 ML. With further increases in film thickness, the percentage of surface coverage increases until it reaches 100 ML, remaining constant at the highest thickness studied. In contrast, for the surface without the interface (ITO control), the lowest IL film thickness studied (20 ML) exhibits the lowest percentage of surface coverage, which is even lower than all the results observed on the ITO surface with an interface with Ag, and the surface coverage increases thereafter, eventually reaching a similar percentage of surface coverage as the surface with an interface.

All these results show the impact of an interface on the nucleation and growth mechanisms of $[C_2C_1im][OTf]$. Based on these findings, it is hypothesized that the interface may influence the surface mobility of the ion pairs. For smaller quantities of IL deposition, the clusters exhibit a similar size to those formed on the control substrates (ITO surfaces without any interface with Ag), indicating that the interface does not change the conditions necessary for IL nucleation. As film thickness increases for higher values, it is observed that the modal diameter becomes smaller for the surface with an interface when compared to the control sample. However, there is a tendency for the percentage of coverage surface to become similar. For 150 ML thickness, the change in the behavior could be attributed to the coalescence of the larger droplets that are in closer proximity (second-order of coalescence) on the ITO surface with an interface. This results in the formation of larger droplets when compared to the ITO control.

Regarding the results for $[C_8C_1im][OTf]$ modal diameter distribution (Figure 48A), it is evident that for the lowest film thicknesses (20 ML and 40 ML), the modal diameter is significantly larger on the ITO surface without the interface (ITO control) compared to the ITO surface with an interface. As the film thickness increases to 80 ML, the modal diameter for the control samples becomes similar to the droplets formed on the ITO surface with a 40 nm Ag film interface and exceeds that of the droplets on the ITO surface with a 100 nm Ag film interface. For the 100 ML film thickness, the modal diameter for the control group falls between the modal diameter observed for the droplets on the ITO with a 40 nm film (which has a larger modal diameter) and those on the ITO surface with a 100 nm film (which as a smaller modal diameter). At an IL film thickness of 150 ML, the IL droplets deposited on ITO without an interface exhibit the smallest modal diameter. Once again, for this film thickness, the deviation in the modal diameter is higher when compared to the order results, introducing some uncertainty related to the interpretation of these results. However, is possible to theorize that the increase of the partial Ag film thickness may contribute to the droplet differentiation observed. The higher roughness of the Ag surface with 40 nm may exert influence over nucleation and growth mechanisms on the Ag film, by enhancing the dislocation of the ionic pairs into the interstitial spaces of the Ag particles, especially for the lower's quantities deposited (20 ML and 40 ML). For the results for the ITO surface with 100 nm Ag film interface, the uniform Ag film allows for a decrease in surface mobility, facilitating nucleation and slower growth of the droplets on both of the surfaces under study. Based on these results, it is possible to theorize that the presence of a small Ag film may enhance the nucleation process; however, for the growth of the IL, a completely covered surface with Ag film is necessary. Beyond 80 ML of $[C_8C_1im][OTf]$ films, there is a noticeable increase

in droplet size for the ITO surfaces with an Ag film interface, while for the ITO control, the growth of the droplet sizes is less significant. For the IL film to reach 150 ML, the droplet sizes on the ITO with a 100 nm Ag film surpass the ITO control.

Looking at the percentage of surface coverage (Figure 48B), it is apparent that there are small variations among the three surfaces under investigation, but theses curves exhibit similar behaviors across all the surfaces studied, considering the experimental error.

These findings suggest that the presence of an interface has a modifying effect on the surface characteristics, particularly the surface energy. This modification on the surface leads to a reduction in droplet size within the ITO region when compared to the ITO control, for the lower thicknesses. The introduction of the Ag interface onto the surface creates areas more energetically stable where ionic pairs diffuse and form clusters more easily. This phenomenon arises during the formation of an interface, the ITO area presents some Ag clusters, which act as a magnet for the IL accumulation. These clusters reduce the energetic differences between the Ag and ITO surfaces, enhancing the nucleation process on the junction area, a phenomenon that is subsequently manifested on the ITO surface. When increasing the amount of the IL deposited (beyond 80 ML) the presence of an interface enhances the second-order coalescence mechanisms when compared to the ITO alone control.

4.3. The Influence of Amorphous Carbon on the Nucleation and Growth of Ionic Liquid Thin Films

One aspect that requires some attention when studying the influence of surface interactions on the morphology of IL films is the potential effect of surface contamination. One specific contaminant that deserves thorough discussion is the presence of amorphous carbon and its derivates on the surfaces used to deposit the IL films. Carbon contamination is virtually unavoidable, even when the surface is exposed to a vacuum system, except when rigorous in-situ cleaning procedures are employed. Based on this information, it becomes crucial to understand how the presence of carbon can influence the morphology of IL films on some of the surfaces previously studied, in the conditions of these studies.

In prior studies related to the deposition of ILs onto different surfaces, such as glass coated with conductive oxides, silver, graphene, graphite, or mica surfaces, the formation

of droplets was observed for the imidazolium-based ILs [10,62,64,81,109,110]. In the studies conducted on carbon surfaces, structured materials such as graphene were used, which possess different properties when compared to amorphous carbon. Surface contaminations with carbon can be of various forms, including both amorphous and structured carbon. Therefore, it is also important to understand the effect of the amorphous carbon on the morphology of IL films.

For this study, various ILs were used to have a better perspective of the correlation between the inherent properties of the ILs and their interactions with carbon-coated surfaces, which can affect the observed film morphology. To accomplish this study, short and long-chain alkylimidazolium cations (C_2C_1im and C_8C_1im, respectively) combined with either bis(trifluoromethyl)sulfonylimide (NTf_2) or triflate (OTf) anions, were used. The fabrication of the IL films was conducted as described previously. All deposition conditions are described in Table A4 in the Attachments section. To assess the morphology of the IL films on surfaces, high-resolution SEM was employed, together with the ImageJ software, as also described before. Some of this information was organized into histograms and graphs, as in 4.1 and 4.2, to enable an easier visualization and consequent understanding of the changes in the IL film's behavior introduced by the amorphous carbon.

It was crucial to first gain a comprehensive understanding of the distinct characteristics of the different studied surfaces when coated with carbon. Figure 49 provides SEM micrographs of the different surfaces used in this study, both with and without ≈ 20 nm of carbon coating. Indeed, we are using a carbon content well above any possible surface contamination, but this was necessary to enable the observation of any possible effect. The SEM micrographs reveal that although the differences observed between the surfaces with the presence or absence of carbon are not very pronounced, surfaces with a carbon film appear to be more uniform and smoother compared to the "clean" surfaces, where it is possible to observe the presence of irregularities and surface defects. This might lead to the hypothesis that the primary factor influencing the changes in the morphology of ILs might be the interaction between the ILs and the carbon film.

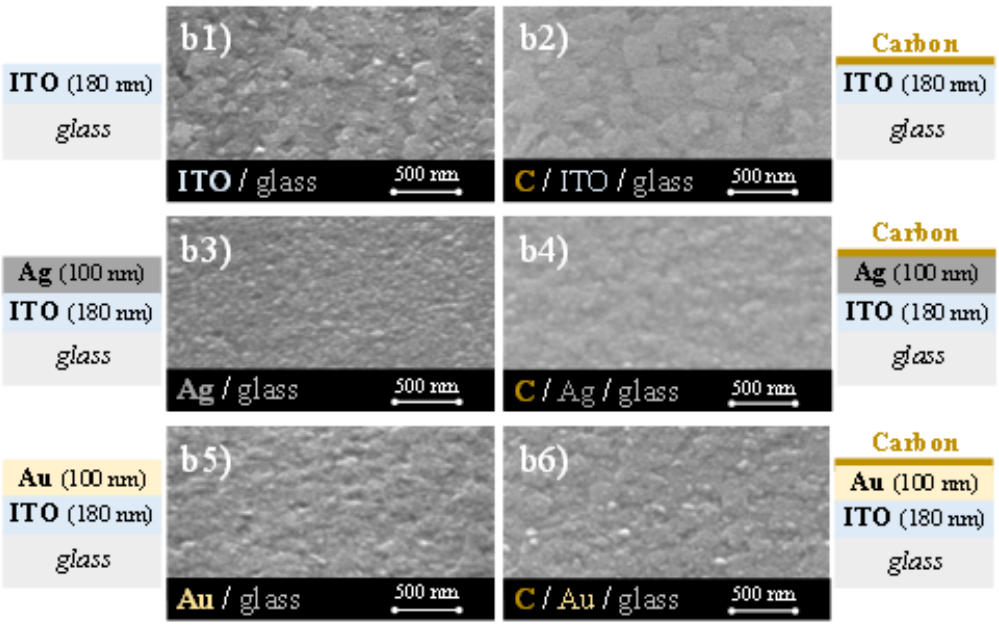

Figure 49. Schematic representation and respective micrographs of the different substrates used in this study (b): ITO/glass (b1); carbon/ITO/glass (b2); Ag/ITO/glass (b3); carbon/Ag/ITO/glass (b4); Au/ITO/glass (b5); carbon/Au/ITO/glass (b6). For the micrographs related to the surfaces coated with carbon, carbon films with an approximate thickness of 20 nm were fabricated. The SEM micrographs were acquired, using a high-resolution SEM equipped with a secondary electron detector (SE). Images were obtained at a 45°lateral view and a magnification of 100,000×.

4.3.1. Effect of Carbon Coating on the Morphology of IL Films with Varied Thickness

Initially, the influence of the carbon coating on the nucleation and growth mechanisms of IL films was explored on ITO substrates. This was achieved by analyzing the morphology of IL films as a function of the IL quantity deposited on both ITO and carbon/ITO (C/ITO) surfaces. For this first study, two ILs with the same anion and distinct alkyl chains were used ($[C_2C_1im][NTf_2]$ and $[C_8C_1im][NTf_2]$). The surfaces used in this work consisted of a "clean" ITO/glass substrate and an ITO/glass substrate coated with an amorphous carbon film of 20 nm (Figure 49, images b1 and b2). Various quantities of IL were deposited onto these surfaces under similar conditions (Table A4 from Attachments): 50 ML, 100 ML, 150 ML, and 200 ML. This enabled us to investigate how the carbon surface affects the morphology of IL films at various thicknesses. Figure 50 and Figure A34 (Attachments) show the morphology of $[C_2C_1im][NTf_2]$ and $[C_8C_1im][NTf_2]$ deposited on both ITO and C/ITO surfaces.

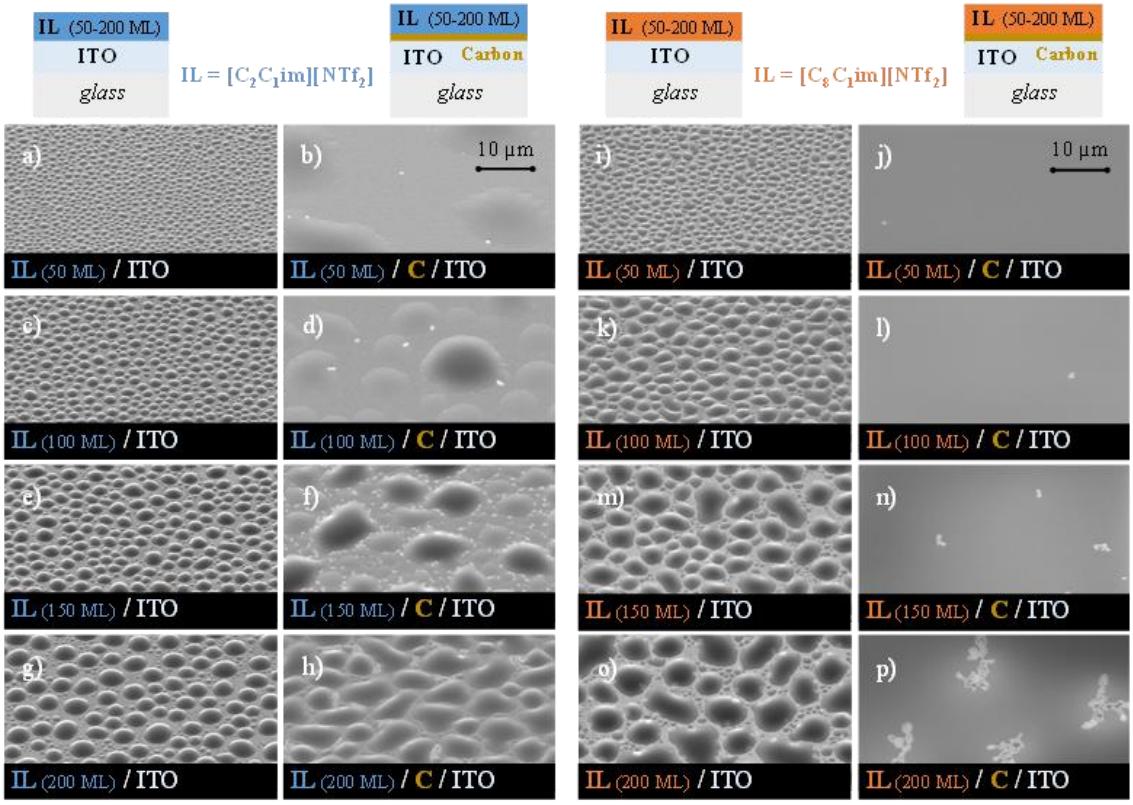

Figure 50. Schematic representation of the different films fabricated on ITO and C/ITO (carbon thickness ≈ 20 nm) surfaces. Detailed micrographs for the $[C_2C_1im][NTf_2]$ (images a-h) and $[C_8C_1im][NTf_2]$ (images i-p). The deposition of each IL with different thicknesses (50 ML, 100 ML, 150 ML, and 200 ML) occurred simultaneously on both of the surfaces studied. Micrographs were acquired at a lateral view of 45° with a magnification of 5000×, using a high-reso-olution SEM and employing a SE detector.

Regarding the results related to the ITO surface in Figure 50 and Figure A34 from the Attachments, the SEM micrographs illustrate that, as the IL film thickness increases, there is an increase in the droplet size, mirroring similar outcomes observed during this dissertation. For $[C_2C_1im][NTf_2]$, the increase in IL thickness leads to an enlargement of droplet size with relatively uniform sizes and some sphericity. However, a distinct behavior is observed for $[C_8C_1im][NTf_2]$. In the initial stages of the influence of the thickness study, there is the formation of small droplets with some sphericity (when compared to the $[C_2C_1im]$ for the same IL film thickness, these droplets are larger and slightly more heterogeneous in their morphology). As the IL film thickness increases, the droplets become more heterogeneous in both morphology and size. This behavior indicates that there is an intensification of the coalescence mechanisms, usually observed in ILs with larger alkyl chains. In addition, the droplets seemed to exhibit lower contact angles when compared to those observed for $[C_2C_1im]$. The contact angle offers insights into the interactions that occur between the IL under study and its environment. For a better understanding of this influence, Young's Equation can be employed, which

relates the contact angle to the three interfacial tensions (as detailed in subchapter 2.3.). In this work, both ILs were deposited on the same surface, allowing us to infer that the difference in the contact angles may be attributed to the interactions between the IL and solid surface or the gas phase. The lower contact angles for the $[C_8C_1im][NTf_2]$ on the ITO surface may result from a more dominant contribution of the lower gas-liquid interfacial tension (surface tension) over the solid-liquid interfacial tension for this IL (as shown in Table 2) when compared to the $[C_2C_1im][NTf_2]$.

Comparing the results of the ITO surfaces with those obtained for the C/ITO surfaces, there is a significant change in the IL film morphology in this later case, even for the same thickness studied. In the case of $[C_2C_1im][NTf_2]$, different behaviors were observed with the increase of IL film thickness. In the lower IL film study (50 ML), it is evident the formation of some larger droplets above a continuous IL film. These droplets are more spread across the surface and seem to have lower contact angles compared to the "clean" ITO surface. This suggests a stronger affinity of the IL for the carbon film. As the IL film thickness increases, a higher number of droplets are formed above the initial layer of IL film. When examining the SEM micrographs referent to the highest thickness studied (200 ML), larger droplets are observed, with sizes exceeding those on the ITO surface (without the carbon film). In the interstitial spaces between the droplets, the ITO surface becomes exposed, allowing the formation of small droplets. The presence of these areas might indicate the occurrence of diffusion of the carbon along the surface, suggesting partial miscibility between the IL and carbon film when this high IL amount is deposited on the surface. One of the more interesting aspects observed for the $[C_2C_1im][NTf_2]$ deposited on the carbon film is the formation of larger droplets and reduced contact angles at lower thicknesses. The improvement in the IL spreading into the surface suggests a stronger affinity of the IL for the carbon surface. The reduction of the solid-liquid interfacial tension results in a better wetting behavior of this IL on the surface. Another consequence is the intensification of the coalescence mechanisms, due to the reducing distance between the droplets.

Turning to the $[C_8C_1im][NTf_2]$, it is possible to observe the formation of a continuous IL film in the C/ITO surface, regardless of the IL film thickness. The total wettability of this IL on this surface may be the result of reduced interfacial tensions experienced by the IL. For the largest film thickness study (200 ML), some exposed areas can be observed, indicating the diffusion of the carbon film. The IL deposited into these exposed areas behaves similarly to what is observed for the "clean" ITO, leading to the formation of droplets on this surface (Figure A34 from Attachments). The formation of a continuous

film is attributed to the better stabilization of the cation on this surface when compared to the “clean” ITO. The ILs with longer alkyl chains exhibit regions with different polarities (as shown in the subchapter 1.1.). The carbon surface provides a better stabilization of the non-polar region due to its similar nature to the alkyl chain of the cation. Therefore, the IL shows an enhanced wettability on the C/ITO surface, leading to the formation of a high-coverage continuous film.

4.3.2. Stability of the IL Films on the Carbon Surfaces

One of the most crucial aspects when studying IL films on different surfaces is the stability of these films over time. This is especially important when investigating a new surface, to determine whether the results observed can be correlated solely to the intrinsic properties of the IL and its interaction with the surface, or if the element of time should be considered to better understand the IL film morphology. Therefore, a stability study was conducted for the C_2C_1im films ([C_2C_1im][NTf_2] and [C_2C_1im][OTf]) with two different thicknesses (50 ML and 150 ML). These films were fabricated on different days relative to the day of SEM analysis (7 days prior, 4 days prior, and 2 days prior to the SEM analysis). The deposition conditions were similar throughout this work, using an orifice diameter of 2.1 mm, a T_{subst} = 283 K, and a deposition rate of 0.30 ± 0.10 Å/s. The study of two different thicknesses aimed at understanding the correlation between the amount of IL film and its stability over time. The exclusive use of ILs with shorter alkyl chains is related to the previously obtained results. The C_8C_1im ILs deposited on the C/ITO surface, consistently formed a continuous film regardless of the IL film thickness study, making it more challenging to visualize any possible modification of the IL film with time. Conversely, the shorter alkyl chains ILs formed droplets on the surface, facilitating a better visualization of possible time-related modification and comprehending the size distribution on the carbon surface, by using the ImageJ software. Lastly, this study was conducted on an ITO coated with ≈ 20 nm film, as well as on a “clean” ITO surface. Figure 51 and Figure 52 display the SEM micrographs and the corresponding histograms for the [C_2C_1im][NTf_2] films deposited on ITO and C/ITO surfaces, with 50 ML and 150 ML, respectively. The results referent for the [C_2C_1im][OTf] samples are available in the Attachments Section (Figure A35 and Figure A36).

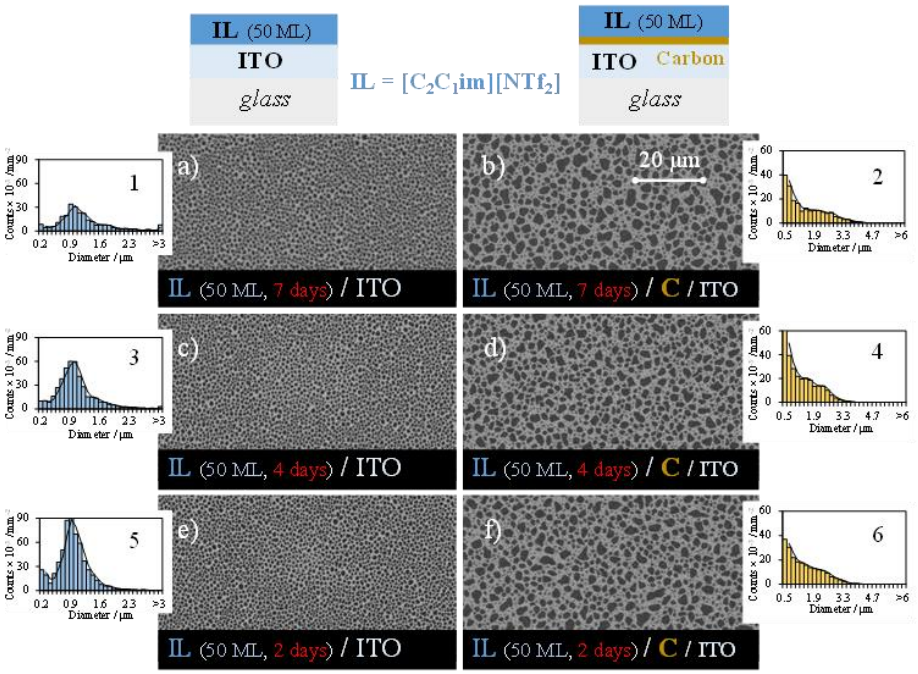

Figure 51. Detailed micrographs of $[C_2C_1im][NTf_2]$ films deposited on ITO/glass (images a, c, and e) and carbon/ITO/glass surfaces (images b, d, and f). The SEM micrographs were obtained after 7 days (images a and b), 4 days (images d and f), and 2 days (images e and f) of film deposition. Histograms 1-6 present the droplet size distribution obtained for each sample. Both films were deposited under similar experimental conditions with a thickness of 50 ML on both surfaces. Micrographs were acquired with a SEM technique using a BSE detector.

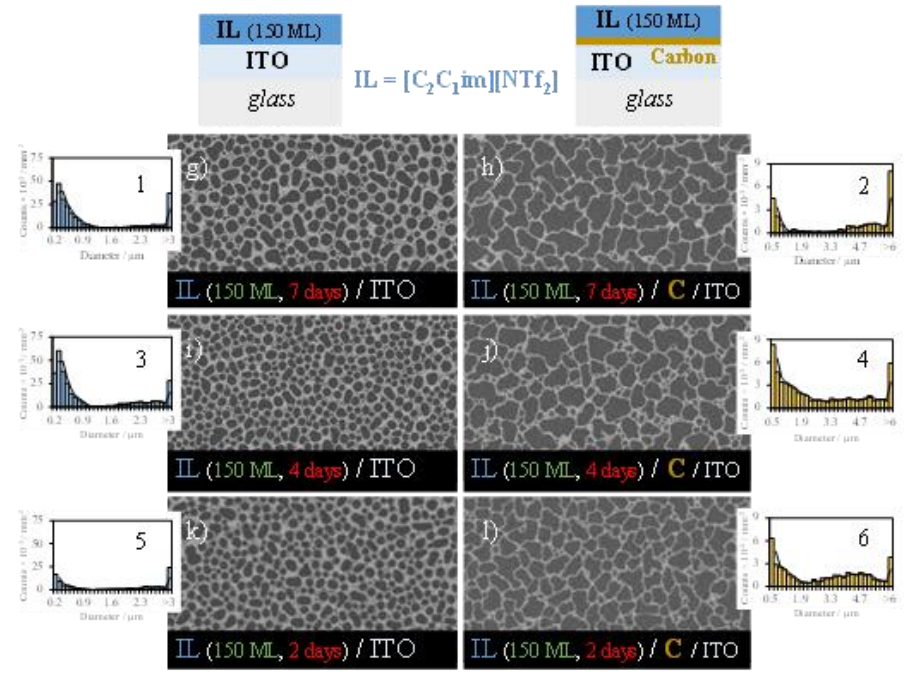

Figure 52. Detailed micrographs of $[C_2C_1im][NTf_2]$ films deposited on ITO/glass (images a, c, and e) and carbon/ITO/glass surfaces (images b, d, and f). The SEM micrographs were obtained after 7 days (images a and b), 4 days (images d and f), and 2 days (images e and f) of film deposition. Histograms 1-6 present the droplet size distribution obtained for each sample. Both films were deposited under similar experimental conditions with a thickness of 150 ML on both surfaces. Micrographs were acquired with a SEM technique using a BSE detector.

Upon initial observation of the SEM micrographs for the different ILs, it is evident that the morphology of the IL film appears to be similar across the different post-deposition times studied, for both surfaces. Focusing on the results related to the 50 ML IL films, it is noteworthy that, for the ITO surface, droplets with similar sizes and some sphericity form consistently across all the days observed. The histograms depict a Gaussian distribution with comparable modal diameters for the ILs examined (a modal diameter of (0.9 ± 0.1) μm. In contrast, the results related to the C/ITO surface show the formation of larger droplets with heterogeneous shapes and a higher number of smaller droplets in the spaces between them. The histograms reveal the existence of two distinct regions: one with a significant count of small droplets and a second region with larger droplets (this last region of the histogram is formed by different droplets, forming a large interval of dimensions observed). However, for both surfaces investigated, the histograms show similar trends across the different pos-deposition times considered. This suggests that there is no kinetic factor influencing the morphology of these IL films (at these thicknesses) once the IL deposition process is completed. Consequently, it is possible to state that, for the conditions here studied, the morphology of the ILs on these surfaces is primarily governed by the kinetic and thermodynamic processes during the deposition time, which impact the nucleation and growth mechanisms. When examining the stability of the IL films with the increase in time after deposition for IL films with higher thicknesses (150 ML), similar trends are apparent. Upon further analysis of the SEM micrographs referent to the ITO surface, it is possible to see the formation of larger droplets, with some smaller ones surrounding them. These droplets seem to lose some of their sphericity when compared to the results for the 50 ML films. The histograms illustrate this behavior by showcasing two distinct regions in the size distribution: one near the beginning of the graphic, illustrating the smaller sizes of droplets in the system; and a second one, starting at ≈ 2 μm and extending to higher values, denoting an increase in the distribution of the droplets, corresponding to the larger droplets.

On the C/ITO surface, an increase in the droplet size is also observed when compared to the results for the 50 ML films. Additionally, a reduction in sphericity is evident, as well as the formation of smaller droplets in the interstitial spaces between the larger ones. This behavior is reflected in the size distribution, described in the histograms, by the existence of two predominant regions in the size distribution. For both IL film thicknesses studied, there is an observable intensification of the coalescence mechanisms due to the improvement of the C_2C_1im spreading on the carbon surface. This results in the formation of much larger droplets on the C/ITO, evident in the histograms of Figure 51, Figure 52, Figure A35, and Figure A36 from the Attachments. On both surfaces studied, the size

distribution remains rather stable over different post-deposition times, indicating the stability of the IL film morphology after deposition.

4.3.3. Effect of Carbon on the Morphology of IL Films

Another aspect to consider was the influence of the amorphous carbon film on other surfaces and its impact on the morphology of IL films. Therefore, the study described below aimed at understanding whether the observed change in behavior on the C/ITO surface was solely the result of the presence of the carbon film or if the underlying ITO surface beneath the carbon film could also affect the morphology of the IL films.

For this, different surfaces were used, the ITO/glass substrate, Ag/ITO/glass substrate, and Au/ITO/glass substrate. All these substrates were subject to electron beam evaporation to fabricate an amorphous carbon film with ≈ 20 nm. Thereafter, similar conditions were used on the different substrates to fabricate 100 ML IL films (Figure 53).

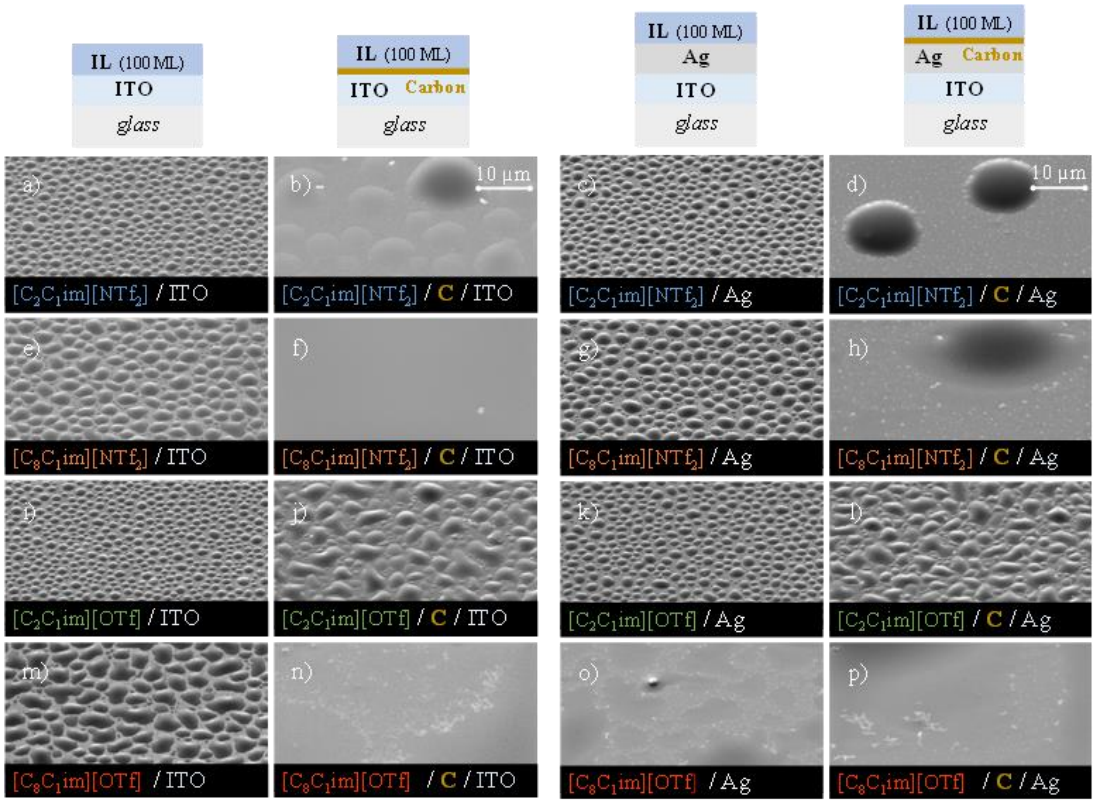

Figure 53. Detailed micrographs of the 100 ML thin films for $[C_2C_1im][NT_2]$ (images a-d), $[C_8C_1im][NTf_2]$ (images e-h), $[C_2C_1im][OTf]$ (images i-l), and $[C_8C_1im][OTf]$ (images m-p) deposited on the ITO (images a, e, i, m), C/ITO (b, f, j, n), Ag (c, g, k, o) and C/Ag (d, h, l, p) surfaces. It's worth noting that the carbon film used in all cases is approximately 20 nm thick. Simultaneous deposition of the IL film takes place on both the surface with the carbon film and the surface without it. Micrographs were acquired at a 45° lateral view with a 5000× magnification using a high-resolution SEM and employing a SE detector.

The deposition conditions are described in Table A5 from the Attachments. Figure 53 and Figure A37 illustrate the results obtained for the deposition of 100 ML of different ILs on ITO and Ag surfaces, both with and without a 20 nm carbon film. Analyzing the results related to the ITO and Ag surfaces without the carbon film, it is possible to observe different behavior depending on the size of the alkyl side chain in the ILs. For the C_2C_1im ILs, the formation of small droplets with some sphericity is clear, while for ILs with longer alkyl side chains (C_8C_1im), the formation of larger droplets with a heterogenous shape is observed. Furthermore, for longer chain ILs, it is possible to observe smaller droplets in the interstitial spaces between the larger droplets. It is also noteworthy that there is no significant difference in the film morphology when modifying the anion in the C_2C_1im films, in agreement with findings in other studies [10,64,108]. The behavior described is very similar for both studied surfaces (ITO and Ag), with the exception of [C_8C_1im][OTf], where on the Ag surface, the droplets formed exhibit reduced contact angles as compared to the ITO surface. Based on these results, it is possible to conclude that the surface characteristics and the IL anion do not have a significant influence on the morphology of C_2C_1im films in the absence of carbon film. Regarding the results referent to the ILs deposited on ITO and Ag surfaces coated with ≈ 20 nm carbon film, different behavior is observed when compared to the “clean” surfaces. In the case of the C_8C_1im films, is possible to observe a complete spreading of C_8C_1im onto the surfaces, leading to the formation of a continuous film on both surfaces. Therefore, it is possible to conclude that the C_8C_1im films exhibit a 2D growth on both C/ITO and C/Ag surfaces.

For the C_2C_1im films, two different behaviors can be detected when modifying the anion on both studied surfaces (C/ITO and C/Ag surfaces). The SEM micrographs for [C_2C_1im][NTf_2] show the formation of larger droplets above the continuous IL film (this behavior is especially clear in Figure A37). These droplets appear to have lower contact angles compared to those formed on a “clean” surface. This indicates a better affinity of the IL to the surface due to the similar nature between the film and the alkyl chain. Based on the results, it can be concluded that [C_2C_1im][NTf_2] exhibits a 2D growth followed by a 3D growth on the carbon surface. The results related to the [C_2C_1im][OTf] film morphology on the C/ITO and C/Ag surfaces showed different outcomes. On the carbon surfaces, the IL tends to form larger droplets compared to the “clean” surface but smaller when compared to the [C_2C_1im][NTf_2] on carbon surfaces. The contact angles for [C_2C_1im][OTf] droplets on the carbon surfaces are higher compared to the [C_2C_1im][NTf_2] droplets on the same surface. Furthermore, especially for the higher magnification micrographs (Figure A37), it is possible to see areas where the larger droplets of [C_2C_1im][OTf] expose the underlying ITO surface. In these areas, the IL appears to have

caused carbon diffusion into other areas, resulting in the formation of smaller droplets, like those observed on surfaces without the carbon film. The carbon film diffusion for the 100 ML [C_2C_1im][OTf] film may indicate some miscibility of the carbon with the quantity of this IL deposited. It is also possible to infer that [C_2C_1im][OTf] on the carbon surfaces appears to have a 3D growth.

As mentioned at the beginning of this subchapter, the primary aim of this study was to investigate the influence of carbon on the IL morphology for different surfaces, including the Au/ITO surface. For this last surface, a slightly different approach was taken. Previous studies have revealed that ILs with longer alkyl chains, such as C_8C_1im ILs, tend to spread onto Au surfaces, resulting in the formation of a continuous film (2D/Frank-van der Merwe growth) [10,65]. Based on the results obtained for C_8C_1im ILs on both C/ITO and C/Ag surfaces, as well as the results for these ILs on Au/ITO surfaces, it was decided to exclude these ILs from this study.

Taking this into consideration, the study proceeded with the use of ILs with shorter alkyl chains, namely [C_2C_1im][NTf_2] and [C_2C_1im][OTf]. Results for the deposition of 100 ML of [C_2C_1im] ILs on Au/ITO and C/Au surfaces are presented in Figure 54 and Figure A38 from the Attachments section. All the deposition conditions are described in Table A5.

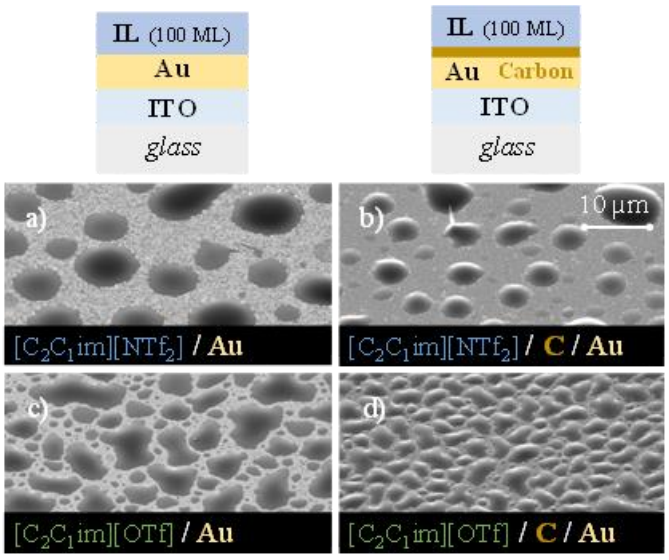

Figure 54. Detailed micrographs of 100 ML [C_2C_1im][NTf_2] (images a, b) and [C_2C_1im][OTf] (images c, d) thin films, deposited on Au/ITO/glass (images a, c) and C/Au/ITO/glass (images b, d). It's worth noting that the carbon film used in all cases is approximately 20 nm thick. Simultaneous deposition of the IL film takes place on both the surface with the carbon film and the surface without it. Micrographs were acquired at a lateral view of 45° with a magnification of 5000×, using a high-resolution SEM and employing a SE detector.

Overall, both ILs exhibited similar behavior on both of the surfaces studied. On the Au/ITO and C/Au/ITO surfaces, the two ILs studied tend to form droplets with larger dimensions. For the C/Au surface, in addition to the formation of larger droplets, it is possible to observe the existence of smaller droplets in proximity areas of the larger droplets. However, these differences were not very significant when compared to the changes observed on other surfaces coated with carbon films. The similarities in the results for the C_2C_1im films on the Au and C/Au surface can be attributed to the similarity of the roughness between the Au/ITO substrate coated with a 20 nm carbon film and the clean Au/ITO substrate.

Comparing the characteristics of the films across surfaces, despite overall similarities in the behavior of the two ILs studied on the different surfaces, some differences in the droplet morphology can be noted. The [C_2C_1im][OTf] films formed droplets with similar morphologies throughout the three coated surfaces studied (C/ITO, C/Ag/ITO, C/Au/ITO). Furthermore, when compared to the [C_2C_1im][NTf_2] films on the Au/ITO and C/Au/ITO, it is possible to observe that the [C_2C_1im][OTf] tend to form droplets with a more heterogeneous distribution of sizes and less spherical shape on the same surfaces. Examining the SEM micrographs with higher magnification (Figure A38 from Attachments), it becomes apparent that the interstitial spaces between the larger droplets on the Au surface are uncovered. In these areas it was not possible to verify the presence of IL, a behavior different from the one observed with [C_2C_1im][NTf_2]. This suggests that the [C_2C_1im][NTf_2] follows a Stranski-Krastanov growth (2D followed by 3D) on the Au surface, while the [C_2C_1im][OTf] follows Volmer-Weber (3D) mode of growth. Another aspect that differentiates these ILs is the contact angle between the IL and the surfaces. Based on the SEM micrographs, it is possible to verify that the contact angle for [C_2C_1im][NTf_2] is higher when compared to [C_2C_1im][OTf]. This indicates a better spreading of the [OTf]-based ILs onto the surfaces, which can enhance the coalescence mechanisms for this IL in comparison to the [C_2C_1im][NTf_2].

Quartz crystal microbalance (QCM) was used in the deposition equipment to monitor the amount of IL deposited into the surface. The QCMs used in this investigation are coated with a gold film; therefore, it was interesting to understand how the carbon film may influence the morphology of [C_2C_1im][NTf_2] film, given the higher morphological irregularities of this surface compared to the Au/ITO surface. In previous work, it was observed that the IL deposited on these surfaces tends to first occupy the confined spaces before forming droplets or a film on the surface [11]. For this study, a gold-coated QCM was coated with ≈ 20 nm of amorphous carbon, followed by the deposition of 400 ML of [C_2C_1im][NTf_2]. The deposition conditions are described in Table A6 from the

Attachments section. Figure 55 shows the results related to the deposition of 400 ML of $[C_2C_1im][NTf_2]$ on the gold-coated QCM with and without a carbon film on top.

The SEM micrographs reveal a different behavior depending on the surface under study. When focusing on the “clean” Au/QCM surface, it is possible to observe the existence of regions covered with IL on the substrate surface. This becomes especially clear when examining the micrographs at higher magnification (Figure 55c), where darker regions corresponding to the IL deposited are evident. However, most of the IL tends to dislocate into confined spaces. Previous studies demonstrated that when the ILs come in contact with a surface, the ionic pairs have the tendency to diffuse on the surface into more energetically stable spaces. In the case of quartz crystals, these locations are the confined spaces present on the surface. Only after all the confined spaces are filled does the IL film begin to grow on the QCM surface [93].

When observing the micrographs referent to the quartz crystal coated with an amorphous carbon film, a slight difference in behavior is apparent, as it was not possible to detect the presence of the IL film on the surface. This result may indicate that the amount deposited on this surface allows the diffusion of the carbon film along with the ionic pairs into the confined spaces or the formation of an ultrathin IL film in the QCM surface, undetectable for the SEM equipment utilized.

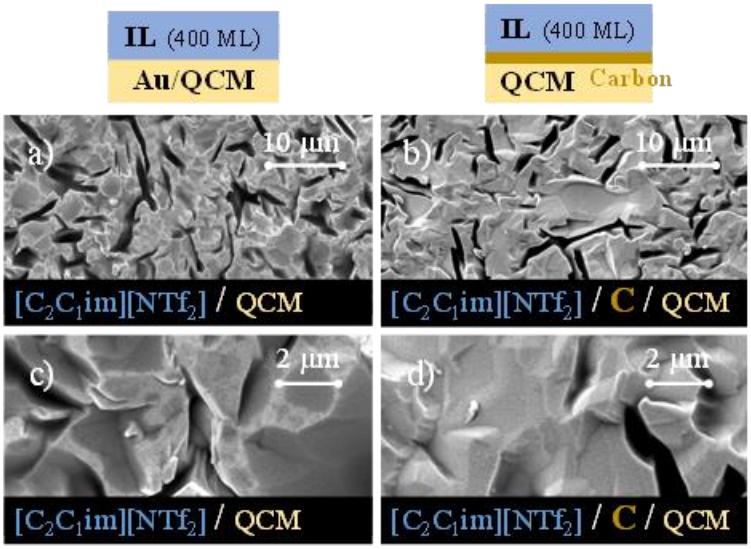

Figure 55. Detailed micrographs of 400 ML $[C_2C_1im][NTf_2]$ films, deposited on Au/QCM (images a, c) and C/Au/QCM (images b, d). It's worth noting that the carbon film used in all cases is approximately 20 nm thick. Simultaneous deposition of the IL film takes place on both the surface with the carbon film and the surface without it. Micrographs were acquired at a 45° lateral view with magnifications of 5000× (images a, b) and 20000× (images c, d), using a high-resolution SEM and employing the SE detector.

4.3.4. Effect of Carbon Thickness on the Morphology of IL Films

During the previous studies here reported, the primary focus was to understand the influence of an amorphous carbon film on the morphology of various ILs deposited onto different surfaces, as some studies have shown that diverse surfaces may contain traces of carbon and its derivatives due to various factors, including exposure to the air and sample handling. Some additional contamination can also occur within the vacuum chamber, as a result of IL evaporation under moderate vacuum conditions [109,110]. These studies have shown that the presence of amorphous carbon on the surface is not uniform among all surfaces, but it should be stressed that the amount they detected on these surfaces is significantly lower than the amount of amorphous carbon that we did deposit in this study on the different surfaces used.

We observed that the presence of the carbon film influences the morphology of the IL films, suggesting that the initial stages of the nucleation and growth of the IL film are affected by the properties of the carbon surface and the interactions between the carbon film and the IL. Given this observation, it became necessary to understand the impact of the amount of carbon on the morphology of ILs, to enable inference and consequences of carbon presence on the nucleation and growth processes. For this, two ILs were investigated: one with a shorter alkyl chain, $[C_2C_1im][OTf]$, and another with a longer alkyl chain, $[C_8C_1im][OTf]$. Equal amounts of the ILs were deposited (100 ML) on to ITO surfaces carbon-coated with different thicknesses (10 nm, 20 nm, and 30 nm). The deposition conditions were similar throughout the work (Table A7 from the Attachments). The morphology of the different films is illustrated in Figure 56.

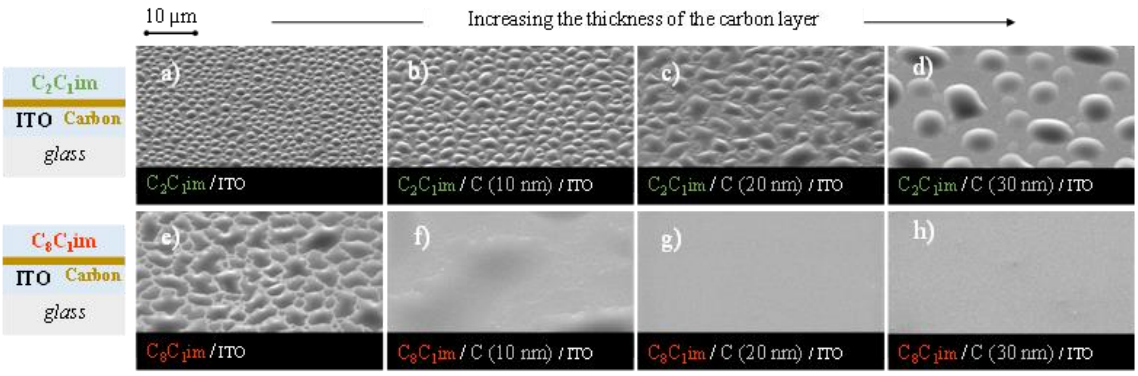

Figure 56. Detailed micrographs of 100 ML of $[C_2C_1im][OTf]$ (images a-d) and $[C_8C_1im][OTf]$ (images e-h) films, deposited on ITO/glass (images a, e) and C/ITO/glass (images b, c, d, f, g, h). Each IL was deposited on ITO surfaces coated with varied amounts of carbon: 0 nm (a and e); 10 nm (b and f); 20 nm (c and g); 30 nm (d and h). Micrographs were acquired at a 45° lateral view with a magnification of 5000×, using a high-resolution SEM and employing the SE detector.

Figure 56 displays the results as the carbon thickness is varied from 10 to 30 nm. The SEM micrographs on the left correspond to the ITO surface without the carbon film (Figure 56a and Figure 56e), supposedly free from carbon on the surface (indeed the presence of vestigial carbon contamination from the environment and/or the techniques used can never be totally ruled out).

When examining the results related to the shorter-chain IL deposited on the ITO surface covered with different amounts of amorphous carbon, the formation of droplets can be seen on all studied surfaces. As the carbon film thickness increases, there is a noticeable increase in droplet size, together with a partial loss of sphericity. This is especially clear when comparing the micrograph of the “clean” ITO (Figure 56a) and the micrograph of the $[C_2C_1im][OTf]$ deposited on the ITO coated with ≈ 30 nm of carbon film (Figure 56d). In the micrographs of $[C_2C_1im][OTf]$ deposited in the lower carbon film thickness (Figure 56b), it appears that the IL initially has 2D growth followed by 3D island growth. As the carbon film thickness increased, larger droplets formed on the surface. This phenomenon can be explained by the reduction of the surface roughness and changes in the surface energy, which influence the spreading of ionic pairs, leading to an intensification of the coalescence mechanisms and, consequently, the formation of larger droplets of $[C_2C_1im][OTf]$.

In the case of $[C_8C_1im][OTf]$, it is possible to detect differences in the IL morphology on the “clean” ITO and ITO coated with carbon (Figure 56e - 56f). On the ITO surface, the formation of droplets with different sizes and heterogenous morphologies is evident, whereas when the $[C_8C_1im][OTf]$ is deposited onto a C/ITO surface, even with a lower carbon film thickness (10 nm), a continuous film is formed. As the thickness of the carbon film increases, the IL film becomes more compact. It appears that the carbon film creates a favorable surface for the IL, likely due to the better alignment of the larger alkyl chain of the cation on the carbon film. The better affinity and stronger interactions between the non-polar alkyl chain cation and the amorphous carbon reduce the interfacial tension experienced by the IL. This results in a better wettability of this IL on this carbon-coated surface.

To get further details on the influence of carbon on IL films, studies were also performed with an ITO surface that was partially coated with an amorphous carbon film. To obtain this surface, a methodology similar to the one described in Figure 31 was employed. However, instead of using the sputtering technique, the electron beam evaporation instrumentation was used, fabricating a 30 nm carbon film in half of the ITO/glass substrate. Figure 57 illustrates the results for 100 ML IL films ($[C_2C_1im][OTf]$ and

[C_8C_1im][OTf]) deposited on both ITO and C/ITO surfaces. The deposition conditions are described in Table A7 from the Attachments section. In the SEM micrographs, it is possible to observe not only the two surfaces mentioned above but also the region near the interface of these surfaces.

In the case of [C_2C_1im][OTf], it is noticeable that there is the formation of larger droplets in the carbon region. As we come closer to the interface region between the two surfaces, an increase in droplet size becomes apparent, indicating a higher surface diffusion and an intensification of the coalescence mechanisms. In the ITO region, a similar behavior can be observed, but the droplets on the ITO region appear to be smaller when compared to the C/ITO surface. This indicates a better affinity of IL with the C/ITO surface, which allows for better spreading and, consequently, an increase in the coalescence mechanisms.

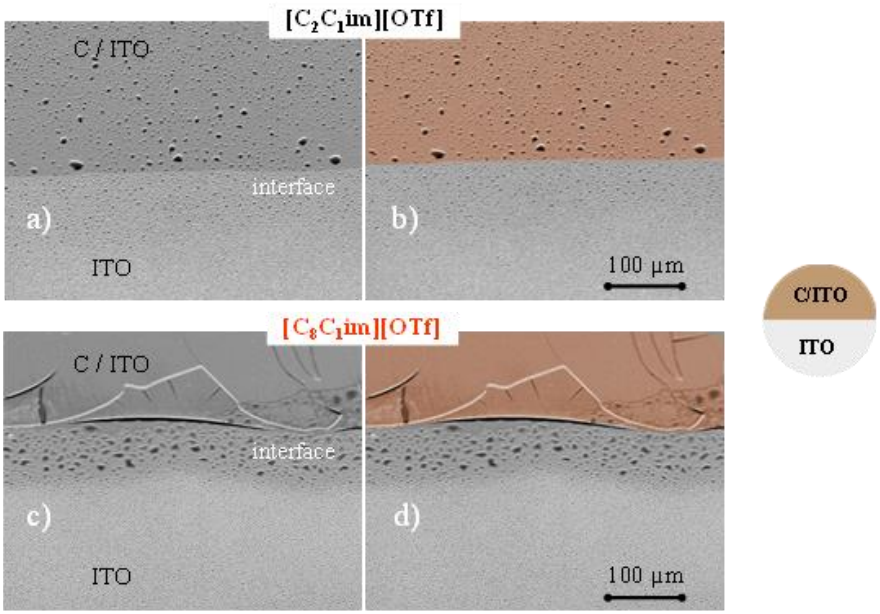

Figure 57. Micrographs of [C_2C_1im][OTf] (a and b) and [C_8C_1im][OTf] (c and d) deposited on both ITO/glass and C/ITO/glass surfaces. Images b and d are colorized versions of SEM micrographs a and c, respectively, highlighting the carbon-covered portion of the substrate. Micrographs were acquired at a lateral view of 45° with a magnification of 500× using a high-resolution scanning electron microscope and employing a secondary electron detector.

For $[C_8C_1im][OTf]$, in the case of the ITO surface, there is the formation of droplets that tend to increase in size in the vicinity of the interface. On the other hand, for the C/ITO region, the $[C_8C_1im][OTf]$ tends to form a continuous film. In this system, the formation of larger droplets is observed on a surface previously coated with the carbon film. This phenomenon is attributed to the weaker adhesion of the carbon film to the ITO surface in the interface region. These results confirm the increased diffusion of ionic pairs into regions with higher carbon content. In these areas, there is a higher probability of adsorbed carbon atoms, which enhanced the spreading and subsequently intensification of droplet coalescence.

These results reinforce previous studies that emphasize the importance of adventitious carbon when studying IL film morphology and their wetting behavior on different surfaces. The extent of morphological changes observed in the IL films was found to be influenced by two factors: the thickness of the carbon film on the substrate surface and the amount of IL deposition. Based on these results, it can be concluded that the presence of carbon on the surface may influence the spreading of ILs with longer chains, leading to a change in the film morphology, whereas, for shorter alkyl chains ILs, the presence of thin carbon film on the surface does not significantly influence the film morphology. Therefore, although we observed that the presence of carbon only induces significant changes in the longer chain ILs and that when the carbon content is much higher than the one resulting from small surface contamination, to draw safe conclusions regarding the influence of the multiple factors on the IL morphology, it is crucial to consider the possible carbon presence on the surface and make all efforts to minimize possible surface carbon contamination. In research at the nanoscale, the work should be conducted by using solid substrate characterization systems, since the minimal traces of carbon on a surface may significantly impact the nucleation and growth mechanisms in the first stages of IL deposition. For the mesoscopic scale, as used in this work, the changes in the surface induced by the carbon might also play some role in the wettability, morphology, and growth patterns of IL films for the long-chain ILs, when the amount of carbon is significant.

Conclusion

In conclusion, this work has successfully achieved all the objectives proposed, shedding light on the complex interplay of factors that influence the morphology of ionic liquid films. These factors included the deposition conditions under which the IL films were fabricated, the influence of an interface, and the presence of carbon contamination on the surface. Throughout this work, thermal evaporation with reduced pressure based on the Knudsen effusion methodology was employed to fabricate various IL films with higher precision and reproducibility. Additionally, sputtering and electron beam evaporation enabled the modification of previous surfaces (ITO and QCM), resulting in the creation of new surfaces where different effects related to the interaction between the IL and the surface could be studied.

In the investigation of the effect of deposition conditions on the morphology of IL films on ITO and Ag surfaces, it was evident that the modification of the evaporation temperature and/or the Knudsen cell orifice area influenced the morphology of the studied ILs. Increasing the mass flow rate led to larger and more heterogeneous droplet formation, attributed to the intensification of the coalescence mechanism as a higher number of ionic pairs reached the surface. This increase was more significant on the ITO surface compared to the Ag surface due to the better affinity of the imidazolium ILs for metallic surfaces. Furthermore, the study involved the differentiation of IL films with modified characteristics. The [C_2C_1im]-based ILs produced smaller and more spherical droplets on ITO surfaces compared to the [C_8C_1im]-based ILs. An analysis of anion modification did not reveal significant differences in the droplet modal diameter with increasing mass flow rate for the C_2C_1im ILs on both surfaces. Another key aspect of this study was the influence of substrate temperature on the IL films formed when the remaining deposition conditions were kept constant. For the C_8C_1im ILs on ITO surfaces, the formation of larger droplets was observed, due to the intensification of coalescence mechanisms. Less intense changes were observed for the C_2C_1im-ILs. On Ag surfaces, the modal diameter remained relatively consistent with increasing substrate temperature, whereas, on the ITO surface, some differences were observed depending on the anion.

A second major aspect of this dissertation was to explore the influence of an ITO/Ag interface on the dynamics of two different ILs, impacting both surfaces as well as the region near the ITO-metal interface. Differentiation of the deposited amount revealed that increasing the quantity led to an enlargement of the droplets formed, indicating different stages of the nucleation and growth mechanisms. The [C_2C_1im][OTf] displayed smaller droplets and a similar size distribution for thinner films, showing that the

nucleation and growth mechanisms were primarily responsible for the films' morphology. Increasing the amounts deposited, larger droplets were formed, surrounded by smaller ones, due to second-order coalescence mechanisms. For the $[C_8C_1im][OTf]$, it was more challenging to observe the presence of different stages of film growth compared to their congener $[C_2C_1im]$. This is due to the higher nucleation and first-order coalescence kinetics for the $[C_8C_1im][OTf]$ and the prevalence of the second-order coalescence process, forming larger droplets even for the smaller amount deposited.

Another aspect focused on the influence of Ag film thickness that constituted the ITO partially covered with an Ag film substrate, which may influence the nucleation and growth mechanisms of $[C_8C_1im][OTf]$. Thinner Ag surfaces promoted IL displacement into the interstitial spaces of the Ag clusters, whereas thicker Ag films reduced the surface mobility of the ionic pairs, resulting in the formation of droplets (for lower amounts of IL film) or the formation of a continuous film (for higher amounts of IL film). The effect of the Ag film thickness extended to the ITO surface, especially for higher amounts of IL deposited. On the ITO surface partially covered by a 40 nm Ag film, larger droplets formed compared to the ITO surface coated with a 100 nm Ag film. For smaller amounts of IL deposited, the modal sizes were similar for the ITO surfaces coated with the Ag film. These differences were related to the availability on the surface of places more energetically stable, which influenced the mobility of ionic pairs that arrived on the surface and enhanced the coalescence mechanisms.

Finally, this dissertation examined the influence of carbon contamination by analyzing the effect of an amorphous carbon coating on the morphologies of different ILs on various surfaces. The results demonstrated that even for lower amounts of the C_2C_1im-based ILs, better droplet spreading occurred on the carbon surface as compared to a clean surface, accompanied by a reduction in the contact angle, suggesting a stronger affinity between the IL film and the carbon surfaces. The C_8C_1im-based ILs exhibited better spreading on the carbon surface, even better when compared to the IL with a shorter alkyl side chain, forming a continuous film. For higher IL thicknesses, carbon diffusion exposed the ITO and Ag surfaces. These films remained stable after deposition. The effect of the anion in the morphology of the IL films on the carbon-coated ITO and Ag surfaces did not significantly change. The presence of a carbon coating had a minimal impact on the C_2C_1im film morphology on an Au surface, attributed to similar surface roughness compared to a clean Au surface and carbon-coated Au surface and the higher affinity of imidazolium ILs for Au surfaces. For the QCM surface, the presence of carbon modified the dynamic of the IL film on this surface. This difference in behavior may

indicate that the IL deposited on the surface may have diffused into the carbon coating in confined spaces or that there is an ultrathin IL layer on the QCM surface that is not detectable using SEM equipment. The increase in carbon coating thickness showed that for shorter alkyl side chain films, there was an increase in the spreading of the IL droplets and a decrease in sphericity as the carbon coating thickness increased. For $[C_8C_1im][OTf]$, the presence of a small amount of carbon allowed the formation of a continuous film, whereas, on the 'clean' ITO, there was the formation of droplets with different sizes and morphologies. As the thickness of the carbon coating increased, it was possible to observe an increase in the compactness of the IL film, suggesting that the carbon surface created a favorable surface for the IL. Overall, these results emphasize the need for conducting nanoscale studies with precisely defined solid substrates, as even small amounts of carbon can have a significant influence on the nucleation and growth of the first monolayers. Furthermore, at a mesoscopic level, carbon-induced changes can also be relevant to the wetting behavior, morphology, and growth tendencies of thin ionic liquid films, particularly in the case of long-chain ILs, as shown in this work.

References

[1] Hajipour, A. R.; Rafiee, F. Basic Ionic Liquids. A Short Review. *Journal of the Iranian Chemical Society* **2009**, *6* (4), 647–678.

[2] de Jesus, S. S.; Maciel Filho, R. Are Ionic Liquids Eco-Friendly? *Renewable and Sustainable Energy Reviews* **2022**, *157*, 112039.

[3] Ghandi, K. A Review of Ionic Liquids, Their Limits and Applications. *Green and Sustainable Chemistry* **2014**, *04* (01), 44–53.

[4] Hayes, R.; Warr, G. G.; Atkin, R. Structure and Nanostructure in Ionic Liquids. *Chemical Reviews* **2015**, *115* (13), 6357–6426.

[5] Canongia Lopes, J. N. A.; Pádua, A. A. H. Nanostructural Organization in Ionic Liquids. *The Journal of Physical Chemistry B* **2006**, *110* (7), 3330–3335.

[6] Del Pópolo, M. G.; Voth, G. A. On the Structure and Dynamics of Ionic Liquids. *The Journal of Physical Chemistry B* **2004**, *108* (5), 1744–1752.

[7] Lei, Z.; Chen, B.; Koo, Y.-M.; MacFarlane, D. R. Introduction: Ionic Liquids. *Chemical Reviews* **2017**, *117* (10), 6633–6635.

[8] Ren, F.; Wang, J.; Xie, F.; Zan, K.; Wang, S.; Wang, S. Applications of Ionic Liquids in Starch Chemistry: A Review. *Green Chemistry* **2020**, *22* (7), 2162–2183.

[9] Rocha, M. A. A.; Lima, C. F. R. A. C.; Gomes, L. R.; Schröder, B.; Coutinho, J. A. P.; Marrucho, I. M.; Esperança, J. M. S. S.; Rebelo, L. P. N.; Shimizu, K.; Lopes, J. N. C.; Santos, L. M. N. B. F. High-Accuracy Vapor Pressure Data of the Extended $[C_nC_1Im][Ntf_2]$ Ionic Liquid Series: Trend Changes and Structural Shifts. *The Journal of Physical Chemistry B* **2011**, *115* (37), 10919–10926.

[10] Costa, J. C. S.; Alves, A.; Bastos, M.; Santos, L. M. N. B. F. The Impact of the Cation Alkyl Chain Length on the Wettability of Alkylimidazolium-Based Ionic Liquids at the Nanoscale. *Physical Chemistry Chemical Physics* **2022**, *24* (21), 13343–13355.

[11] Zhang, S.; Zhang, J.; Zhang, Y.; Deng, Y. Nanoconfined Ionic Liquids. *Chemical Reviews* **2016**, *117* (10), 6755–6833.

[12] Pei, Y.; Zhang, Y.; Ma, J.; Fan, M.; Zhang, S.; Wang, J. Ionic Liquids for Advanced Materials. *Materials Today Nano* **2022**, *17*, 100159.

[13] Katsyuba, S. A.; Vener, M. V.; Zvereva, E. E.; Fei, Z.; Scopelliti, R.; Laurenczy, G.; Yan, N.; Paunescu, E.; Dyson, P. J. How Strong Is Hydrogen Bonding in Ionic Liquids? Combined X-Ray Crystallographic, Infrared/Raman Spectroscopic, and Density Functional Theory Study. *The Journal of Physical Chemistry B* **2013**, *117* (30), 9094–9105.

[14] Kurnia, K. A.; Lima, F.; Cláudio, A. F. M.; Coutinho, J. A. P.; Freire, M. G. Hydrogen-Bond Acidity of Ionic Liquids: An Extended Scale. *Physical Chemistry Chemical Physics* **2015**, *17* (29), 18980–18990.

[15] Bica, K.; Deetlefs, M.; Schröder, C.; Seddon, K. R. Polarisabilities of Alkylimidazolium Ionic Liquids. *Physical Chemistry Chemical Physics* **2013**, *15* (8), 2703.

[16] Fadeeva, Yu. A.; Gruzdev, M. S.; Kudryakova, N. O.; Shmukler, L. E.; Safonova, L. P. Physico-Chemical Characterization of Alkyl-Imidazolium Protic Ionic Liquids. *Journal of Molecular Liquids* **2020**, *297*, 111305.

[17] Plechkova, N. V.; Seddon, K. R. Applications of Ionic Liquids in the Chemical Industry. *Chem. Soc. Rev.* **2008**, *37* (1), 123–150.

[18] Kaur, G.; Kumar, H.; Singla, M. Diverse Applications of Ionic Liquids: A Comprehensive Review. *Journal of Molecular Liquids* **2022**, *351*, 118556.

[19] Zhang, S.; Sun, N.; He, X.; Lu, X.; Zhang, X. Physical Properties of Ionic Liquids: Database and Evaluation. *Journal of Physical and Chemical Reference Data* **2006**, *35* (4), 1475–1517.

[20] Fredlake, C. P.; Crosthwaite, J. M.; Hert, D. G.; Aki, S. N. V. K.; Brennecke, J. F. Thermophysical Properties of Imidazolium-Based Ionic Liquids. *Journal of Chemical & Engineering Data* **2004**, *49* (4), 954–964.

[21] Wishart, J. F. Energy Applications of Ionic Liquids. *Energy & Environmental Science* **2009**, *2* (9), 956.

[22] Hallett, J. P.; Welton, T. Room-Temperature Ionic Liquids: Solvents for Synthesis and Catalysis. 2. *Chemical Reviews* **2011**, *111* (5), 3508–3576.

[23] Almeida, H. F. D.; Freire, M. G.; Fernandes, A. M.; Lopes-da-Silva, J. A.; Morgado, P.; Shimizu, K.; Filipe, E. J. M.; Canongia Lopes, J. N.; Santos, L. M. N. B. F.; Coutinho, J. A. P. Cation Alkyl Side Chain Length and Symmetry Effects on the Surface Tension of Ionic Liquids. *Langmuir* **2014**, *30* (22), 6408–6418.

[24] Ebrahimi, M.; Moosavi, F. The Effects of Temperature, Alkyl Chain Length, and Anion Type on Thermophysical Properties of the Imidazolium Based Amino Acid Ionic Liquids. *Journal of Molecular Liquids* **2018**, *250*, 121–130.

[25] Micaelo, N. M.; Soares, C. M. Parametrization of 1-Butyl-3-Methylimidazolium Hexafluorophosphate/Nitrate Ionic Liquid for the GROMOS Force Field. *Journal of Physical Chemistry B* **2006**, *110* (29), 14444–14451.

[26] Zaitsau, D. H.; Kabo, G. J.; A.A. Strechan; Paulechka, Y. U.; A. Tschersich; Verevkin, S. P.; Heintz, A. Experimental Vapor Pressures of 1-Alkyl-3-Methylimidazolium Bis(Trifluoromethylsulfonyl)Imides and a Correlation Scheme for Estimation of Vaporization Enthalpies of Ionic Liquids. **2006**, *110* (22), 7303–7306.

[27] Marsh, K. N.; Boxall, J. A.; Lichtenthaler, R. Room Temperature Ionic Liquids and Their Mixtures—a Review. *Fluid Phase Equilibria* **2004**, *219* (1), 93–98.

[28] Azita Ahosseini; Scurto, A. M. Viscosity of Imidazolium-Based Ionic Liquids at Elevated Pressures: Cation and Anion Effects. *International Journal of Thermophysics* **2008**, *29* (4), 1222–1243.

[29] Jacquemin, J.; Husson, P.; Padua, A. A. H.; Majer, V. Density and Viscosity of Several Pure and Water-Saturated Ionic Liquids. *Green Chem.* **2006**, *8* (2), 172–180.

[30] Yu, B.; Zhou, F.; Liu, G.; Liang, Y.-M.; Wilhelm; Liu, W. The Electrolyte Switchable Solubility of Multi-Walled Carbon Nanotube/Ionic Liquid (MWCNT/IL) Hybrids. *Chemical Communications* **2006**, No. 22, 2356–2356.

[31] Pensado, A. S.; Comuñas, M. J. P.; Fernández, J. The Pressure–Viscosity Coefficient of Several Ionic Liquids. *Tribology Letters* **2008**, *31* (2), 107–118.

[32] Li, W.; Banuelos, J.; Guo, J.; Anovitz, L. M.; Rother, G.; Shaw, R. A.; Hillesheim, P. C.; Dai, S.; Baker, G. A.; Cummings, P. T. Alkyl Chain Length and Temperature Effects on Structural Properties of Pyrrolidinium-Based Ionic Liquids: A Combined Atomistic Simulation and Small-Angle X-Ray Scattering Study. *Journal of Physical Chemistry Letters* **2012**, *3* (1), 125–130.

[33] Sanchora, P.; Pandey, D. K.; Kagdada, H. L.; Materny, A.; Singh, D. K. Impact of Alkyl Chain Length and Water on the Structure and Properties of 1-Alkyl-3-Methylimidazolium Chloride Ionic Liquids. *Physical Chemistry Chemical Physics* **2020**, *22* (31), 17687–17704.

[34] Rocha, M. A. A.; Neves, C. M. S. S.; Freire, M. G.; Russina, O.; Triolo, A.; Coutinho, J. A. P.; Santos, L. M. N. B. F. Alkylimidazolium Based Ionic Liquids: Impact of Cation Symmetry on Their Nanoscale Structural Organization. *The Journal of Physical Chemistry B* **2013**, *117* (37), 10889–10897.

[35] Xue, L.; Gurung, E.; Tamas, G.; Koh, Y. P.; Shadeck, M.; Simon, S. L.; Maroncelli, M.; Quitevis, E. L. Effect of Alkyl Chain Branching on Physicochemical Properties of Imidazolium-Based Ionic Liquids. *Journal of Chemical & Engineering Data* **2016**, *61* (3), 1078–1091.

[36] Perkin, S.; Crowhurst, L.; Niedermeyer, H.; Welton, T.; Smith, A. M.; Gosvami, N. N. Self-Assembly in the Electrical Double Layer of Ionic Liquids. *Chemical Communications* **2011**, *47* (23), 6572.

[37] Díaz-Rodríguez, P.; Cancilla, J.; Matute, G.; Torrecilla, J. S. Conductivity of Ionic Liquids: A Neural Network Approach. *Industrial & Engineering Chemistry Research* **2014**, *54* (1), 55–58.

[38] Shahiduzzaman, Md.; Muslih, E. Y.; Hasan, A. K. M.; Wang, L.; Fukaya, S.; Nakano, M.; Karakawa, M.; Takahashi, K.; Akhtaruzzaman, Md.; Nunzi, J.-M.; Taima, T. The Benefits of Ionic Liquids for the Fabrication of Efficient and Stable Perovskite Photovoltaics. *Chemical Engineering Journal* **2021**, *411*, 128461.

[39] Sun, P.; Armstrong, D. W. Ionic Liquids in Analytical Chemistry. *Analytica Chimica Acta* **2010**, *661* (1), 1–16.

[40] Borghi, F.; Podestà, A. Ionic Liquids under Nanoscale Confinement. *Advances in Physics: X* **2020**, *5* (1), 1736949.

[41] Calandra, P.; Szerb, E. I.; Lombardo, D.; Algieri, V.; De Nino, A.; Maiuolo, L. A Presentation of Ionic Liquids as Lubricants: Some Critical Comments. *Applied Sciences* **2021**, *11* (12), 5677.

[42] Yoo, E.; Kim, J.; Hosono, E.; Zhou, H.; Kudo, T.; Honma, I. Large Reversible Li Storage of Graphene Nanosheet Families for Use in Rechargeable Lithium Ion Batteries. *Nano Letters* **2008**, *8* (8), 2277–2282.

[43] Erto, A.; Silvestre-Albero, A.; Silvestre-Albero, J.; Rodríguez-Reinoso, F.; Balsamo, M.; Lancia, A.; Montagnaro, F. Carbon-Supported Ionic Liquids as Innovative Adsorbents for CO_2 Separation from Synthetic Flue-Gas. *Journal of Colloid and Interface Science* **2015**, *448*, 41–50.

[44] Benelmekki, M.; Erbe, A. Nanostructured Thin Films–Background, Preparation and Relation to the Technological Revolution of the 21st Century. *Frontiers of Nanoscience* **2019**, 1–34.

[45] *Techniques - Thin Film | Core Facilities*. cores.research.asu.edu. https://cores.research.asu.edu/nanofabrication-and-cleanroom/techniques-thin-film (accessed 2023-02).

[46] Costa, J. C. S. Estudo Termodinâmico E Morfológico de Materiais Semicondutores Orgânicos. PhD Thesis, Faculdade de Ciências da Universidade do Porto, 2015.

[47] Kafle, B. P. Introduction to Nanomaterials and Application of UV–Visible Spectroscopy for Their Characterization. *Chemical Analysis and Material Characterization by Spectrophotometry* **2020**, 147–198.

[48] Cremer, T.; Stark, M.; Alexey Deyko; Hans-Peter Steinrück; Maier, F. Liquid/Solid Interface of Ultrathin Ionic Liquid Films: $[c_1c_1Im][Tf_2N]$ and $[c_8c_1Im][Tf_2N]$ on Au(111). *Langmuir* **2011**, *27* (7), 3662–3671.

[49] Comsol. *The Joule Heating Effect*. www.comsol.com. https://www.comsol.com/multiphysics/the-joule-heating-effect (accessed 2023-06-15).

[50] *How does molecular beam epitaxy work?* Explain that Stuff. https://www.explainthatstuff.com/molecular-beam-epitaxy-introduction.html (accessed 2023-02).

[51] Alavi, K. Molecular Beam Epitaxy. *Encyclopedia of Materials: Science and Technology* **2001**, 5765–5780.

[52] Ptak, A. J. Principles of Molecular Beam Epitaxy. *Elsevier eBooks* **2015**, 161–192.

[53] Hansen, D. M.; Kuech, T. F. Epitaxial Technology for Integrated Circuit Manufacturing. *Elsevier eBooks* **2003**, 641–652. https://doi.org/10.1016/b0-12-227410-5/00232-5.

[54] Floro, J. A.; Hearne, S. M.; Hunter, J. A.; Kotula, P. G.; Chason, E.; Seel, S. C.; Thompson, C. V. The Dynamic Competition between Stress Generation and Relaxation Mechanisms during Coalescence of Volmer–Weber Thin Films. *Journal of Applied Physics* **2001**, *89* (9), 4886–4897.

[55] Martin, P. M. *Handbook of Deposition Technologies for Films and Coatings*; William Andrew, 2009.

[56] *What Is Sputtering?* | *Sputtering Targets*. JX Nippon Mining & Metals. https://www.jx-nmm.com/english/products/sputtering/about_sputtering.html (accessed 2023-03).

[57] *Magnetron Sputtering Overview*. Angstrom Engineering. https://angstromengineering.com/tech/magnetron-sputtering/?msclkid=060d48d3c47c10628ca92b3f6059f26a&utm_source=bing&utm_medium=cpc&utm_campaign=s-magnetron-sputtering&utm_term=Sputtering&utm_content=Sputtering (accessed 2023-02).

[58] Hughes, M. *Thin Film Deposition By Sputtering: Essential Basics*. Semicore Equipment Inc. https://www.semicore.com/news/70-thin-film-deposition-sputtering (accessed 2023-02).

[59] *Atomic Layer Deposition* | *Argonne National Laboratory*. www.anl.gov. https://www.anl.gov/amd/atomic-layer-deposition (accessed 2023-02).

[60] Song, S.; M. Michael Yovanovich. Correlation of Thermal Accommodation Coefficient for “Engineering” Surfaces. *IN: Fundamentals of conduction and recent developments in contact resistance; Proceedings of the Twenty-fourth National Heat Transfer Conference and Exhibition* **1987**, 107–116.

[61] Venables, J. A.; Spiller, G. D. T.; Hanbucken, M. Nucleation and Growth of Thin Films. *Reports on Progress in Physics* **1984**, *47* (4), 399–459.

[62] Costa, J. C. S.; Coelho, A. F. S. M. G.; Mendes, A.; Santos, L. M. N. B. F. Nucleation and Growth of Microdroplets of Ionic Liquids Deposited by Physical Vapor Method onto Different Surfaces. *Applied Surface Science* **2018**, *428*, 242–249.

[63] Greene, J. E. Thin Film Nucleation, Growth, and Microstructural Evolution. *Elsevier eBooks* **2010**, 554–620.

[64] Teixeira, M. S. M.; Santos, L. M. N. B. F.; Costa, J. C. S. Nucleation, Coalescence, and Thin-Film Growth of Triflate-Based Ionic Liquids on ITO, Ag, and Au Surfaces. *Colloids and Interfaces* **2022**, *6* (3), 46.

[65] Ratsch, C.; Venables, J. A. Nucleation Theory and the Early Stages of Thin Film Growth. *Journal of Vacuum Science & Technology A: Vacuum, Surfaces, and Films* **2003**, *21* (5), S96–S109.

[66] Richey, N. E.; de Paula, C.; Bent, S. F. Understanding Chemical and Physical Mechanisms in Atomic Layer Deposition. *The Journal of Chemical Physics* **2020**, *152* (4), 040902.

[67] Rietzler, F.; May, B.; Steinrück, H.-P.; Maier, F. Switching Adsorption and Growth Behavior of Ultrathin [C_2C_1im][OTf] Films on Au(111) by Pd Deposition. *Physical Chemistry Chemical Physics* **2016**, *18* (36), 25143–25150.

[68] Costa, J. C. S.; Rocha, R. M.; Vaz, I. C. M.; Torres, M. C.; Mendes, A.; Santos, L. M. N. B. F. Description and Test of a New Multilayer Thin Film Vapor Deposition Apparatus for Organic Semiconductor Materials. *Journal of Chemical & Engineering Data* **2015**, *60* (12), 3776–3791.

[69] Borghi, F.; Piazzoni, C.; Matteo Ghidelli; Milani, P.; Alessandro Podestà. Nanoconfinement of Ionic Liquid into Porous Carbon Electrodes. *Journal of Physical Chemistry C* **2021**, *125* (2), 1292–1303.

[70] Singh, M. P.; Singh, R. K.; Chandra, S. Ionic Liquids Confined in Porous Matrices: Physicochemical Properties and Applications. *Progress in Materials Science* **2014**, *64*, 73–120.

[71] Comtet, J.; Niguès, A.; Kaiser, V.; Benoit Coasne; Lydéric Bocquet; Siria, A. Nanoscale Capillary Freezing of Ionic Liquids Confined between Metallic Interfaces and the Role of Electronic Screening. *Nature Materials* **2017**, *16* (6), 634–639.

[72] Wei, J.-F.; Jiao, J.; Feng, J.-J.; Lv, J.; Zhang, X.-R.; Shi, X.-Y.; Chen, Z.-G. PdEDTA Held in an Ionic Liquid Brush as a Highly Efficient and Reusable Catalyst for Suzuki Reactions in Water. *The Journal of Organic Chemistry* **2009**, *74* (16), 6283–6286.

[73] Alba-Simionesco, C.; Coasne, B.; Dosseh, G.; Dudziak, G.; Gubbins, K. E.; Radhakrishnan, R.; Sliwinska-Bartkowiak, M. Effects of Confinement on Freezing and Melting. *Journal of Physics: Condensed Matter* **2006**, *18* (6), R15–R68.

[74] Hartland, S. *Surface and Interfacial Tension*; CRC Press, 2004.

[75] Berry, J. D.; Neeson, M. J.; Dagastine, R. R.; Chan, D. Y. C.; Tabor, R. F. Measurement of Surface and Interfacial Tension Using Pendant Drop Tensiometry. *Journal of Colloid and Interface Science* **2015**, *454*, 226–237.

[76] Birdi, K. S. *Handbook of Surface and Colloid Chemistry*; CRC Press, 2002.

[77] Kolleboyina Jayaramulu; Geyer, F.; Schneemann, A.; Kment, S.; Otyepka, M.; Zboril, R.; Vollmer, D.; Fischer, R. A. Hydrophobic Metal–Organic Frameworks. *Advanced Materials* **2019**, 1900820–1900820.

[78] Pereira, M. M.; Kurnia, K. A.; Sousa, F. L.; Silva, N. J. O.; Lopes-da-Silva, J. A.; Coutinho, J. A. P.; Freire, M. G. Contact Angles and Wettability of Ionic Liquids on Polar and Non-Polar Surfaces. *Physical chemistry chemical physics: PCCP* **2015**, *17* (47), 31653–31661.

[79] Tariq, M.; Freire, M. G.; Saramago, B.; Coutinho, J. A. P.; Lopes, J. N. C.; Rebelo, L. P. N. Surface Tension of Ionic Liquids and Ionic Liquid Solutions. *Chem. Soc. Rev.* **2012**, *41* (2), 829–868.

[80] Lexow, M.; Maier, F.; Steinrück, H.-P. Ultrathin Ionic Liquid Films on Metal Surfaces: Adsorption, Growth, Stability and Exchange Phenomena. *Advances in Physics: X* **2020**, *5* (1), 1761266.

[81] Costa, J. C. S.; Campos, R.; Castro, Â.; Farinha, A.; Nuno, G.; Araujo, J. P.; Santos, L. M. N. B. F. The Effect of Ionic Liquids on the Nucleation and Growth of Perylene Films Obtained by Vapor Deposition. *CrystEngComm* **2023**, *25* (6), 913–924.

[82] Campos, R. M.; Alves, A. C. P. M.; Lima, M. A. L.; Farinha, A. F. M.; Cardoso, J. P. S.; Mendes, A.; Costa, J. C. S.; Santos, L. M. N. B. F. Morphology, Structure, and Dynamics of Pentacene Thin Films and Their Nanocomposites with $[C_2C_1im][NTf_2]$ and $[C_2C_1Im][OTf]$ Ionic Liquids. *ChemPhysChem* **2020**, *21* (16), 1814–1825.

[83] Tariq, M.; Carvalho, P.; Coutinho, P.; Marrucho, I. M.; José Manuel Lopes; Paulo, L. Viscosity of (C2–C14) 1-Alkyl-3-Methylimidazolium Bis(Trifluoromethylsulfonyl)Amide

Ionic Liquids in an Extended Temperature Range. *Fluid Phase Equilibria* **2011**, *301* (1), 22–32.

[84] Rodrigues, A. S. M. C.; Santos, L. M. N. B. F., Nanostructuration Effect on the Thermal Behavior of Ionic Liquids. ChemPhysChem, 2016, 17 (10), 1512–1517.

[85] Krossing, I.; Slattery, J. M.; Daguenet, C.; Dyson, P. J.; Oleinikova, A.; Weingärtner, H. Why Are Ionic Liquids Liquid? A Simple Explanation Based on Lattice and Solvation Energies. *Journal of the American Chemical Society* **2006**, *128* (41), 13427–13434.

[86] Paulechka, Y. U.; Blokhin, A. V.; Kabo, G. J.; A.A. Strechan. Thermodynamic Properties and Polymorphism of 1-Alkyl-3-Methylimidazolium Bis(Triflamides). *The Journal of Chemical Thermodynamics* **2007**, *39* (6), 866–877.

[87] Carvalho, P.; Freire, M. G.; Marrucho, I. M.; Queimada, A. J.; Coutinho, P. Surface Tensions for the 1-Alkyl-3-Methylimidazolium Bis(Trifluoromethylsulfonyl)Imide Ionic Liquids. *Journal of Chemical & Engineering Data* **2008**, *53* (6), 1346–1350.

[88] Jaroslav Klomfar; Součková, M. Temperature Dependence Measurements of the Density at 0.1 MPa for 1-Alkyl-3-Methylimidazolium-Based Ionic Liquids with the Trifluoromethanesulfonate and Tetrafluoroborate Anion. *Journal of Chemical & Engineering Data* **2010**, *55* (9), 4054–4057.

[89] Every, H.; Bishop, A. G.; Forsyth, M.; MacFarlane, D. R. Ion Diffusion in Molten Salt Mixtures. *Electrochimica Acta* **2000**, *45* (8-9), 1279–1284.

[90] Nebig, S.; Gmehling, J. Measurements of Different Thermodynamic Properties of Systems Containing Ionic Liquids and Correlation of These Properties Using Modified UNIFAC (Dortmund). *Fluid Phase Equilibria* **2010**, *294* (1-2), 206–212.

[91]Diejomaoh Abafe, O. T.; Azim, M. M.; Martincigh, B. S.; Stark, A. Cation-Fluorinated Ionic Liquids: Synthesis, Physicochemical Properties and Comparison with Non-Fluorinated Analogues. *Journal of Molecular Liquids* **2022**, *349*, 118104.

[92] Anwar, N.; Riyazuddeen. Excess Molar Volumes, Excess Molar Isentropic Compressibilities, Viscosity Deviations, and Activation Parameters for 1-Ethyl-3-Methyl-Imidazolium Trifluoro-Methanesulfonate + Dimethyl Sulfoxide And/or Acetonitrile at T = 298.15 to 323.15 K and P = 0.1 MPa. *Journal of Chemical & Engineering Data* **2018**, *63* (2), 269–289.

[93] Santos, L. M. N. B. F; Lobo Ferreira, A. I. M. C.; Vojtěch Štejfa; Lúcia, A. S. M. C.; Rocha, M: A. A.; Torres, M. C.; Tavares, F.M. S.; Francisco S. Carpinteiro. Development of the Knudsen Effusion Methodology for Vapour Pressure Measurements of Low Volatile Liquids and Solids Based on a Quartz Crystal Microbalance. *The Journal of Chemical Thermodynamics* **2018**, 126, 171–186*.*

[94] Santos, L. M. N. B. F.; Lima, L. M. S. S.; Lima, C. F. R. A. C.; Magalhães, F. D.; Torres, M. C.; Schröder, B.; Ribeiro da Silva, M. A. V. New Knudsen Effusion Apparatus with Simultaneous Gravimetric and Quartz Crystal Microbalance Mass Loss Detection J. Chem. Thermodyn. **2011**, 43, 834– 843

[95] Ribeiro da Silva, M. A. V.; Monte, M. J. S.; Santos, L. M. N. B. F. The Design, Construction, and Testing of a New Knudsen Effusion Apparatus J. Chem. Thermodyn. **2006**, 38, 778– 787

[96] Clausing, P., No Title. Ann. Phys., 1932, 404, 961–989

[97] Costa, J. C. S.; Mendes, A.; Santos, L. M. N. B. F. Morphology of Imidazolium-Based Ionic Liquids as Deposited by Vapor Deposition: Micro-/Nanodroplets and Thin Films. *ChemPhysChem* **2016**, *17* (14), 2123–2127.

[98]*Cressington 108 Auto Sputter Coater*. https://www.tedpella.com/cressington_html/Cressington-108-Auto-Sputter-Coater.aspx (accessed 2023-07-14).

[99] Davidson, M. W.; Abramowitz, M. Optical Microscopy. *Encyclopedia of Imaging Science and Technology* **2002**.

[100] Schädler, K. *An Introduction to the Light Microscope, Light Microscopy Techniques and Applications*. Analysis & Separations from Technology Networks. https://www.technologynetworks.com/analysis/articles/an-introduction-to-the-light-microscope-light-microscopy-techniques-and-applications-351924 (accessed 2023-05).

[101] Mohammed, A., & Abdullah, A. (2018, November). Scanning electron microscopy (SEM): A review. In *Proceedings of the 2018 International Conference on Hydraulics and Pneumatics—HERVEX, Băile Govora, Romania* (Vol. 2018, pp. 7-9).

[102] Schneider, C. A.; Rasband, W. S.; Eliceiri, K. W. NIH Image to ImageJ: 25 Years of Image Analysis. Nature Methods 2012, 9 (7), 671–675.

[103] Soon Wee Ho. A Review on Thin Films on Indium Tin Oxide Coated Glass Substrate. *Asian Journal of Chemistry* **2016**, *28* (3), 469–472.

[104] *ITO coatings | Indium Tin Oxide coated high-quality glass*. www.pgo-online.com. https://www.pgo-online.com/intl/ito.html (accessed 2023-05).

[105] Vashist, S. K.; Vashist, P. Recent Advances in Quartz Crystal Microbalance-Based Sensors. *Journal of Sensors* **2011**, *2011*, 1–13.

[106] Zaitsau, D.H.; Topp, A.; Siegesmund, A.; Papcke, A.; Kockerling, M.; Verevkin, S.P. In the Footsteps of August Michaelis: Syntheses and Thermodynamics of Extremely Low-Volatile Ionic Liquids. ChemistryOpen 2021, 10, 243–247.

[107] Maruyama, S.; Takeyama, Y.; Taniguchi, H.; Fukumoto, H.; Itoh, M.; Hiroshi Kumigashira; Oshima, M.; Yamamoto, T.; Matsumoto, Y. Molecular Beam Deposition of Nanoscale Ionic Liquids in Ultrahigh Vacuum. American Chemical Society 2010, 4 (10), 5946–5952.

[108] Carvalho, R. M.; Neto, C.; Santos, L. M. N. B. F.; Bastos, M.; Costa, J. C. S. Influence of the Deposition Rate and Substrate Temperature on the Morphology of Thermally Evaporated Ionic Liquids. Fluids 2023, 8 (3), 105.

[109] Deyko, A.; Cremer, T.; Rietzler, F.; Perkin, S.; Crowhurst, L.; Welton, T.; Steinrück, H.-P.; Maier, F. Interfacial Behavior of Thin Ionic Liquid Films on Mica. *The Journal of Physical Chemistry C* **2013**, *117* (10), 5101–5111.

[110] Lockett, V.; Sedev, R.; Bassell, C.; Ralston, J. Angle-Resolved X-Ray Photoelectron Spectroscopy of the Surface of Imidazolium Ionic Liquids. *Physical Chemistry Chemical Physics* **2008**, *10* (9), 1330.

Attachments

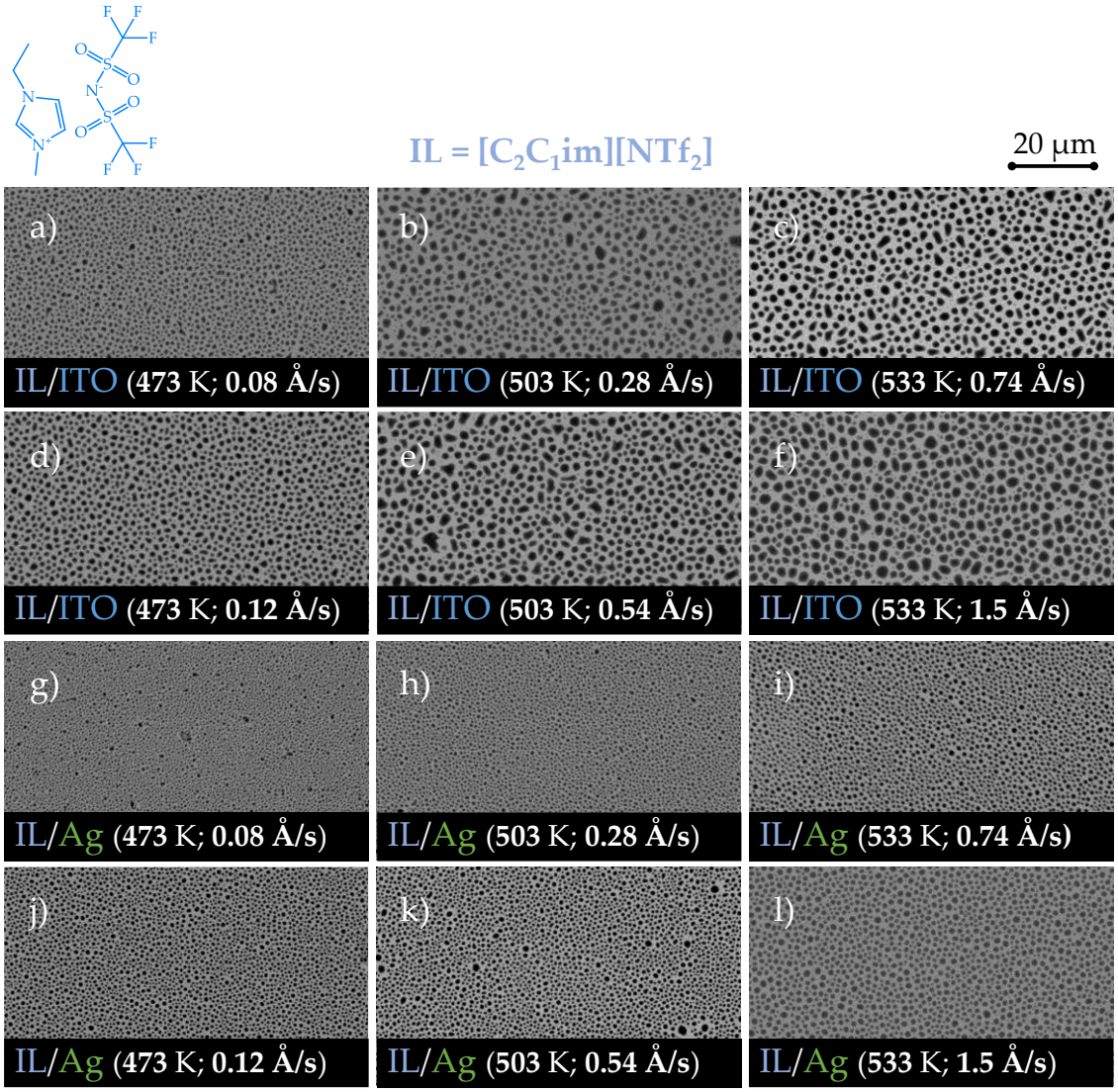

Figure A1. Micro-/nanodroplets morphology of $[C_2C_1im][NTf_2]$ (with a thickness of 40 ML) obtained through vacuum thermal evaporation onto ITO/glass (a, b, c, d, e, f) and Ag/ITO/glass (g, h, i, j, k, l) using Knudsen effusion cells with different orifice diameters (2.1 or 3.1 mm) and employing distinct evaporation temperatures (473, 503, or 533 K): 2.1 mm, 473 K (a, g); 3.1 mm, 473 K (d, j); 2.1 mm, 503 K (b, h); 3.1 mm, 503 K (e, k); 2.1 mm, 533 K (c, i); 3.1 mm, 533 K (f, l). The average surface coverage (SC) of the microdroplets was determined through image processing of the SEM micrographs (images a to l). The SC values obtained were (34.1 ± 3.6) % for IL films deposited on ITO surfaces and (34.0 ± 1.3) % for IL films deposited

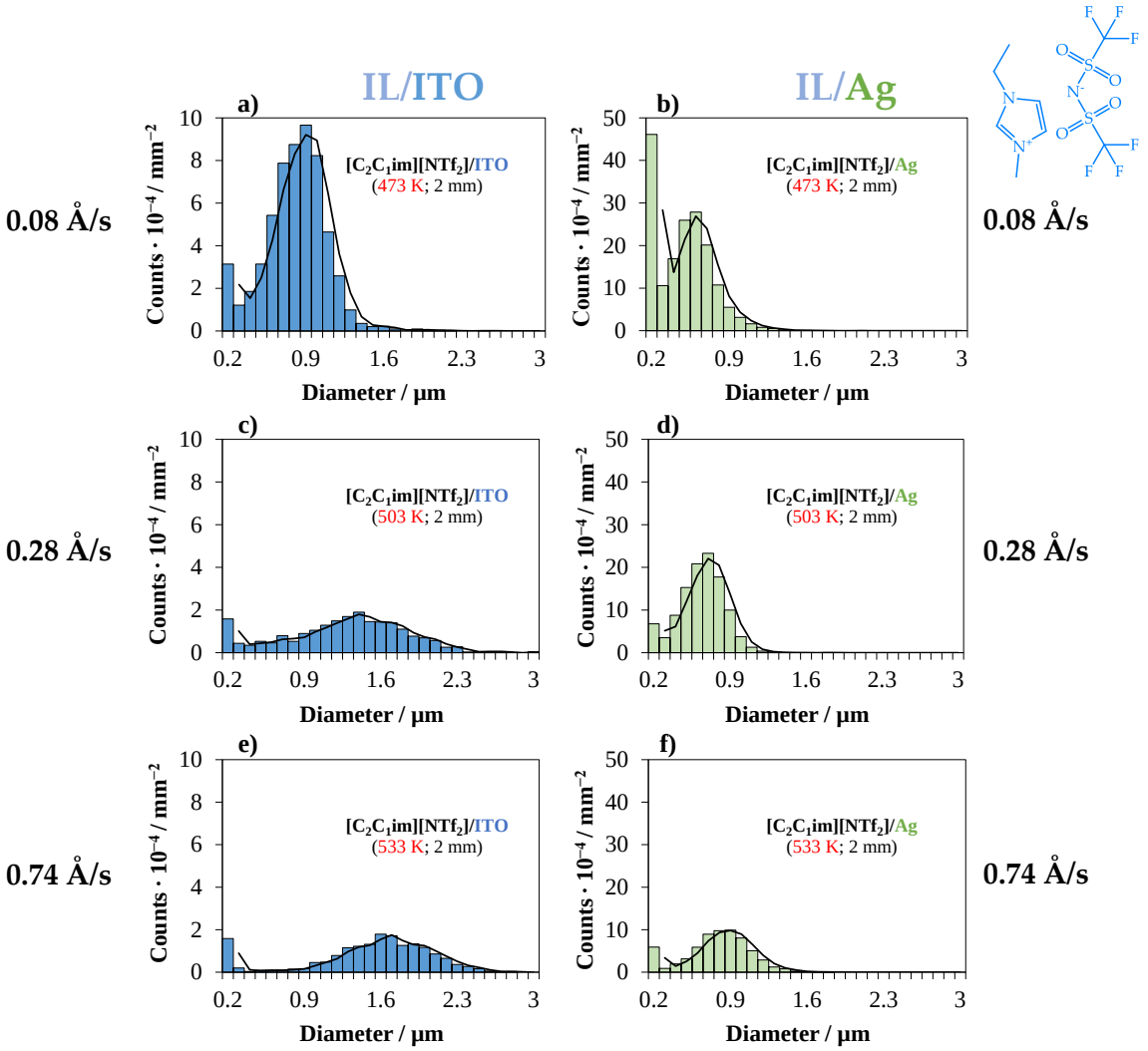

Figure A2. Size distribution of micro-/nanodroplets of $[C_2C_1im][NTf_2]$ (40 ML) obtained through vacuum thermal evaporation onto ITO/glass (a, c, e) and Ag/ITO/glass (b, d, f) using a Knudsen effusion cell (orifice diameter of 2.1 mm) and employing different evaporation temperatures/different deposition rates: 473 K (a, b); 503 K (c, d); 533 K (e, f). The substrate temperature was maintained at 283 K.

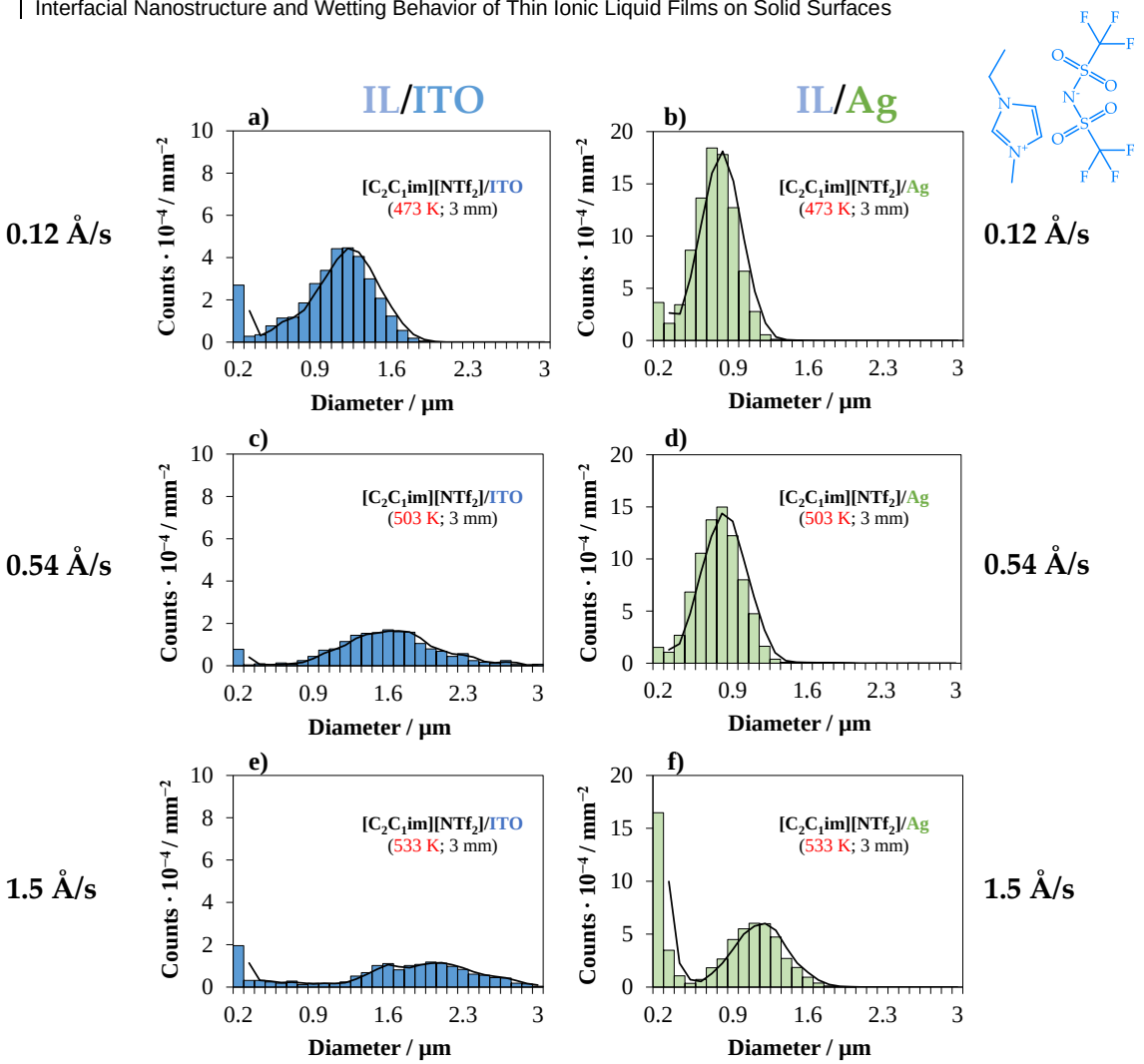

Figure A3. Size distribution of micro-/nanodroplets of $[C_2C_1im][NTf_2]$ (40 ML) obtained through vacuum thermal evaporation onto ITO/glass (a, c, e) and Ag/ITO/glass (b, d, f) using a Knudsen effusion cell (orifice diameter of 3.1 mm) and employing different evaporation temperatures/different deposition rates: 473 K (a, b); 503 K (c, d); 533 K (e, f). The substrate temperature was maintained at 283 K.

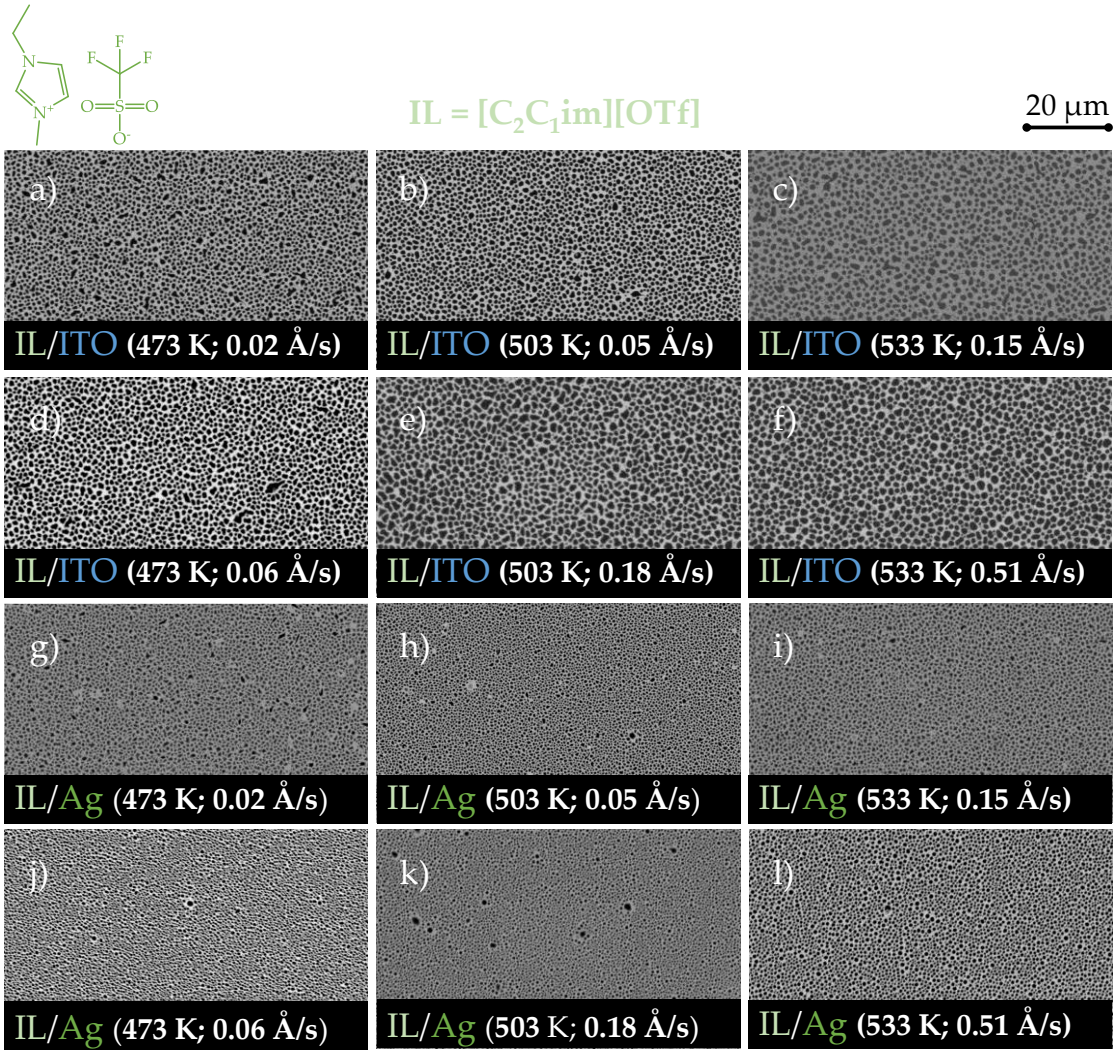

Figure A4. Micro-/nanodroplets morphology of $[C_2C_1im][OTf]$ (with a thickness of 40 ML) obtained through vacuum thermal evaporation onto ITO/glass (a, b, c, d, e, f) and Ag/ITO/glass (g, h, i, j, k, l) using Knudsen effusion cells with different orifice diameters (2.1 or 3.1 mm) and employing distinct evaporation temperatures (473, 503, or 533 K): 2.1 mm, 473 K (a, g); 3.1 mm, 473 K (d, j); 2.1 mm, 503 K (b, h); 3.1 mm, 503 K (e, k); 2.1 mm, 533 K (c, i); 3.1 mm, 533 K (f, l). The average surface coverage (SC) of the microdroplets was determined through image processing of the SEM micrographs (images a to l). The SC values obtained were (43.9 ± 3.6) % for IL films deposited on ITO surfaces and (38.9 ± 1.6) % for IL films deposited on Ag surfaces. The substrate temperature was maintained at 283 K. SEM micrographs (top views) were obtained by backscattered electron imaging (BSE).

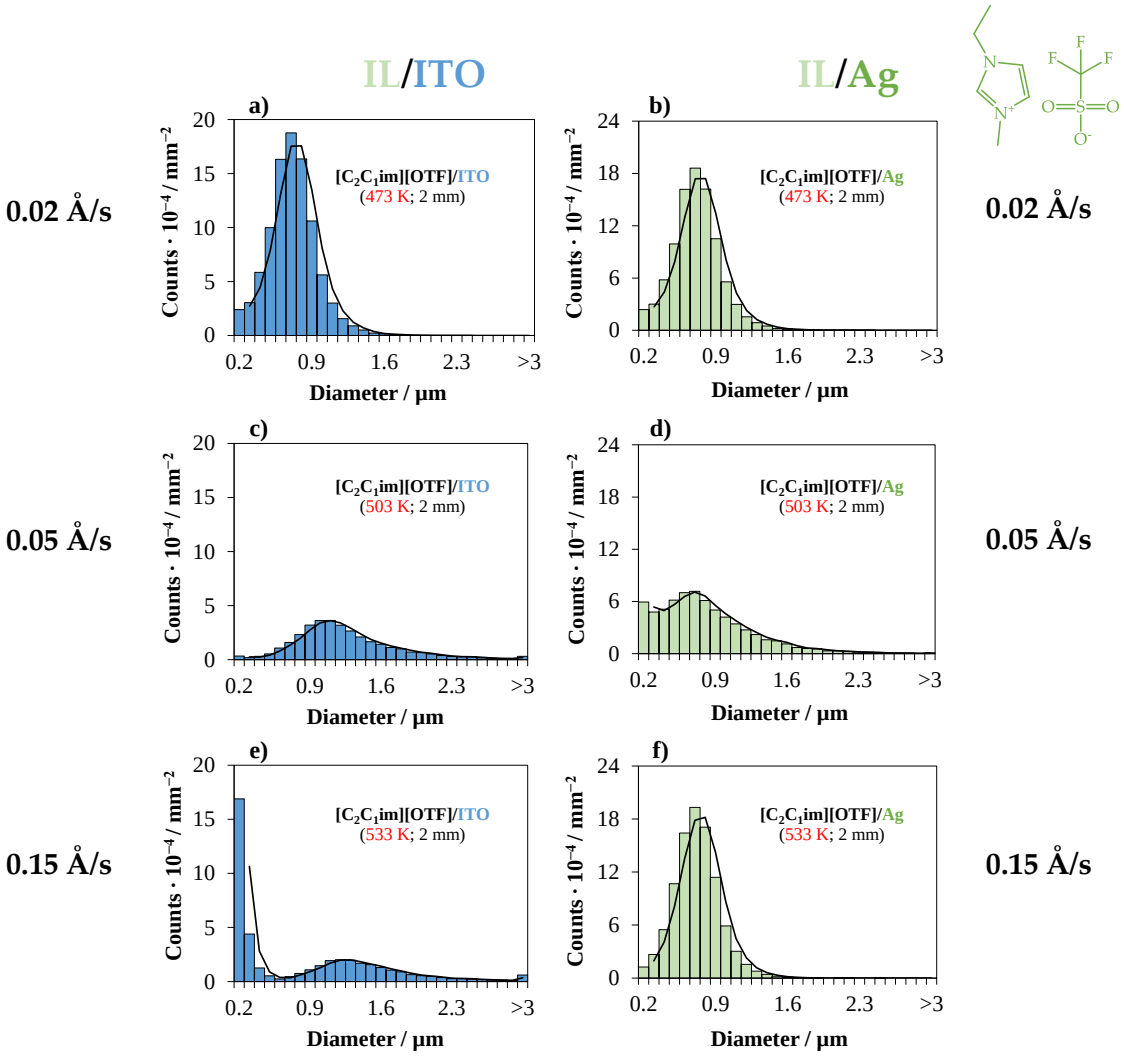

Figure A5. Size distribution of micro-/nanodroplets of [C_2C_1im][OTf] (40 ML) obtained through vacuum thermal evaporation onto ITO/glass (a, c, e) and Ag/ITO/glass (b, d, f) using a Knudsen effusion cell (orifice diameter of 2.1 mm) and employing different evaporation temperatures/different deposition rates: 473 K (a, b); 503 K (c, d); 533 K (e, f). The substrate temperature was maintained at 283 K.

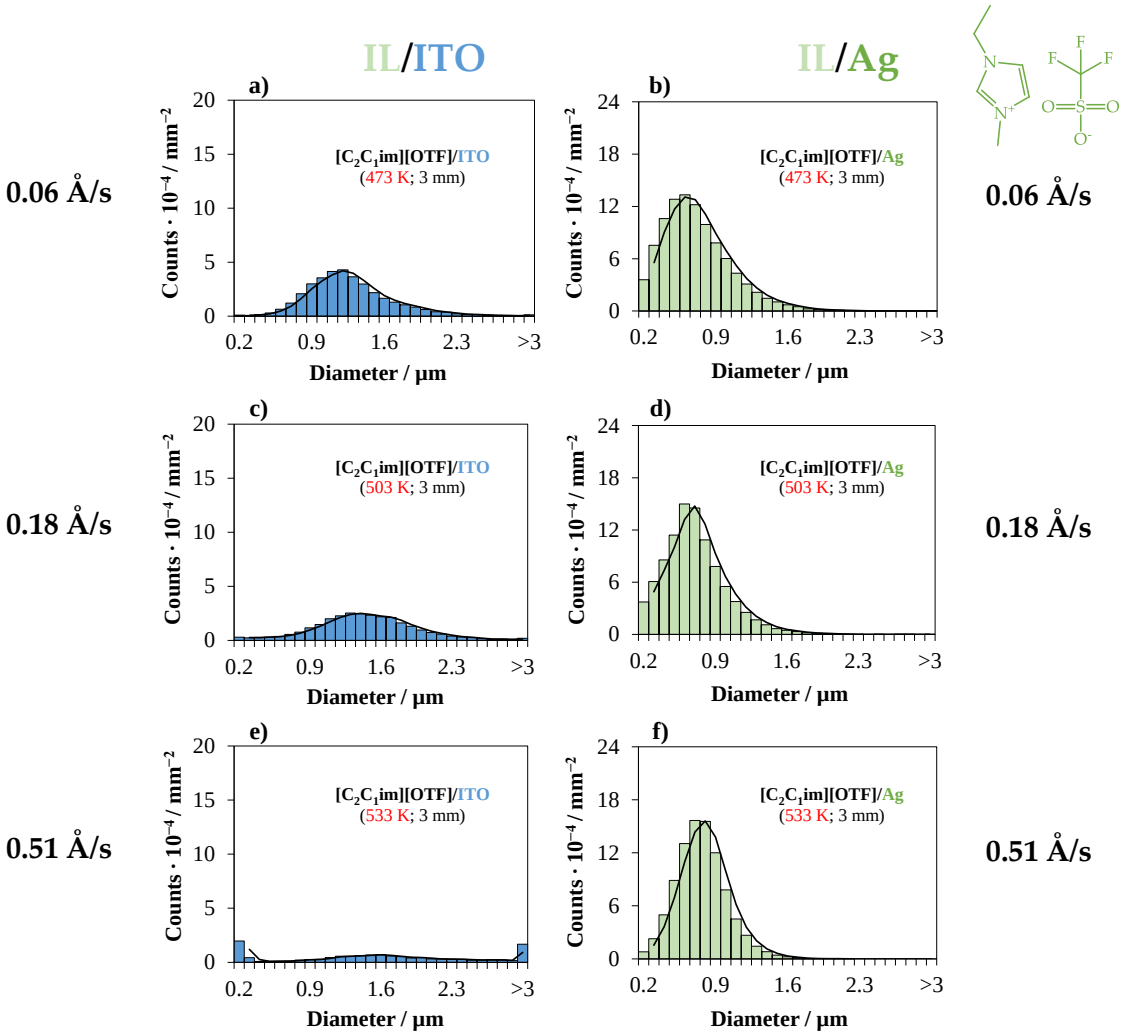

Figure A6. Size distribution of micro-/nanodroplets of $[C_2C_1im][NTf_2]$ (40 ML) obtained through vacuum thermal evaporation onto ITO/glass (a, c, e) and Ag/ITO/glass (b, d, f) using a Knudsen effusion cell (orifice diameter of 3.1 mm) and employing different evaporation temperatures/different deposition rates: 473 K (a, b); 503 K (c, d); 533 K (e, f). The substrate temperature was maintained at 283 K.

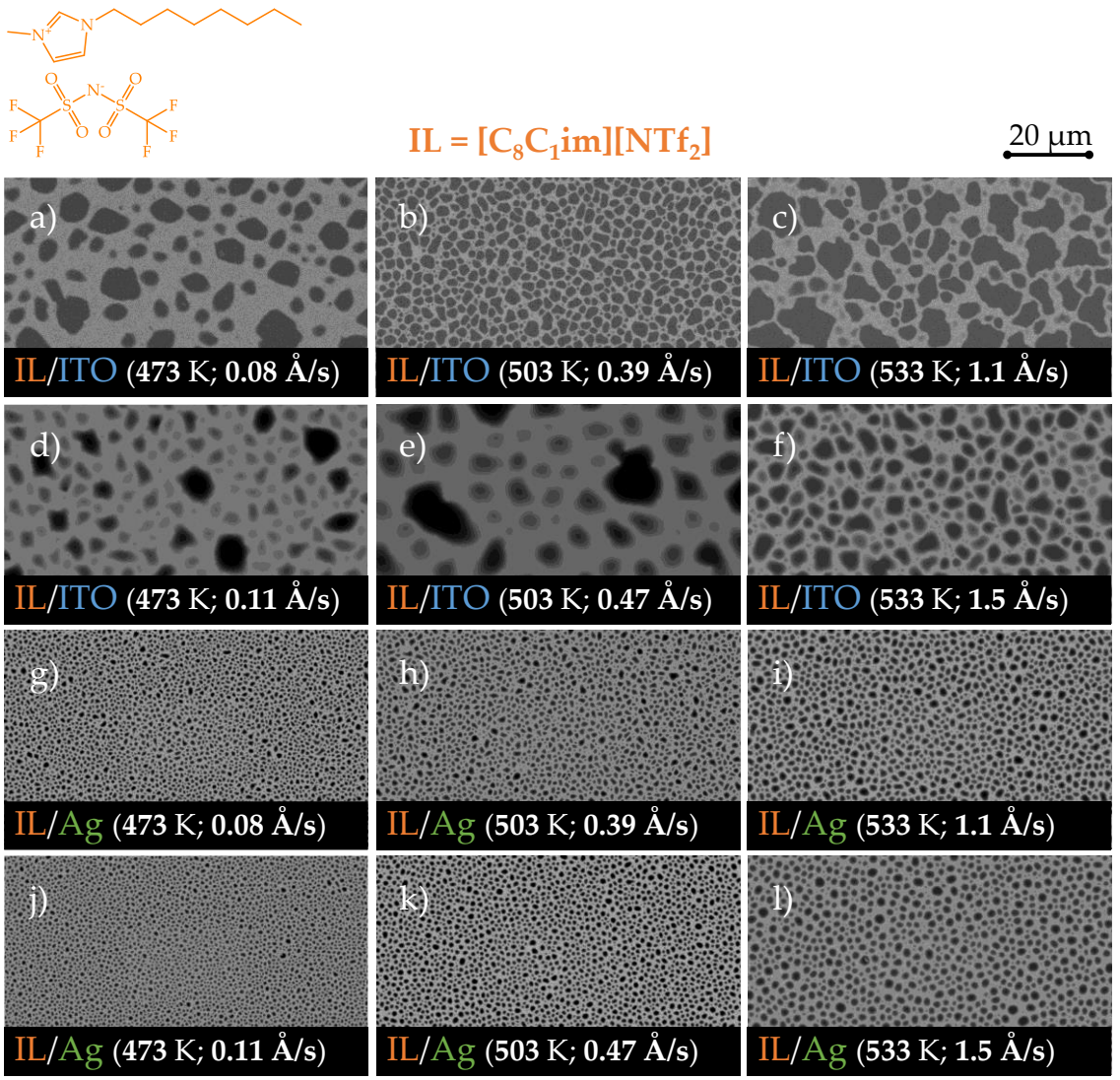

Figure A7. Micro-/nanodroplets morphology of $[C_8C_1im][NTf_2]$ (with a thickness of 40 ML) obtained through vacuum thermal evaporation onto ITO/glass (a, b, c, d, e, f) and Ag/ITO/glass (g, h, i, j, k, l) using Knudsen effusion cells with different orifice diameters (2.1 or 3.1 mm) and employing distinct evaporation temperatures (473, 503, or 533 K): 2.1 mm, 473 K (a, g); 3.1 mm, 473 K (d, j); 2.1 mm, 503 K (b, h); 3.1 mm, 503 K (e, k); 2.1 mm, 533 K (c, i); 3.1 mm, 533 K (f, l). The image processing did not accurately determine the surface coverage of the films, but it is estimated to be higher than 40%. The substrate temperature was maintained at 283 K. SEM micrographs (top views) were obtained by backscattered electron imaging (BSE).

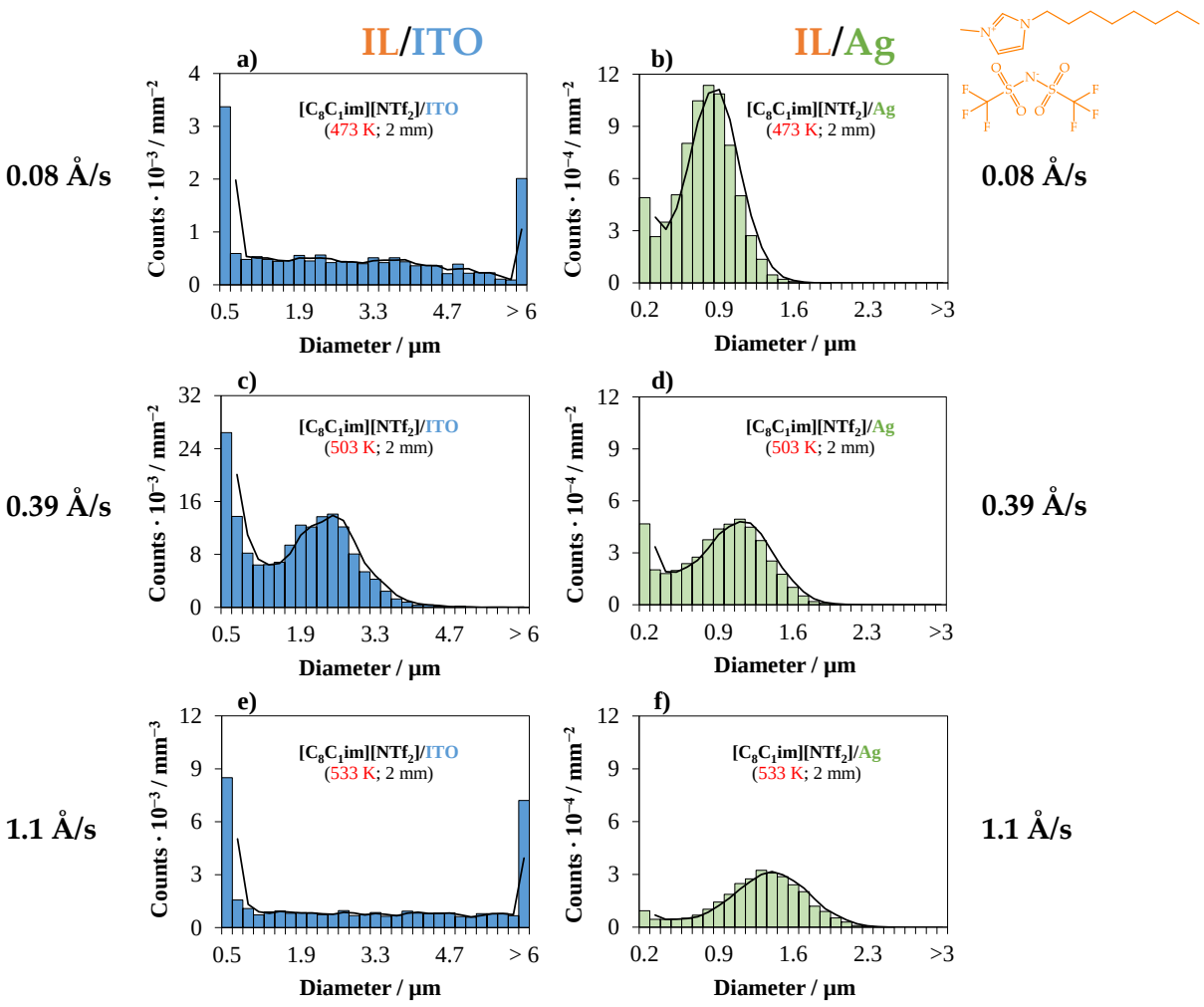

Figure A8. Size distribution of micro-/nanodroplets of $[C_8C_1im][NTf_2]$ (40 ML) obtained through vacuum thermal evaporation onto ITO/glass (a, c, e) and Ag/ITO/glass (b, d, f) using a Knudsen effusion cell (orifice diameter of 2.1 mm) and employing different evaporation temperatures/different deposition rates: 473 K (a, b); 503 K (c, d); 533 K (e, f). The substrate temperature was maintained at 283 K.

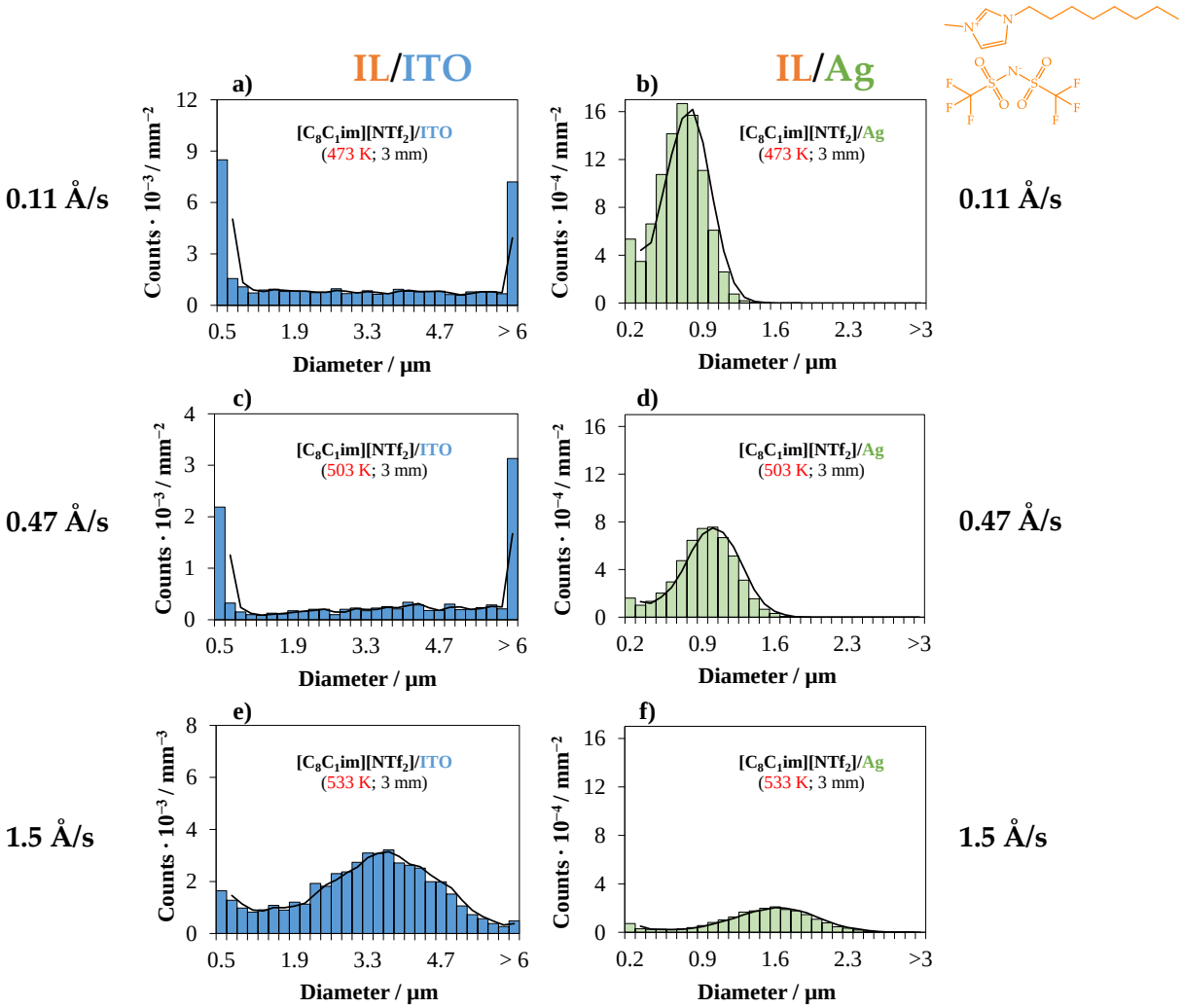

Figure A9. Size distribution of micro-/nanodroplets of $[C_8C_1im][NTf_2]$ (40 ML) obtained through vacuum thermal evaporation onto ITO/glass (a, c, e) and Ag/ITO/glass (b, d, f) using a Knudsen effusion cell (orifice diameter of 3.1 mm) and employing different evaporation temperatures/different deposition rates: 473 K (a, b); 503 K (c, d); 533 K (e, f). The substrate temperature was maintained at 283 K.

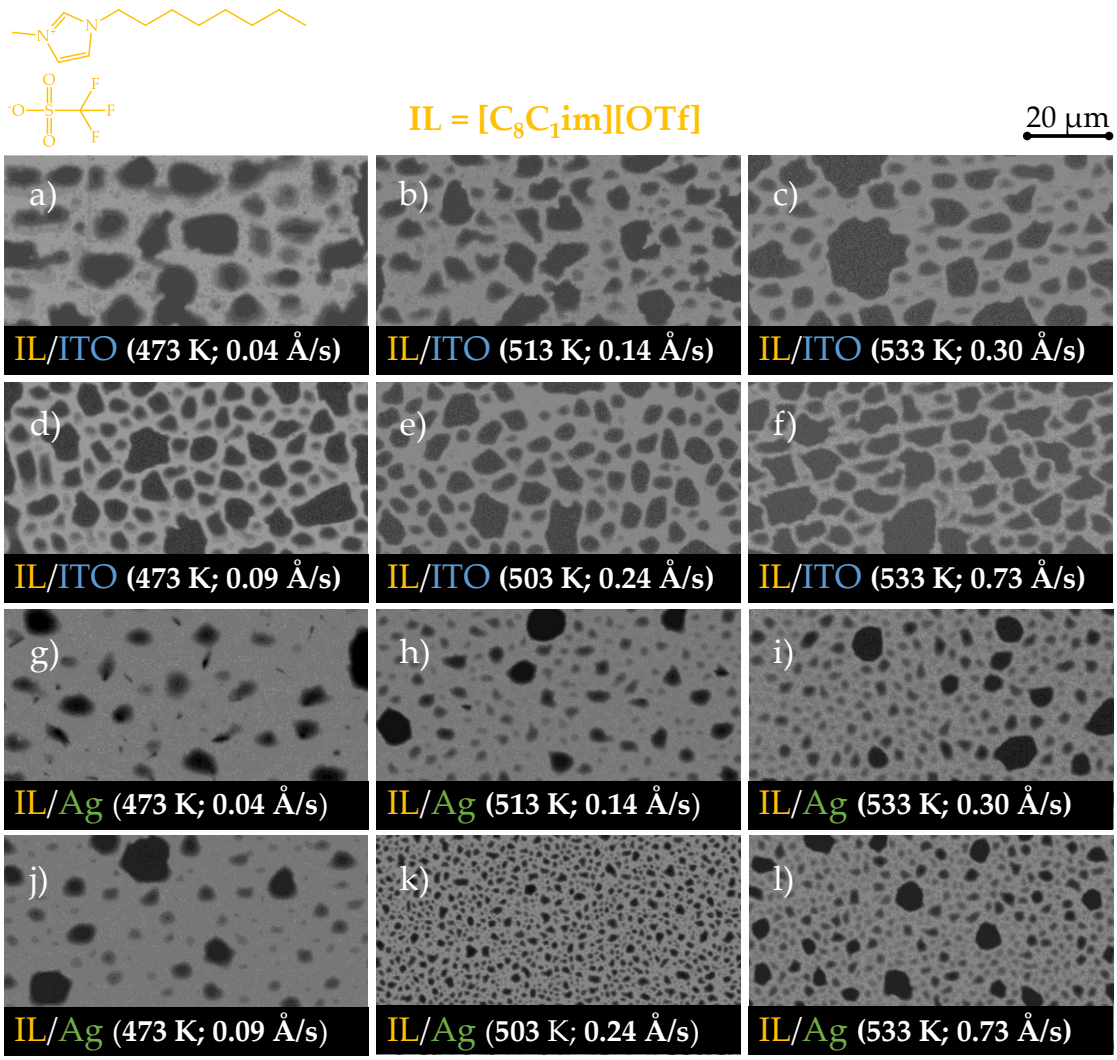

Figure A10. Micro-/nanodroplets morphology of $[C_8C_1im][OTf]$ (with a thickness of 40 ML) obtained through vacuum thermal evaporation onto ITO/glass (a, b, c, d, e, f) and Ag/ITO/glass (g, h, i, j, k, l) using Knudsen effusion cells with different orifice diameters (2.1 or 3.1 mm) and employing distinct evaporation temperatures (473, 503, or 533 K): 2.1 mm, 473 K (a, g); 3.1 mm, 473 K (d, j); 2.1 mm, 513 K (b, h); 3.1 mm, 503 K (e, k); 2.1 mm, 533 K (c, i); 3.1 mm, 533 K (f, l). The image processing did not accurately determine the surface coverage of the films, but it is estimated to be higher than 40%. The substrate temperature was maintained at 283 K. SEM micrographs (top views) were obtained by backscattered electron imaging (BSE).

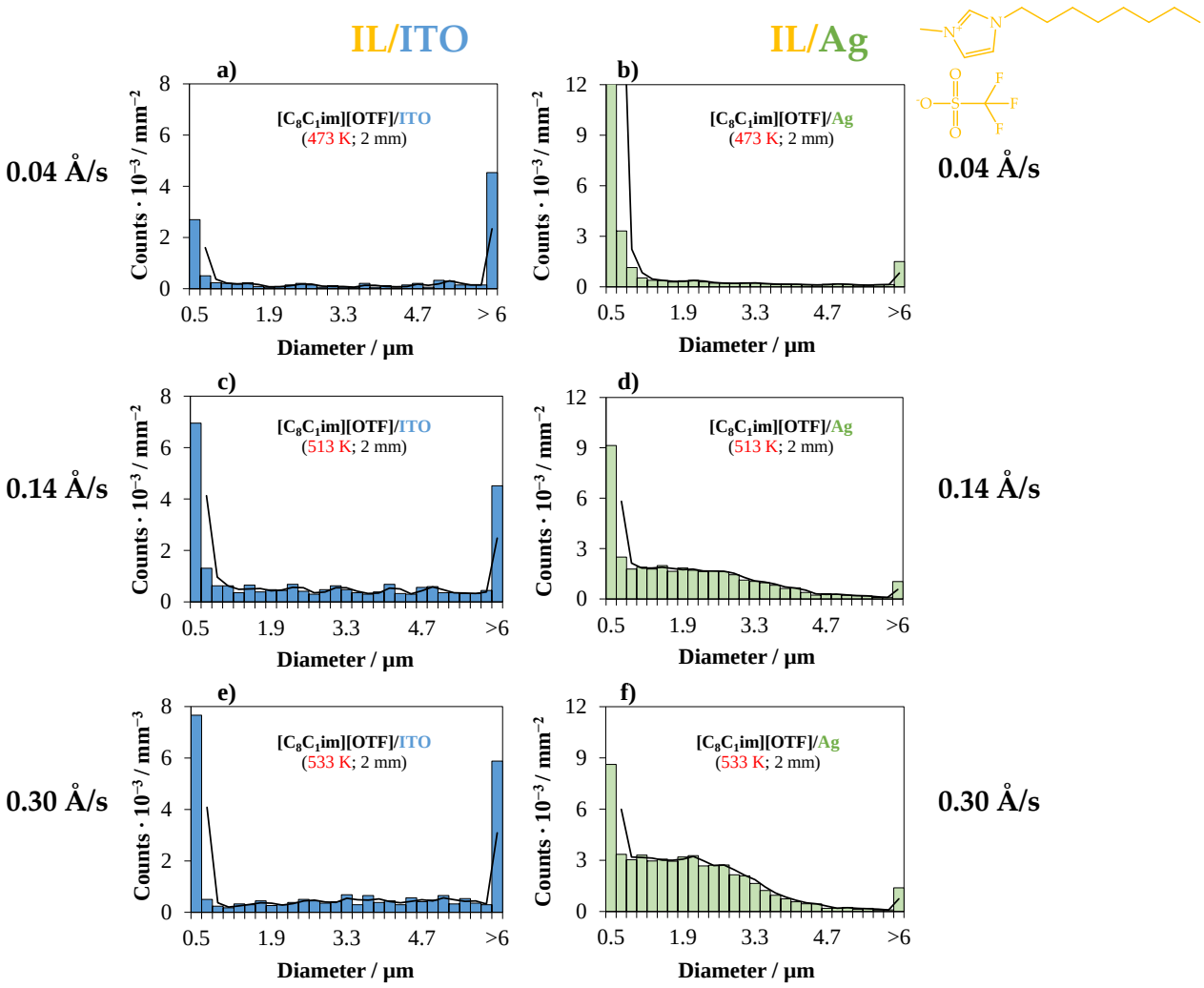

Figure A11. Size distribution of micro-/nanodroplets of $[C_8C_1im][OTf]$ (40 ML) obtained through vacuum thermal evaporation onto ITO/glass (a, c, e) and Ag/ITO/glass (b, d, f) using a Knudsen effusion cell (orifice diameter of 2.1 mm) and employing different evaporation temperatures/different deposition rates: 473 K (a, b); 513 K (c, d); 533 K (e, f). The substrate temperature was maintained at 283 K.

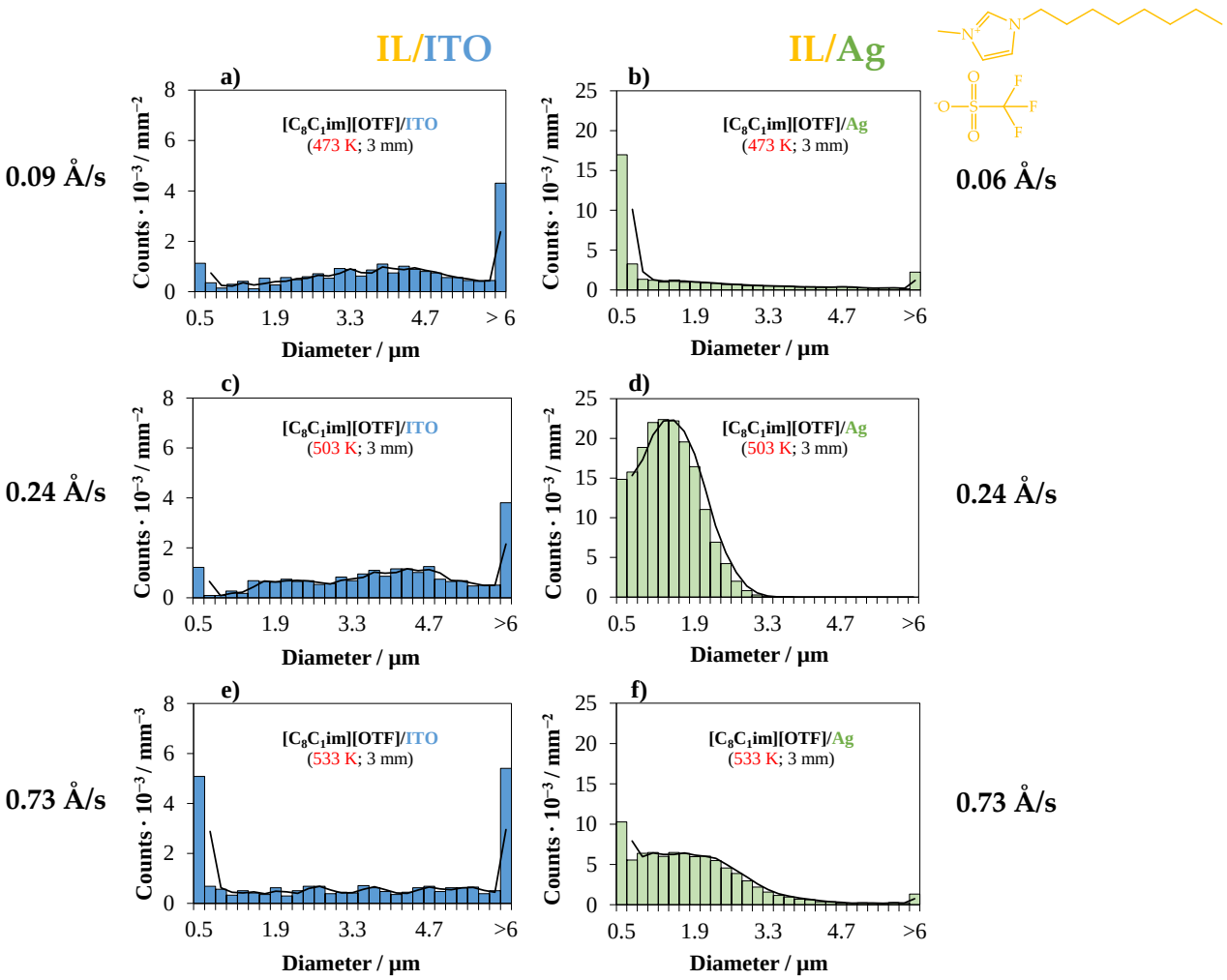

Figure A12. Size distribution of micro-/nanodroplets of $[C_8C_1im][OTf]$ (40 ML) obtained through vacuum thermal evaporation onto ITO/glass (a, c, e) and Ag/ITO/glass (b, d, f) using a Knudsen effusion cell (orifice diameter of 3.1 mm) and employing different evaporation temperatures/different deposition rates: 473 K (a, b); 503 K (c, d); 533 K (e, f). The substrate temperature was maintained at 283 K.

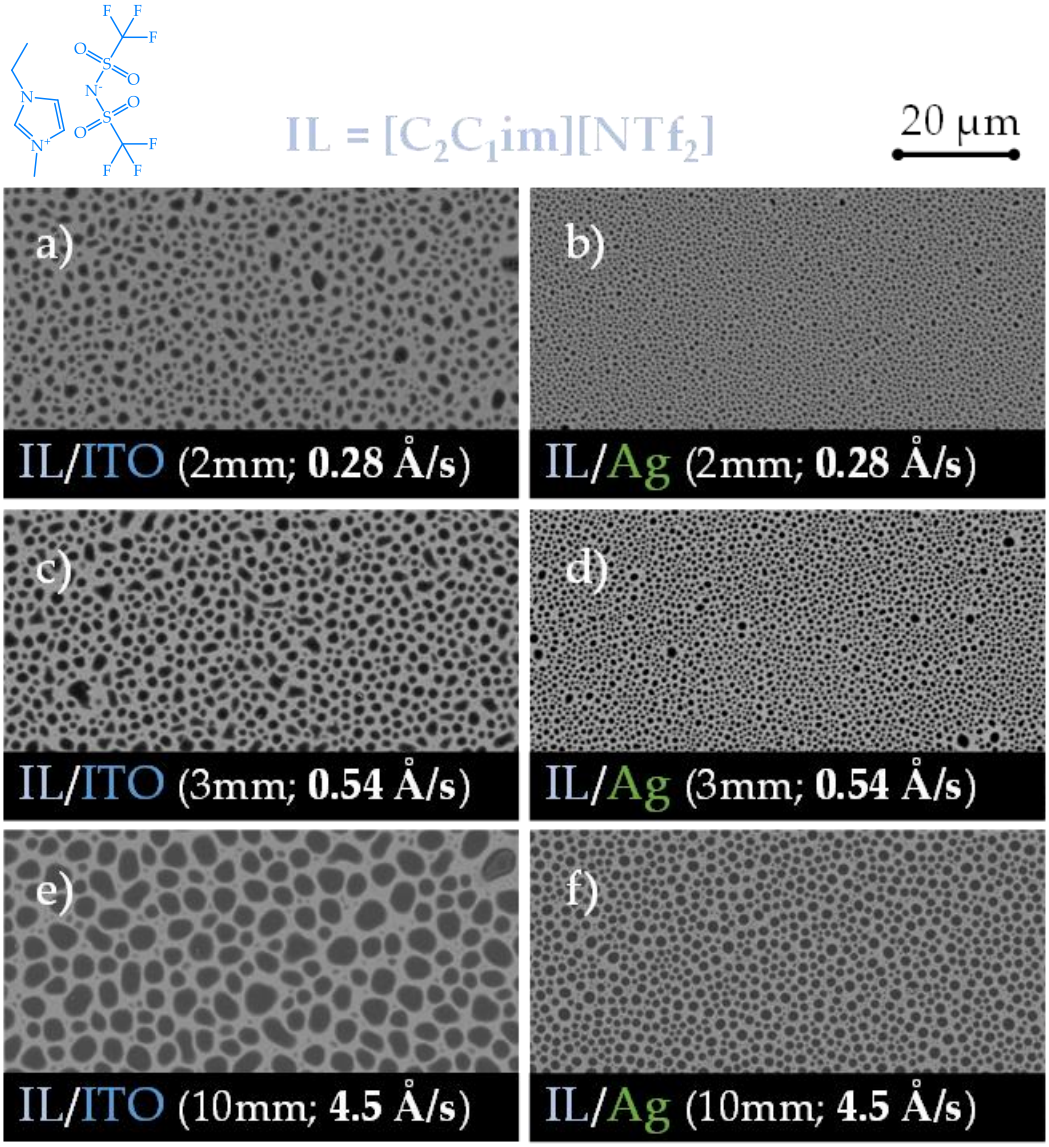

Figure A13. Micro-/nanodroplets morphology of $[C_2C_1im][NTf_2]$ (40 ML) obtained through vacuum thermal evaporation onto ITO/glass (a, c, e) and Ag/ITO/glass (b, d, f), maintaining an evaporation temperature of 503 K and using Knudsen effusion cells with different orifice diameters: 2.1 mm (a, b); 3.1 mm (c, d); no disk with orifice/evaporation done directly from the cell body (e, f). The substrate temperature was maintained at 283 K. Surface coverages of 30, 34, 36, 35, 46, and 43 % were derived by image processing of Figures a, b, c, d, e, and f, respectively. SEM micrographs (top views) obtained by backscattered electron imaging (BSE).

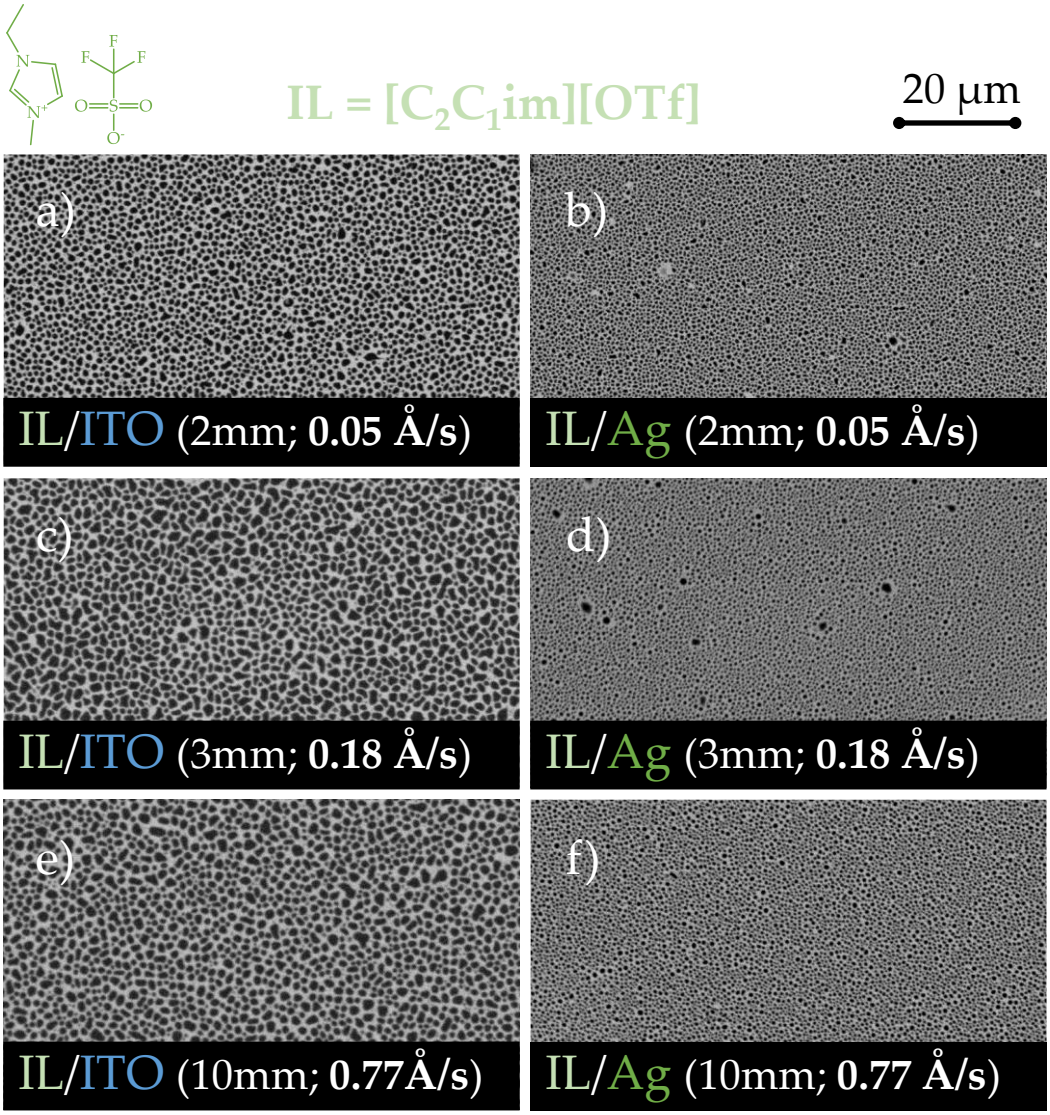

Figure A14. Micro-/nanodroplets morphology of $[C_2C_1im][OTf]$ (40 ML) obtained through vacuum thermal evaporation onto ITO/glass (a, c, e) and Ag/ITO/glass (b, d, f), maintaining an evaporation temperature of 503 K and 513 K, and using Knudsen effusion cells with different orifice diameters: 2.1 mm (a, b); 3.1 mm (c, d); no disk with orifice/evaporation done directly from the cell body (e, f). The substrate temperature was maintained at 283 K. Surface coverages of 46, 41, 49, 38, 46, and 39 % were derived by image processing of Figures a, b, c, d, e, and f, respectively. SEM micrographs (top views) obtained by backscattered electron imaging (BSE).

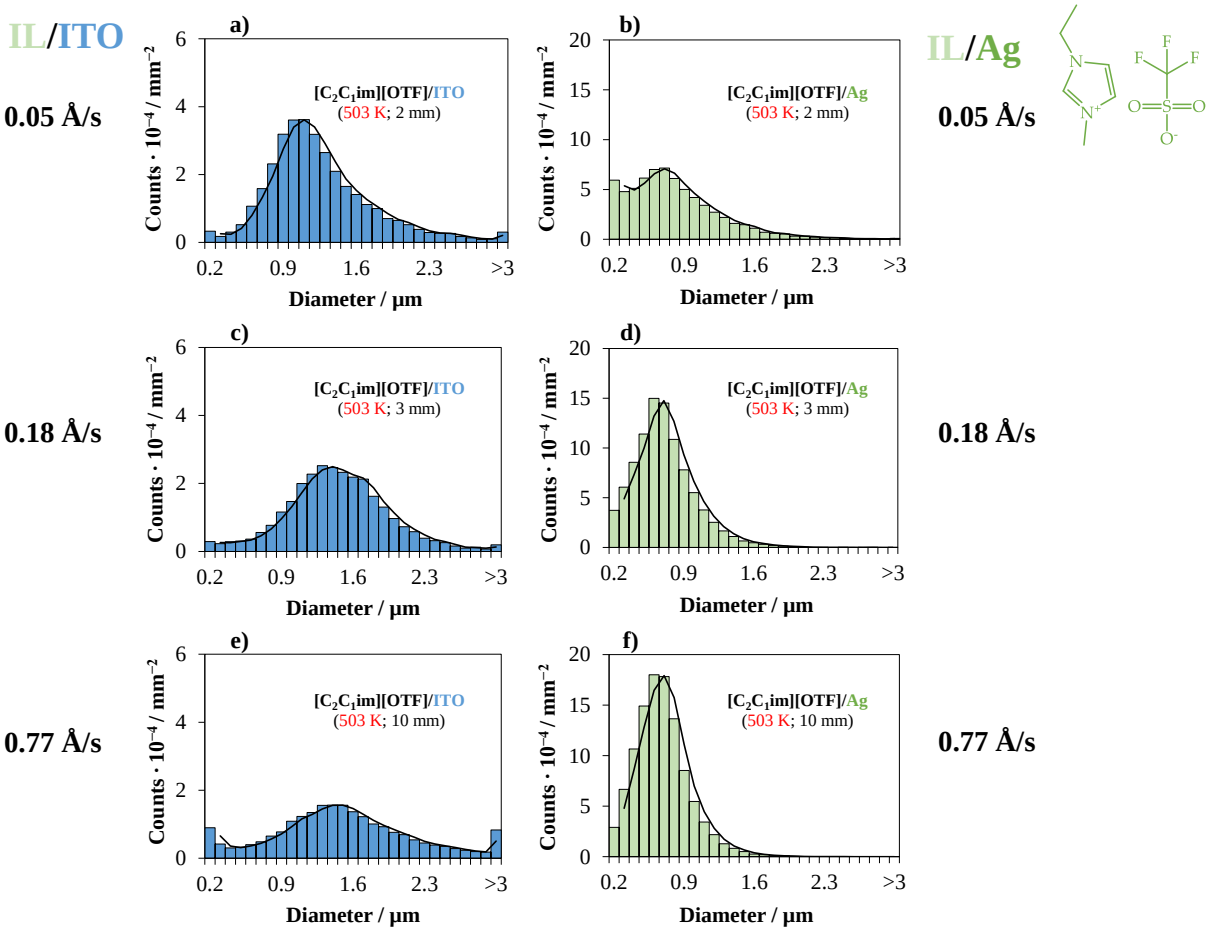

Figure A15. Size distribution of micro-/nanodroplets of [C_2C_1im][OTf] (40 ML) achieved through vacuum thermal evaporation onto ITO/glass (a, c, e) and Ag/ITO/glass (b, d, f) using a Knudsen effusion cell with different orifice diameters: 2.1 mm (a, b); 3.1 mm (c, d); no disk with orifice/evaporation done directly from the cell body (e, f) and employing an evaporation temperature of 503 K. The substrate temperature was maintained at 283 K.

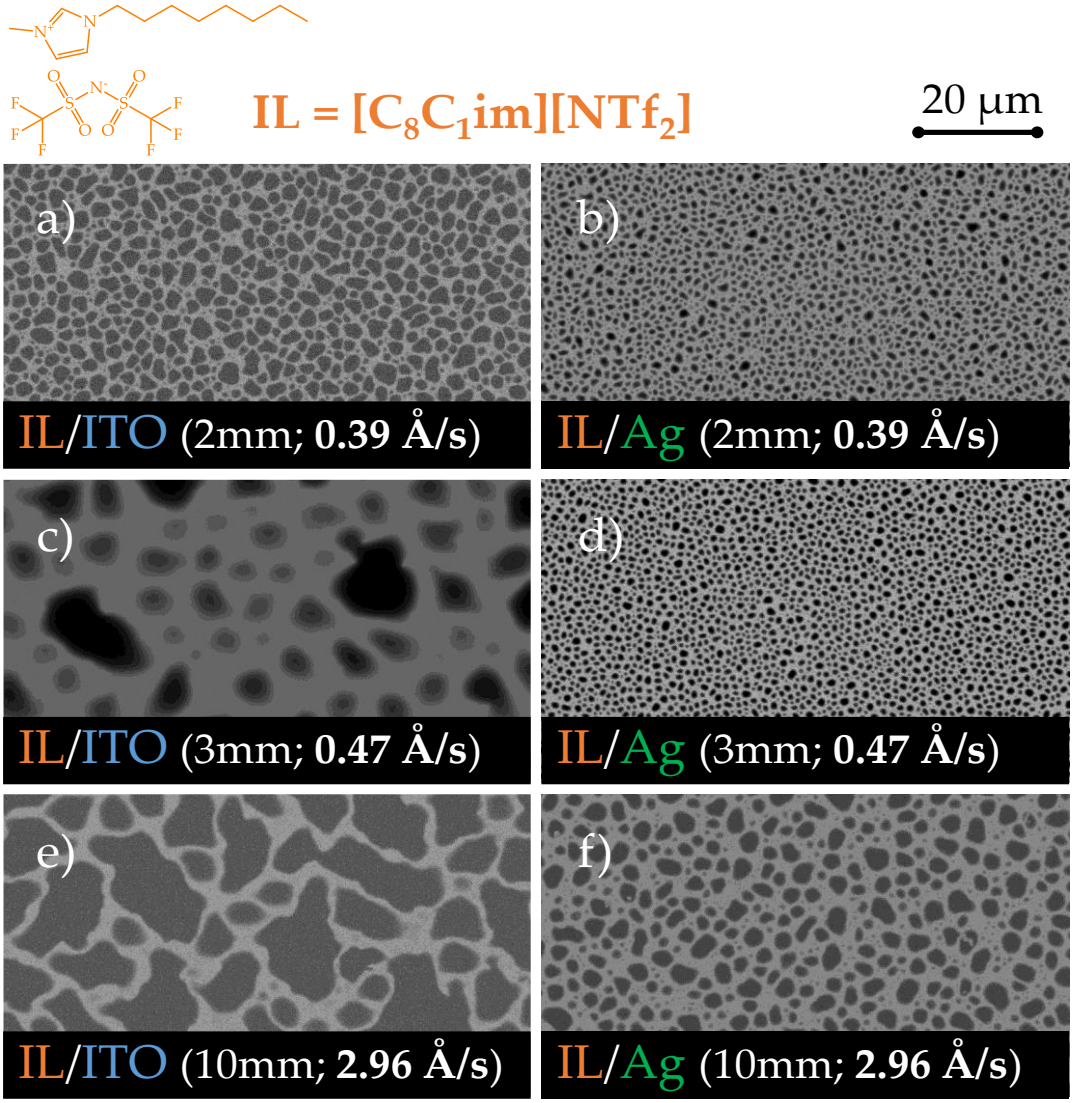

Figure A16. Micro-/nanodroplets morphology of $[C_8C_1im][NTf_2]$ (40 ML) achieved through vacuum thermal evaporation onto ITO/glass (a, c, e) and Ag/ITO/glass (b, d, f), maintaining an evaporation temperature of 503 K and 513K, and using Knudsen effusion cells with different orifice diameters: 2.1 mm (a, b); 3.1 mm (c, d); no disk with orifice/evaporation done directly from the cell body (e, f). The substrate temperature was maintained at 283 K. The image processing did not accurately determine the surface coverage of the films. SEM micrographs (top views) obtained by backscattered electron imaging (BSE).

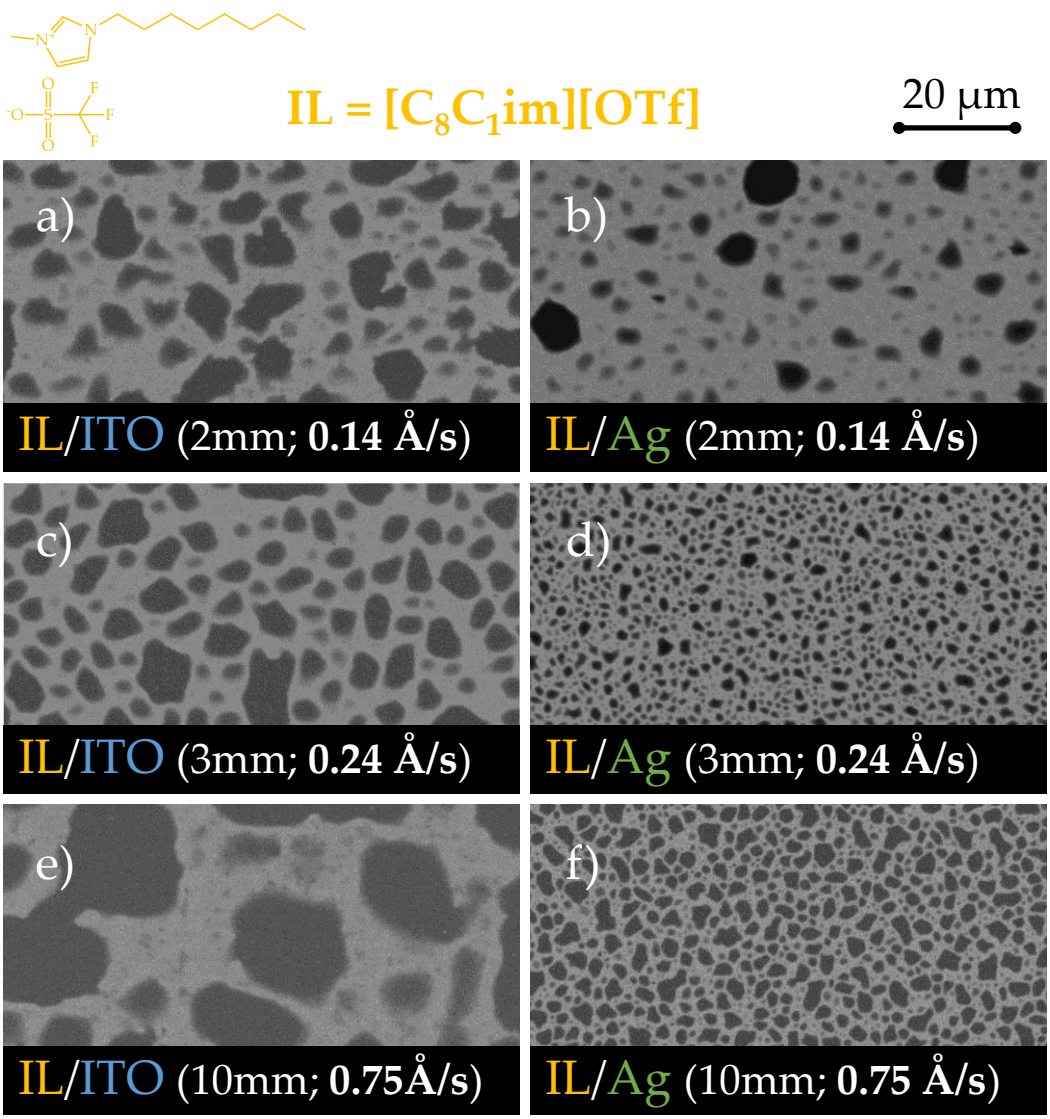

Figure A17. Micro-/nanodroplets morphology of [C_8C_1im][OTf] (40 ML) obtained through vacuum thermal evaporation onto ITO/glass (a, c, e) and Ag/ITO/glass (b, d, f), maintaining an evaporation temperature of 503 K and 513K, and using Knudsen effusion cells with different orifice diameters: 2.1 mm (a, b); 3.1 mm (c, d); no disk with orifice/evaporation done directly from the cell body (e, f). The substrate temperature was maintained at 283 K. The image processing did not accurately determine the surface coverage of the films. SEM micrographs (top views) obtained by backscattered electron imaging (BSE).

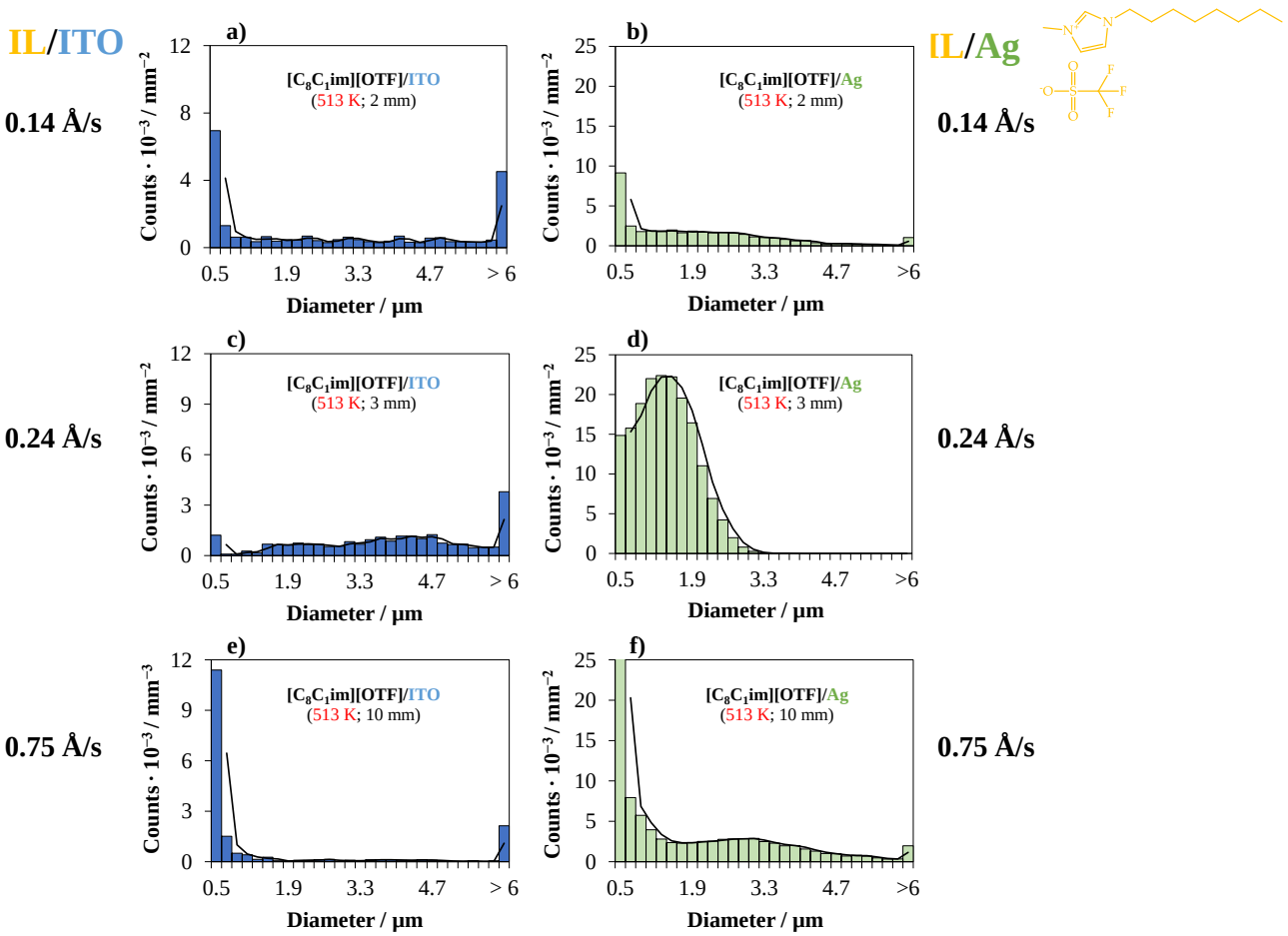

Figure A18. Size distribution of micro-/nanodroplets of $[C_8C_1im][OTf]$ (40 ML) obtained through vacuum thermal evaporation onto ITO/glass (a, c, e) and Ag/ITO/glass (b, d, f) using a Knudsen effusion cell with different orifice diameters: 2.1 mm (a, b); 3.1 mm (c, d); no disk with orifice/evaporation done directly from the cell body (e, f) and employing an evaporation temperature of 503 K and 513K. The substrate temperature was maintained at 283 K.

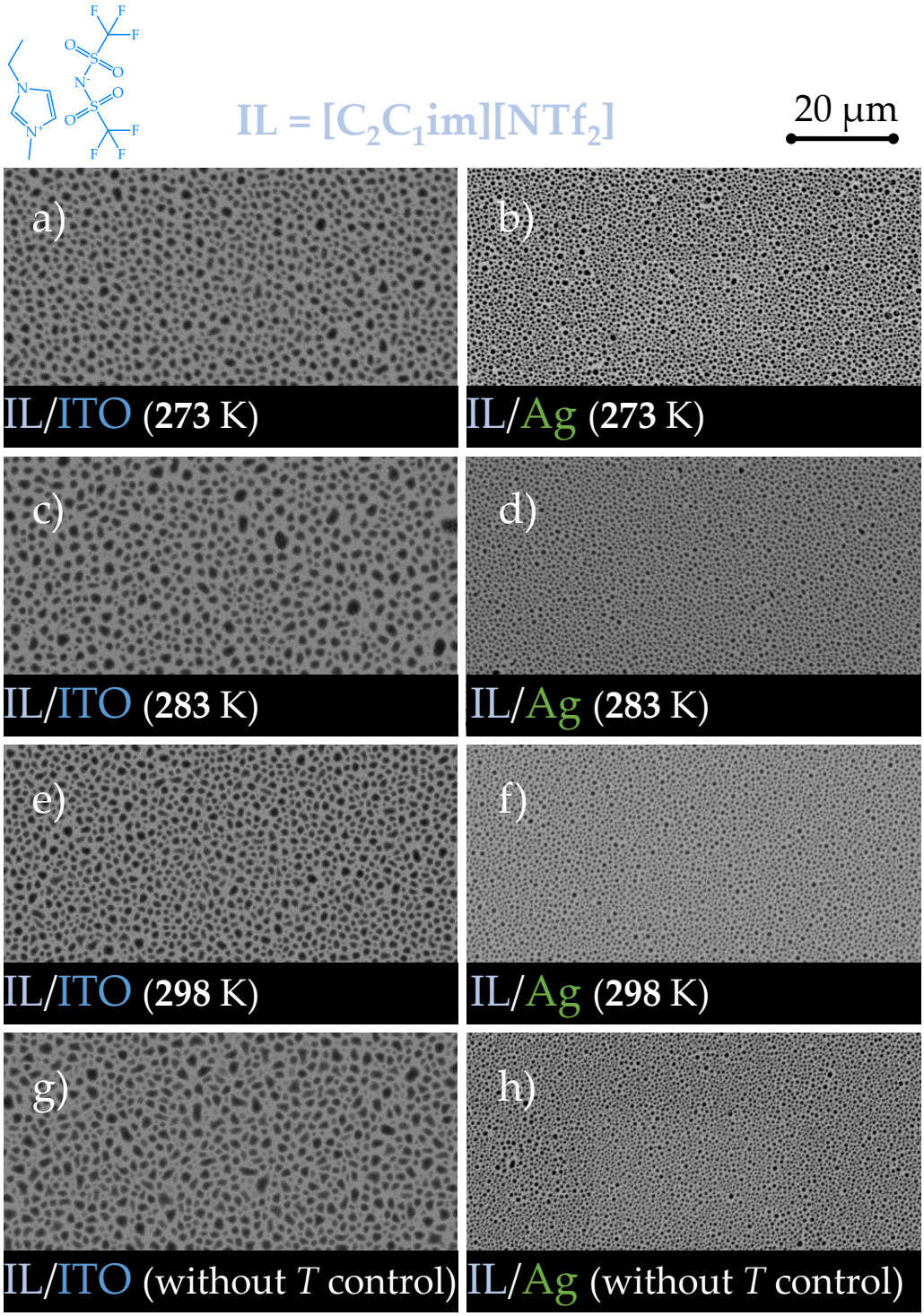

Figure A19. Micro-/nanodroplets morphology of $[C_2C_1im][NTf_2]$ (40 ML) obtained through vacuum thermal evaporation onto ITO/glass (a, c, e) and Ag/ITO/glass (b, d, f), maintaining an evaporation temperature of 503 K and 513 K, and using Knudsen effusion cells with orifice diameters of 2.1 mm. The substrate temperature was varied: 273 K (a, b); 283 K (c, d); 298 K (e, f); without temperature control (g, h). Surface coverages of 30, 34, 30, 34, 34, 32, 32, and 37 % were derived by image processing of Figures a, b, c, d, e, f, g, and h, respectively. SEM micrographs (top views) obtained by backscattered electron imaging (BSE).

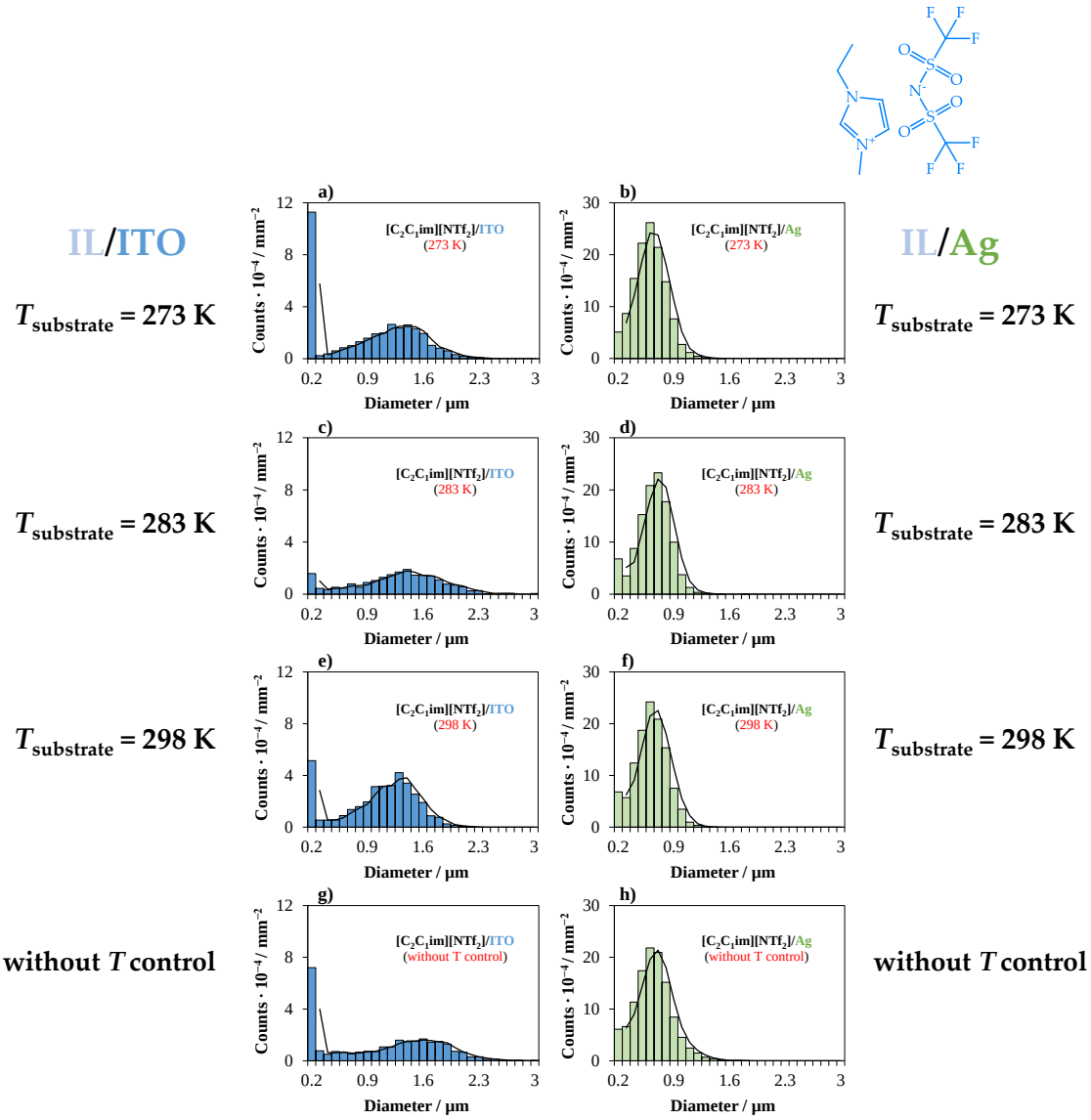

Figure A20. Size distribution of micro-/nanodroplets of $[C_2C_1im][NTf_2]$ (40 ML) obtained through vacuum thermal evaporation onto ITO/glass (a, c, e) and Ag/ITO/glass (b, d, f) using Knudsen effusion cells with orifice diameters of 2.1 mm, maintaining an evaporation temperature of 503 K and variating the substrate temperature: 273 K (a, b); 283 K (c, d); 298 K (e, f); without temperature control (g, h).

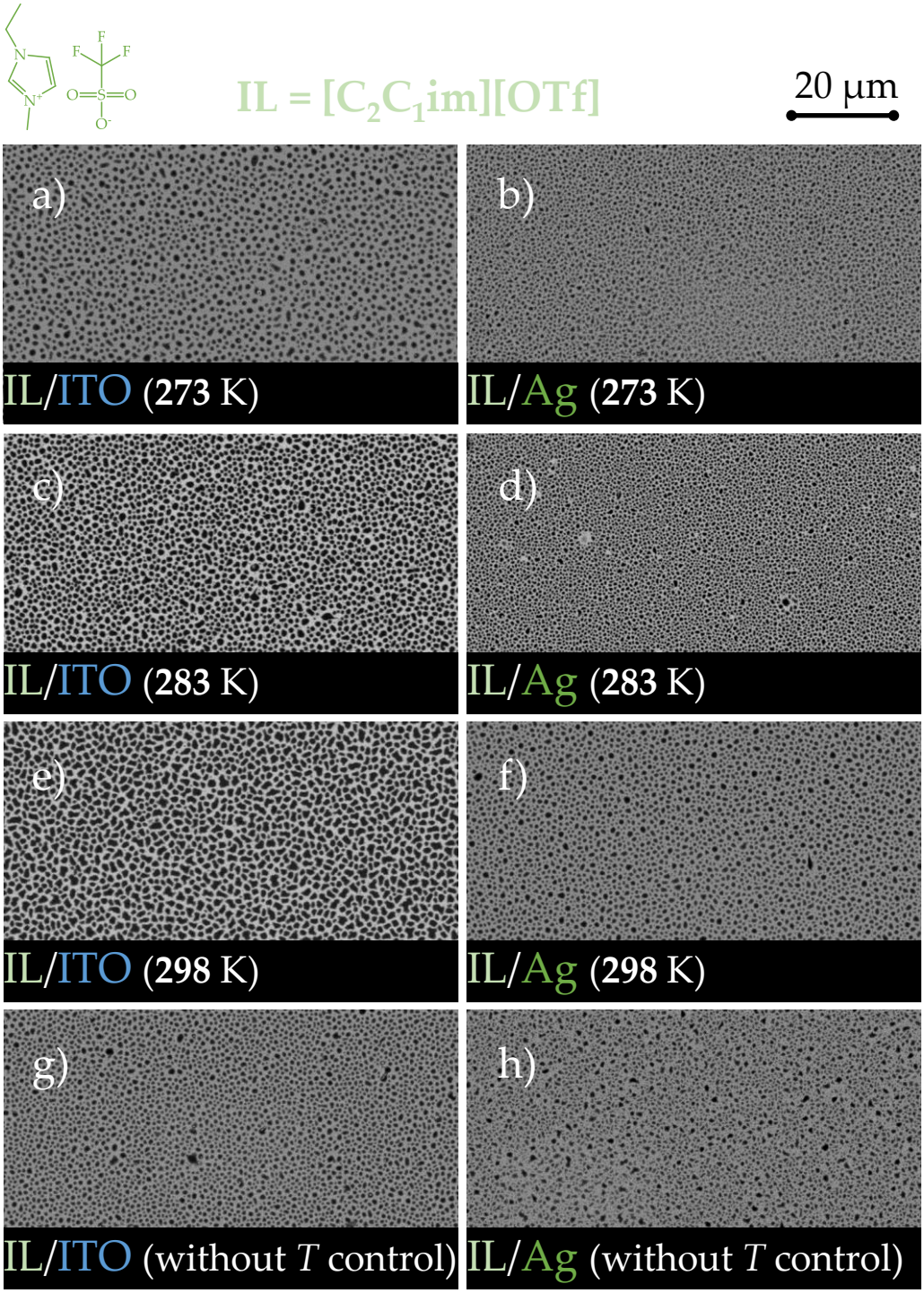

Figure A21. Micro-/nanodroplets morphology of $[C_2C_1im][OTf]$ (40 ML) obtained through vacuum thermal evaporation onto ITO/glass (a, c, e) and Ag/ITO/glass (b, d, f), maintaining an evaporation temperature of 503 K and 513 K, and using Knudsen effusion cells with orifice diameters of 2.1 mm. The substrate temperature was varied: 273 K (a, b); 283 K (c, d); 298 K (e, f); without temperature control (g, h). Surface coverages of 29, 35, 46, 41, 47, 34, 36, and 34 % were derived by image processing of Figures a, b, c, d, e, f, g, and h, respectively. SEM micrographs (top views) obtained by backscattered electron imaging (BSE).

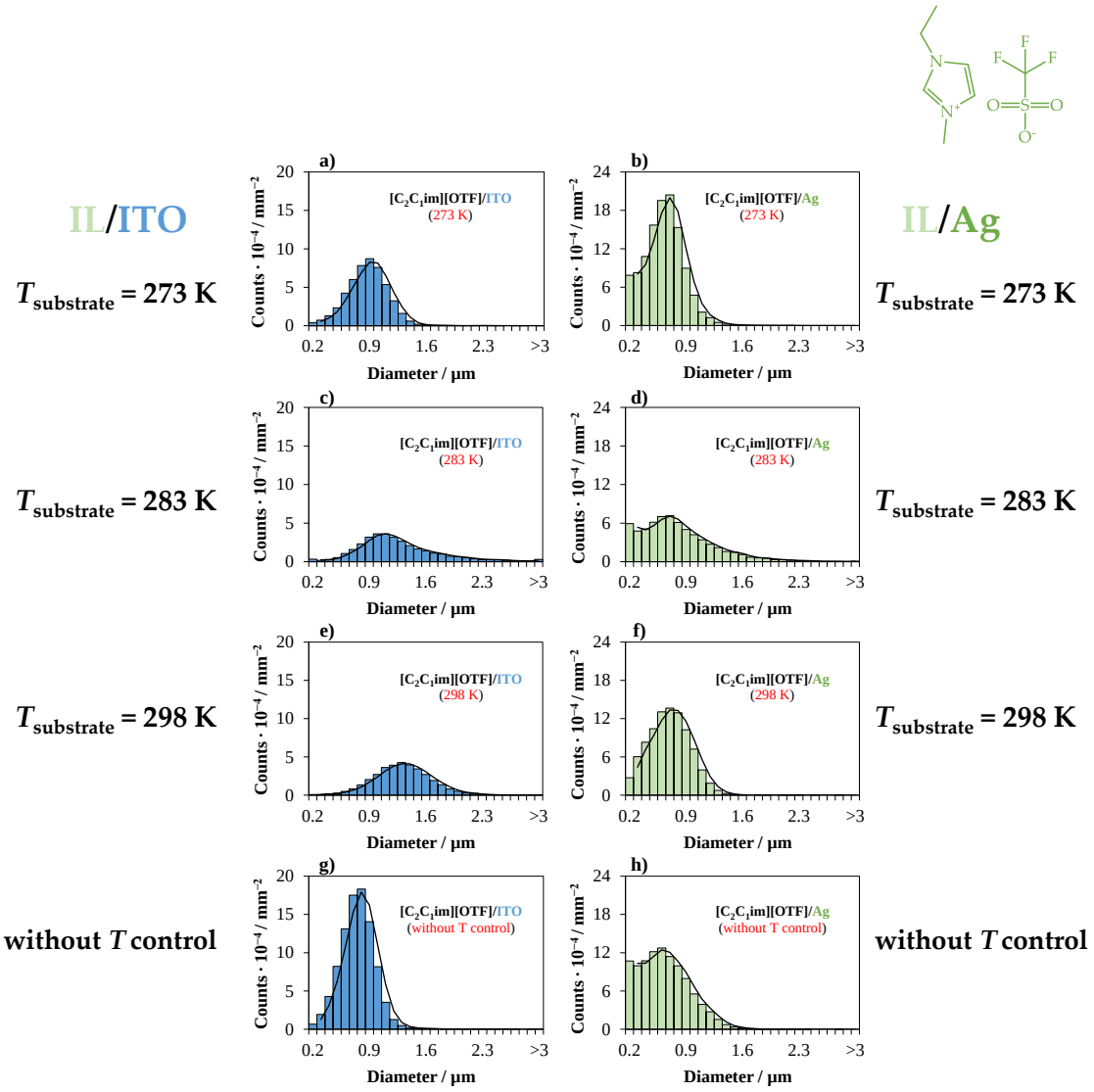

Figure A22. Size distribution of micro-/nanodroplets of $[C_2C_1im][OTf]$ (40 ML) obtained through vacuum thermal evaporation onto ITO/glass (a, c, e) and Ag/ITO/glass (b, d, f) using Knudsen effusion cell with orifice diameters of 2.1 mm, maintaining an evaporation temperature of 503 K and variating the substrate temperature: 273 K (a, b); 283 K (c, d); 298 K (e, f); without temperature control (g, h).

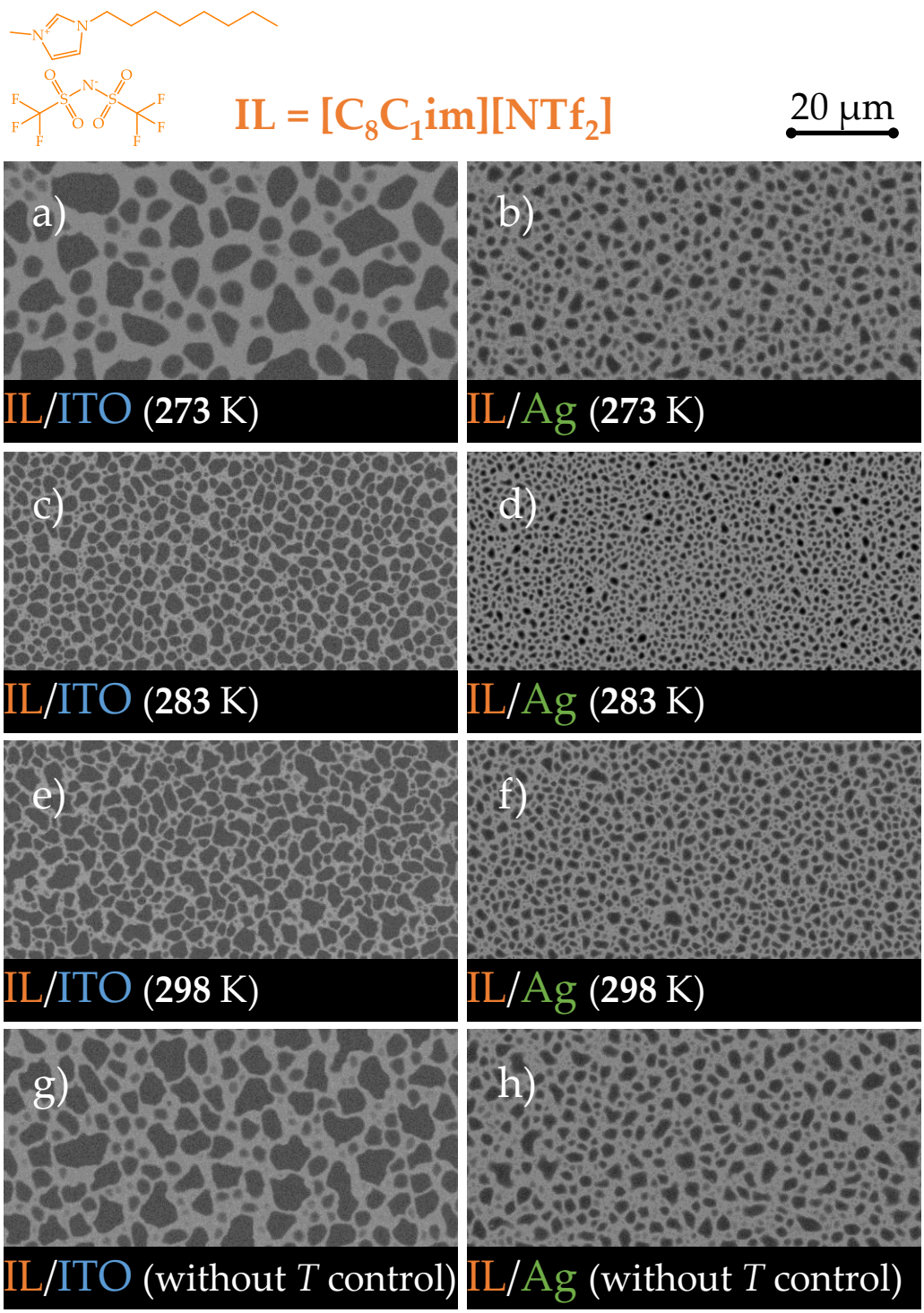

Figure A23. Micro-/nanodroplets morphology of $[C_8C_1im][NTf_2]$ (40 ML) obtained through vacuum thermal evaporation onto ITO/glass (a, c, e) and Ag/ITO/glass (b, d, f), maintaining an evaporation temperature of 503 K and 513 K, and using Knudsen effusion cells with orifice diameters of 2.1 mm. The substrate temperature was varied: 273 K (a, b); 283 K (c, d); 298 K (e, f); without temperature control (g, h). The image processing did not accurately determine the surface coverage of the films. SEM micrographs (top views) obtained by backscattered electron imaging (BSE).

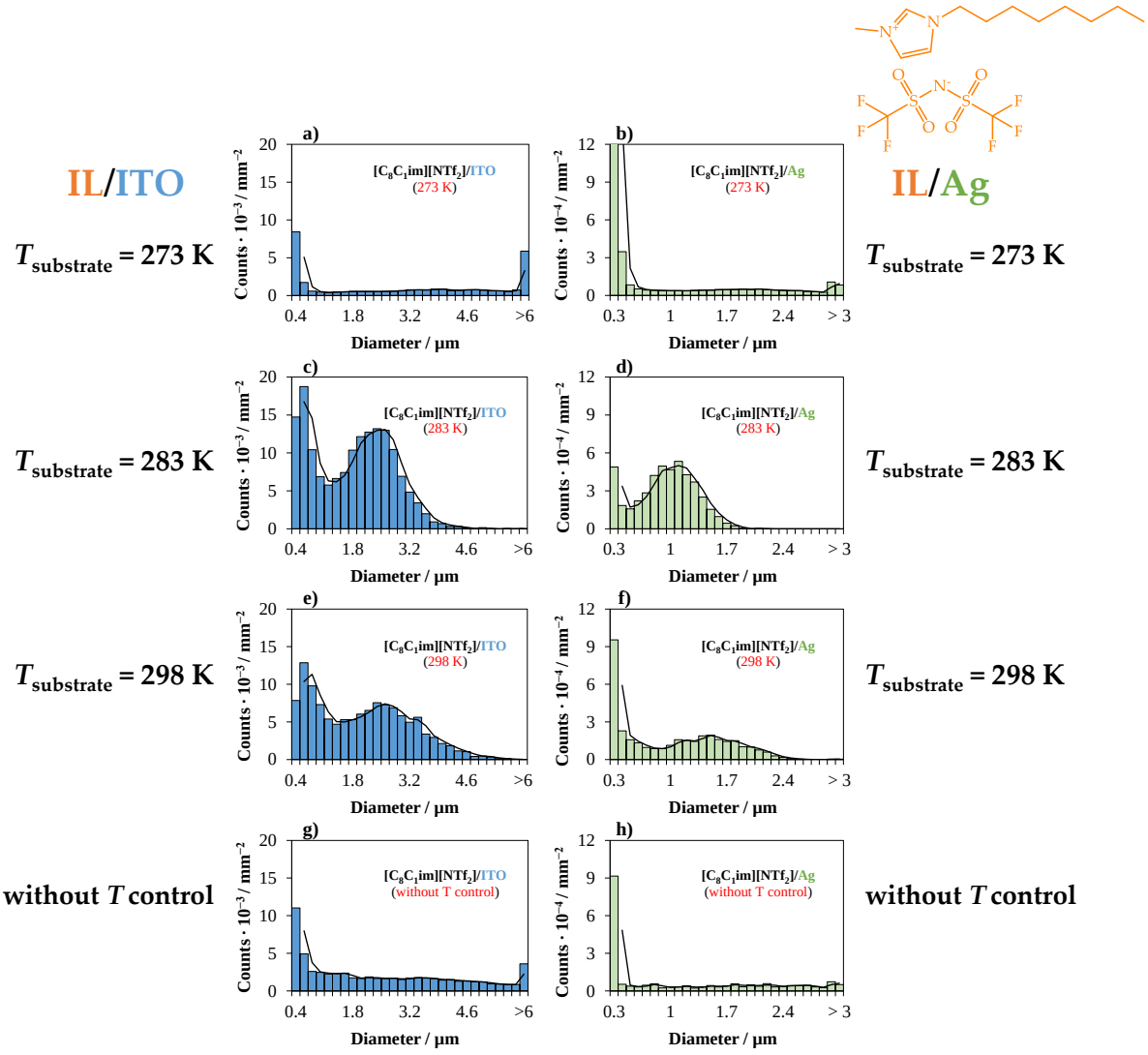

Figure A24. Size distribution of micro-/nanodroplets of $[C_8C_1im][NTf_2]$ (40 ML) obtained through vacuum thermal evaporation onto ITO/glass (a, c, e) and Ag/ITO/glass (b, d, f) using Knudsen effusion cell with orifice diameters of 2.1 mm, maintaining an evaporation temperature of 503 K and variating the substrate temperature: 273 K (a, b); 283 K (c, d); 298 K (e, f); without temperature control (g, h).

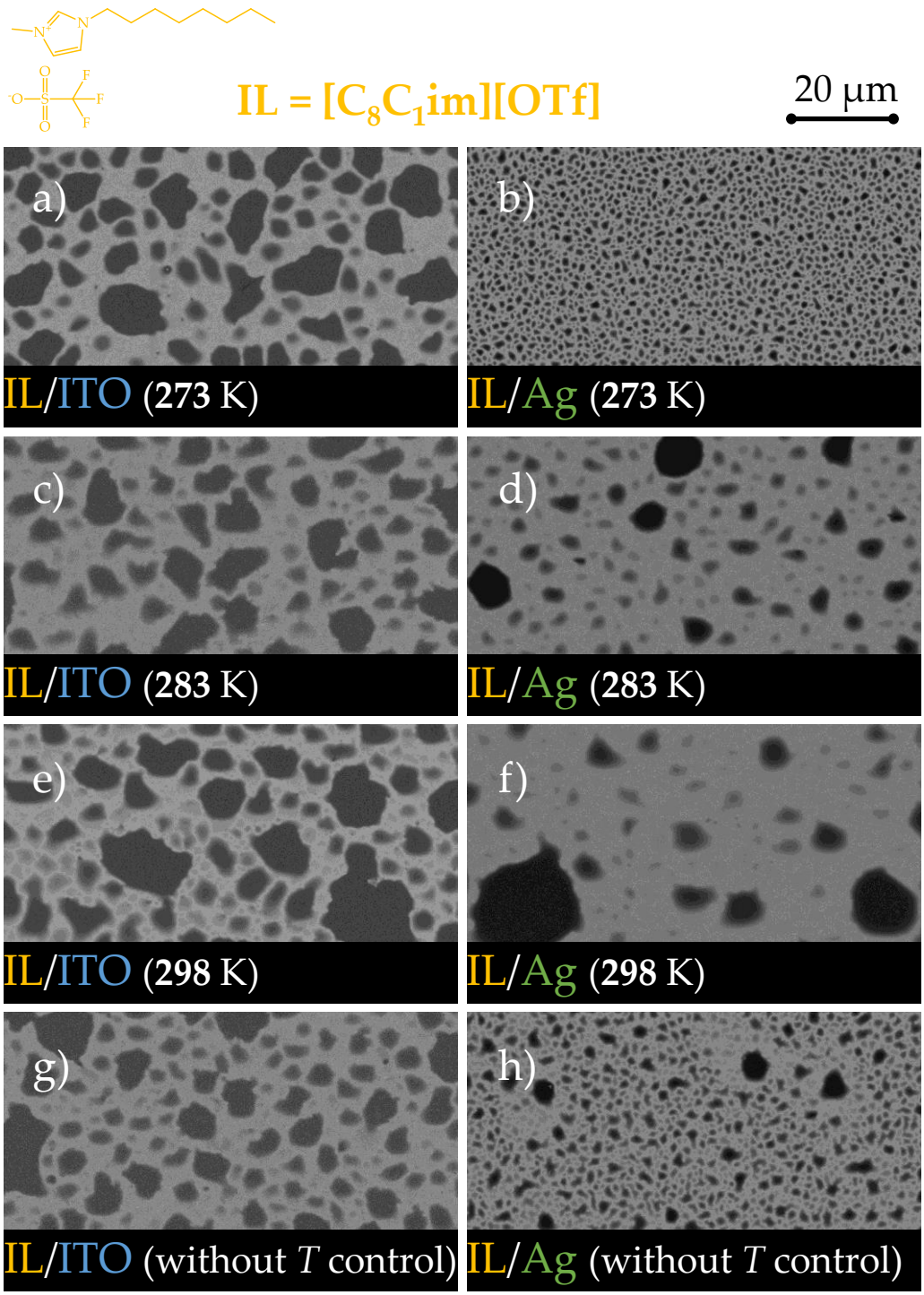

Figure A25. Micro-/nanodroplets morphology of $[C_8C_1im][OTf]$ (40 ML) obtained through vacuum thermal evaporation onto ITO/glass (a, c, e) and Ag/ITO/glass (b, d, f), maintaining an evaporation temperature of 513 K and 513 K, and using Knudsen effusion cells with orifice diameters of 2.1 mm. The substrate temperature was varied: 273 K (a, b); 283 K (c, d); 298 K (e, f); without temperature control (g, h). The image processing did not accurately determine the surface coverage of the films. SEM micrographs (top views) obtained by backscattered electron imaging (BSE).

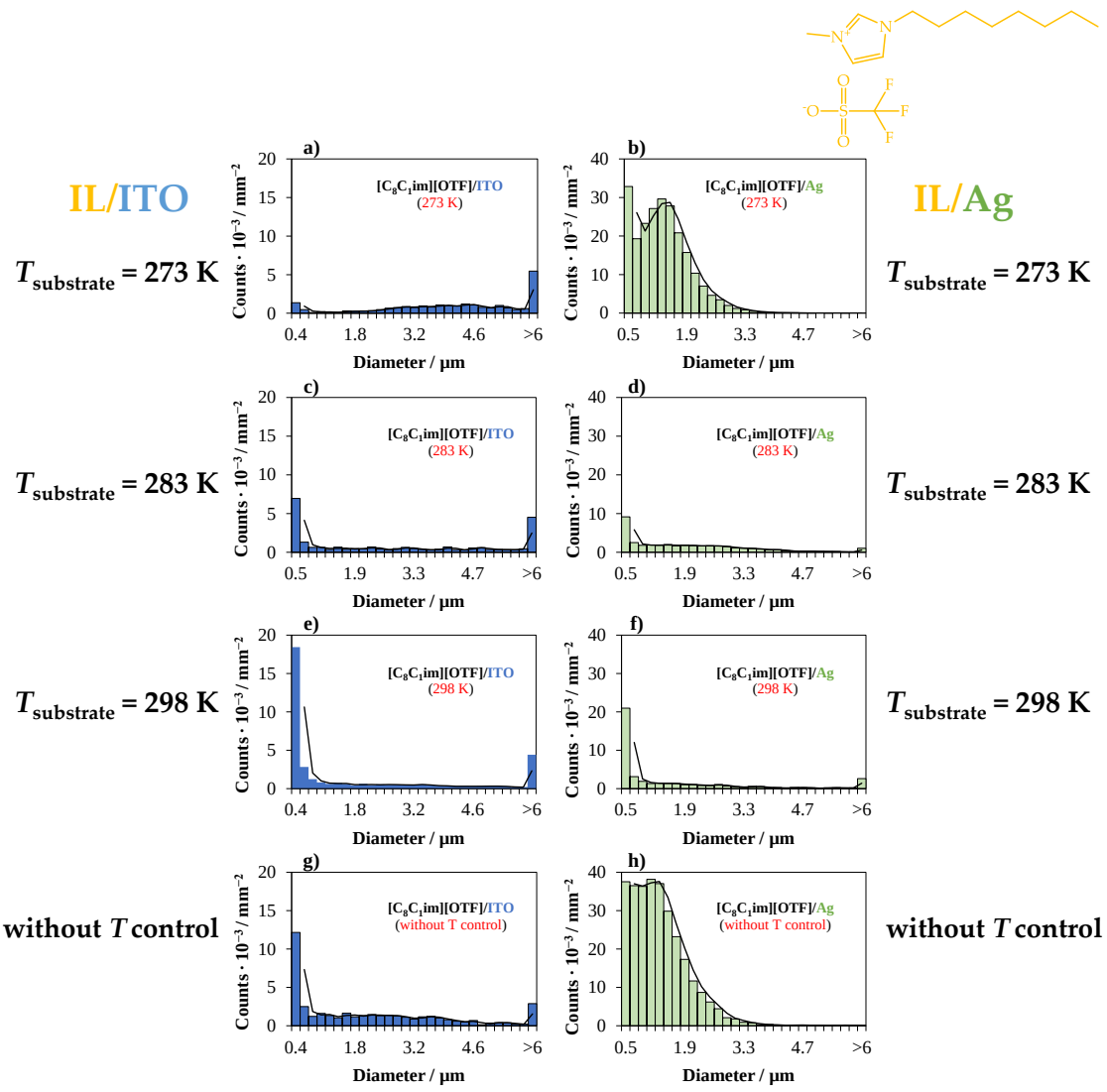

Figure A26. Size distribution of micro-/nanodroplets of $[C_8C_1im][OTf]$ (40 ML) obtained through vacuum thermal evaporation onto ITO/glass (a, c, e) and Ag/ITO/glass (b, d, f) using Knudsen effusion cell with orifice diameters of 2.1 mm, maintaining an evaporation temperature of 513 K and variating the substrate temperature: 273 K (a, b); 283 K (c, d); 298 K (e, f); without temperature control (g, h).

Table A1- Experimental conditions for the physical vapor deposition/thermal evaporation of each ionic liquid: effusion temperature ($T_{eff.}$); equilibrium vapor pressure (*EVP*); orifice diameter of the Knudsen effusion cell; substrate temperature ($T_{subst.}$); mass flow rate at the substrate surface [Φ (QCM)] and corresponding deposition rate in $Å \cdot s^{-1}$; deposition time. Experimental variables related to the study of the effect of the mass flow rate on the morphology of different ionic liquids deposited with 40 ML on the ITO/glass and Ag/ITO/glass surfaces.

Precursor	$T_{eff.}$	$T_{subst.}$	*EVP*	Orifice diameter	Φ (QCM)	Deposition rate	Deposition time
	K	K	Pa	Mm	$ng \cdot cm^{-2} \cdot s^{-1}$	$Å \cdot s^{-1}$	s
			[C$_n$C$_1$im][NTf$_2$] (40 ML) / substrate | substrates: Ag/ITO/glass; ITO/glass				
	473.2		0.04 [a]	2.1	1.2	0.08 ± 0.01	3750
	503.2		0.25 [a]	2.1	4.3	0.39 ± 0.08	1071
	533.2		1.00 [a]	2.1	11.2	0.74 ± 0.10	395
[C$_2$C$_1$im][NTf$_2$]	473.2	283	0.04 [a]	3.1	1.8	0.12 ± 0.05	2500
	503.2		0.25 [a]	3.1	8.2	0.54 ± 0.05	556
	533.2		1.00 [a]	3.1	22.8	1.50 ± 0.18	200
	503.2			[b]	68.4	4.50 ± 0.52	67
	473.2		0.02 [a]	2.1	1.0	0.08 ± 0.004	4200
	503.2		0.16 [a]	2.1	5.1	0.39 ± 0.04	862
	533.2		0.90 [a]	2.1	14.4	1.10 ± 0.11	305
[C$_8$C$_1$im][NTf$_2$]	473.2	283	0.02 [a]	3.1	1.4	0.11 ± 0.05	3055
	503.2		0.16 [a]	3.1	6.2	0.47 ± 0.06	715
	533.2		0.90 [a]	3.1	19.7	1.50 ± 0.26	224
	503.2			[b]	39.3	2.96 ± 0.25	114
			[C$_n$C$_1$im][OTf] (40 ML) / substrate | substrates: Ag/ITO/glass; ITO/glass				
	473.2			2.1	0.3	0.02 ± 0.02	13600
	503.2			2.1	0.7	0.05 ± 0.04	5440
	533.2			2.1	2.1	0.15 ± 0.06	1813
[C$_2$C$_1$im][OTf]	473.2	283	[c]	3.1	0.8	0.06 ± 0.01	4533
	503.2			3.1	2.5	0.18 ± 0.07	1511
	533.2			3.1	7.1	0.51 ± 0.04	533
	503.2			[b]	10.7	0.77 ± 0.16	353
	473.2			2.1	0.5	0.04 ± 0.02	7800
	513.2			2.1	1.7	0.14 ± 0.02	2229
	533.2			2.1	3.6	0.30 ± 0.05	1040
[C$_8$C$_1$im][OTf]	473.2	283	[c]	3.1	1.1	0.09 ± 0.02	3467
	503.2			3.1	2.9	0.24 ± 0.09	1300
	533.2			3.1	8.8	0.73 ± 0.05	427
	503.2			[b]	9.0	0.75 ± 0.10	416

[a] The *EVP* at each evaporation temperature was derived from literature data reporting volatility studies of the ILs: [C$_2$C$_1$im][NTf$_2$] and [C$_8$C$_1$im][NTf$_2$], [9].

[b] These experiments were performed by removing the disk containing the orifice to maximize the mass flow rate – only the cell body was used.

[c] Accurate data for the *EVP* of [C$_2$C$_1$im][OTf] and [C$_8$C$_1$im][OTf] were not found elsewhere. Nevertheless, there are reports on the determination of vaporization enthalpies indicating the lower volatility of the [OTF]-based ILs in comparison to their congeners [NTf$_2$]-based ILs. In fact, in this work, at the same evaporation temperature lower deposition rates were observed for [OTf]-based ILs. The *EVP* of [C$_2$C$_1$im][OTf] and [C$_8$C$_1$im][OTf] at the studied evaporation temperatures are estimated to be within the interval between 0.01 and 1 Pa. In addition, their *EVP* may be lower than observed for [C$_2$C$_1$im][NTf$_2$] and [C$_8$C$_1$im][NTf$_2$].

Table A2- Experimental conditions for the physical vapor deposition/thermal evaporation of each ionic liquid: effusion temperature ($T_{eff.}$); equilibrium vapor pressure (*EVP*); orifice diameter of the Knudsen effusion cell; substrate temperature ($T_{subst.}$); mass flow rate at the substrate surface [Φ (QCM)] and corresponding deposition rate in Å·s^{-1}; deposition time. Experimental variables related to the study of the effect of the substrate temperature on the morphology of different ionic liquids deposited with 40 ML on the ITO/glass and Ag/ITO/glass surfaces.

Precursor	T_{eff}	$T_{subst.}$	EVP	Orifice diameter	Φ (QCM)	Deposition rate	Deposition time
	K	K	Pa	Mm	ng·cm^{-2}·s^{-1}	Å·s^{-1}	s
[C$_n$C$_1$im][NTf$_2$] (40 ML) / substrate | substrates: Ag/ITO/glass; ITO/glass							
[C$_2$C$_1$im][NTf$_2$]	503.2	273	0.25 [a]	2.1	6.7	0.44 ± 0.09	682
		283			4.3	0.39 ± 0.09	769
		298			6.5	0.43 ± 0.08	698
		Without T control [b]			6.5	0.43 ± 0.05	698
[C$_8$C$_1$im][NTf$_2$]	503.2	273	0.16 [a]	2.1	5.9	0.45 ± 0.05	747
		283			5.1	0.39 ± 0.04	862
		298			5.8	0.44 ± 0.08	764
		Without T control [b]			5.4	0.41 ± 0.09	820
[C$_n$C$_1$im][OTf] (40 ML) / substrate | substrates: Ag/ITO/glass; ITO/glass							
[C$_2$C$_1$im][OTf]	503.2	273	[c]	2.1	1.0	0.07 ± 0.03	3886
		283			0.7	0.05 ± 0.04	5440
		298			0.7	0.05 ± 0.02	5440
		Without T control [b]			0.6	0.04 ± 0.03	6800
[C$_8$C$_1$im][OTf]	513.2	273	[c]	2.1	2.2	0.18 ± 0.03	1733
		283			1.7	0.14 ± 0.02	2229
		298			3.0	0.25 ± 0.01	1248
		Without T control [b]			2.4	0.20 ± 0.03	1560

[a] The EVP at each evaporation temperature was derived from literature data reporting volatility studies of the ILs: [C$_2$C$_1$im][NTf$_2$] and [C$_8$C$_1$im][NTf$_2$], [9].

[b] These experiments were performed by turning the refrigerated circulating bath responsible for keeping $T_{subst.}$ constant.

[c] Accurate data for the EVP of [C$_2$C$_1$im][OTf] and [C$_8$C$_1$im][OTf] were not found elsewhere. The EVP of [C$_2$C$_1$im][OTf] and [C$_8$C$_1$im][OTf] at the studied evaporation temperatures are estimated to be within the interval between 0.01 and 1 Pa. In addition, their EVP may be lower than observed for [C$_2$C$_1$im][NTf$_2$] and [C$_8$C$_1$im][NTf$_2$].

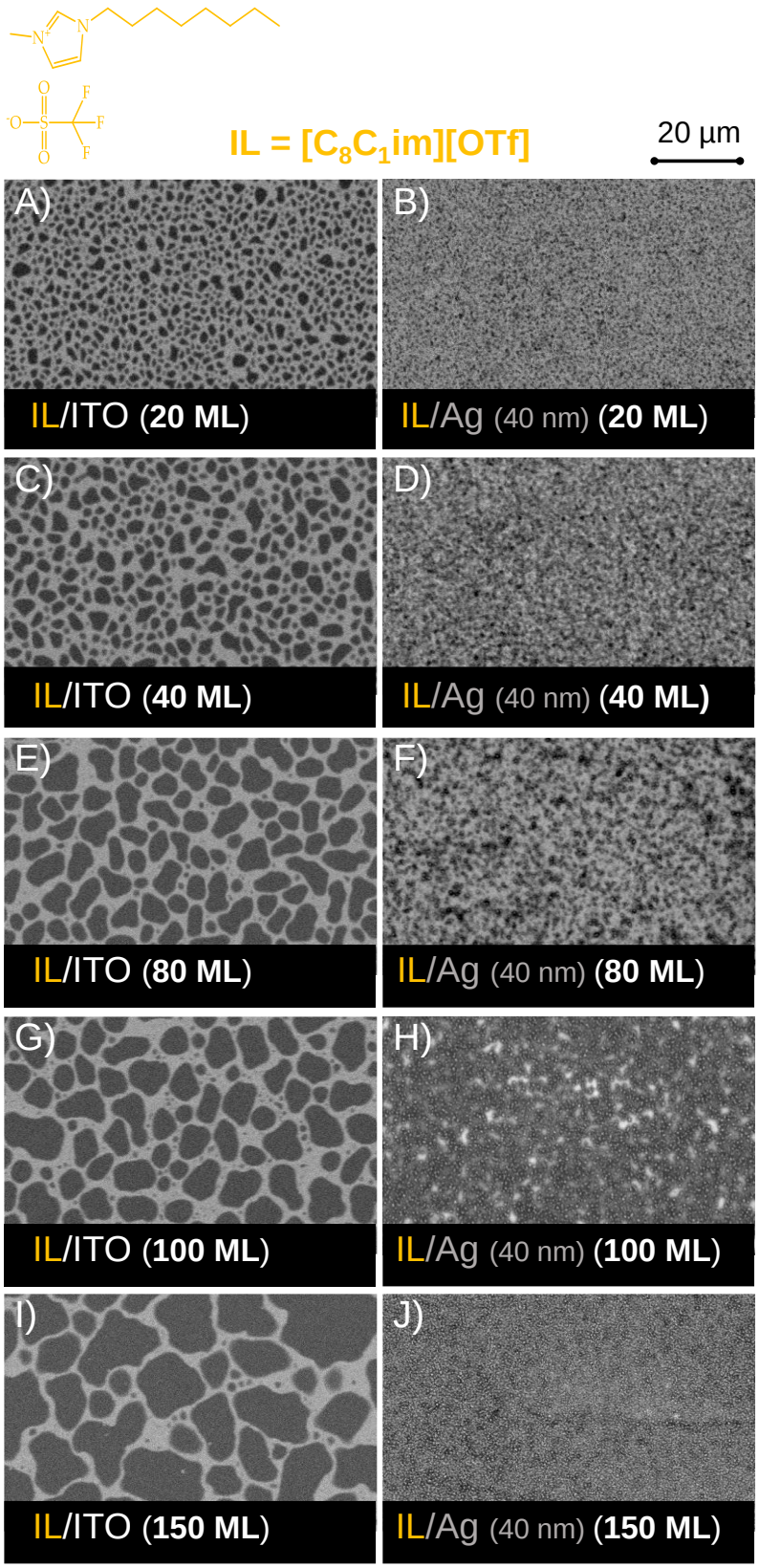

Figure A27. Morphology of [C_8C_1im][OTf] thin films (A-J) deposited simultaneously (by PVD) onto ITO surfaces (images A, C, E, G, H) and Ag surfaces (40 nm) (images B, D, F, H, J) at varying quantities: 20 ML (A, B); 40 ML (C, D); 80 ML (E, F); 100 ML (G, H); 150 ML (I, J). All experiments were conducted with a consistent mass flow rate (≈ 0.30 Å/s). Top view images (A-J) were acquired through scanning electron microscopy by using a backscattered electron detector (BSE).

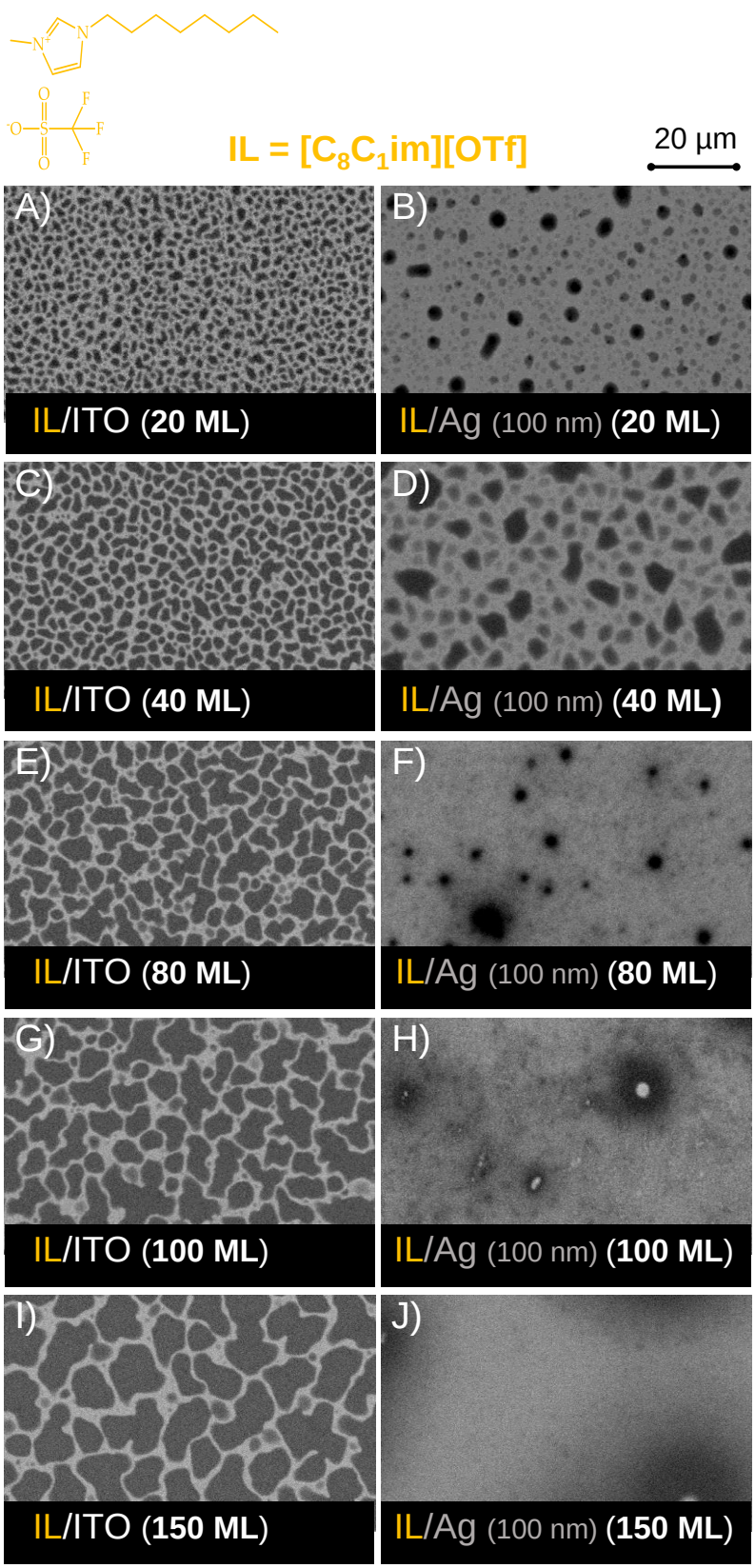

Figure A28. Morphology of $[C_8C_1im][OTf]$ thin films (A-J) deposited simultaneously (by PVD) onto ITO surfaces (images A, C, E, G, H) and Ag surfaces (100 nm) (images B, D, F, H, J) at varying quantities: 20 ML (A, B); 40 ML (C, D); 80 ML (E, F); 100 ML (G, H); 150 ML (I, J). All experiments were conducted with a consistent mass flow rate (≈ 0.30 Å/s). Top view images (A-J) were acquired through scanning electron microscopy by using a backscattered electron detector (BSE).

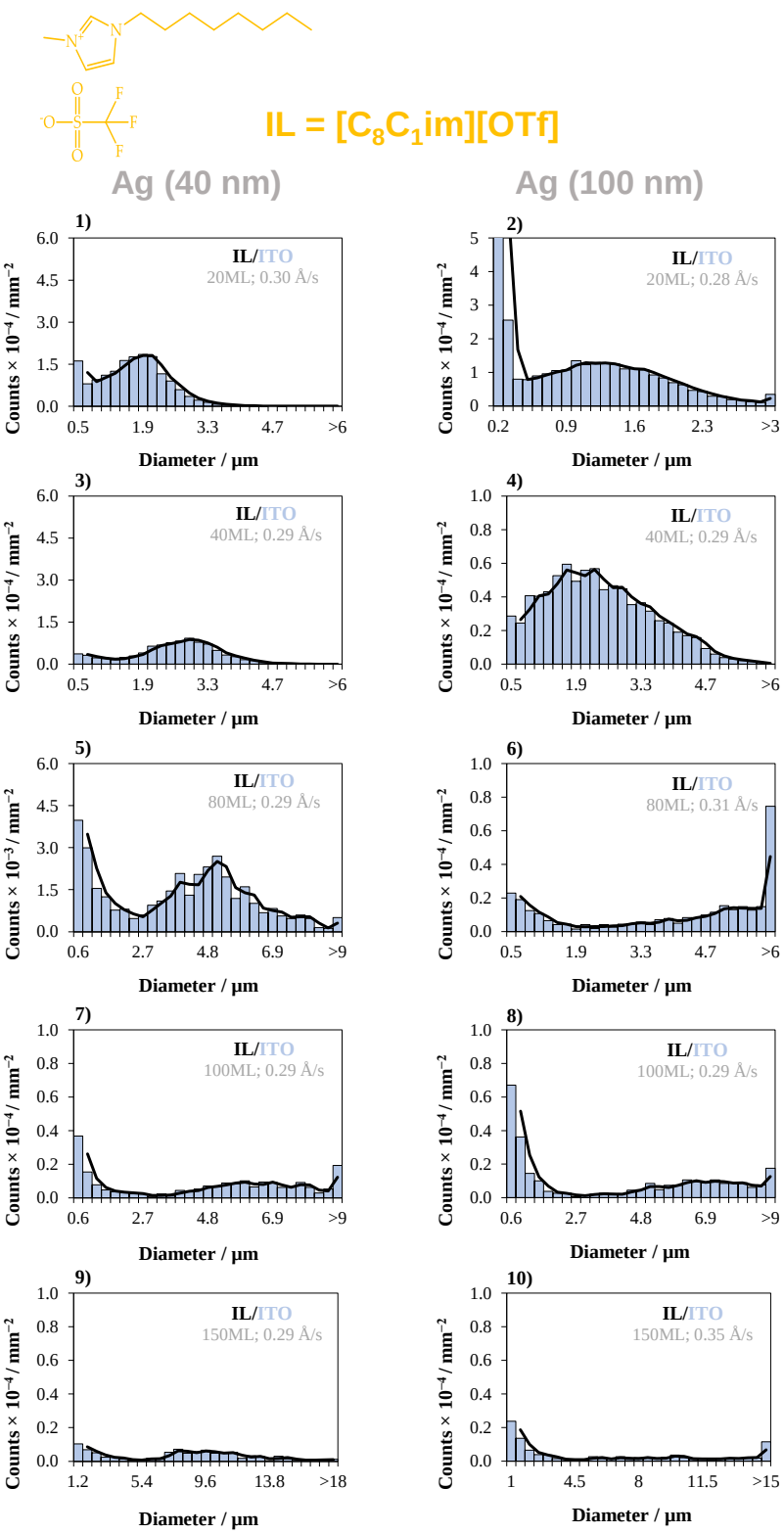

Figure A29. Size distribution of micro-/nanodroplets of [C_8C_1im][OTf], obtained through vacuum thermal evaporation using a Knudsen effusion cell with an orifice diameter of 3.1 mm. The process maintains a mass flow rate of 0.30 A/s and a substrate temperature of 283 K. The IL films were simultaneously deposited (by PVD) onto ITO substrates that were partially coated with Ag films of different thicknesses: 40 nm (1, 3, 5, 7, 9) and 100 nm (2, 4, 6, 8, 10). The IL was deposited at varying quantities: 20 ML (1, 2); 40 ML (3, 4); 80 ML (5, 6); 100 ML (7, 8); 150 ML (9, 10). The results pertain to droplet size deposition on the substrate area not covered by Ag, i.e., on the ITO surface.

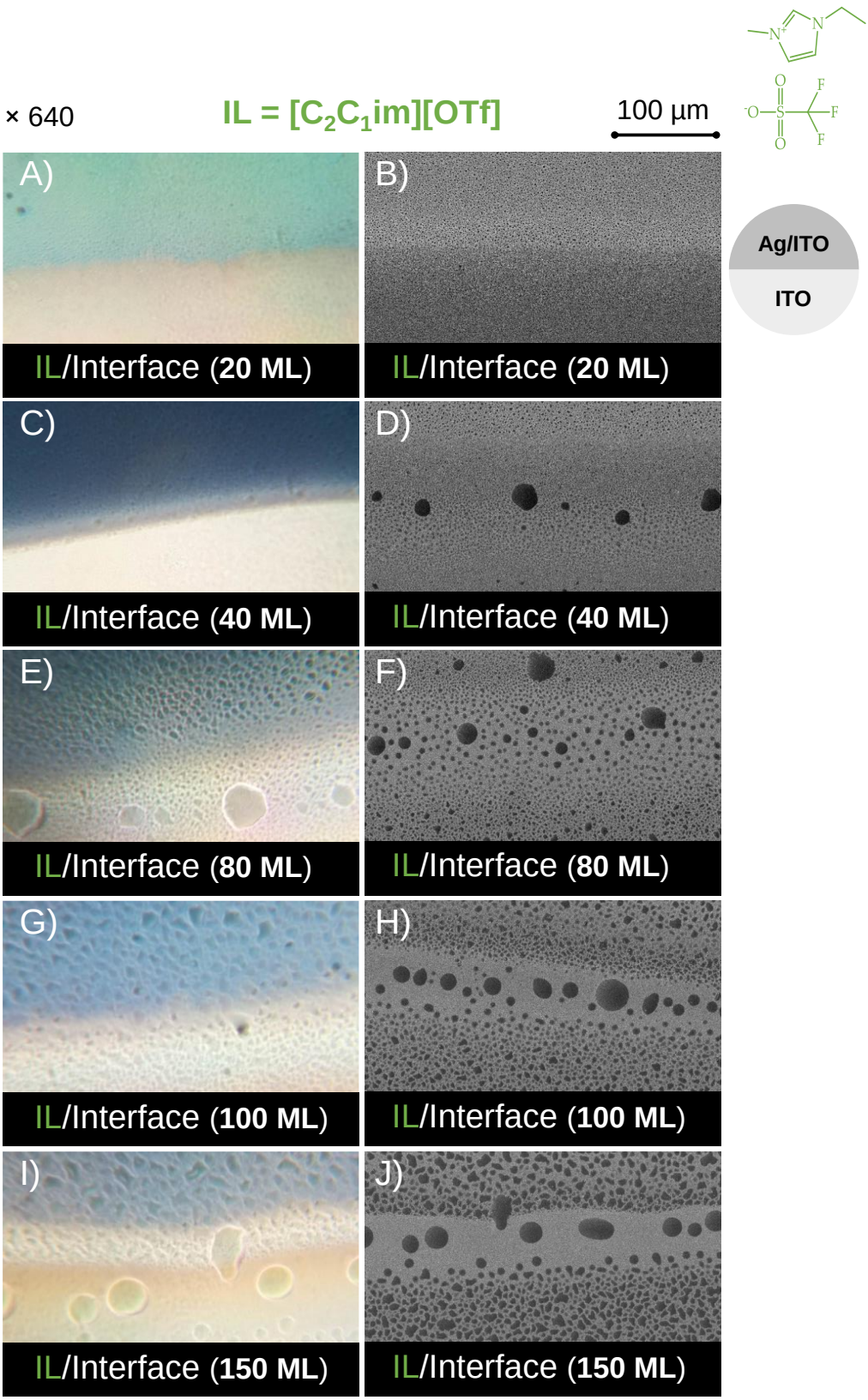

Figure A30. Morphology of [C_2C_1im][OTf] thin films (A-J) in the interface of Ag (100 nm of thickness) and ITO surfaces. The IL films were deposited simultaneously (by PVD) onto ITO and Ag surfaces at varying quantities: 20 ML (A, B); 40 ML (C, D); 80 ML (E, F); 100 ML (G, H); 150 ML (I, J). All experiments were conducted with a similar mass flow rate (≈ 0.30 Å/s). Optical microscopy images (A, C, E, G, I) were obtained with a magnification of 640x. Top views (B, D, F, H, J) were acquired through scanning electron microscopy by using a secondary electron detector (SE)

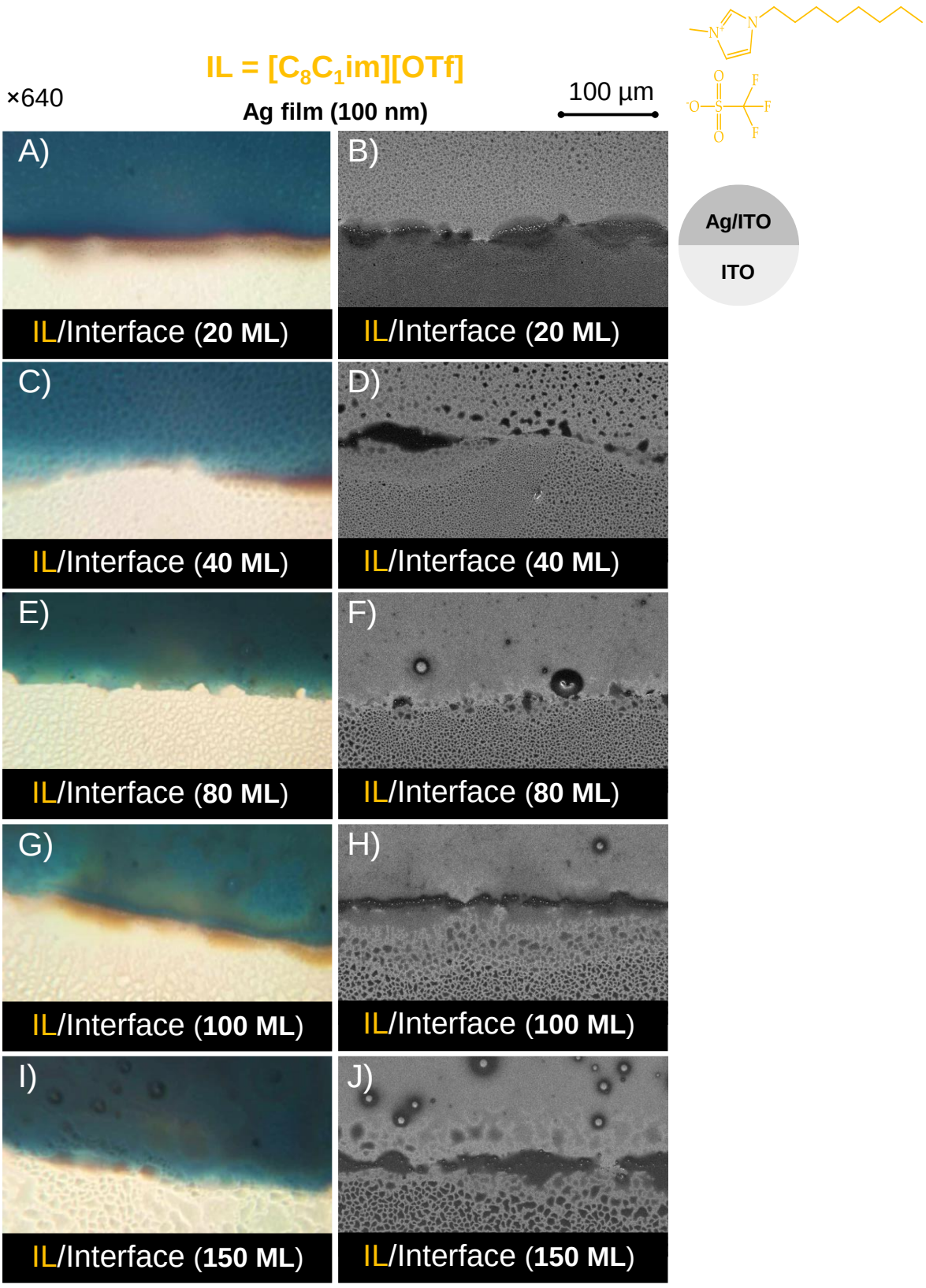

Figure A31. Morphology of $[C_8C_1im][OTf]$ thin films (A-J) in the interface of Ag (100 nm of thickness) and ITO surfaces. The IL films were deposited simultaneously (by PVD) onto ITO and Ag surfaces at varying quantities: 20 ML (A, B); 40 ML (C, D); 80 ML (E, F); 100 ML (G, H); 150 ML (I, J). All experiments were conducted with a similar mass flow rate (≈ 0.30 Å/s). Optical microscopy images (A, C, E, G, I) were obtained with a magnification of 640x. Top views (B, D, F, H, J) were acquired through scanning electron microscopy by using a secondary electron detector (SE).

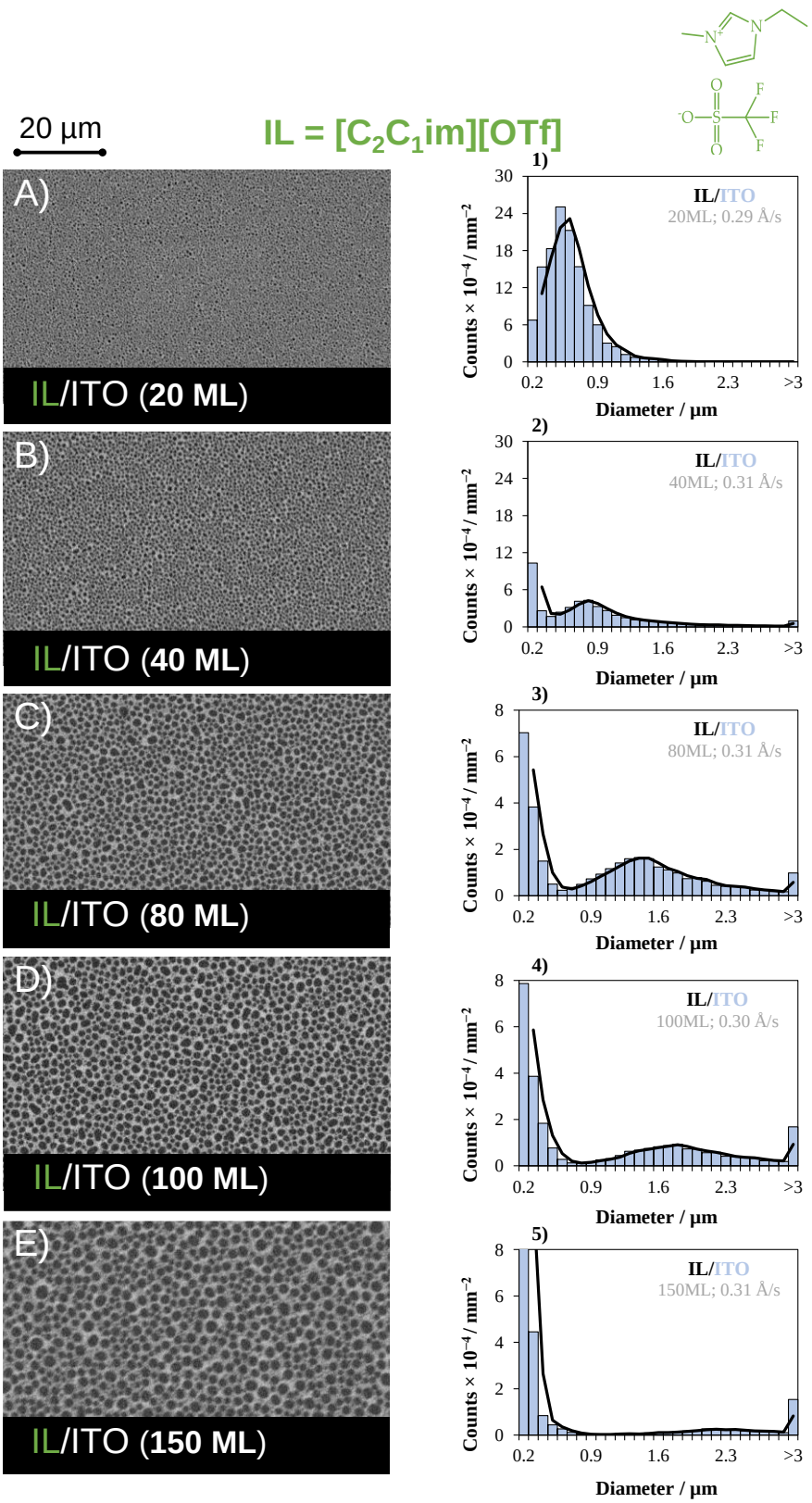

Figure A32. Morphology of $[C_2C_1im][OTf]$ thin films (A-E) and the respective histograms (1-5) referent to the droplet size distribution on ITO surfaces (control samples, i.e., results for ITO surfaces without any interface with Ag). The IL films were deposited (by PVD) on ITO (images A- E) surfaces at varying quantities: 20 ML (A); 40 ML (B); 80 ML (C); 100 ML (D); 150 ML (E). All the experiments occur with similar mass flow rates (≈ 0.30 Å/s). Top views (A-J) were acquired through scanning electron microscopy by using a backscattered electron detector (BSE).

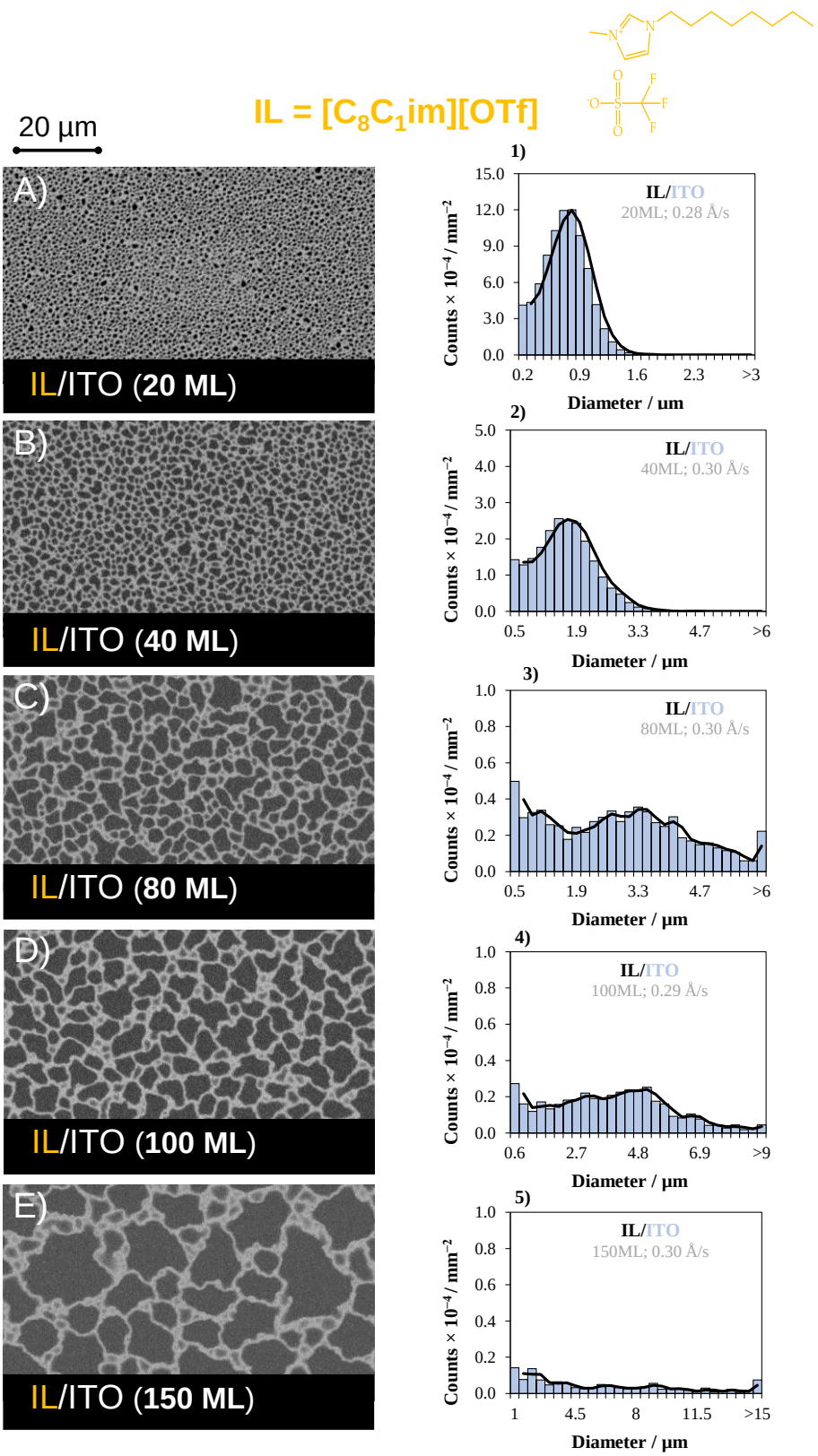

Figure A33. Morphology of [C_8C_1im][OTf] thin films (A-E) and the respective histograms (1-5) referent to the droplet size distribution on ITO surfaces (control samples, i.e., results for ITO surfaces without any interface with Ag). The IL films were deposited (by PVD) on ITO (images A- E) surfaces at varying quantities: 20 ML (A); 40 ML (B); 80 ML (C); 100 ML (D); 150 ML (E). All the experiments occur with similar mass flow rates (≈ 0.30 Å/s). Top views (A-J) were acquired through scanning electron microscopy by using a backscattered electron detector (BSE).

Table A3- Experimental conditions for the physical vapor deposition/thermal evaporation of each ionic liquid: monolayers (ML); effusion temperature ($T_{eff.}$); equilibrium vapor pressure (*EVP*); orifice diameter of the Knudsen effusion cell; substrate temperature ($T_{subst.}$); mass flow rate at the substrate surface [Φ (QCM)] and corresponding deposition rate in Å·s^{-1}; deposition time. Experimental variables related to the study of the effect of an interface on the morphology of different ionic liquids deposited at different quantities on ITO/glass surfaces and ITO/glass substrates partially covered with Ag.

Precursor	ML	$T_{eff.}$ K	$T_{subst.}$ K	*EVP* Pa	Orifice diameter mm	Φ (QCM) ng·cm^{-2}·s^{-1}	Deposition rate Å·s^{-1}	Deposition time s
[C$_n$C$_1$im][OTf] / substrate | substrates: ITO/glass partially cover with 100 nm Ag film								
[C$_2$C$_1$im][OTf]	20	528.2	283	0.10 [a)]	3.1	2.4	0.17 ± 0.14	797
	40	528.2				4.2	0.30 ± 0.02	903
	80	527.2				4.3	0.31 ± 0.01	1748
	100	529.2				4.2	0.30 ± 0.01	2258
	150	526.2				4.3	0.31 ± 0.02	3278
[C$_8$C$_1$im][OTf]	20	475.2	283	0.10 [a)]	3.1	3.6	0.30 ± 0.01	521
	40	516.2				3.5	0.29 ± 0.02	1078
	80	478.2				3.5	0.29 ± 0.02	2155
	100	477.2				3.5	0.29 ± 0.01	2694
	150	480.2				3.5	0.29 ± 0.01	4041
[C$_n$C$_1$im][OTf] / substrate | substrates: ITO/glass partially cover with 40 nm Ag film								
[C$_8$C$_1$im][OTf]	20	516.2	283	0.10 [a)]	3.1	3.4	0.28 ± 0.02	521
	40	512.2				3.5	0.29 ± 0.01	1078
	80	513.2				3.7	0.31 ± 0.01	2155
	100	518.2				3.5	0.29 ± 0.01	2694
	150	522.2				4.2	0.35 ± 0.08	4041
[C$_n$C$_1$im][OTf] / substrate | substrates: ITO/glass (control samples)								
[C$_2$C$_1$im][OTf]	20	521.2	283	0.10 [a)]	3.1	4.0	0.29 ± 0.03	467
	40	520.2				4.3	0.31 ± 0.02	874
	80	523.2				4.3	0.31 ± 0.02	1748
	100	519.2				4.2	0.30 ± 0.01	2258
	150	519.2				4.3	0.31 ± 0.02	3278
[C$_8$C$_1$im][OTf]	20	512.2	283	0.10 [a)]	3.1	3.4	0.28 ± 0.05	558
	40	514.2				3.6	0.30 ± 0.02	1042
	80	510.2				3.6	0.30 ± 0.02	2083
	100	500.2				3.5	0.29 ± 0.01	2694
	150	513.2				3.6	0.30 ± 0.01	3906

a) Accurate data for the *EVP* of [C$_2$C$_1$im][OTf] and [C$_8$C$_1$im][OTf] were not found elsewhere. Nevertheless, there are reports on the determination of vaporization enthalpies indicating the lower volatility of the [OTf]-based ILs in comparison to their congeners [NTf$_2$]-based ILs. In fact, in this work, at the same evaporation temperature lower deposition rates were observed for [OTf]-based ILs. The *EVP* of [C$_2$C$_1$im][OTf] and [C$_8$C$_1$im][OTf] at the studied evaporation temperatures are estimated to be within the interval between 0.01 and 1 Pa. In addition, their *EVP* may be lower than observed for [C$_2$C$_1$im][NTf$_2$] and [C$_8$C$_1$im][NTf$_2$].

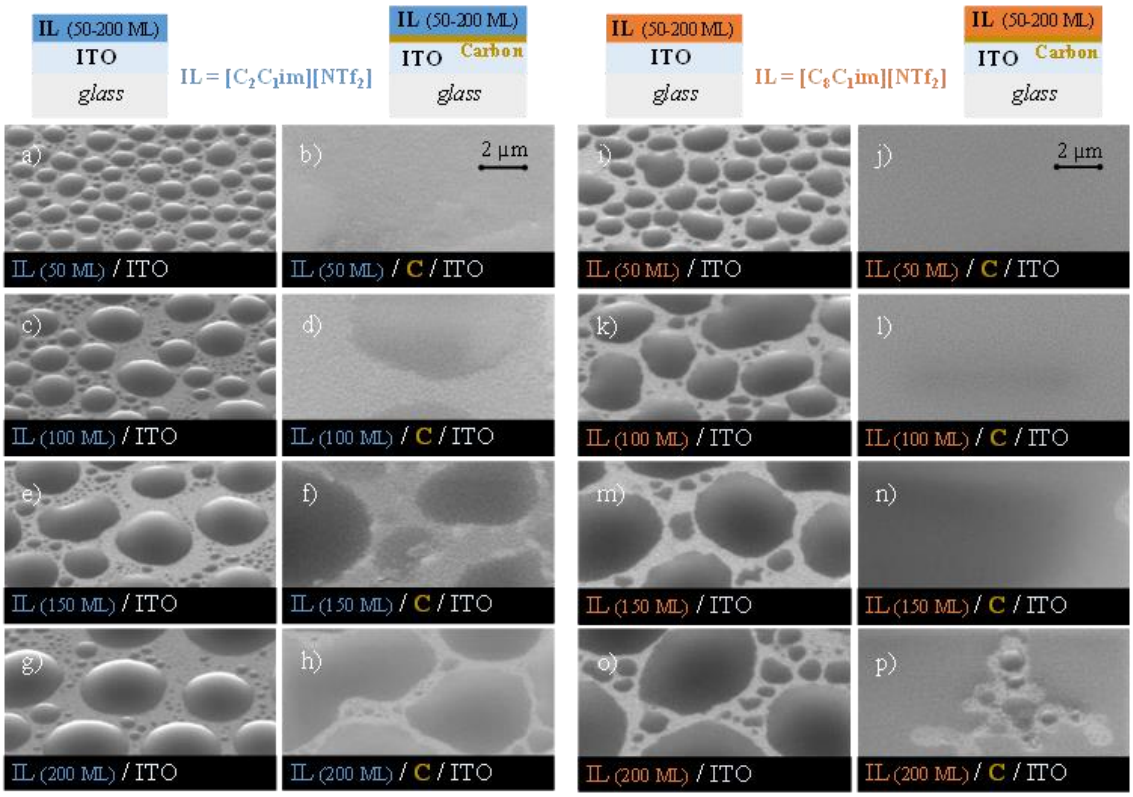

Figure A34. Morphology of the different films fabricated on ITO and C/ITO (carbon thickness ≈ 20 nm) surfaces. Detailed micrographs for $[C_2C_1im][NTf_2]$ (images a-h) and $[C_8C_1im][NTf_2]$ (images i-p). The deposition of each IL with different thicknesses (50 ML, 100 ML, 150 ML, and 200 ML) occurred simultaneously on both of the surfaces studied. Micrographs were acquired at a lateral view of 45° with a magnification of 20 000×, using a high-resolution SEM and employing a SE detector.

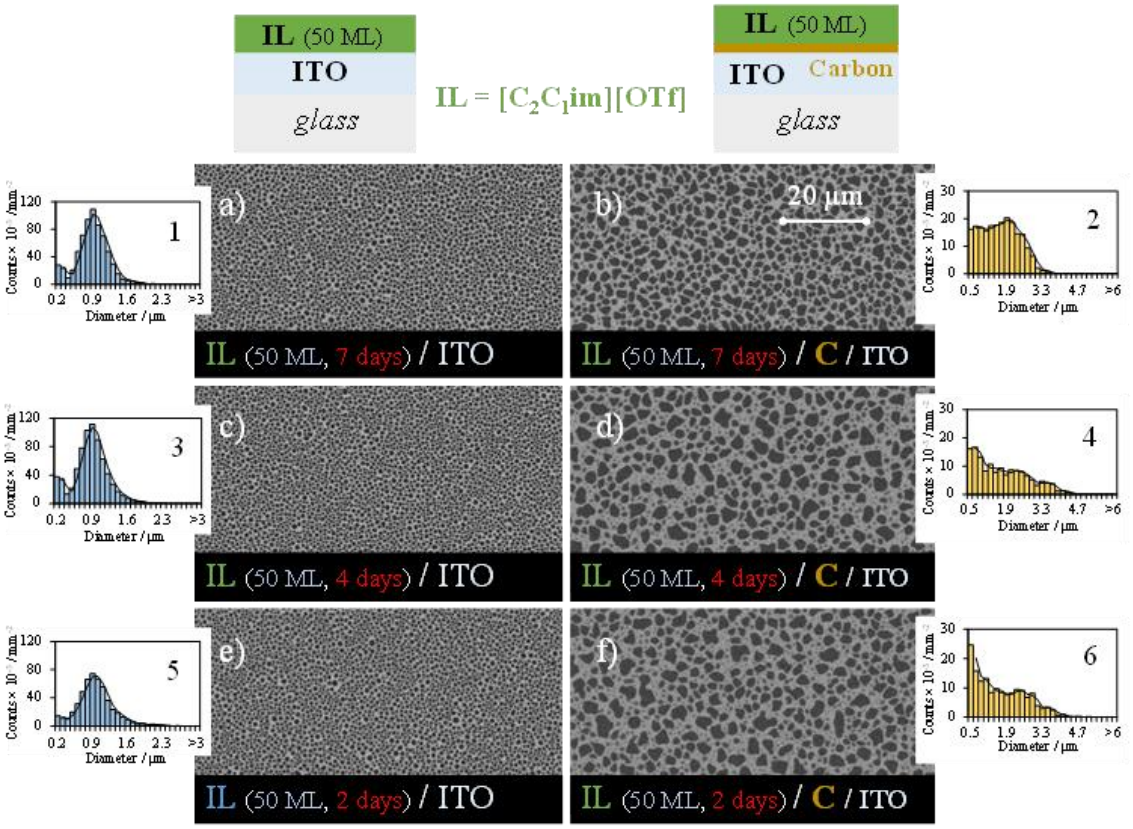

Figure A35. Detailed micrographs of [C_2C_1im][OTf] films deposited on ITO/glass (images a, c, and e) and carbon/ITO/glass surfaces (images b, d, and f). The SEM micrographs were obtained after 7 days (images a and b), 4 days (images d and f), and 2 days (images e and f) of film deposition. Histograms 1-6 present the droplet size distribution obtained for each sample. Both films were deposited under similar experimental conditions with a thickness of 50 ML on both surfaces. Micrographs were acquired with the SEM technique using a BSE detector.

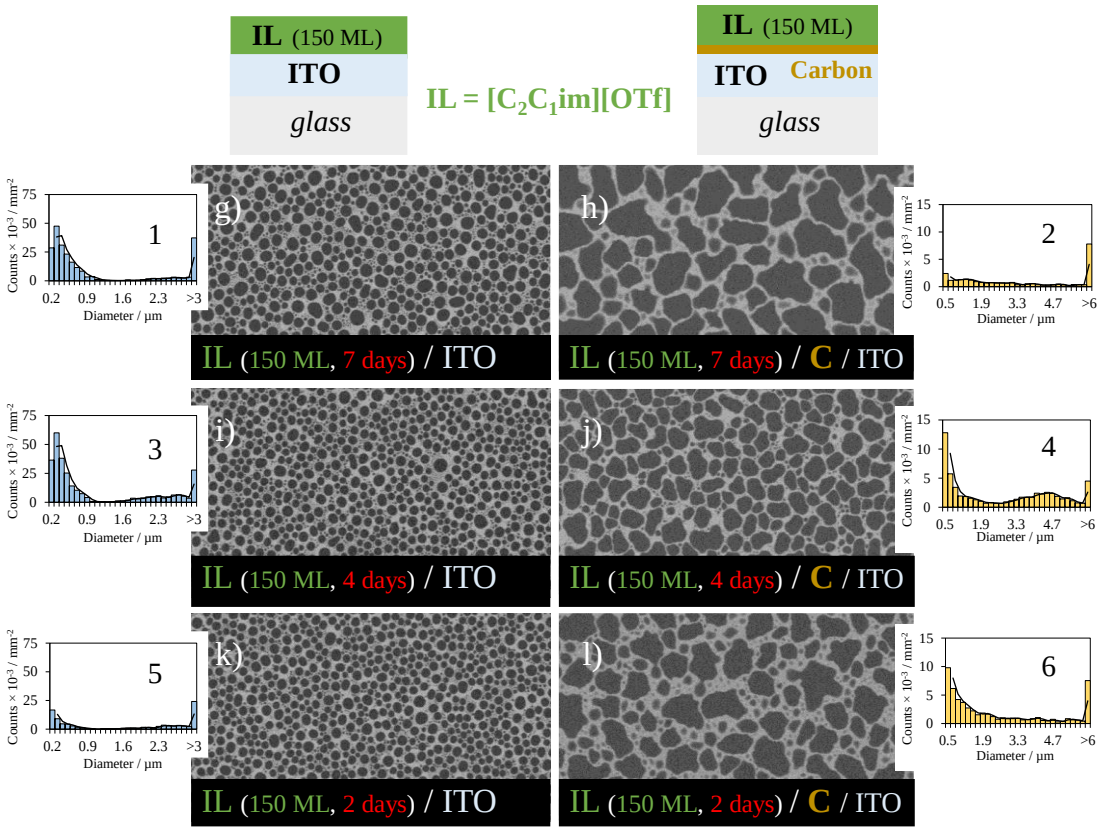

Figure A36. Detailed micrographs of $[C_2C_1im][OTf]$ films deposited on ITO/glass (images a, c, and e) and carbon/ITO/glass surfaces (images b, d, and f). The SEM micrographs were obtained after 7 days (images a and b), 4 days (images d and f), and 2 days (images e and f) of film deposition. Histograms 1-6 present the droplet size distribution obtained for each sample. Both films were deposited under similar experimental conditions with a thickness of 150 ML on both surfaces. Micrographs were acquired with the SEM technique using a BSE detector.

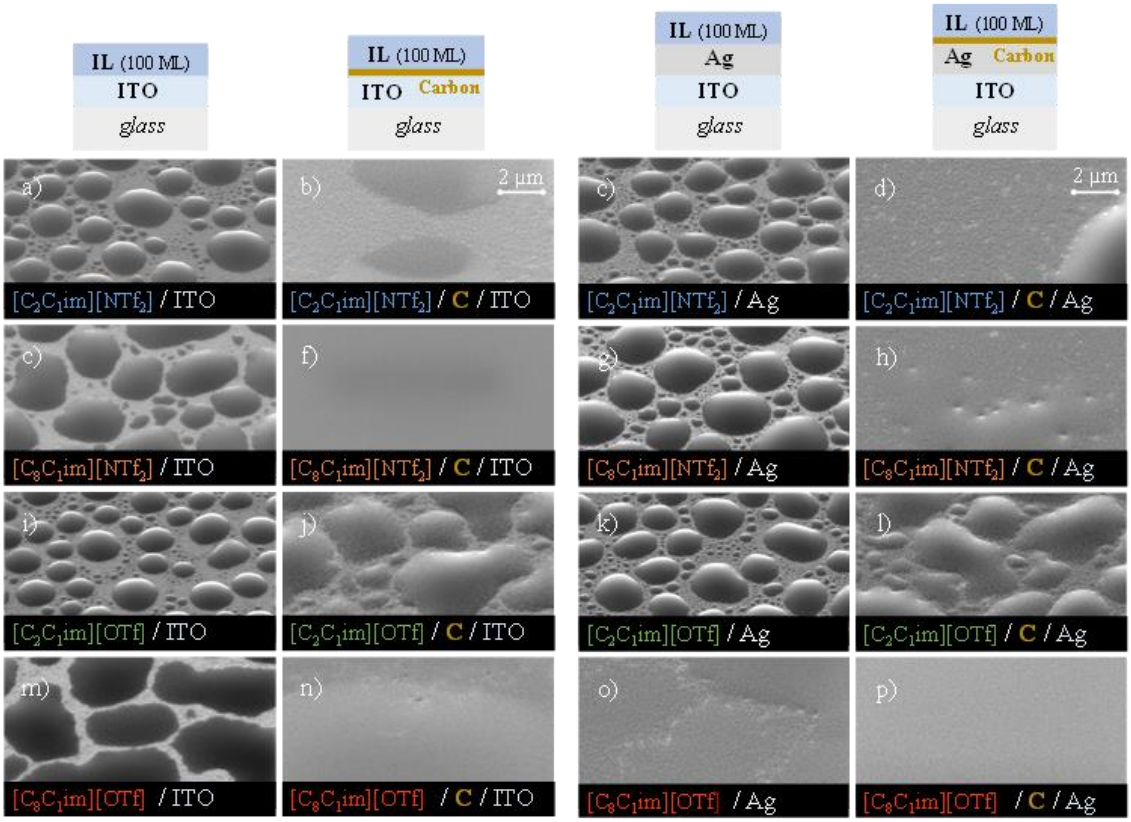

Figure A37. Detailed micrographs of the 100 ML thin films for $[C_2C_1im][NT_2]$ (images a-d), $[C_8C_1im][NTf_2]$ (images e-h), $[C_2C_1im][OTf]$ (images i-l), and $[C_8C_1im][OTf]$ (images m-p) deposited on the ITO (images a, e, i, m), C/ITO (b, f, j, n), Ag (c, g, k, o) and C/Ag (d, h, l, p) surfaces. It's worth noting that the carbon film used in all cases has a thickness of 20 nm, approximately. Simultaneous deposition of the IL film takes place on both the surface with the carbon film and the surface without it. Micrographs were acquired at a lateral view of 45° with a magnification of 20 000×, using a high-resolution SEM and employing a SE detector.

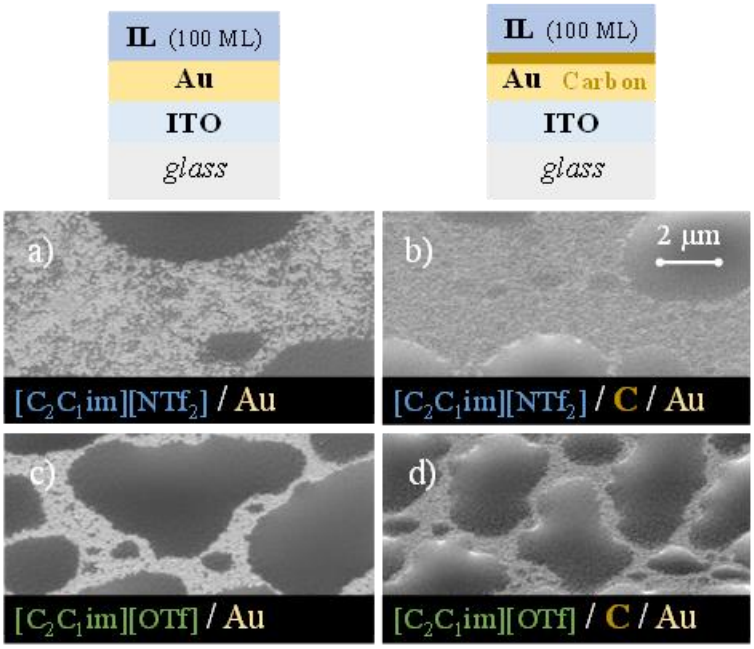

Figure A38. Detailed micrographs of 100 ML of $[C_2C_1im][NTf_2]$ (images a, b) and $[C_2C_1im][OTf]$ (images c, d) thin films, deposited on Au/ITO/glass (images a, c) and C/Au/ITO/glass (images b, d). It's worth noting that the carbon film used in all cases has a thickness of 20 nm, approximately. Simultaneous deposition of the IL film takes place on both the surface with the carbon film and the surface without it. Micrographs were acquired at a lateral view of 45° with a magnification of 20 000×, using a high-resolution SEM and employing a SE detector.

Table A4. Experimental conditions for the physical vapor deposition/thermal evaporation of each ionic liquid: monolayers (ML); effusion temperature ($T_{eff.}$); equilibrium vapor pressure (*EVP*); orifice diameter of the Knudsen effusion cell; substrate temperature ($T_{subst.}$); mass flow rate at the substrate surface [Φ (QCM)] and corresponding deposition rate in Å·s^{-1}; deposition time. Experimental variables related to the study of the influence of carbon on the morphology of different ionic liquids deposited at different quantities on ITO/glass surfaces and C/ITO/glass surfaces.

Precursor	ML	$T_{eff.}$	$T_{subst.}$	EVP[a]	Orifice diameter	Φ (QCM)	Deposition rate	Deposition time
		K	K	Pa	Mm	ng·cm^{-2}·s^{-1}	Å·s^{-1}	S
[C$_n$C$_1$im][NTf$_2$]/ substrate | substrates: ITO/glass; C/ITO/glass								
[C$_2$C$_1$im][NTf$_2$]	50	493.2	283.2	0.14	2.1	4.7	0.31 ± 0.02	1306
	100	491.2		0.13	2.1	4.9	0.32 ± 0.05	2512
	150	480.2		0.07	2.1	5.2	0.34 ± 0.07	3375
	200	498.2		0.19	2.1	5.6	0.37 ± 0.20	4260
[C$_8$C$_1$im][NTf$_2$]	50	501.2	283.2	0.14	2.1	4.1	0.31 ± 0.02	1500
	100	493.2		0.09	2.1	4.1	0.31 ± 0.02	2896
	150	498.2		0.12	2.1	3.9	0.30 ± 0.01	4331
	200	501.2		0.14	2.1	3.8	0.29 ± 0.05	5777

a) The EVP at each evaporation temperature was derived from literature data reporting volatility studies of the ILs: [C$_2$C$_1$im][NTf$_2$] and [C$_8$C$_1$im][NTf$_2$] [9].

Table A5. Experimental conditions for the physical vapor deposition/thermal evaporation of each ionic liquid: monolayers (ML); effusion temperature ($T_{eff.}$); equilibrium vapor pressure (*EVP*); orifice diameter of the Knudsen effusion cell; substrate temperature ($T_{subst.}$); mass flow rate at the substrate surface [Φ (QCM)] and corresponding deposition rate in Å·s^{-1}; deposition time. Experimental variables related to the study of the influence of carbon on the morphology of different ionic liquids deposited with 100 ML on the ITO/glass and C/ITO/glass, Ag/ITO/glass and C/Ag/ITO/glass surfaces, and Au/ITO/glass and C/Au/ITO/glass surfaces.

Precursor	Thickness	$T_{eff.}$	$T_{subst.}$	EVP	Orifice diameter	Φ (QCM)	Deposition rate	Deposition time
	ML	K	K	Pa	mm	ng·cm^{-2}·s^{-1}	Å·s^{-1}	S
[C$_n$C$_1$im][anion] / substrate | substrates: ITO/glass; C/ITO/glass								
[C$_2$C$_1$im][NTf$_2$]	100	491.2	283.2	0.13[a]	2.1	4.9	0.32±0.05	2512
[C$_8$C$_1$im][NTf$_2$]		493.2		0.09[a]	2.1	4.1	0.31±0.02	2896
[C$_2$C$_1$im][OTf]		543.2		[b]	2.1	4.0	0.29±0.02	2785
[C$_8$C$_1$im][OTf]		519.2		[b]	2.1	3.5	0.29±0.01	3080
[C$_n$C$_1$im][anion]/ substrate | substrates: Ag/ITO/glass; C/Ag/ITO/glass								
[C$_2$C$_1$im][NTf$_2$]	100	496.2	283.2	0.17[a]	2.1	4.4	0.29±0.02	2790
[C$_8$C$_1$im][NTf$_2$]		506.2		0.19[a]	2.1	4.1	0.31±0.01	3041
[C$_2$C$_1$im][OTf]		542.2		[b]	2.1	3.9	0.28±0.03	1306
[C$_8$C$_1$im][OTf]		505.2		[b]	2.1	3.6	0.30±0.02	2880
[C$_2$C$_1$im][anion] / substrate | substrates: Au/ITO/glass; C/Au/ITO/glass								
[C$_2$C$_1$im][NTf$_2$]	100	496.2	283.2	0.17[a]	2.1	4.6	0.30±0.01	2785
[C$_2$C$_1$im][OTf]		543.2		[b]	2.1	4.0	0.29±0.03	2867

a) The EVP at each evaporation temperature was derived from literature data reporting volatility studies of the ILs: [C$_2$C$_1$im][NTf$_2$] and [C$_8$C$_1$im][NTf$_2$] [9].

b) Accurate data for the EVP of [C$_2$C$_1$im][OTf] and [C$_8$C$_1$im][OTf] were not found elsewhere. Nevertheless, there are reports on the determination of vaporization enthalpies indicating the lower volatility of the [OTF]-based ILs in comparison to their congeners [NTf$_2$]-based ILs. In fact, in this work, at the same evaporation temperature lower deposition rates were observed for [OTf]-based. The EVP of [C$_2$C$_1$im][OTf] and [C$_8$C$_1$im][OTf] at the studied evaporation temperatures are estimated to be within the interval between 0.01 and 1 Pa. In addition, their EVP may be lower than observed for [C$_2$C$_1$im][NTf$_2$] and [C$_8$C$_1$im][NTf$_2$].

Table A6. Experimental conditions for the physical vapor deposition/thermal evaporation of each ionic liquid: monolayers (ML); effusion temperature ($T_{eff.}$); equilibrium vapor pressure (*EVP*); orifice diameter of the Knudsen effusion cell; substrate temperature ($T_{subst.}$); mass flow rate at the substrate surface [Φ (QCM)] and corresponding deposition rate in Å·s^{-1}; deposition time. Experimental variables related to the influence of carbon on the morphology of different ionic liquids deposited with 400 ML on the gold-coated quartz crystal (QC) and on the carbon-coated QC (C/QC).

Substrate	$T_{eff.}$	$T_{subst.}$	EVP[a)]	Orifice diameter	Φ (QCM)	Deposition rate	Deposition time
	K	K	Pa	Mm	ng·cm^{-2}·s^{-1}	Å·s^{-1}	s
[C_2C_1im][NTf_2]/ substrate							
QC	483.2	283.2	0.08	2.1	4.7	0.31 ± 0.05	9680
C/QC	480.2		0.07	2.1	4.6	0.30 ± 0.04	10165

a) The EVP at each evaporation temperature was derived from literature data reporting volatility studies of the ILs: [C_2C_1im][NTf_2] and [C_8C_1im][NTf_2] [9].

Table A7. Experimental conditions for the physical vapor deposition/thermal evaporation of each ionic liquid: monolayers (ML); effusion temperature ($T_{eff.}$); equilibrium vapor pressure (*EVP*); orifice diameter of the Knudsen effusion cell; substrate temperature ($T_{subst.}$); mass flow rate at the substrate surface [Φ (QCM)] and corresponding deposition rate in Å·s^{-1}; deposition time. Experimental variables related to the study of the influence of carbon thickness on the morphology of different ionic liquids deposited with 100 ML on ITO/glass substrates.

Precursor	Substrate	$T_{eff.}$	$T_{subst.}$	EVP	Orifice diameter	Φ (QCM)	Deposition rate	Deposition time
		K	K	Pa	mm	ng·cm^{-2}·s^{-1}	Å·s^{-1}	S
[$C_nC_1$im][OTf] (100ML) / substrate								
[C_2C_1im][OTf]	ITO	537.2	283	a)	2.1	4.0	0.29 ± 0.02	2660
	C(10 nm)	543.2			2.1	4.2	0.30 ± 0.02	2552
	C(20 nm)	528.2			2.1	4.3	0.31 ± 0.01	2340
	C(30 nm)	528.2			2.1	4.2	0.30 ± 0.03	2418
	Interface	531.2			2.1	4.3	0.31 ± 0.04	2300
[C_8C_1im][OTf]	ITO	506.2	283	a)	2.1	3.4	0.28 ± 0.02	2892
	C(10 nm)	525.2			2.1	3.5	0.29 ± 0.03	2785
	C(20 nm)	503.2			2.1	3.5	0.29 ± 0.01	2796
	C(30 nm)	510.2			2.1	3.4	0.28 ± 0.02	2876
	Interface	508.2			2.1	3.5	0.29 ± 0.02	2758

a) Accurate data for the EVP of [C_2C_1im][OTf] and [C_8C_1im][OTf] were not found elsewhere. Nevertheless, there are reports on the determination of vaporization enthalpies indicating the lower volatility of the [OTF]-based ILs in comparison to their congeners [NTf_2]-based ILs. In fact, in this work, at the same evaporation temperature lower deposition rates were observed for [OTf]-based. The EVP of [C_2C_1im][OTf] and [C_8C_1im][OTf] at the studied evaporation temperatures are estimated to be within the interval between 0.01 and 1 Pa. In addition, their EVP may be lower than observed for [C_2C_1im][NTf_2] and [C_8C_1im][NTf_2].